FIELD-DIRECTED FABRICATION OF HIERARCHICAL STRUCTURES TOWARD ELECTROCHEMICAL APPLICATIONS

by

Anirudh Balram

DISSERTATION

Submitted in partial fulfillment of the requirements
for the degree of Doctor of Philosophy at
The University of Texas at Arlington
August, 2017

Arlington, Texas

Supervising Committee:

Hyejin Moon, Committee Chair and Supervising Professor
Sunand Santhanagopalan, Co-advisor
Cheng Luo
Ashfaq Adnan
Jiechao Jiang

ABSTRACT

Field-Directed Fabrication of Hierarchical Structures

Toward Electrochemical Applications

Anirudh Balram, Ph.D.

The University of Texas at Arlington, 2017

Supervising Professor(s): Hyejin Moon and Sunand Santhanagopalan

The ubiquity of hierarchical structures in nature indicates an inherent advantage to having morphological features comprised of multiple length scales. Such structures help maximize interfacial surface area, allowing for efficient chemical reactions and mass transport despite volumetric constraints. In electrochemical applications such as batteries, supercapacitors, electrolysis, fuel cells, catalysis etc. there is a similar necessity to maximize electrochemically active surface area to facilitate facile charge and mass transport. Inspired by examples in nature, this work seeks to develop scalable fabrication techniques to obtain hierarchically structured high-performance electrodes for electrochemical applications, with a focus on energy applications. Particular emphasis was laid on improving oxygen evolution reaction and hydrogen evolution reaction catalyst performance in alkaline electrolytic water splitting, an extremely promising technology for a sustainable clean energy future. Utilizing field-directed nanomaterial assembly techniques such as electrophoretic deposition, electrodeposition, and magnetophoresis, a variety of carbon nanotube, metal and mixed-metal hydroxide based hierarchical

nanocomposites geared towards superior electrochemical performance were prepared. By virtue of the intimate attachment between various components within the deposits, synergistic performance enhancements could be exploited, greatly reducing water splitting overpotentials. Such high performance catalysts produced with earth abundant materials are critical to the large-scale viability of this technology. Additionally, these field-directed assembly techniques offer control over nanomaterial orientation in the deposits. Through rational choice of deposition technique, deposition parameters, and material selection, extreme surface wetting properties such as superhydrophobicity, superhydrophilicity, underwater superaerophobicity and superoleophobicity could be induced in some of the deposits. The ideas demonstrated in this work are broadly applicable toward the improvement of a variety of next generation electrochemical applications.

.

ACKNOWLEDGEMENTS

I would not be at this position had it not been for my incredible mentor, the late Dr. Dennis Desheng Meng. He is missed more than I could ever adequately convey here. Thank you, Dr. Meng for giving me an opportunity to work with you and for all the values you instilled in me.

I would like the acknowledge my committee members: Dr. Hyejin Moon, Dr. Cheng Luo, Dr. Jiechao Jiang, Dr. Ashfaq Adnan, and Dr, Sunand Santhanagopalan for their valuable time and inputs. Particularly Dr. Jiang, whose expertise, guidance, and assistance has been invaluable during the extensive material characterization required for my PhD research. I would also like to thank Dr. David Yan from the Characterization Center for Materials & Biology for all his help.

I would like to extend my sincere thanks to Dr. Erian Armanios who with his leadership and kindness has helped me (and the MuSES Lab) successfully navigate the last two years. A special thank you to all the support staff at the Mechanical and Aerospace department. I would like to thank past and present members of the MuSES Lab at UTA and Michigan Tech (Ryan Lemmens and Xiaobao Geng among others), who have all contributed in some capacity during my research. Particular mention to Hanfei Zhang, for all the TGA data he collected for me, taking time away from his own research.

I express my deepest gratitude to Dr. Hyejin Moon, who has been amazing with her support and time. I greatly appreciate what she has done for me over the past year and a half.

I would like to acknowledge National Science Foundation for the financial support (NSF Awards 1439494 and 1444473) and the Mechanical and Aerospace Engineering Department at

UTA for funding during the course of my study. I am also thankful for the support provided by the Graduate School in the form of the Summer 2017 Dissertation Fellowship.

I cannot express enough how important Dr. Sunand Santhanagopalan's role has been. I sincerely appreciate everything he has done for me over the last several years. Taking over under unbelievably challenging circumstances, he has done a phenomenal job bringing the lab to where it stands today. He has a tremendous ability to effectively manage multiple projects while never losing sight of the big picture. It is a quality I hope to have inherited in some measure from our time working together. It has been a great learning experience for me to watch him effectively manage completely different personality types to bring out the best in each of them. He has always been available with research advice, ideas, and remained a patient sounding board for my own ideas. Finally, our long animated chats about the state of Indian cricket kept me going during some of the toughest times.

DEDICATION

I have to thank my incredible mother and father for having kept me afloat all these years. Their unconditional love provided me a support structure without which I would have found myself completely lost on several occasions.

Thank you to my loving grandmothers, awesome aunts, and uncles for their constant support and encouragement. To my text buddies – Jez, Vishnu, my boys from The Council (Piyush, Saurabh, Mahir, Varun and Karan) – thank you for the laughs and virtual company during the many long lonely hours in the lab.

To my dissertation muse – thank you for providing me with inspiration when I needed it the most!

Madhavi & Rajeev, Unni & Dee- I love you all! Thank you for everything.

TABLE OF CONTENTS

CHAPTER 1

INTRODUCTION

1.1 Introduction

One of the most pressing needs of this century is the development of energy production, supply, and storage solutions with a minimal environmental footprint, particularly greenhouse gas emissions.[1-3] Meeting the energy needs of the future will involve significant improvement[3-5] in a wide variety of both, established as well as burgeoning electrochemical energy technologies ranging from fuel cells, photochemical and electrochemical water splitting, photovoltaics, supercapacitors, batteries such as flow batteries, sodium ion batteries and so on. Development of novel chemistries, materials and morphologies, along with improved electrode assembly techniques are all critical aspects of achieving next generation devices capable of meeting the escalating demands.[6-7] Efficient assembly techniques are especially necessary to be able to exploit maximum performance out of the various nanomaterials with unique morphological features that continue to be produced. For example, having control over assembly of 1D nanomaterials, like carbon nanotubes (CNT), in a desired orientation on a substrate of choice is essential in order to realize their true potential by minimizing losses and taking advantage of their unique morphological traits. In this particular instance, typically used chemical vapor deposition (CVD) while capable of producing vertically aligned CNT forests, tends to be limited in terms of substrate choice and size.[8]

Often, exciting hierarchical nanostructures are produced in ex situ methods such as hydrothermal synthesis with the traits desirable for an application. However, their morphological advantages can be diminished on account of limitations of the commonly used pasting based assembly techniques. The pasting technique essentially assembles randomly oriented nanomaterials within a non-conductive or low conductivity polymeric matrix,[9] negating any potential benefit offered by the unique nanostructure of the material. Another consideration especially for applications that

produce gaseous products (such as water electrolysis) is eliminating carbonaceous additives that diminish electrochemical performance by increasing hydrophobicity and increasing overall electrode impedance.[10] Ideally electrode assembly techniques should be able to provide a low impedance route for electron transfer from the active material to the current collector. Direct growth onto conductive substrates could provide direct conductive path from the nanomaterial to the current collector. For non-conductive or low conductivity active materials, decoration on a conductive pathway material such as carbon nanotubes, graphene etc. could reduce charge transfer impedance. Such intimate attachment has been known to generate synergistic enhancements that greatly boost performance.[11] Thus, assembly or deposition techniques should be able to engender an intimate attachment between the nanomaterial and substrate or alternatively an intimate bond between the nanomaterial and its conductive support which is then intimately attached to the current collector. Ability to control the morphology, orientation,[3] crystallinity[12] etc. *in situ*, directly on to the electrode would all be very useful in an assembly technique. There are other instances, however, where *ex situ* synthesis of the nanomaterial is more favorable and efficient assembly techniques that can maximize the nanomaterial's potential are essential.[13-14]

To this end, the work in this dissertation looks at primarily, but not exclusively, electric field-directed fabrication techniques for deposits geared towards excellent electrochemical performance. In the course of this work, several interesting phenomena as a consequence of the assembly method were observed and exploited as detailed in latter chapters. While the individual chapters will provide more detailed discussions, briefly, the field-directed deposition techniques developed and demonstrated in this dissertation work eliminate the need for polymeric binder significantly decreasing electrode impedances, could engender extreme wetting states (superhydrophobicity, superhydrophilicity, superaerophobicity, underwater superaerophobicity),

allow for control over the relative orientation of deposited nanomaterials, allow for *in situ* fabrication of hierarchical nanomaterial deposits, assemble nanomaterials produced *ex situ* while still exploiting their 1D dimensionality, help exploit some synergistic substrate/deposit interactions to name a few. Beyond the deposition techniques mentioned, extensive material and electrochemical characterization was also performed to improve and maximize electrochemical performance of deposits.

Toward the end of this chapter, brief descriptions and context to all the works that appear in the course of this document are presented. While a significant portion of this dissertation is dedicated to improving catalysis of water electrolysis, which is introduced in Section 1.2, similar principles can be employed to achieve hierarchical structures toward several other applications relevant to electrochemical applications. Broadly speaking, the foundational principles for improving the electrode performance, applied here prominently towards specific catalysis applications, are similar for most electrochemical applications. For instance, nanostructuring the active material, improving surface wettability to improve electrolyte access, reducing internal resistances within electrode architecture by avoiding binder or vertical alignment of nanomaterials, hierarchical structuring leading to efficient mass and charge transport by shortening diffusion distances are critical considerations for applications from HER, OER, ORR, supercapacitors, batteries, electrochemical detection of electroactive species and so on.[5, 10, 13, 15-17] In that sense, the scope and applicability of the principles and techniques presented in this work are quite broad.

1.2 The Importance of Electrochemical Water Splitting

The urgent need to mitigate the environmental and economic impact of unchecked CO_2 generated during energy consumption has brought to the forefront the need for carbon-neutral or carbon-free energy production. The 'hydrogen economy' is widely seen as a means to that end.[18-20] Since the

only by-product of hydrogen fuel cell operation is water,[21] it is a highly desirable clean power source. Hydrogen powered fuel cells are capable of producing energy for applications of smaller scale portable power applications, large-scale stationary power supply, and importantly, transportation applications.[21] The significant research and development with regard to fuel cells has brought about massive improvements and reduction in prices, although several technological challenges still remain. Apart from specific development of fuel cells systems, however, another aspect requires significant attention. Despite not being close to a hydrogen economy yet, hydrogen is an already highly utilized industrial commodity.[22]

A vast majority of this hydrogen is produced via steam reformation, not ideal given the associated CO_2 emissions.[22] Given the already high demand of hydrogen, the key is to produce the hydrogen used in the fuel cell by a carbon-free means, as opposed to say, running electrolysis powered via electricity generated via fossil fuels.[18] When the hydrogen used in the fuel cell is generated via clean renewable sources like wind and solar, the emission footprint of the power produced via the H_2 fuel cell can be close to zero. There has been progress around the world over recent years with respect to wind and solar energy.[23] The main drawback of these renewable sources, however, is their daily and seasonal fluctuations. The intermittency of these renewable resources means that reliable on-demand power supply is a challenge.[2, 19] A potential solution to this hurdle is seen to be power-to-gas conversion.[2, 24] This is where electrochemical systems can and will play a major role in harnessing the promise held by these clean energy sources. Electrochemical solutions are required both in the production as well as storage stages of this application. While improved electrocatalytic systems are required to efficiently split water to produce gas, electrochemical storage systems are also required to either store the intermittently produced energy or also convert the energy stored as hydrogen into usable electricity through fuel cells.

This is why a lot of attention was particularly focused on electrochemical water splitting reaction, in this work. Specifically, water electrolysis[25] could produce on a large scale, high purity hydrogen sustainably. The hydrogen thus acquired could power high efficiency and clean conversion systems such as a hydrogen fuel cells. It has also been proposed that hydrogen thus produced could be diverted to the natural gas infrastructure assisting with the cooling and heating needs.[24] While hydrogen production towards future energy needs is the main focus here, it is worth noting the widespread and growing industrial consumption of hydrogen even at the present moment.[26] Interestingly, a major roadblock when it comes to hydrogen production via water splitting tends to be overpotentials related to the counter electrode i.e. the oxygen producing electrode. This is a feature of the intrinsic sluggishness of the reaction that involves a four electron transfer process.[27] Therefore, while one of the manuscripts presented later directly addresses HER catalysis, three of the works demonstrated tackle the problem of minimizing OER catalysis during alkaline water electrolysis. While hydrogen remains the desired end product, it is important to note that the produced oxygen is also of commercial value and mitigating some of the associated costs of electrolysis.[28] As elaborated previously, hierarchical electrode structures were thus employed to try and minimize OER and HER overpotentials in a bid to reduce overall cell potentials required to split water. These hierarchical structures were completely bubble repellent in some cases and highly accessible to electrolyte leading to efficient catalysis in such gas producing reactions. In course of the studies, optimal substrate and deposit interactions were uncovered, leading to excellent OER and HER catalyst performance with low overpotentials, some among the lowest reported. The next section provides more detail into the motivation to generate such hierarchical structures and their significance.

1.3 Hierarchical Structures in Nature

Hierarchical structures are ubiquitous in nature. A primary reason is the incredible benefit such morphological features bring to organisms.[29] Unique wetting properties of surfaces in nature are the most readily apparent consequence of hierarchical structuring.[30] Natural hierarchically structured surfaces[31-34] like those seen on the Lotus leaf, Rose petals, insect wings etc. impart those surfaces with unique properties relating to water adhesion. The extreme non-wetting state, superhydrophobicity, arises when an inherently hydrophobic material (wax, in the case of the Lotus leaf) is hierarchically structured.[35] The multiple length scales of the micro/nanostructured surface when coupled with an intrinsically hydrophilic surface, on the other hand, bestow a superwetting quality to a surface.[31] This state of extreme water affinity results in phenomena such as superoleophobicity (oil repellence)[36] and superaerophobicity (bubble repellence) which are of tremendous practical importance.[31] The adhesion of the gecko to surfaces is also attributed to hierarchical features under their feet.[37]

While less intuitively apparent, a more significant benefit of hierarchical structures is seen in interfacial charge and mass transport phenomena as observed in mammalian lungs and vasculature, venation in leaves, roots, etc.[29, 38-40] The presence of hierarchical features is often critical to the survival of the organisms involved. The hierarchical structuring allows for confining of the organs in the available space, for example the chest cavity in the case of the human lungs,[38] while still maximizing the interfacial area available for efficient transfer of gaseous components required for survival. Similarly, the hierarchical structure is able to minimize the mass transport distances to optimize efficiency. Effectively developing such hierarchical structures of active materials on functional electrodes could revolutionize the performance of materials and surfaces used for electrochemical energy applications.[1, 3, 5, 39, 41] Field-directed methods are uniquely capable of

producing such structures. Rather than trying to strictly produce structures identical to the ones on nature, the work gains inspiration from the principles seen in nature that efficiently increase interfacial area and reactant accessibility.[30] The field directed methods studied and utilized in this work will be briefly introduced in the next section. More process specific details are provided in subsequent chapters as they appear.

1.4 Field-Directed Deposition Techniques

Electrophoretic deposition (EPD)

EPD is a very versatile nanomaterial assembly technique amenable to a wide variety of materials.[42] EPD was especially appealing on account of the ability to assemble desired nanomaterials that have already been produced by other ex situ techniques.[13-14] Typically, colloidal nanoparticles are deposited onto conductive substrates/electrodes via an applied electric field. The electrophoretic migration and deposition only occurs when the nanomaterials carry sufficient surface charge.[42] The key to facilitating EPD is to first produce nanomaterials suspensions containing adequately charged nanoparticles in the appropriate dispersion medium. The choice of dispersion medium can dictate the charge of the nanoparticles and also the electrode reactions during reactions. The surface charges could be native or externally induced via additives. Non-participating charging agents have previously been used to produce a stable suspension, but similar to the use of binders during paste-based electrode assembly, this leads to unnecessary impedance increases. In the work presented in this dissertation, nanoparticles- CNTs and stainless steel nanoparticles (SSNP) are charged with positively charged metal ions made available in the dispersion media by dissolving various metal salts. Upon contact with the electrode, they take the form of metals or metal hydroxides depending on electrode/electrolyte interfacial conditions present.[43] Thus polymeric binder-free functional electrodes could be prepared with excellent electrochemical applicability.

Significantly, EPD also provides the ability to control the orientation of 1D nanoparticles such as CNT, MnO_2 nanorods and so on.[13-14, 44] This allows for fabrication of relatively vertically aligned 1D nanomaterial deposits very advantageous electrochemical applications. As will be demonstrated in Chapter 2, EPD was utilized to produce hierarchical structures of metal decorated conductive CNTs deposits. EPD was also utilized in chapters 4, 5 and 6 to produce other functional deposits.

Electrodeposition

Electrodeposition is another highly versatile deposition technique to produce functional deposits for metals, metal hydroxides, metal oxides, phosphides, selenides and so on.[45-49] Most popularly, electroplating[50-51] is a widely used industrial technique for metal coating. Electrodeposition, like EPD, is also field directed. Metal ions present in the deposition solution migrate towards the appropriate electrode and are anodically or cathodically deposited (depending upon the formulation) under the influence of an electric field. The deposited material and morphology can be controlled by a variety of parameters such as solution pH, solvent medium, additives, temperature, ion concentration to name a few. This provides wide scope for control and manipulation of final deposit structure and properties. The electrodeposition technique presented in Chapter 3 utilizes water as an additive in an alcohol-based solvent medium to deposit unprecedented nanodendritic metal hydroxide deposits. The EPD techniques presented in Chapter 2, 4 and 5 although primarily may be considered EPD, a more accurate classification would be that they are a combination of EPD and electrodeposition. The combination of the two processes yields highly active catalyst deposits produced in situ on the electrode surface wherein all three components of the electrode – substrate and the two nanomaterials typically deposited, in this specific case – share intimate contact with each other. Finally, although lacking an externally

applied field, another deposition technique namely galvanic replacement[39] was also utilized to form hybrid CNT/metal hydroxide/platinum deposits in Chapter 5. The difference in electrode potentials of the components allows for spontaneous decoration of CNT/metal hydroxide deposits with the noble metal nanoparticles.

Magnetophoretic Deposition

Magnetophoretic assembly,[52] as the name suggests, involves the use of a magnetic field to accumulate and assemble nanomaterials. Unlike EPD, however, the process is limited to nanoparticles susceptible to the magnetic field. Significantly, structures such as magnetic nanotubes, nanorods etc. can be vertically aligned using a magnetic field. Using this principle, hollow nickel nanorolls produced in Chapter 6 were aligned vertically using a magnetic field and subsequently fixed in place using electroplating.

1.5 Outline of Chapters

Chapter 2: ***Electrophoretically-Deposited Metal-Decorated CNT Nanoforests with High Thermal/Electric Conductivity and Wettability Tunable from Hydrophilic to Superhydrophobic[53]***

This chapter demonstrates the ability of a field-directed assembly technique, electrophoretic deposition (EPD) as a facile means to produce hierarchical structures with unique wetting properties. The work presented in Chapter 2 demonstrates the ability of high-voltage electrophoretic deposition (HVEPD) to assemble in-situ, hierarchical conductive superhydrophobic surfaces. The ability to control the orientation during assembly while decorating with nanoparticles and induce extreme wettability could potentially be extended to a wide variety of 1D nanomaterials toward a variety of electrochemical applications. It documents a study

utilizing high-voltage EPD to produce deposits of hierarchical micro/nanostructures of metal nanoparticle decorated CNTs. Briefly, this work demonstrates a case of extreme wettability, namely superhydrophobicity. This wetting state of complete water repellence is induced specifically by virtue of the field-induced deposition process developed in this work. One factor is the hierarchical morphology involving a combination of micro and nanostructured surface features. The HV-EPD process employed here engenders this combination on account of the field induced alignment of the CNTs in the dispersion solution during deposition. By controlling the deposition voltage, the quantity of deposited CNT and their relative vertical alignment within the deposit can be manipulated. Such a surface texture can induce superhydrophobic behavior from a naturally hydrophobic material.

The choice of dispersant used also significantly affected the wetting nature of the CNT. Firstly, the choice of isopropanol allowed for metal decoration of the CNTs. Additionally, the hydrophobic moieties, likely adsorbed from the solvent during the CNT dispersion preparation process provided the CNT deposit an overall hydrophobic nature. This hydrophobic nature in combination with the hierarchical morphology could produce metal decorated superhydrophobic CNT deposits. Beyond a certain threshold voltage, the deposit is dense and 'rough' enough, consisting of an adequate combination of microscale and nanoscale features, which allow the deposit the resist penetration from a water droplet. The unique aspect of this work is that the deposits does not require any hydrophobic polymeric coating (PTFE, PDMS, Nafion etc.) typically employed for fabrication of superhydrophobic surfaces. Finally, using the knowledge gained on deposit wettability with respect to choice of dispersion medium, a facile technique was demonstrated to pattern superhydrophilic/superhydrophobic CNT surfaces.

Co-author contributions: Sunand Santhanagopalan contributed to this particular work by performing FESEM imaging (Figure 2 in Chapter 2). Boyi Hao assisted with collection of the FTIR data for the paper.

Chapter 3: ***Enhanced Oxygen Evolution Reaction Electrocatalysis via Electrodeposited Amorphous α-Phase Nickel-Cobalt Hydroxide Nanodendrite Forests***[54]

Having established the ability of field-based techniques to produce hierarchical structures with the work in Chapter 2, special effort was made to utilize similar principles to produce electrochemically relevant catalyst deposits with extreme wetting properties. In Chapter 3, another field-directed deposition technique namely, electrodeposition is demonstrated. Electrodeposition is a widely utilized versatile technique capable of producing a wide range of materials ranging from metals, metal oxides, hydroxides, selenides, phosphides etc. Nickel-based hydroxides are a specifically useful material utilized extensively in batteries and several other electrochemical applications. Particularly of interest is the performance of $Ni(OH)_2$ in catalyzing the OER reacting in alkaline water electrolysis. Consistently over the past few years, $Ni(OH)_2$ deposits have outperformed benchmark IrO_x catalysts. Due to their inherent hydrophilicity, hierarchical structures of $Ni(OH)_2$ and $Co(OH)_2$ would allow for excellent electrolyte penetration By utilizing a hydrogen –bubble templating based technique, novel metal hydroxide deposits were prepared. Typically such nanodendritic metal hydroxide electrodeposits have not been achieved, to the best of our knowledge. To achieve these unprecedented structures, the choice of solvent was a critical factor. Moving away from the aqueous solvents usually used for metal hydroxide deposition, the use of a primarily alcohol based medium. This allowed for the control of water content within the deposition solution.

The tuning of water content within the deposition solution, allowed for control over the rate of electrolysis i.e. the H_2 bubble production at the cathode during deposition. When appropriately controlled, these bubbles served as templates, guiding the growth of vertically aligned nanodendritic structures. Due to the locally generated alkaline conditions, the metal ions are forced to deposit in the form of the corresponding hydroxides. The technique was initially developed for $Ni(OH)_2$. But on account of its versatility was extended to $Co(OH)_2$ and various mixed nickel-cobalt hydroxides. On account of their unique hierarchical structure, vertical alignment, dense packing, and inherent hydrophilicity of the metal hydroxides, the resultant deposits show extreme wetting behavior. Unlike the previous superhydrophobic deposits in Chapter 1, these deposits show superhydrophilicity, i.e. complete wetting due to extreme water affinity and consequently superaerophobicity- complete bubble repellence when submerged under water. Consequently, their unique micro/nano structure leads to bubble repellent nature under water, critical to minimizing OER overpotentials in practical applications. Owing to their hierarchical structure, superaerophobicity, amorphous crystal structure and intimate contact with the substrate, these deposits could catalyze alkaline oxygen evolution at 10 $mA.cm^{-2}$ at as low as 255 mV on planar stainless steel substrates. This unique combination of properties, typically unattainable in conjunction, further ensures superior durability with trivial performance deterioration over 10,000 cycles.

These three-dimensional (3-D) nanodendrite forests of amorphous nickel-cobalt hydroxides geared towards outstanding oxygen evolution reaction (OER) catalysis. In our knowledge, such vertically-aligned nanodendritic structures of amorphous, mixed metal hydroxides are unprecedented. Elimination of non-conductive, non-participating binder coating, together with the orientation of the nanodendritic metal hydroxide structures ensures maximum electrolyte access

and catalyst availability. Owing to their hierarchical structure, superaerophobicity, amorphous crystal structure and intimate contact with the substrate, these deposits could catalyze alkaline oxygen evolution at 10 $mA.cm^{-2}$ at as low as 255 mV on planar stainless steel substrates. This unique combination of properties, typically unattainable in conjunction, further ensures superior durability with trivial performance deterioration over 10,000 cycles.

We propose a hydrogen bubble-templated deposition mechanism facilitated by carefully tuning the water content in a primarily alcohol based electrolyte. We attribute this dendritic growth to the controlled electrolysis of the small water content in the deposition solution. The facile technique allows for rapid fabrication of various mixed nickel-cobalt hydroxide deposits with similar morphological and wetting properties, making it highly versatile. The manuscript provides detailed electrochemical and material characterization for our samples, along with a brief exploration of optimal substrate in order to exploit maximal performance due to synergistic substrate/deposit interfacial interactions. Specifically, stainless steel substrates caused a significant lowering of OER overpotentials for all the samples tested The observation of stainless steel substrate induced enhancement of catalytic activity of $Ni(OH)_2$ towards OER is especially significant. Enhanced performance achieved via the inexpensive substrate merely by virtue of its presence greatly simplifies high activity catalyst fabrication, as will be demonstrated in Chapter 4.

Co-author contributions: Hanfei Zhang collected all the thermogravimetric analysis (TGA) data seen in Chapter 3. All other sample preparation, experimental design, execution and analysis, writing was performed by me.

Chapter 4: ***In Situ Decoration of Stainless Steel Nanoparticles for Synergistic Enhancement of α-Ni(OH)$_2$ Oxygen Evolution Reaction Catalysis***

Reliable high activity earth-abundant OER catalysts are critical for the large-scale economic viability of sustainable alkaline water splitting. Therefore, based on knowledge gained previously, we employed $Ni(OH)_2$ nanoparticles decorated on synergistic stainless steel nanoparticle support to produce durable OER catalysts capable of generating oxygen at extremely low overpotentials. Chapter 4 documents this work. Although it is known for noble metal nanoparticle supports to enhance OER activity of such materials, in our knowledge, exploiting the interaction between stainless steel nanoparticle support and $Ni(OH)_2$ has never been reported previously. The facile single-step, electrophoretic co-deposition process we demonstrate, allows for consistent production of excellent OER catalyst deposits with minimal process controls and inexpensive materials.

In 1 M KOH, our SSNP/$Ni(OH)_2$ deposits required an overpotential of only 220 and 250 mV to generate 10 and 125 mA cm^{-2} respectively. For higher current density applications, in 10 M KOH electrolyte, 500 mA cm^{-2} could be sustained at an overpotential of just 450 mV (*i*R-uncorrected). We attribute the enhanced performance to the serendipitous doping of the $Ni(OH)_2$ with some Fe from the steel support. To our best knowledge, this is the first work consciously employing the interaction between the stainless steel support and the α-$Ni(OH)_2$ deposit to enhance OER performance. Despite not having polymeric binders, our durable deposits survive the rigors of electrolysis with no apparent loss in activity even after 1000 accelerated stability test cycles and high current density electrolysis for long periods.

Co-author contributions: Hanfei Zhang collected the thermogravimetric analysis (TGA) curves in Chapter 4. All other sample preparation, experimental design, execution and analysis, writing was performed by me.

Chapter 5: ***Adaptable Electrophoretic Deposits of Amorphous Metal Hydroxide Decorated Carbon Nanotubes for Overall Water Splitting***

The focus then shifts to producing catalysts that can catalyze both sides of the water splitting reaction. From our knowledge, typically reported bifunctional OER/HER catalysts are generally excellent catalysts on one side of the reaction but often merely adequate or even mediocre on the other side. Our novel strategy therefore, as demonstrated in Chapter 5, is to produce an adaptable catalyst deposit that excels at one side of the reaction, as-prepared. At the same time, it should lend itself to subsequent modification such that it can optimally catalyze the other side of the reaction at minimal overpotentials. We demonstrate such adaptable mixed nickel-cobalt hydroxide decorated carbon nanotube (CNT) deposits produced with a versatile yet facile, single-step electrophoretic deposition (EPD) process. While we had previously utilized a completely aqueous medium to produce CNT/metal hydroxide deposits (Appendix A),[55] their adhesion was found lacking under the demanding conditions of electrolysis. Deposition medium was selected appropriately to ensure deposition of metal hydroxide which still ensuring the integrity of the deposit could be maintained. Like in the previous chapters, the ethanol-isopropanol based dispersion was found to be ideal. By eliminating non-participating binder and decorating amorphous nanoparticles intimately attached to the CNTs assembled in-situ on the substrate, we are able to obtain overall water-splitting at extremely low overpotentials. The as-produced CNT/nickel-cobalt hydroxide and modified novel hybrid CNT/Pt/nickel-cobalt hydroxide

deposits, in combination, could split water at only ~1.55 V (@10 $mA.cm^{-2}$) durably over 24 hours of testing in a two-electrode configuration.

As prepared, the CNT/nickel-cobalt hydroxide deposits on inexpensive steel mesh substrates could facilitate the oxygen evolution reaction at overpotentials as low as 245 mV @ 10 $mA.cm^{-2}$. These highly active deposits serve as ideal templates for further downstream modification to optimize their HER catalyst performance. As a demonstration, we modified these deposits by further decorating them with platinum nanoparticles using a simple galvanic replacement process. This unique material combination could overcome the kinetic bottlenecks experienced by metal hydroxide and platinum when used in isolation to generate hydrogen. Specifically, the quaternary hybrid containing CNT, Ni-Co hydroxide and Pt nanoparticles could generate hydrogen at 10 $mA.cm^{-2}$ at an overpotential of merely 50 mV. It is worth noting that such metal hydroxides are typically the precursors to other noble-metal free formulations capable of excellent HER catalysis such as metal/metal oxide hybrids, phosphides, nitrides etc. The versatility afforded by the CNT/metal hydroxides deposits with regard to subsequent phase transformation could open exciting opportunities both in water-splitting applications as well as other areas of electrochemistry.

Co-author contributions: Again, Hanfei Zhang collected the thermogravimetric analysis (TGA) curves in Chapter 5. All other sample preparation, experimental design, execution and analysis, writing was performed by me.

Chapter 6: ***Scalable Fabrication of Vertically Aligned Nanomaterial Coated Hierarchical Structures via Self-wound Nickel Nanomembranes***

Beyond the work already discussed, Chapter 6 combines several field-based assembly techniques namely electodeposition, magnetophoretic deposition, as well as electrophoretic deposition to

fabricate unique hierarchical structures. The strategy was to develop high surface area 3D Ni structures to serve as a conductive backbone amenable to deposition using techniques introduced thus far. Typically 3D substrates have been limited to nickel or copper foams. Utilizing strain engineered self-wound Ni nanomembranes assembled via magnetophoretic alignment and electroplating, 3D nickel substrates can be deposited for potentially high surface area substrates. The hollow nickel posts can serve as conductive paths efficiently carrying current down to the substrate from the active materials, while offering a high surface area for nanomaterial deposition. In this proof of concept work, first a scalable electroplating/wet etching technique to produce self-wound nickel nanomembranes is demonstrated. Subsequently, the high aspect ratio hollow Ni nanocylinders were assembled the magnetophoretically. Using EPD, several nanomaterials such as CNT, MnO_2 nanorods, $Ni(OH)_2$ nanodendrites could then be deposited on these structures creating truly hierarchical structures. This work utilizes all the knowledge gained in the course of this work to produce truly hierarchical structures with dimensions ranging from 100s of microns to a few nanometers.

Chapter 7: *Conclusion*

This final chapter contains concluding remarks and observations with some exploration of potential future work stemming from the projects detailed in this dissertation document.

1.6 References

1. Hwan Ko, S. Chapter 1. Introduction: Hierarchical Nanostructures for Energy Devices. **2014,** 1-6.

2. Gahleitner, G. Hydrogen from Renewable Electricity: An International Review of Power-to-Gas Pilot Plants for Stationary Applications. *International Journal of Hydrogen Energy* **2013,** *38*, 2039-2061.

3. Liu, J.; Cao, G.; Yang, Z.; Wang, D.; Dubois, D.; Zhou, X.; Graff, G. L.; Pederson, L. R.; Zhang, J. G. Oriented Nanostructures for Energy Conversion and Storage. *ChemSusChem* **2008,** *1*, 676-97.

4. Mulder, F. M.; Weninger, B. M. H.; Middelkoop, J.; Ooms, F. G. B.; Schreuders, H. Efficient Electricity Storage with a Battolyser, an Integrated Ni–Fe Battery and Electrolyser. *Energy and Environmental Science* **2017,** *10*, 756-764.

5. Bueno, P. R.; Gabrielli, C. Electrochemistry, Nanomaterials, and Nanostructures. **2009,** 81-149.

6. Mao, S. S.; Shen, S.; Guo, L. Nanomaterials for Renewable Hydrogen Production, Storage and Utilization. *Progress in Natural Science: Materials International* **2012,** *22*, 522-534.

7. Liu, C. J.; Burghaus, U.; Besenbacher, F.; Wang, Z. L. Preparation and Characterization of Nanomaterials for Sustainable Energy Production. *ACS Nano* **2010,** *4*, 5517-26.

8. Tsuji, T.; Hata, K.; Futaba, D. N.; Sakurai, S. Unexpected Efficient Synthesis of Millimeter-Scale Single-Wall Carbon Nanotube Forests Using a Sputtered MgO Catalyst Underlayer Enabled by a Simple Treatment Process. *Journal of the American Chemical Society* **2016,** *138*, 16608-16611.

9. Ludwig, B.; Zheng, Z.; Shou, W.; Wang, Y.; Pan, H. Solvent-Free Manufacturing of Electrodes for Lithium-Ion Batteries. *Scientific reports* **2016,** *6*, 23150.

10. Wang, H.; Lee, H. W.; Deng, Y.; Lu, Z.; Hsu, P. C.; Liu, Y.; Lin, D.; Cui, Y. Bifunctional Non-Noble Metal Oxide Nanoparticle Electrocatalysts through Lithium-Induced Conversion for Overall Water Splitting. *Nature Communications* **2015,** *6*, 7261.

11. Liang, Y.; Li, Y.; Wang, H.; Zhou, J.; Wang, J.; Regier, T.; Dai, H. Co_3O_4 Nanocrystals on Graphene as a Synergistic Catalyst for Oxygen Reduction Reaction. *Nature Materials* **2011,** *10*, 780-6.

12. Koza, J. A.; He, Z.; Miller, A. S.; Switzer, J. A. Electrodeposition of Crystalline Co_3O_4—a Catalyst for the Oxygen Evolution Reaction. *Chemistry of Materials* **2012,** *24*, 3567-3573.

13. Santhanagopalan, S.; Balram, A.; Meng, D. D. Scalable High-Power Redox Capacitors with Aligned Nanoforests of Crystalline MnO_2 Nanorods by High Voltage Electrophoretic Deposition. *ACS Nano* **2013,** *7*, 2114-25.

14. Santhanagopalan, S.; Teng, F.; Meng, D. D. High-Voltage Electrophoretic Deposition for Vertically Aligned Forests of One-Dimensional Nanoparticles. *Langmuir* **2011,** *27*, 561-9.

15. Li, Y.; Zhao, C. Enhancing Water Oxidation Catalysis on a Synergistic Phosphorylated NiFe Hydroxide by Adjusting Catalyst Wettability. *Acs Catal* **2017,** *7*, 2535-2541.

16. Chen, T.; Zhang, Q.; Xu, J.; Pan, J.; Cheng, Y.-T. Binder-Free Lithium Ion Battery Electrodes Made of Silicon and Pyrolized Lignin. *RSC Advances* **2016,** *6*, 29308-29313.

17. Li, Z.; Xin, Y.; Zhang, Z.; Wu, H.; Wang, P. Rational Design of Binder-Free Noble Metal/Metal Oxide Arrays with Nanocauliflower Structure for Wide Linear Range Nonenzymatic Glucose Detection. *Scientific reports* **2015,** *5*, 10617.

18. Gökçek, M. Hydrogen Generation from Small-Scale Wind-Powered Electrolysis System in Different Power Matching Modes. *International Journal of Hydrogen Energy* **2010,** *35*, 10050-10059.

19. Preuster, P.; Alekseev, A.; Wasserscheid, P. Hydrogen Storage Technologies for Future Energy Systems. *The Annual Review of Chemical and Biomolecular Engineering* **2017,** *8*, 445-471.

20. Bockris, J. O. M. The Hydrogen Economy: Its History. *International Journal of Hydrogen Energy* **2013,** *38*, 2579-2588.

21. Hoogers, G. *Fuel Cell Technology Handbook*. CRC press: **2002**.

22. Kalamaras, C. M.; Efstathiou, A. M. Hydrogen Production Technologies: Current State and Future Developments. *Conference Papers in Energy* **2013,** *2013*, 1-9.

23. Peters, G. P.; Andrew, R. M.; Canadell, J. G.; Fuss, S.; Jackson, R. B.; Korsbakken, Jan I.; Le Quéré, C.; Nakicenovic, N. Key Indicators to Track Current Progress and Future Ambition of the Paris Agreement. *Nature Climate Change* **2017,** *7*, 118-122.

24. Jentsch, M.; Trost, T.; Sterner, M. Optimal Use of Power-to-Gas Energy Storage Systems in an 85% Renewable Energy Scenario. *Energy Procedia* **2014,** *46*, 254-261.

25. Wang, M.; Wang, Z.; Gong, X.; Guo, Z. The Intensification Technologies to Water Electrolysis for Hydrogen Production – a Review. *Renewable & Sustainable Energy Reviews* **2014,** *29*, 573-588.

26. Levin, D. B.; Chahine, R. Challenges for Renewable Hydrogen Production from Biomass. *International Journal of Hydrogen Energy* **2010,** *35*, 4962-4969.

27. Gong, M.; Li, Y.; Wang, H.; Liang, Y.; Wu, J. Z.; Zhou, J.; Wang, J.; Regier, T.; Wei, F.; Dai, H. An Advanced Ni-Fe Layered Double Hydroxide Electrocatalyst for Water Oxidation. *Journal of the American Chemical Society* **2013,** *135*, 8452-5.

28. Kato, T.; Kubota, M.; Kobayashi, N.; Suzuoki, Y. Effective Utilization of by-Product Oxygen from Electrolysis Hydrogen Production. *Energy* **2005,** *30*, 2580-2595.

29. Zheng, X.; Shen, G.; Wang, C.; Li, Y.; Dunphy, D.; Hasan, T.; Brinker, C. J.; Su, B. L. Bio-Inspired Murray Materials for Mass Transfer and Activity. *Nature Communications* **2017,** *8*, 14921.

30. Nosonovsky, M.; Bhushan, B. Multiscale Effects and Capillary Interactions in Functional Biomimetic Surfaces for Energy Conversion and Green Engineering. *Philos Trans A Math Phys Eng Sci* **2009,** *367*, 1511-39.

31. Feng, X. J.; Jiang, L. Design and Creation of Superwetting/Antiwetting Surfaces. *Advanced Materials* **2006,** *18*, 3063-3078.

32. Su, Y.; Ji, B.; Huang, Y.; Hwang, K. C. Nature's Design of Hierarchical Superhydrophobic Surfaces of a Water Strider for Low Adhesion and Low-Energy Dissipation. *Langmuir* **2010,** *26*, 18926-37.

33. Koch, K.; Barthlott, W. Superhydrophobic and Superhydrophilic Plant Surfaces: An Inspiration for Biomimetic Materials. *Philosophical Transactions. Series A, Mathematical, Physical, and Engineering Sciences* **2009,** *367*, 1487-509.

34. Koch, K.; Bhushan, B.; Barthlott, W. Multifunctional Surface Structures of Plants: An Inspiration for Biomimetics. *Progress in Materials Science* **2009,** *54*, 137-178.

35. Bhushan, B.; Jung, Y. C. Natural and Biomimetic Artificial Surfaces for Superhydrophobicity, Self-Cleaning, Low Adhesion, and Drag Reduction. *Progress in Materials Science* **2011,** *56*, 1-108.

36. Zhang, H.; Balram, A.; Meng, D. D.; Sun, Y. Optofluidic Lasers with Monolayer Gain at the Liquid–Liquid Interface. *ACS Photonics* **2017,** *4*, 621-625.

37. Boesel, L. F.; Greiner, C.; Arzt, E.; del Campo, A. Gecko-Inspired Surfaces: A Path to Strong and Reversible Dry Adhesives. *Advanced Materials* **2010,** *22*, 2125-37.

38. Glenny, R. W. Emergence of Matched Airway and Vascular Trees from Fractal Rules. *Journal of Applied Physiology* **2011,** *110*, 1119-29.

39. Trogadas, P.; Ramani, V.; Strasser, P.; Fuller, T. F.; Coppens, M. O. Hierarchically Structured Nanomaterials for Electrochemical Energy Conversion. *Angewandte Chemie International Edition* **2016,** *55*, 122-48.

40. Coppens, M.-O. A Nature-Inspired Approach to Reactor and Catalysis Engineering. *Current Opinion in Chemical Engineering* **2012,** *1*, 281-289.

41. Wang, M.; Yu, X.; Wang, Z.; Gong, X.; Guo, Z.; Dai, L. Hierarchically 3D Porous Films Electrochemically Constructed on Gas–Liquid–Solid Three-Phase Interface for Energy Application. *Journal of Materials Chemistry A* **2017,** *5*, 9488-9513.

42. Boccaccini, A. R.; Keim, S.; Ma, R.; Li, Y.; Zhitomirsky, I. Electrophoretic Deposition of Biomaterials. *Journal of the Royal Society, Interface* **2010,** *7 Suppl 5*, S581-613.

43. Mishra, M.; Sakka, Y.; Uchikoshi, T.; Besra, L. pH Localization: A Case Study During Electrophoretic Deposition of Ternary Max Phase Carbide-Ti_3SiC_2. *Journal of the Ceramic Society of Japan* **2013,** *121*, 348-354.

44. Santhanagopalan, S.; Balram, A.; Lucas, E.; Marcano, F.; Meng, D. D. S. High Voltage Electrophoretic Deposition of Aligned Nanoforests for Scalable Nanomanufacturing of Electrochemical Energy Storage Devices. *Key Engineering Materials* **2012,** *507*, 67-72.

45. Masud, J.; Swesi, A. T.; Liyanage, W. P.; Nath, M. Cobalt Selenide Nanostructures: An Efficient Bifunctional Catalyst with High Current Density at Low Coverage. *ACS Applied Materials & Interfaces* **2016,** *8*, 17292-302.

46. Li, Y.; Zhang, H.; Xu, T.; Lu, Z.; Wu, X.; Wan, P.; Sun, X.; Jiang, L. Under-Water Superaerophobic Pine-Shaped Pt Nanoarray Electrode for Ultrahigh-Performance Hydrogen Evolution. *Advanced Functional Materials* **2015,** *25*, 1737-1744.

47. Lu, Z.; Sun, M.; Xu, T.; Li, Y.; Xu, W.; Chang, Z.; Ding, Y.; Sun, X.; Jiang, L. Superaerophobic Electrodes for Direct Hydrazine Fuel Cells. *Advanced Materials* **2015,** *27*, 2361-6.

48. Therese, G. H. A.; Kamath, P. V. Electrochemical Synthesis of Metal Oxides and Hydroxides. *Chemistry of Materials* **2000,** *12*, 1195-1204.

49. Plowman, B. J.; Jones, L. A.; Bhargava, S. K. Building with Bubbles: The Formation of High Surface Area Honeycomb-Like Films via Hydrogen Bubble Templated Electrodeposition. *Chemical Communications* **2015,** *51*, 4331-46.

50. Electrochemical, S. *Modern Electroplating / Edited by Frederick A. Lowenheim*. Wiley: New York [N.Y.], **1974**.

51. Schlesinger, M.; Paunovic, M. *Modern Electroplating*. John Wiley & Sons: **2011**; Vol. 55.

52. Wright, A. C.; Faulkner, M. Magnetophoretic Assembly and Printing of Nanowires. *Journal of Vacuum Science & Technology B, Nanotechnology and Microelectronics: Materials, Processing, Measurement, and Phenomena* **2012,** *30*, 021603.

53. Balram, A.; Santhanagopalan, S.; Hao, B.; Yap, Y. K.; Meng, D. D. Electrophoretically-Deposited Metal-Decorated Cnt Nanoforests with High Thermal/Electric Conductivity and Wettability Tunable from Hydrophilic to Superhydrophobic. *Advanced Functional Materials* **2016,** n/a-n/a.

54. Balram, A.; Zhang, H.; Santhanagopalan, S. Enhanced Oxygen Evolution Reaction Electrocatalysis Via Electrodeposited Amorphous α-Phase Nickel-Cobalt Hydroxide Nanodendrite Forests. *ACS Applied Materials & Interfaces* **2017**.

55. Balram, A.; Jiang, J. C.; Hernández Fernández, M.; Meng, D. D. S. Nickel-Cobalt Double Hydroxide Decorated Carbon Nanotubes Via Aqueous Electrophoretic Deposition Towards Catalytic Glucose Detection. *Key Engineering Materials* **2015,** *654*, 70-75.

CHAPTER 2

ELECTROPHORETICALLY-DEPOSITED METAL-DECORATED CNT NANOFORESTS WITH HIGH THERMAL/ELECTRIC CONDUCTIVITY AND WETTABILITY TUNABLE FROM HYDROPHILIC TO SUPERHYDROPHOBIC

Balram, A.; Santhanagopalan, S.; Hao, B.; Yap, Y. K.; Meng, D. D. Electrophoretically-Deposited Metal-Decorated CNT Nanoforests with High Thermal/Electric Conductivity and Wettability Tunable from Hydrophilic to Superhydrophobic. *Adv. Funct. Mater.* **2016,** *26*, 2571-2579.

2.1 Abstract

We report a single-step, room-temperature and scalable electrophoretic deposition (EPD) process to form nanocomposites on any electrically conductive surface with metal nanoparticle decorated carbon nanotubes (CNTs). The contact angles (CA) can be easily tuned from ~60 to 168 degrees by varying the deposition voltage, while hydrophobicity and superhydrophobicity surprisingly arise from the hydrophilic CNTs being deposited. The relatively high voltage tends to vertically align CNTs during deposition, leading to architectural micro/nano-scale roughness on the surface. The combination of the multi-scale roughness along with the low surface energy of hydrocarbon functional groups on the CNT surface has enabled facile wettability control, including the Petal and Lotus effects. Further, the relatively vertical orientation of the CNTs, without any coating, allows for current and heat transfer along their axis with superior conductivity. Similar behavior in terms of CA control is seen for all three divalent metal ions in the deposition solution (i.e., Cu^{2+}, Ni^{2+} and Zn^{2+}) that are used to charge the CNTs while eventually getting co-deposited. This implies that this method could possibly be extended to other metals by selecting appropriate charging salt. A patterning technique is also demonstrated for facile fabrication of superhydrophobic CNT-metal islands surrounded by hydrophilic CNT coating.

2.2 Introduction

Control of surface wettability has been proven as a powerful tool in many applications such as microfluidics,[1-3] fuel cells[4] and phase-change heat transfer[5, 6]. Particularly, superhydrophobic surfaces with water contact angles (CA) larger than 150^{o} have garnered a lot of interest due to their unique properties such as drag-reduction,[7] corrosion-prevention,[8] anti-icing,[9, 10] self-cleaning,[11, 12] etc. However, it is usually difficult to simultaneously achieve stable superhydrophobicity and high thermal/electric conductivity, which can be very beneficial in many of the aforementioned applications, where electrochemical and thermal transportation processes are usually involved simultaneously. In practice, a superhydrophobic surface is usually obtained by increasing roughness of a surface in conjunction with a reduction in surface free energy. In the lotus leaf,[7] for example, this is achieved through micro and nanoscale protuberances on the surface of the leaf, coupled with the low surface energy of its waxy coating. As a result, water droplets can easily roll off the leaf to clean the leaf. It is thus natural that most methods reported in literatures employ two steps to mimic the nature-inspired superhydrophobic surfaces. Firstly, surface roughness is increased using methods such as microfabrication of pillars,[13] electrodeposition under varying conditions,[14-16] etching,[17] block co-polymer based patterning[18] etc. Then a coating of low surface energy polymers (e.g., PTFE[19, 20] or PDMS[21]) are typically required to reduce the surface energy. However, the polymer coatings usually render lower thermal and electric conductivities to the surface. The adhesion between polymer and other substance has been known as typically weak, which can impair the long-term reliability of the surface especially when subjected to severe environments. Although chemical modification or functionalization has also been reported,[15, 16] such processes are often time

consuming and require toxic materials. The thermal stability and long-term durability can also be a concern.[22]

Carbon nanotubes (CNTs)[23] offer a unique solution for superhydrophobic surfaces. At the same time, CNTs are known for their very high thermal/electric conductivity along their longitudinal axes. Indeed, large CA of more than 150^{o} have been previously observed on vertically aligned forests of pristine carbon nanotubes (VACNTs) grown by chemical vapor deposition (CVD).[24] However, the CVD process can be a major challenge for many practical applications due to the harsh deposition conditions, particularly high temperature, and limitations on substrate material and size. Moreover, a water droplet placed on the pristine VACNTs tends to penetrate the CNT forests after a few minutes due to the relatively high surface energy of the graphitic CNT side walls, leading to the loss of superhydrophobicity.[19] Therefore, coating with low surface energy[19] polymers is still typically applied in these cases to prevent liquid penetration, inevitably leading to the issues previously discussed. Recent efforts have been reported to achieve superhydrophobic surfaces using graphitic materials such as carbon nanotubes (CNT)[9, 25] and graphene[26] without any polymer coatings. However, the reported methods offer little control over the orientation of the deposited nanomaterials, resulting in randomly-oriented bundles instead of aligned nanoforests. It is thus not the preferable way to take advantage of the anisotropic high thermal/electric conductivity of CNT and graphene. In addition, most of the existing fabrication methods do not offer a convenient way to obtain a wide range of tunable contact angles, particularly when the CNTs need to be decorated with nanoparticles[27] of metals or their compounds (e.g., oxides or hydroxides) to enhance their catalytic activity or energy storage capacity in electrochemical devices.

Electrophoretic deposition (EPD)[28, 29] has been explored in recent years as a versatile, scalable, economical, facile, room-temperature method to deposit a variety of nanomaterials. The existing reports of superhydrophobic coatings produced by EPD usually employ spherical particles with additional non-conductive coatings.[21, 30, 31] Previous works by our team[32, 33] have demonstrated the ability to control the orientation of electrophoretically deposited one-dimensional (1D) nanomaterials such as CNT and MnO_2 nanorods. The technology has also been employed to align[34] highly crystalline MnO_2 nanorods as high-performance redox capacitors with excellent durability along with demonstration of a continuous deposition process to scale up the fabrication.[34] It is thus established that vertical alignment of these nanoparticles can be achieved by polarizing them with strong electric field. In such a process, named high-voltage EPD (HVEPD), a thin metallic holding layer is also co-deposited to keep the nanoforest vertically aligned after deposition while a relative low concentration of nanomaterial is adopted in the dispersion to prevent bundle formation during the polarization process.

In this work, we further exploit this method to deposit CNT-metal nanocomposites with controlled alignment and microstructure under room temperature and mild environment. Meanwhile, we report that the contact angle of the nanocomposite surface can be reliably tuned from ~60° to 168° by simply manipulating the deposition voltage. Since the hydrophobicity and superhydrophobicity have been achieved without polymer coating, the nanocomposites also show high thermal/electric conductivity, an ideal characteristic for electrochemical and thermal applications. Furthermore, it is found that small amount of metal, from the extra precursor for the metallic holding layer, can be co-deposited to decorate the individual nanotubes. The unique properties of CNTs can thus be further coupled with metal decoration to potentially enhance their catalytic activity or energy storage capacity in electrochemical devices. Patterning surfaces with

regions of different wettability[35, 36] may lead to certain exciting capability for applications such as cell culture and heat transfer[5]. In this work, such a capability is demonstrated by fabricating superhydrophobic CNT-metal islands surrounded by a coating of hydrophilic CNTs. The process is achieved by a single physical mask with a low-cost, lithography-free masking technique, while the second deposition (*i.e.*, hydrophilic CNTs around superhydrophobic islands) is masked by self-assembled gas bubbles. We thus demonstrate EPD as a facile technique to obtain patternable tunable wettability with the potential to treat any conductive substrate, including those with large areas.

2.3 Results and Discussion

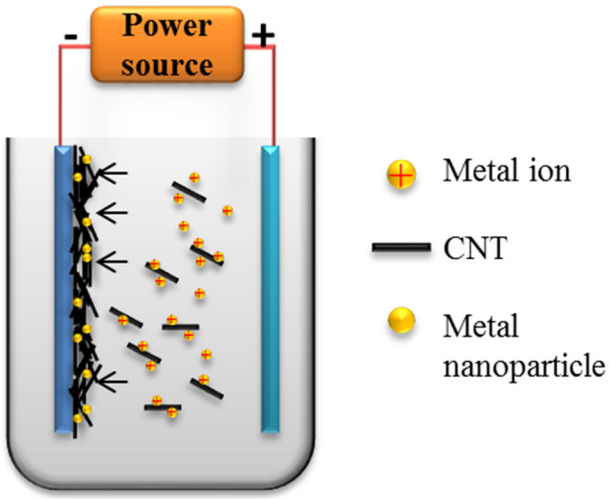

Figure 2-1 Working mechanism of electrophoretic deposition (EPD) of CNT-metal nanocomposites.

As seen in **Figure 2-1**, EPD involves the use of the voltage-induced migration of charged colloidal particles in a liquid medium towards an oppositely-charged electrode, which leads to

their eventual deposition onto that surface. For that purpose, it is typically essential to suspend the particles in a medium wherein it carries sufficient charge so as to produce a stable dispersion in which nanomaterials remain suspended instead of agglomerating and settling down. Moreover, the rate of deposition and the quality of the deposits (in terms of uniformity and adhesion to the substrate) is also greatly influenced by the charges on the dispersed nanomaterials. In the approach reported herein, the CNTs have been pre-treated by acid, which introduces the polar functional groups onto their surface and enables their dispersion in IPA *via* ultrasonication. However, the negative charges of the IPA-dispersed CNTs are often found insufficient to support their effective deposition using EPD. In order to improve the deposition characteristics of the dispersed CNTs, charging agents such as surfactants[37] and charging salts[32, 33, 38] are often used. The metal salts dissolved in the dispersion medium typically provide metal ions with positive charges to the CNTs. During the ultrasonication process, the positively-charged metal ions can be adsorbed onto the surface of the dispersed CNTs on account of the weak negative charges of the latter. As a result, CNTs in the dispersion are rendered net positive charges, which can be adjusted to the appropriate value so that the EPD deposition characteristics can be improved tremendously. Therefore, when an electric field is applied between the two electrodes, the charged CNTs along with the free metal ions in the solution move towards the negatively charged electrode. Upon contact with the negative electrode, the CNTs are deposited while metal ions are simultaneously reduced on the CNT surface at the adsorbed locations (to form metal nanoparticles) as well as the substrate (to form the holding layer for the CNTs). The selection of isopropyl alcohol (IPA) as the dispersion medium allows for the use of high voltages without the problems associated with electrolysis in aqueous media.

As **Figure 2-2** shows, the values of static contact angles show a clear trend of increasing with the deposition voltage, while other conditions maintaining constant (e.g., salt concentration and deposition time). As the deposition voltage increased from 50V to 550V, the static contact angles measured on the surfaces increased from ~60° to over 160°. For all three divalent metal ions that were used to charge the CNTs (i.e., Cu^{2+}, Ni^{2+} and Zn^{2+}), a near identical correlation between the contact angle and the deposition voltage is seen, indicating that the wettability of the deposits is independent of the type of metal being co-deposited. Such observation implies that the wettability of the deposit is primarily controlled by the CNTs. The contact angle of ~60° at low deposition voltage resembles that of bare stainless steel substrate which is measured as 52°. The steady increase in hydrophobicity of the surface with deposition voltage when it is relatively low can thus firstly be attributed to an increased coverage of the substrate surface by CNTs. Since the deposition time remains constant in all cases, larger amount of CNTs reach the steel electrode surface at higher deposition voltage as predicted by Hamaker's equation.[39] As the steel surface is increasingly covered with CNTs, a droplet placed on the surface would make more contact

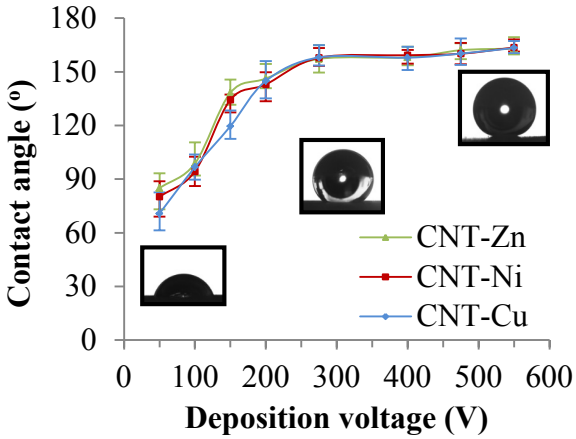

Figure 2-2 The contact angle of CNT-metal nanocomposites as a function of the deposition voltage. The contact angle is seen to steadily increase with an increase in deposition voltage due to the increased amount of CNT being deposited and their vertical alignment.

with the CNT deposit and less contact with the underlying steel substrate. Consequently, there is a continuous change in contact angle as the depositions are carried out at higher voltages.

However, the deposition voltage serves a far more important role beyond merely increasing the amount of CNTs deposited in a given time. At higher deposition voltage, the electric field during deposition controls the surface wettability mainly by influencing the orientation of the deposited CNTs and thus the surface roughness. It is known that the surface roughness can have a profound impact on the wetting behavior of a surface, which has been exemplified by many superhydrophobic surfaces that are obtained by roughening hydrophobic surfaces.[40, 41] As previously mentioned, voltage-induced torque exerted on nanotubes has been previously employed during EPD to deposit nanoforests with vertical alignment. Beyond a certain threshold, the voltage serves to overcome the Brownian motion while exerting a torque on the nanotubes/nanorods and aligning them along the electric field.

When the nanotube makes contact with the substrate, the metal ions adsorbed on the CNT surface will be quickly reduced to form the nuclei for metal nanoparticles. Meanwhile, the free metal ions in the dispersion will be reduced (i.e., electrodeposited) simultaneously, forming a layer of metal to hold the aligned nanotubes in position. **Figure S2-3a-c** further illustrates the change in orientation as well as the tremendous increase in the number of the deposited CNTs as a function of the deposition voltage. To simplify, all the SEM images are of CNT-Ni deposits, since the deposits with the other two types of metal show similar characteristics. CNT-Ni deposits were thus reported as the representative cases. It can also be seen that in the case of deposits at relatively low voltage, for example, 50V (**Figure 2-3a**), the CNTs are primarily oriented horizontally. However, when deposition voltage increases, as seen in the side-view

image of the deposit in **Figure 2-3b-c**, the orientation of many deposited CNTs becomes relatively vertical, with their tips exposed and sticking out of the bundles.

The change in orientation from relatively horizontal to relatively vertical with increasing deposition voltage if further corroborated by the Raman spectra of the deposits shown in **Figure S2-1**. As noted in previous polarized Raman studies of MWCNTs,[42, 43] the Raman intensity of D and G-band of CNT are orientation dependent. Specifically, weakest scattering intensities are

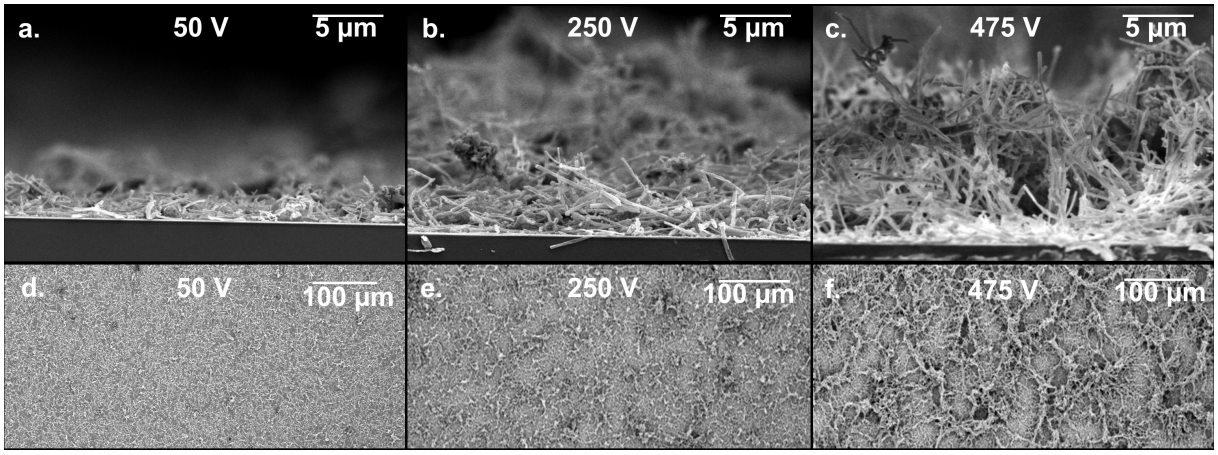

Figure 2-3 a-c) FE-SEM images show that the morphology of the deposited CNT-Ni nanocomposites evolves with deposition voltage of 50, 250 and 475V respectively. The orientation of the deposited CNTs changes from horizontal at 50V to vertically aligned at 475V due to voltage-induced polarization of the CNTs during EPD. d-f) FE-SEM images of top views of CNT-Ni corresponding to a-c respectively. Patterns can be clearly seen to emerge as deposition voltage increases and gives rise to micro- and nanoscale roughness.

obtained when nanotube axis is perpendicular to the exciting laser beam. In our case, such a scenario arises in the 50 V sample where the deposition voltage is unable to induce alignment via

polarization. Thus, the primarily horizontally aligned MWCNTs as obtained at 50 V consistently produce the lowest Raman intensities for both the D and G- band peaks seen at 1310 and 1590 cm^{-1} respectively. All samples produced at voltages higher than 50 V show ~25% higher peak intensity owing to their relative vertical orientation as compared to the low voltage sample. No significant differences are seen among the deposits made at higher voltages. This is reasonable considering the randomness in terms of alignment angle inherent in the orientation of the CNTs within these deposits.

Contrary to the behavior of surfaces coated by EPD spherical nanoparticles where roughness and consequently CA decrease with increased time of deposition,[21] surface roughness increases tremendously during EPD of the CNT-metal nanocomposites at a voltage enough to introduce polarization and thus vertical alignment. As a result, roughness and hydrophobicity increase dramatically with either voltage or deposition time. As previously revealed, after the first few vertically-aligned CNTs are deposited on the substrate, these aligned CNTs tend to distort the electric field around them, resulting in clusters of vertically oriented CNTs as the deposition process progresses.[33] This is particularly apparent in the case of the 475 V deposit, where deposition of the CNTs continues to preferentially occur around these clusters and leads to the narrowing of the gap between them. Consequently, a denser array of interconnected clusters starts to form and give rise to consistent microscale roughness seen as the patterns on the deposited surface (**Figure 2-3f**). The increased microscale roughness causes the air trapped below the droplets to cushion a water droplet and dramatically reduce the area of the solid-liquid contact. In combination with the protruding nanoscale tips of the aligned CNT, the interconnected CNT clusters provide hierarchical micro-nano roughness, a preferable recipe for heterogeneous solid-air-water interface and thus reliable superhydrophobicity.[44]

Merely static CA, however, does not completely describe the wetting nature of a surface or the behavior of a droplet on it. In addition to the static CA, contact angle hysteresis, *i.e.*, the difference between the advancing and receding contact angles is another important consideration for superhydrophobic surfaces. For surfaces such as a Lotus leaf, low contact angle hysteresis indicates that the droplet can easily roll off the surface at a typical tilt angle of $<10^{o}$. Meanwhile, another interesting phenomenon has been observed, for example, in several Rose species, wherein despite large CA, droplets remain impinged on the surface. In this case, the droplet pinning despite high static contact angles has been attributed to high CA hysteresis and called 'sticky' superhydrophobicity or the petal effect. **Figure S2-2** of the Supplemental Information shows deposit at 250 V with a static CA of 154^{0} (*i.e.,* superhydrophobic), while the hysteresis value of 46^{0} indicates the highly adhesive nature of the droplet to the surface. To illustrate this, the inset shows a droplet pinned on the surface even when surface is held perpendicular. However, as **Figure S2-3** shows, when the deposition voltage is increased beyond 275 V, the CA hysteresis value dramatically drops to $\sim 2^{o}$ indicating the low adhesion of the droplet to the surface which has been confirmed by observing the droplets rolling off the surface at low angles of tilt without leaving a water trace. Gao and McCarthy[45] revealed the importance of the combination of nanoscale topological features with microscale roughness in terms of reducing contact angle hysteresis. Work by Bhushan and Her[46] also showed the important roles of the spacing between the micro-features and the nanoscaled roughness in determining the adhesion properties of the superhydrophobic surfaces. In brief, the spacing between the micro-features allows for droplet penetration within them, known as Cassie impregnating state. On the other hand, the nanoscale roughness brings about the apparent high contact angles because the air

trapped within them can help to cushion the droplet. This phenomenon has attracted attention for applications such as transferring low-volume liquid droplets.

As previously mentioned, the microscale roughness in the CNT-metal deposits arises from the vertically-oriented CNT clusters along with the nanoscale roughness produced by the exposed tips of CNTs. At 250 V, although alignment due to polarization and subsequent bundle formation occurs, the distance between the clusters is still large, as shown in Figure 2-S2, which allows for droplet penetration and subsequent pinning of the droplet to the surface. In contrast, **Figure S2-4** shows a much denser array of interconnected clusters due to the higher deposition voltage, leading to a low adhesion surface with small CA hysteresis. This kind of combination of micro and nanostructures provides for lower contact area with the droplet, prevents droplet penetration and gives rise to the Cassie-Baxter state. Therefore, the reported EPD method can be used to control not only the static CA of a surface but also the CA hysteresis and the adhesion between the droplet and the surface.

Deposits made at 275, 400, 475 and 550 V all showed superhydrophobic property as characterized by the CA > 150^{o} observed in Figure 2. However, given the differences in the amount of CNTs deposited at higher voltages along with the corresponding reduction in the spacing between the observed structures, one expects a difference in maximum hydrostatic pressure that the deposits can sustain. We estimated the critical transition pressure from the Cassie state to the Wenzel state of wetting by immersing our superhydrophobic samples to various depths of water until wetting occurred.[47] Figure S2-5a shows a representative image of the plastron or the thin air film formed on an immersed deposit when viewed at an appropriate angle.[48] When transition occurred, the silvery layer can be seen to rapidly dissipate making the

underlying CNT coating visible (Figure S2-5b). The 275 V sample sustained the lowest pressure of around 1 kPa after which higher pressures i.e. greater immersion depths resulted in wetting the sample. [49] Sample prepared at 400 V was able to sustain 2-3 kPa pressure corresponding to 20-30 cm depth of immersion. The samples prepared at 475 and 550 V were able to sustain the plastron even at 10 and beyond 12 kPa (the maximum pressure we obtained) respectively owing to their denser and more closely packed structures. Figure S2-6 shows representative tilted FE-SEM views of 275 V and 550 V samples illustrating the denser, almost honeycomb-like structure

of the deposit made at the higher voltage. It should be noted that 12 kPa was the highest pressure that could be applied using our setup. The 550 V sample could perhaps tolerate significantly higher pressures before transiting to the Wenzel state. These results suggest that static CA alone

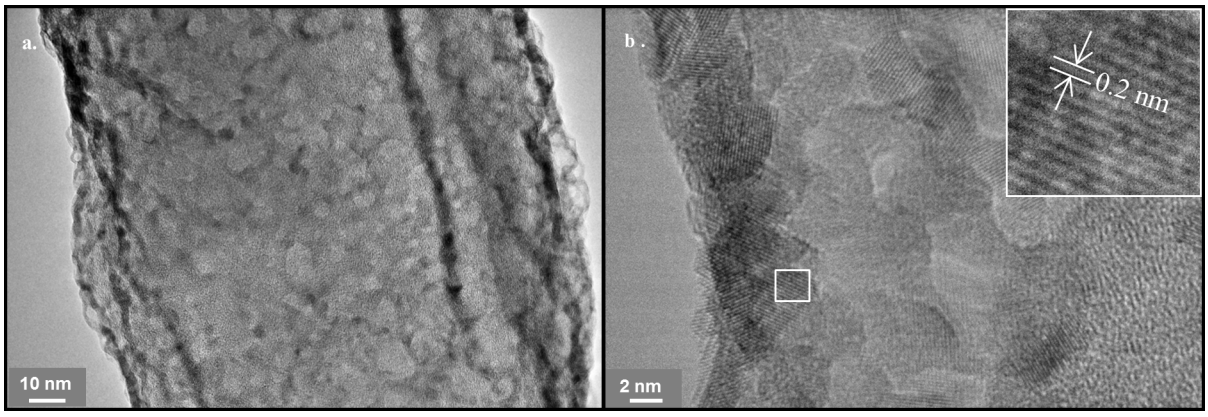

Figure 2-4 a, b) HR-TEM images of CNT-nickel nanocomposites showing deposits of nanoscale nickel on the CNT surfaces at lower and higher magnifications respectively. Inset in (b) shows lattice spacing of corresponding to the (111) plane of nickel.

is insufficient in revealing the true nature of the samples.

Figure 2-4 shows HR-TEM images of the CNT-Ni nanocomposite. The images show nanoparticles (<10 nm) decorating the surface of the nanotubes. (Similar images of CNT-Cu and CNT-Zn are shown in Figure S2-7.) Certain regions that appear darker in the images indicate a larger amount of deposited metal in those regions. This can be attributed to the higher density of functional groups in these regions due to the acid refluxing process. Since the functional groups provide anchoring sites for the metal ions, more functional groups at a certain location will cause for a greater number of metal ions to be adsorbed and eventually reduced. The variation in the size of nanoparticles can thus also be understood as a reflection of the metal ion adsorption capacity of a certain region on the surface of a specific CNT.

In this study, we employ acid-refluxing to functionalize the CNTs and allow for more metal deposition sites on their sidewalls. It is worth noting that the acid-treated CNTs were highly hydrophilic prior to the deposition. This can be attributed to the hydrophilic polar functional groups introduced onto the CNT surface during acid treatment. It is thus surprising that these CNT-metal nanocomposite coatings, once deposited, display hydrophobic and even superhydrophobic behavior. Therefore, merely microscopic morphology, such as the confirmed hierarchical micro/nano roughness, does not sufficiently explain the dramatic reverse in wettability show by these deposits (*i.e.*, superhydrophobic coating from highly hydrophilic raw material). Intuitively, a water droplet is expected to easily infiltrate the forest of CNTs because of the high surface energy of their sidewalls and thus wet the surface. To uncover the reason behind this reverse in wetting behavior of the refluxed CNTs upon deposition, Fourier Transform Infrared Spectroscopy (FTIR) studies were carried out on the acid-refluxed hydrophilic CNTs before deposition as well as the superhydrophobic CNT-metal nanocomposite after deposition.

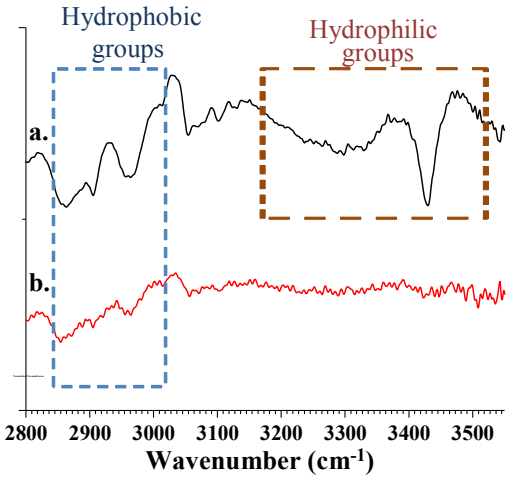

Figure 2-5 a) FTIR spectra of refluxed CNTs, shows hydrophilic functional groups (-OH) as well as hydrophobic hydrocarbon functional groups (*i.e.,* $=CH_2$ and $-CH_3$), with the -OH groups arising from acid treatment prior to EPD; b) FTIR spectra of the CNT-metal composite shows only the presence of hydrophobic groups between 2800 and 3000 cm^{-1} which render the deposits hydrophobicity, while hydrophilic -OH groups are no longer detected. This adsorption of low surface energy groups along with the surface roughening effect during deposition are credited with the superhydrophobic behavior of the deposits.

The FTIR spectrum of the acid-treated CNTs, as seen in **Figure 2-5a** shows the presence of polar -OH groups on the surface of the CNTs arising from the introduction of additional carboxylic acid (-COOH) groups in the heated acidic environment. As a result, the CNTs are rendered hydrophilic after acid treatment, in spite of the coexistence of the hydrophobic non-polar groups. On the other hand, the FTIR spectrum of the CNT-Ni composite in **Figure 2-5b** no longer shows the presence of polar functional groups while the hydrophobic non-polar groups still remain on the surface of the CNTs. This phenomenon, critical for the superhydrophobicity

and wettability control, can be attributed to three mechanisms, most likely their combination. First of all, the polar functional groups on the surfaces of CNTs have been replaced by metal ions. Metal ions are known to be adsorbed onto the CNT surfaces by replacing the H^+ from the polar functional groups introduced on the surfaces of CNT by acid refluxing.[50] As a result, the hydrophilic functional groups are replaced by the ions of nickel, copper or zinc, leaving the hydrophobic non-polar functional groups to dominate the surface property and returning the CNTs to their native hydrophobic state with low surface energy.

Secondly, with regard to the origin of the adsorbed hydrophobic groups responsible for the lowering of the overall surface energy of the deposits, we believe there are two possible explanations. These hydrophobic groups may originate from solvent molecules adsorbed from the dispersion medium during processing prior to deposition and/or from hydrocarbon molecules spontaneously adsorbed from the atmosphere after deposition. The physical adsorption of hydrophobic functional groups via the dispersion medium onto the CNT surfaces during the ultrasonication process could primarily contribute to reducing the overall surface energy of the deposits. This phenomenon has been previously reported in the solvent based contact angle control in graphene deposits[26, 51] and also the fabrication of superhydrophobic CNT coating from an acetone based solution.[9, 52] The ultrasonication of CNTs in isopropanol during the preparation of the CNT dispersion prior to EPD provides ample opportunity for the adsorption of adventitious solvent molecules. Thirdly, the deposited CNT-metal surfaces may be spontaneously adsorbing atmospheric hydrocarbons after the deposition process. Recent reports of stable superhydrophobic surfaces from boron nitride nanotubes[51] without any additional treatments have uncovered a dramatic change in surface energy emerging from the adsorption of non-polar hydrocarbon groups present in the atmosphere. The initially high surface energies of

nanomaterials arising from surface defects, their curvature,[52] have been attributed to this spontaneous adsorption of hydrocarbons, as in the case of boron nitride nanotubes. Such spontaneous adsorption has been seen even in the case of metallic surfaces[53] and could be occurring with the metallic nanoparticles on the CNT surfaces in our deposits. The low surface energy of the CNTs due to the aforementioned mechanisms, together with the electric field induced micro- and nanoscale roughness explains the observed wettability control over a wide

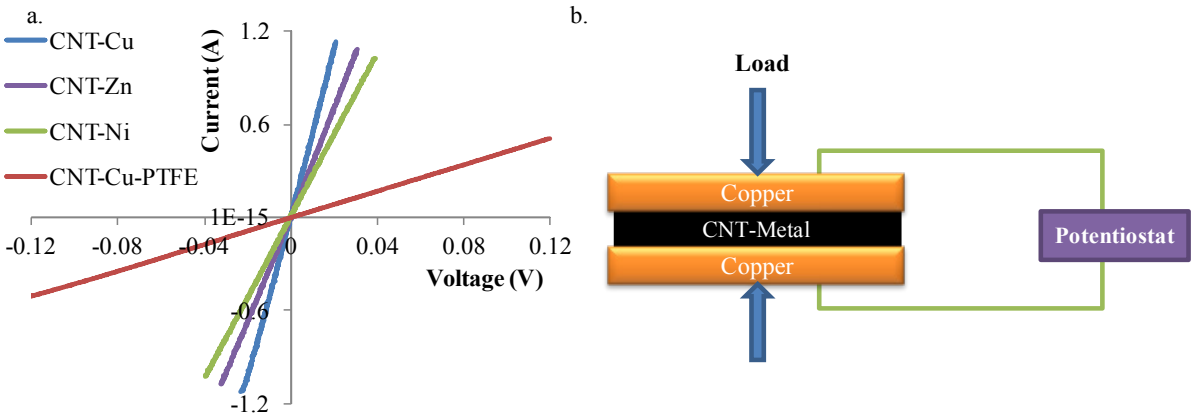

Figure 2-6 a) I-V curves of CNT-metal nanocomposites. The PTFE coated CNT-Cu surface, representing the common practice to get hydrophobic surfaces, shows significantly lower conductivity due to the polymer coating. b) Schematic of test setup used to obtain I-V curves.

range.

Elimination of polymer coating has made the reported method ideal for electrochemical and thermal applications, where high thermal/electric conductivity is needed. In order to access such potential, the thermal and electric conductivities of the superhydrophobic nanocomposites are measured and compared to control samples. The results and test setups are shown in **Figure 2-6 and 2-7** and described further in Section 4.3. To measure electrical contact resistance, CNT-

metal nanocomposites (or the control sample) were deposited on polished copper and placed in contact with another piece of polished copper. The I-V curves were measured by a potentiostat. It can be seen from **Figure 2-6a** that the CNT-metal nanocomposites show far lower contact electric resistance as opposed to the PTFE-coated CNT-Cu specimen. Particularly, the electric resistance of the CNT-Cu sample is only ~8.2% of that of the control sample (i.e., improvement of electric conductivity by about one order of magnitude), proving the superior electrical conductivity of the CNT-metal nanocomposites owing to the lack of insulating coating. Similarly, we evaluated the thermal properties of the CNT-metal composites by measuring the thermal resistance of the deposits when used as thermal interfaces. **Figure 2-7a** compares the values of the thermal resistance obtained with all three CNT-metal nanocomposites showing low thermal resistances of approximately 50 $mm^2K\ W^{-1}$, ~42% of that of PTFE-coated CNT-Cu, all at the same applied pressure of 60 psi. The high thermal conductivities of the reported CNT-metal nanocomposites, in combination with their tunable wettability, have made them very promising in heat transfer applications such as evaporative cooling where surface wettability have been shown to greatly influence critical phenomena and parameters such as nucleation and critical heat flux.[5, 6]

The durability of the sample was also examined. The superhydrophobicity of the samples were observed to maintain after stored in ambient environment for over 9 months. They also did not

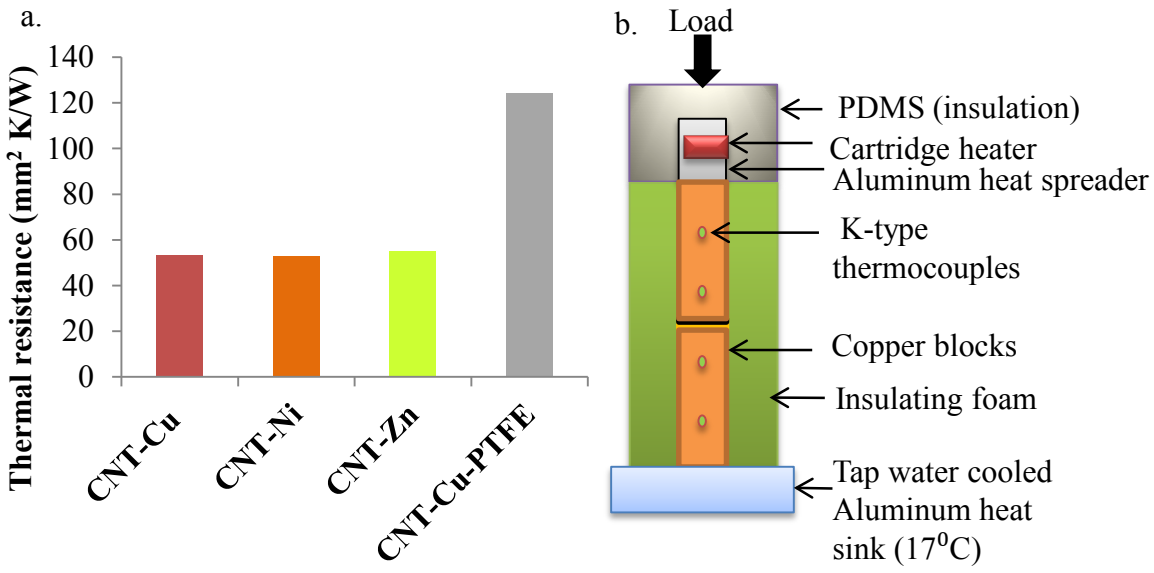

Figure 2-7 a) Thermal resistance of the CNT-metal nanocomposites as compared with PTFE-coated samples as the control, which shows much higher thermal resistance than the proposed CNT-metal nanocomposites; b) Schematic sketch of the thermal interface resistance setup used to obtain thermal resistance values.

show any sign of degradation after being soaked in boiling water for 30 minutes. The CNT-Ni and CNT-Zn samples are superhydrophobic even after keeping at up to 200°C in air for 12 hours**.** The CNT-Cu sample, however, remains superhydrophobic only up to 150 °C in air after a similar period of heating. The different behavior of the CNT-Cu deposits may stem from the easier oxidation of the co-deposited copper layer at relatively low temperature. These samples can retain their wetting characteristics after being heated and cooled back to room temperature.

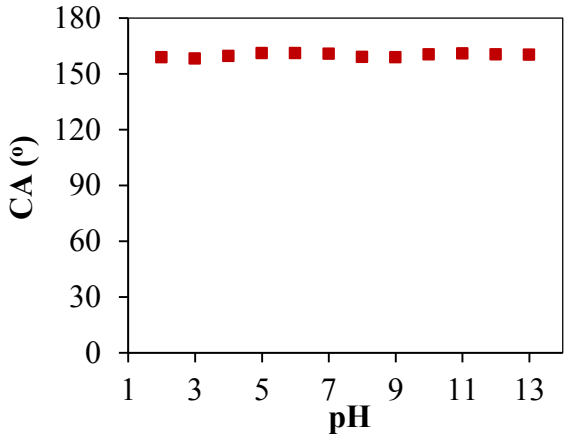

Figure 2-8 Static contact angle variation of superhydrophobic nanocomposites versus pH show that superhydrophobicity is maintained over a wide range of pH (2-13). At pH 1 and pH 14, however, although initially high CAs are measured, the droplets soon spread and permeate the deposit to damage it irreversibly.

However, if the samples are further heated to higher temperature (e.g., 250 ºC) and cooled down, a drop of water applied to the surface can completely damage the deposit and peel it off from the steel surface. This may be attributed to desorption of the adsorbed solvent molecules or premature thermal degradation of the acid treated CNT deposits. Nevertheless, the thermal stability of the superhydrophobic nanocomposites (i.e., 200ºC for CNT-Ni or CNT-Zn and 150 ºC for CNT-Cu), way beyond the boiling point of water, has made them especially attractive for thermal applications. The static contact angles of the deposits prepared at 550 V were also measured by using aqueous solutions with pH values ranging from pH 1 to pH 14, as shown in **Figure 2-8**. Data shown here was acquired from CNT-Ni samples. However, identical behavior was obtained from CNT-Zn and CNT-Cu deposits prepared at the same voltage. The superhydrophobic property remains unaffected over a wide range of pH (2-13) and a droplet rolls

off quite easily with even slight tilting of the sample. With extreme pH values of 1 and 14, however, the droplet pins to the surface after a few seconds, eventually spreads and damages the deposit it contacts. This change in wettability under extreme pH values may be due to removal of the adsorbed low surface energy functional groups under these conditions.

Patterning surfaces with different wettability[35] has also found many applications ranging from cell culture[54], microfluidics[36, 55] to heat transfer[56-58]. We have detailed a facile scalable method in SI utilizing xurography and a combination of organic solvent based and water based EPD to produce CNT coated surfaces with patterned wettability. Details of the process flow are offered in SI. In addition, the optical transparency of the reported highly conductive CNT-metal thin films (deposited at 275V on transparent ITO glass) is demonstrated in Figure S2-8c, proving their potential for applications that need high optical transparency together with superhydrophobicity and high conductivity. The prominently darker deposit around the periphery of the ITO glass can be ascribed to what is known as the edge effect caused by material buildup around the edge due to field line concentration at the particular region. Strategies such as improved deposition chamber design, amended electrode configuration and pulsed voltages can help reduce it. The good optical transparency, subject to further improvement, has been ensured by the vertical alignment of CNTs and the very thin metal holding layer.

2.4 Conclusions

In conclusion, co-EPD of metal and CNTs, assisted by electric field-induced polarization, has been shown to be a facile, scalable and versatile method to deposit thin films of nanocomposites with tunable wettability under room temperature. By eliminating the polymer coating for wettability control, this single-step process has been demonstrated to achieve high

thermal/electric conductivity for potential applications in heat transfer and electrochemical devices. In contrast to most existing methods for superhydrophobic CNT coatings, the nanocomposites in this work achieve excellent conductivity due to the voltage-controlled vertical alignment and the reduction in contact resistance due to the co-deposited metal at the interfaces. Further, the ability to control wettability has been demonstrated in order to produce a wide range of contact angles and superhydrophobic surfaces with both high and low adhesion to water droplets. The wettability control has been attributed to hierarchical micro- and nanoscale roughness as well as the change of surface functional groups during deposition. The compatibility to micro-patterning technology, transparency of the surfaces and the thermal/pH stability of the deposits has been demonstrated to prove their potential for a broad range of applications.

2.5 Methods and Materials

***Electrophoretic deposition*:** As-purchased carbon nanotubes (MER Corporation, Tucson, AZ) were acid-treated (refluxed) in 1:2 H_2SO_4 and HNO_3 mixture at 90°C for 40 minutes. After refluxing, the CNTs were filtered with distilled water to a neutral pH, dispersed in isopropanol (IPA) and then dried at 80 °C. To perform EPD, CNTs were first dispersed in IPA (concentration: 0.02 $mg \cdot ml^{-1}$) for 15 minutes using a probe sonicator (Sonics and Materials Inc., Newtown, CT). $NiCl_2 \cdot 6H_20$, $Zn(NO_3)_2 \cdot 6H_2O$ or $Cu(NO_3)_2 \cdot 3H_2O$ were then added to the CNT dispersions and further sonicated for 15 minutes. The final concentration of metal salts in all dispersions was 0.01 $mg \cdot ml^{-1}$. EPD was conducted on polished 316 stainless steel electrodes (McMaster, Elmhurst, IL) that had been cleaned by sonication in acetone, IPA and distilled water sequentially. Two of such electrodes were separated by a polycarbonate spacer of 1 cm and

placed in a beaker with 40 ml of dispersion added. Deposition voltages ranging from 50 V to 550 V were applied using a high-voltage power source (Stanford Research Systems, Sunnyvale, CA). All depositions were carried out for 3 minutes.

Characterization: A home-built contact angle goniometer with commercial optical components (Edmund Optics, Barrington, NJ) was employed to take images of 4 μL water droplets on the nanocomposite surfaces, that were then analyzed by using ImageJ software (National Institutes of Health, Bethesda, MD) with the LBDSA plugin[59] to obtain contact angle values. Three individual samples per deposition voltage for CNT-Ni, CNT-Zn and CNT-Cu were analyzed to ensure reliability of the results. Contact angles were obtained from three separate locations for every sample. SEM images were obtained using a Hitachi S-4700 FE-SEM. High-resolution transmission electron microscope (HRTEM) images were obtained in a Hitachi H-9500 electron microscope operated at 300 KeV. FTIR analysis was carried out using a Jasco Fourier Transformed Infrared (FTIR) Spectrometer (JASCO, Japan) using 64 scans over a range of 600 to 4000 cm^{-1} at a resolution of 4 cm^{-1}. Raman spectra were collected from the deposits as prepared on SS substrates using a Thermo Scientific DXR™ Raman Microscope system equipped with a 780 nm laser source. At least locations on two separate samples per deposition voltage were analyzed to ensure reliability of results. All spectra were collected under identical laser power (100 mW) and exposure conditions.

Transition pressures from Cassie to Wenzel mode of wetting were estimated by subjecting the superhydrophobic deposits to hydrostatic pressure by slowly immersing samples in deionized water to depths up to 120 cm. A transparent polycarbonate tube was utilized to construct the water column and to facilitate visualization. Reported transition pressure values are based on the

maximum pressure the samples could sustain for 300 s without wetting of the samples. The completely non-wetting Cassie state could be observed by viewing the samples at an angle where silvery air layer was visible. When transition pressure was reached, the plastron was typically seen to dissipate within 60 s.

Electric and thermal characterization: Electric resistances were measured with CNT-metal nanocomposite samples deposited on a polished copper substrate (1 cm x 1 cm) under 550 V deposition voltage. After deposition, cleansing and drying, they are placed in contact with a polished copper piece as the counter electrode. Efforts were taken to carefully deburr all substrates and ensure that only the deposit contacts the counter electrode. A 100g load was placed atop the copper plates to ensure proper contact between the surfaces. A linear voltage scan from -200 mV to +200 mV was then performed using a Versastat 4 potentiostat (Princeton Instruments, Trenton, NJ) to obtain the I-V curve. For comparison, a CNT-Cu nanocomposite sample dip-coated with PTFE were also tested. The PTFE solution was made by dissolving 0.5 mg/ml PTFE powder in FC-72 solvent (Acros Organics, Pittsburgh, PA).

Thermal resistances were measured by adopting methods similar to those previously reported by others.[60] Two copper pieces (2.5 cm x 2.5 cm) were first polished to less than 0.3 μm in average roughness. Four K-type thermocouples (Omega Engineering Inc., Stamford, CT) placed 1 cm apart were used to measure the thermal gradient along the copper pieces. Heating block was produced by inserting 150 W cartridge heater (OEM Heaters, St. Paul, MN) into an insulated aluminum block with only a 2.5 cm x 2.5 cm region in the center exposed. The aluminum heat spreader was insulated with a block of 3 cm-thick polydimethylsiloxane (PDMS) and wrapped in thermally insulating foam so as to prevent heat losses and ensure the unidirectional heat transfer

from the exposed region into the contacting copper block. The temperature of the aluminum heat sink was stabilized by continuously circulating tap water of ~17 °C for all measurements. Steady state was considered achieved when temperature did not change by 0.2 °C for 10 minutes. The thermal resistance was measured by sandwiching a polished copper piece with CNT-metal nanocomposites coating between the two polished copper blocks. The samples are typically a piece of 1 mm-thick polished copper substrate whose one side is coated with CNT-metal nanocomposite. For comparison, a bare copper substrate and a CNT-Cu nanocomposite sample dip-coated with PTFE as previously described are also tested. A uniform load of 60 psi was applied for all measurements using a hydraulic ram arrangement. The thermal resistance between the polished copper surfaces was first derived by using the temperature drop across the interface when there was no sample present, and used as the base value of thermal resistance for the Cu/Cu interface. From the data obtained with the CNT-metal nanocomposite coating, a thermal resistance circuit was then used to calculate the thermal resistance of the deposit, by subtracting the thermal resistance of the Cu/Cu interface from the total thermal resistance of the Cu/coating and Cu/Cu interfaces.

2.6 Acknowledgements

This material is based upon work supported by the National Science Foundation under Grants No. 1130651, No. 1439494, No. 1264549, No. 1444473 and No. 1261910 (DMR). Any opinions, findings, and conclusions or recommendations expressed in this material are those of the authors and do not necessarily reflect the views of the National Science Foundation. The authors would like to thank Dr. Jaroslaw Drelich for helpful discussions on wettability, Dr. Anjana Asthana for

help with preliminary TEM and Mr. Michael LaCourt for assistance with test setup for thermal resistance measurement.

2.7 References

[1] X.-D. Zhao, H.-M. Fan, J. Luo, J. Ding, X.-Y. Liu, B.-S. Zou, Y.-P. Feng, Adv. Funct. Mater. 2011, 21, 184.

[2] D. Zahner, J. Abagat, F. Svec, J. M. Frechet, P. A. Levkin, Adv. Mater. 2011, 23, 3030.

[3] D. D. Meng, J. Kim, C.-J. Kim, J. Micromech. Microeng. 2006, 16, 419.

[4] D. D. Meng, C. J. Kim, J. Power Sources 2009, 194, 445.

[5] A. R. Betz, J. Jenkins, C.-J. C. Kim, D. Attinger, Int. J. Heat Mass Transfer 2013, 57, 733.

[6] R. Chen, M. C. Lu, V. Srinivasan, Z. Wang, H. H. Cho, A. Majumdar, Nano Lett. 2009, 9, 548.

[7] B. Bhushan, Y. C. Jung, Prog. Mater. Sci. 2011, 56, 1.

[8] C. Gu, J. Tu, Langmuir 2011, 27, 10132.

[9] L. Zheng, Z. Li, S. Bourdo, K. R. Khedir, M. P. Asar, C. C. Ryerson, A. S. Biris, Langmuir 2011, 27, 9936.

[10] L. Cao, A. K. Jones, V. K. Sikka, J. Wu, D. Gao, Langmuir 2009, 25, 12444.

[11] A. Nakajima, K. Hashimoto, T. Watanabe, K. Takai, G. Yamauchi, A. Fujishima, Langmuir 2000, 16, 7044.

[12] A. Solga, Z. Cerman, B. F. Striffler, M. Spaeth, W. Barthlott, Bioinspir. Biomim. 2007, 2, S126.

[13] J. Shieh, F. J. Hou, Y. C. Chen, H. M. Chen, S. P. Yang, C. C. Cheng, H. L. Chen, Adv. Mater. 2010, 22, 597.

[14] H. Mertaniemi, V. Jokinen, L. Sainiemi, S. Franssila, A. Marmur, O. Ikkala, R. H. Ras, Adv. Mater. 2011, 23, 2911.

[15] C. Neto, K. R. Joseph, W. R. Brant, Phys. Chem. Chem. Phys. 2009, 11, 9537.

[16] X. Yao, L. Xu, L. Jiang, Adv. Funct. Mater. 2010, 20, 3343.

[17] M. K. Dawood, H. Zheng, T. H. Liew, K. C. Leong, Y. L. Foo, R. Rajagopalan, S. A. Khan, W. K. Choi, Langmuir 2011, 27, 4126.

[18] A. Checco, A. Rahman, C. T. Black, Adv. Mater. 2014, 26, 886.

[19] K. K. S. Lau, J. Bico, K. B. K. Teo, M. Chhowalla, G. A. J. Amaratunga, W. I. Milne, G. H. McKinley, K. K. Gleason, Nano Lett. 2003, 3, 1701.

[20] J. Li, L. Wang, W. Jiang, Carbon 2010, 48, 2668.

[21] Y. S. Joung, C. R. Buie, Langmuir 2011, 27, 4156.

[22] C. F. Herrmann, F. W. DelRio, V. M. Bright, S. M. George, J. Micromech. Microeng. 2005, 15, 984.

[23] D. J. Babu, S. N. Varanakkottu, A. Eifert, D. de Koning, G. Cherkashinin, S. Hardt, J. J. Schneider, Advanced Materials Interfaces 2014, 1, n/a.

[24] H. Li, X. Wang, Y. Song, Y. Liu, Q. Li, L. Jiang, D. Zhu, Angew. Chem. Int. Ed. 2001, 40, 1743.

[25] S. Sethi, A. Dhinojwala, Langmuir 2009, 25, 4311.

[26] J. Rafiee, M. A. Rafiee, Z. Z. Yu, N. Koratkar, Adv. Mater. 2010, 22, 2151.

[27] Y. Jiang, P. Wang, X. Zang, Y. Yang, A. Kozinda, L. Lin, Nano Lett. 2013, 13, 3524.

[28] A. R. Boccaccini, S. Keim, R. Ma, Y. Li, I. Zhitomirsky, J. R. Soc. Interface 2010, 7 Suppl 5, S581.

[29] L. Besra, M. Liu, Prog. Mater. Sci. 2007, 52, 1.

[30] H. Ogihara, T. Katayama, T. Saji, J. Colloid Interface Sci. 2011, 362, 560.

[31] H. Ogihara, J. Okagaki, T. Saji, Chem. Lett. 2009, 38, 132.

[32] S. Santhanagopalan, A. Balram, E. Lucas, F. Marcano, D. D. S. Meng, Key Eng. Mater. 2012, 507, 67.

[33] S. Santhanagopalan, F. Teng, D. D. Meng, Langmuir 2011, 27, 561.

[34] S. Santhanagopalan, A. Balram, D. D. Meng, ACS Nano 2013, 7, 2114.

[35] E. Ueda, P. A. Levkin, Adv. Mater. 2013.

[36] D. Song, B. Song, H. Hu, X. Du, F. Zhou, Phys. Chem. Chem. Phys. 2015.

[37] M. D. Lima, M. J. de Andrade, C. P. Bergmann, S. Roth, J. Mater. Chem. 2008, 18, 776.

[38] Y. Chen, H. Jiang, D. Li, H. Song, Z. Li, X. Sun, G. Miao, H. Zhao, Nanoscale Res. Lett. 2011, 6, 537.

[39] H. C. Hamaker, Trans. Faraday Soc. 1940, 35, 279.

[40] D. Quéré, Physica A 2002, 313, 32.

[41] M. Callies, D. Quere, Soft Matter 2005, 1, 55.

[42] Y. He, Z. Cao, L. Ma, International Journal of Polymer Science 2015, 2015, 1.

[43] X. Yang, M. Yao, W. Lu, S. Chen, M. Du, L. Zhu, H. Li, R. Liu, T. Cui, B. Sundqvist, B. Liu, The Journal of Physical Chemistry C 2015, 119, 27759.

[44] H. Liu, J. Zhai, L. Jiang, Soft Matter 2006, 2, 811.

[45] L. Gao, T. J. McCarthy, Langmuir 2006, 22, 2966.

[46] B. Bhushan, E. K. Her, Langmuir 2010, 26, 8207.

[47] L. H. Li, Y. Chen, Langmuir 2010, 26, 5135.

[48] R. Poetes, K. Holtzmann, K. Franze, U. Steiner, Phys Rev Lett 2010, 105, 166104.

[49] S. Herminghaus, Europhysics Letters (EPL) 2000, 52, 165.

[50] X. Tan, M. Fang, C. Chen, S. Yu, X. Wang, Carbon 2008, 46, 1741.

[51] X. Zhang, S. Wan, J. Pu, L. Wang, X. Liu, J. Mater. Chem. 2011, 21, 12251.

[52] N. Chakrapani, Y. M. M. Zhang, S. K. Nayak, J. A. Moore, D. L. Carroll, Y. Y. Choi, P. M. Ajayan, J. Phys. Chem. B 2003, 107, 9308.

[53] J. Long, M. Zhong, H. Zhang, P. Fan, J Colloid Interface Sci 2015, 441, 1.

[54] W. Song, J. F. Mano, Soft Matter 2013, 9, 2985.

[55] D. Taylor, D. Dyer, V. Lew, M. Khine, Lab Chip 2010, 10, 2472.

[56] B. Peng, X. Ma, Z. Lan, W. Xu, R. Wen, Int. J. Heat Mass Transfer 2015, 83, 27.

[57] A. R. Betz, J. Xu, H. H. Qiu, D. Attinger, Appl Phys Lett 2010, 97.

[58] H. Bai, L. Wang, J. Ju, R. Sun, Y. Zheng, L. Jiang, Adv Mater 2014, 26, 5025.

[59] A. F. Stalder, T. Melchior, M. Müller, D. Sage, T. Blu, M. Unser, Colloids and Surfaces A: Physicochemical and Engineering Aspects 2010, 364, 72.

[60] J. J. Park, M. Taya, J Electron. Packaging 2006, 128, 46.

2.8 Supporting Information

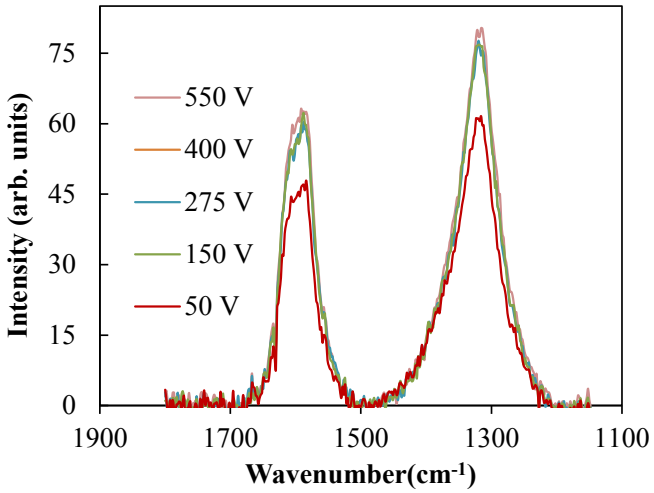

Figure S2-1 Raman spectra of as deposited CNT-Ni samples deposited at 50, 150, 275, 400, 550 V.

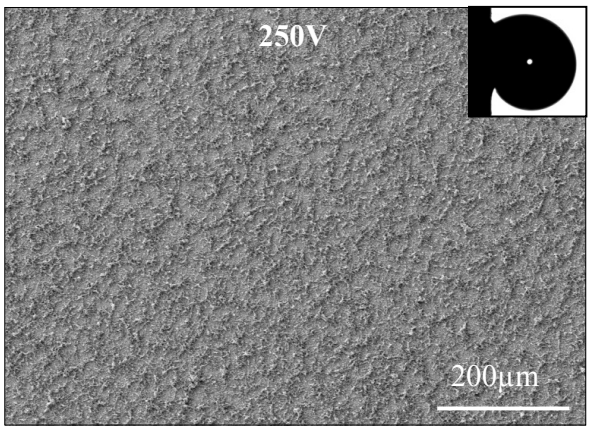

Figure S2-2 SEM top-views of CNT-Ni deposits made at 250V. Inset shows droplet adhered to the surface even when deposited surface is held vertically illustrating the highly adhesive nature of the surface.

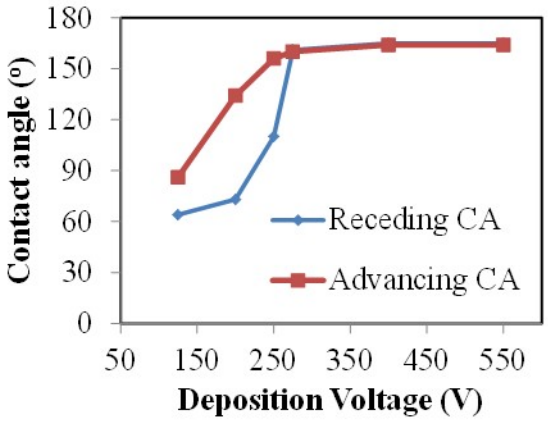

Figure S2-3 Advancing and receding contact angles for CNT-Ni deposits versus deposition voltage. When deposited at 250V for 3 minutes, despite high CA, droplets show high contact angle hysteresis indicating adhesive nature of the deposit (petal effect). Beyond 275V, droplets roll off easily leaving no water trace, displaying the lotus effect.

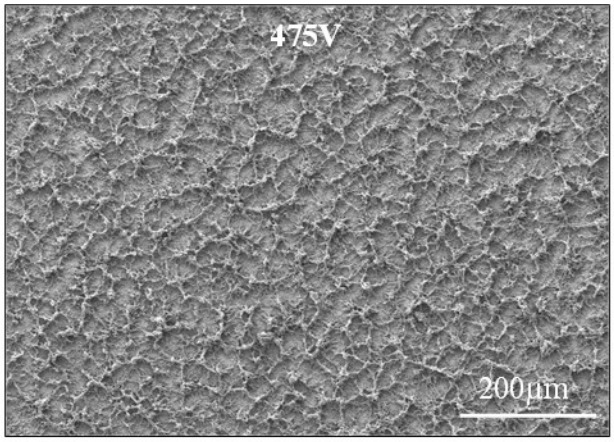

Figure S2-4 SEM top-views of CNT-Ni deposits made at 475V. A much denser array of interconnected clusters are observed. Droplets roll off easily at a few degrees of tilt.

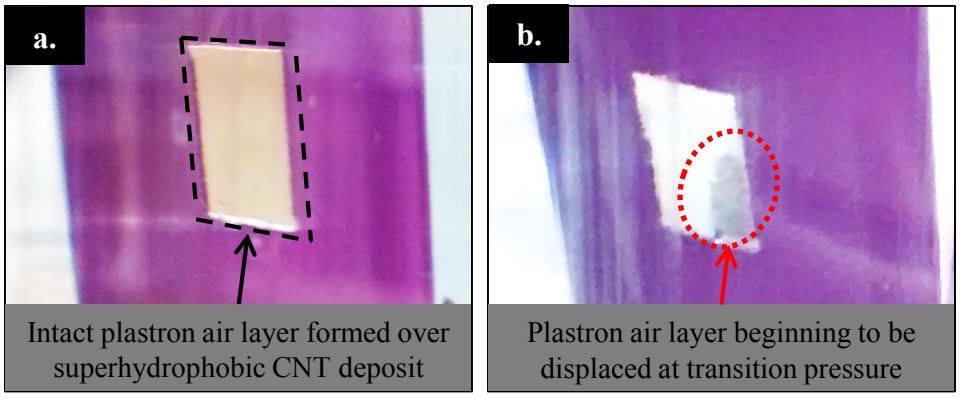

Figure S2-5 Representative images showing behavior of superhydrophobic CNT deposits under hydrostatic pressure. (a) A thin air layer immediately forms on the deposit preventing wetting of the surface representing the Cassie state. (b) The encircled region shows the dissipation of the air layer when critical hydrostatic pressure is reached. Eventually, the entire air layer is displaced, leading to a loss of superhydrophobicity.

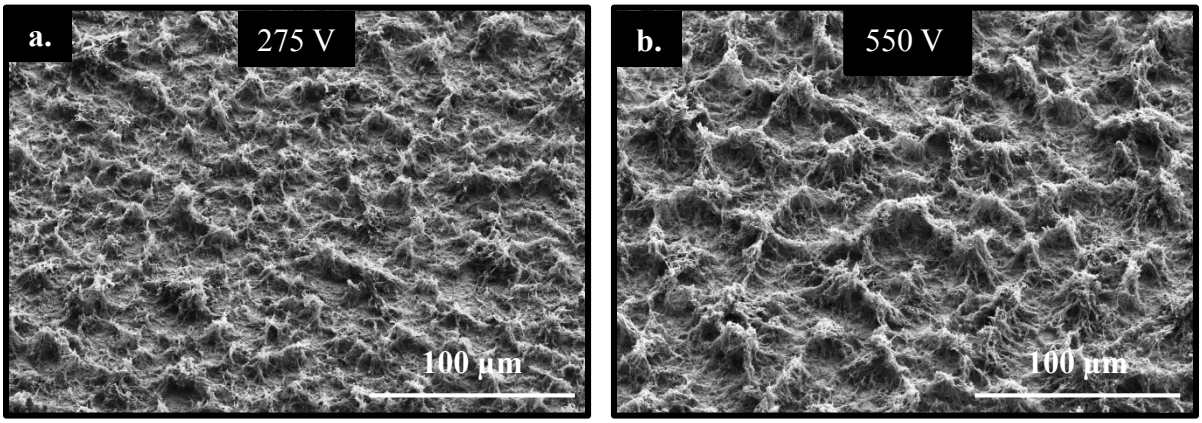

Figure S2-6 Tilted (40º) FE-SEM views of superhydrophobic CNT deposits prepared at (a) 275 V and (b) 550 V, at the same 450x magnification. While both deposits show a highly rough characteristics desirable for superhydrophobicity, the 550 V deposit shows a denser deposit with an almost honeycomb-like structure allowing for greater resistance to hydrostatic pressure.

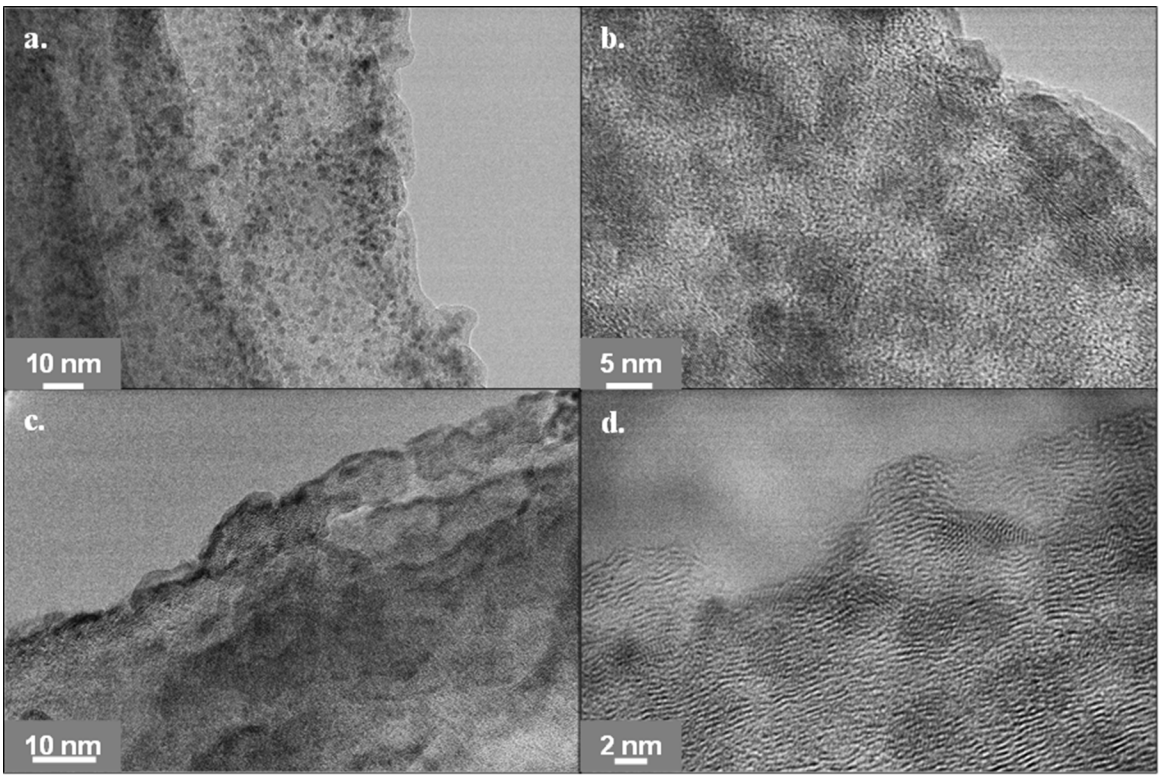

Figure S2-7 HR-TEM images of CNT-Copper(a,b) and CNT-Zinc(c,d) nanocomposites showing deposits of nanoscale particles on the CNT surfaces.

Wettability patterning using electrophoretic deposition of CNTs

Patterning surfaces with different wettability has found many applications recently[1-5]. Typically such patterning has been performed using standard lithographic techniques. A scalable, non-lithographic technique to produce such conductive deposits with patterns of tunable wettability could be very useful. Craft cutters have been employed recently for microchannel fabrication by a few groups in a process known as xurography[6, 7]. Typically, patterns can be easily cut using sketches from generic CAD software or a manufacturer-provided interface, offering a relatively inexpensive microfabrication tool. In this work, a commercial craft cutter was employed to cut patterns in adhesive-backed vinyl from the same manufacturer as the mask to pattern CNT-metal nanocomposites with defined wettability. Figure S2-8a shows the process flow of our patterning technique. Once the patterns are cut out on the vinyl, it is applied to the substrate. The vinyl thus acts as a mask during the IPA-based EPD process, allowing for deposition of superhydrophobic CNTs only on the exposed regions of the substrate. After the deposition and removal of the vinyl mask, the copper surface is rinsed in acetone to remove any residual adhesive from the mask. The cleaned substrate with hydrophobic CNT-metal nanocomposites is then immersed into aqueous CNT dispersion to deposit hydrophilic CNTs as elaborated in the experimental details below. As the patterned substrate is immersed into the aqueous EPD medium, air bubbles spontaneously get trapped over the individual superhydrophobic patterns. The air bubbles thus serve as self-aligned masks to protect the hydrophobic islands and prevent deposition on them during this step. Consequently, the superhydrophobic patterns remain intact during the last step of the deposition (Figure S2-8a4), resulting in a surface with superhydrophobic micro islands surrounded by a hydrophilic coating. This deposit is shown in Figure S2-8b, imaged when immersed in deionized water. The spontaneously trapped air bubbles can be seen atop the

superhydrophobic regions while water wets the surrounding hydrophilic CNT region. Since the masking technology can be easily scaled up to much larger vinyl sheets, this simple method offers a scalable technique to fabricate large scale surfaces with patterned wettability for applications that do not require extremely high resolution. We are currently pursuing techniques to further improve achievable resolution and patterns through this technique.

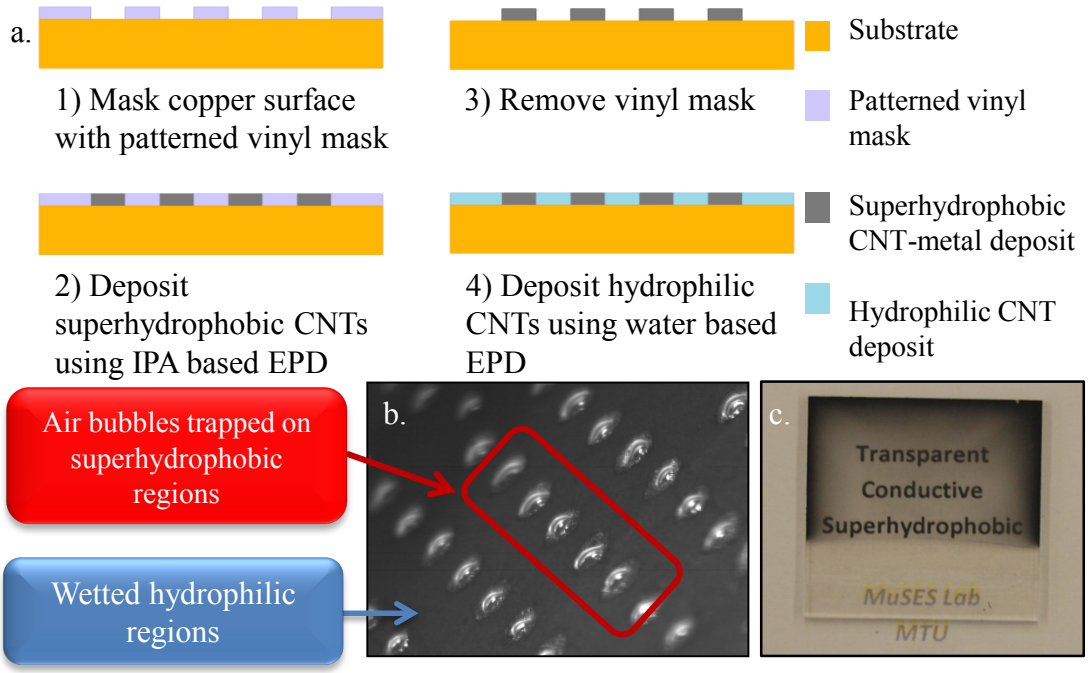

Figure S2-8 a) Process flow showing the patterning technique using a simple craft cutter to deposit superhydrophobic patterns surrounded by hydrophilic CNTs using EPD, b) Microscopic image of patterned substrate immersed in de-ionized water. Bubbles can be seen forming over the superhydrophobic regions because of their water repellent nature and the hydrophilic (black) regions are completely wet by water. c) ITO glass coated with CNT-metal composite at 275V showing the transparent nature of the deposited composite

Experimental details: Micropatterns of 600 μm in diameter were first cut into adhesive-backed vinyl tape using a commercially available craft cutter, Silhouette Cameo (Silhouette America Inc., Orem, UT). Patterned vinyl mask was adhered to the substrate, which is then employed as the deposition electrode. Deposition of superhydrophobic patterns was carried out using the previously detailed IPA based CNT-metal deposition technique. After evaporation of the solvent, vinyl mask was peeled off. This substrate was then immersed in aqueous CNT dispersion containing 0.5 $mg.ml^{-1}$ of acid-refluxed CNTs to deposit at 40 V DC for 5 minutes. The deposit was then taken out and allowed to dry in air.

2.9 Supporting Information References

[1] B. Peng, X. Ma, Z. Lan, W. Xu, R. Wen, Int. J. Heat Mass Transfer 2015, 83, 27.

[2] A. R. Betz, J. Xu, H. H. Qiu, D. Attinger, Appl Phys Lett 2010, 97.

[3] E. Ueda, P. A. Levkin, Adv. Mater. 2013.

[4] D. Zahner, J. Abagat, F. Svec, J. M. Frechet, P. A. Levkin, Adv. Mater. 2011, 23, 3030.

[5] L. Zhang, J. Wu, M. N. Hedhili, X. Yang, P. Wang, J. Mater. Chem. A 2015, 3, 2844.

[6] D. Taylor, D. Dyer, V. Lew, M. Khine, Lab Chip 2010, 10, 2472.

[7] P. K. Yuen, V. N. Goral, Lab Chip 2010, 10, 384.

CHAPTER 3

ENHANCED OXYGEN EVOLUTION REACTION ELECTROCATALYSIS VIA ELECTRODEPOSITED AMORPHOUS α–PHASE NICKEL-COBALT HYDROXIDE NANODENDRITE FORESTS

Adapted with permission from:

Enhanced Oxygen Evolution Reaction Electrocatalysis via Electrodeposited Amorphous α-Phase Nickel-Cobalt Hydroxide Nanodendrite Forests. Anirudh Balram, Hanfei Zhang, and Sunand Santhanagopalan. (2017) ACS Applied Materials & Interfaces Article

DOI: 10.1021/acsami.7b05735

3.1 Abstract

We demonstrate an electrodeposition method to rapidly grow novel three-dimensional (3-D) nanodendrite forests of amorphous α-phase mixed nickel-cobalt hydroxides on stainless steel foil toward high performance electrocatalysis of the oxygen evolution reaction (OER). The proposed hydrogen bubble-templated, diffusion-limited deposition process leads to the unprecedented dendritic growth of vertically-aligned amorphous metal hydroxides, induced by the controlled electrolysis of the tuned water content in the primarily alcohol-based deposition solution. The hierarchical nature of these binder-free, amorphous metal hydroxide deposits leads to their superhydrophilic nature and underwater superaerophobic behavior. The combination of all these qualities leads to exemplary catalytic performance. When directly grown on planar stainless steel substrates, these nanoforests show high OER activity with overpotentials as low as ~255 mV to produce a current density of 10 mA cm^{-2} over 10,000 accelerated stability test cycles. This work demonstrates a novel fabrication technique that can simultaneously achieve dendritic hierarchical structure, vertical alignment, superaerophobicity, amorphous crystal structure, and intimate contact with the substrate that leads to high catalytic activity with excellent durability.

3.2 Introduction

Electrolytic water splitting has great potential to be a widespread and economically viable hydrogen production[1-4] method towards a clean energy future. In order to efficiently harness this potential, however, improving the kinetics of the four-electron oxygen evolution reaction (OER)[5] process is critical. In practice, water electrolysis remains unattainable at the ideal 1.23 V. This is primarily due to huge activation losses (referred to as overpotential) on the OER side along with ohmic losses due to bubble coverage.[1, 6] This has led to a surge in efforts to minimize OER overpotentials, a significant bottleneck, especially for sustainable electrochemical water splitting. Nevertheless, the challenge still remains to produce cost-effective catalyst systems that can achieve water splitting at current densities of 10 mA cm^{-2} at low overpotentials, the proposed Figure 3-of merit for water splitting powered by solar devices.[5, 7] In order to make water splitting more economically feasible, non-precious OER catalyst alternatives are required that can supersede the performance of the benchmark platinum group element catalysts such as IrO_x and RuO_2.[8] In this regard, alkaline electrolysis[1] is particularly appealing. In recent years, several earth-abundant catalysts[4] have been developed that consistently outperform the limited, expensive and unstable benchmark catalysts in terms of overpotential and durability. Among those, transition metal hydroxides[9] and oxides[2, 10] of various morphologies and compositions have emerged as front-runners.

Nickel hydroxides, in particular, have been widely studied due to their excellent electrochemical performance in a variety of electrochemical applications.[11-12] Beyond pure $Ni(OH)_2$, mixed compositions containing nickel and cobalt, are generally known to have superior properties[13-14] to pure $Ni(OH)_2$ or $Co(OH)_2$ due to better conductivity, stability, and synergistic interactions. Several processes such as hydrothermal,[15] wet chemical,[16] and sonochemical[17] synthesis have

been reported to produce these metal hydroxide nanostructures in a wide range of morphologies (hollow nanospheres, nanoplates, nanobelts, etc.). However, the electrochemical performance of such materials suffers due to the need for polymeric binders[1-2, 18] to prepare robust coatings and the inability to control their orientation during electrode assembly. This leads to underutilization of available catalytic sites as well as lack of control over surface wettability. In addition to the intrinsic activity and stability of the catalytic material, a practical consideration to reduce operating overpotentials is addressing the ohmic losses due to catalyst surface blockage between bubble nucleation and release.[1, 3, 6, 19-20] Oxygen bubbles produced during electrolysis generally tend to be larger and have a slightly longer dwelling time on an electrode surface as compared to the hydrogen bubbles generated at the cathode.[19, 21] Given the inherently unfavorable kinetics of the OER process, mitigating bubble related overpotential, is of vital importance. The most cost and energy efficient strategy to minimize bubble overpotentials, would be to engineer a catalyst surface that could rapidly and importantly, passively dissipate generated gas bubbles.

Recently, there have been excellent demonstrations of such nanostructured catalytic surfaces, termed superaerophobic,[22-24] wherein generated gas bubbles experience minimal adhesion to the submerged electrode. Extreme states of wettability such as underwater superaerophobicity and superhydrophilicity arise from hierarchically textured hydrophilic surfaces.[25] Since metal hydroxides are naturally hydrophilic, their hierarchical nanostructures could not only provide a high density of catalytic sites for OER, but also effectively dissipate generated oxygen bubbles, promoting mass transfer at the electrode-electrolyte interface. Another important factor that can influence performance is the crystallinity of the nanomaterial. Recent studies have reported superior performance of amorphous nanomaterials over their crystalline counterparts for applications such as supercapacitors[12, 14] and OER catalysis.[16, 26-30] For instance, Koza et al[30]

observed that amorphous electrodeposits of Co_3O_4 appeared to have more electrochemically active sites as compared to the crystalline deposits. While amorphous metal oxide deposits have been prepared by techniques such as photochemical metal-organic decomposition,[26] spray-based techniques,[31] chemical decomposition,[32] methods to fabricate amorphous metal hydroxides directly on to electrode substrates have been relatively less reported and have generally utilized the same green electrochemistry technique.[27-28, 33] Further, it has been noted more recently that the oxide phases are not thermodynamically stable in oxygen evolving regimes.[34-35]

Electrodeposition,[18, 36] is an extremely versatile technique that lends itself to scalable nanostructuring of binder-free working electrodes with the ability to control the morphology, crystallinity and orientation of the produced structures. The challenge is to be able to fabricate a deposit with the desired amorphous crystal structure, hierarchical morphology, nanomaterial orientation so as to maximize catalyst accessibility along with intimate electrode contact. To the best of our knowledge, the direct growth of three-dimensional (3-D) nanodendritic amorphous metal hydroxides specifically via electrodeposition or even other means has never been reported previously. In fact, previously, $Ni(OH)_2$ thin films have had to be electrodeposited over metal dendrite structures on account of the difficulty to directly achieve dendritic structures composed purely of the metal hydroxide.[37] In this work, we demonstrate a dynamic hydrogen bubble-templated electrodeposition process to concurrently produce binder-free, superaerophobic, vertically aligned, nanodendritic amorphous α-phase mixed metal hydroxide deposits.

The growth of these nanodendrite forests is facilitated by tuning the water content in the primarily alcoholic deposition medium and use of high deposition voltage. After optimizing the deposition technique to achieve high activity nanodendritic $Ni(OH)_2$ deposits, the method could

then be extended to similar deposits of $Co(OH)_2$ and various mixed Ni-Co hydroxides. The resultant robust deposits on planar stainless steel foil exhibit extremely low overpotentials and no activity loss over 10,000 cycles of testing which can in part be attributed to the bubble repellent nature[20] of the hierarchically rough deposit. The choice of stainless steel as the substrate is observed to profoundly enhance the activity of the deposits, establishing the importance of prudent substrate selection to optimize OER catalyst activity. The demonstrated single-step scalable fabrication process provides a technique for rapid direct growth of amorphous mixed α-phase nickel-cobalt hydroxides with 3-D hierarchical nanodendritic morphology tailored for the OER process.

3.3 Results and Discussion

Traditionally, dendritic growth of metal electrodeposits in aqueous media is engendered by specific non-equilibrium[38-39] conditions that control the growth rate and growth direction.[39-41] The deposition rate, controlled by applied potential or current density, serves to produce a diffusion-limited deposition regime.[39, 42] Additives or species[39] present in the deposition medium direct the growth towards higher electric field strengths. In order to specifically induce dendritic growth of the metal hydroxides, we avoided employing the primarily aqueous deposition media generally used in electrodeposition of nickel and cobalt hydroxides. Instead, we used a primarily alcohol-based medium made up of a mixture of equal parts of ethanol-isopropanol containing a low metal salt concentration (0.1 mg ml^{-1} in all cases). The use of alcohol-based electrolytes with low metal ion concentration allows for the use of a high electric field (~250 V cm^{-1}) to produce diffusion-limited deposition. We modified this electrolyte by adding a small amount of deionized (DI) water. The water content served to induce the formation of metal hydroxide and direct the

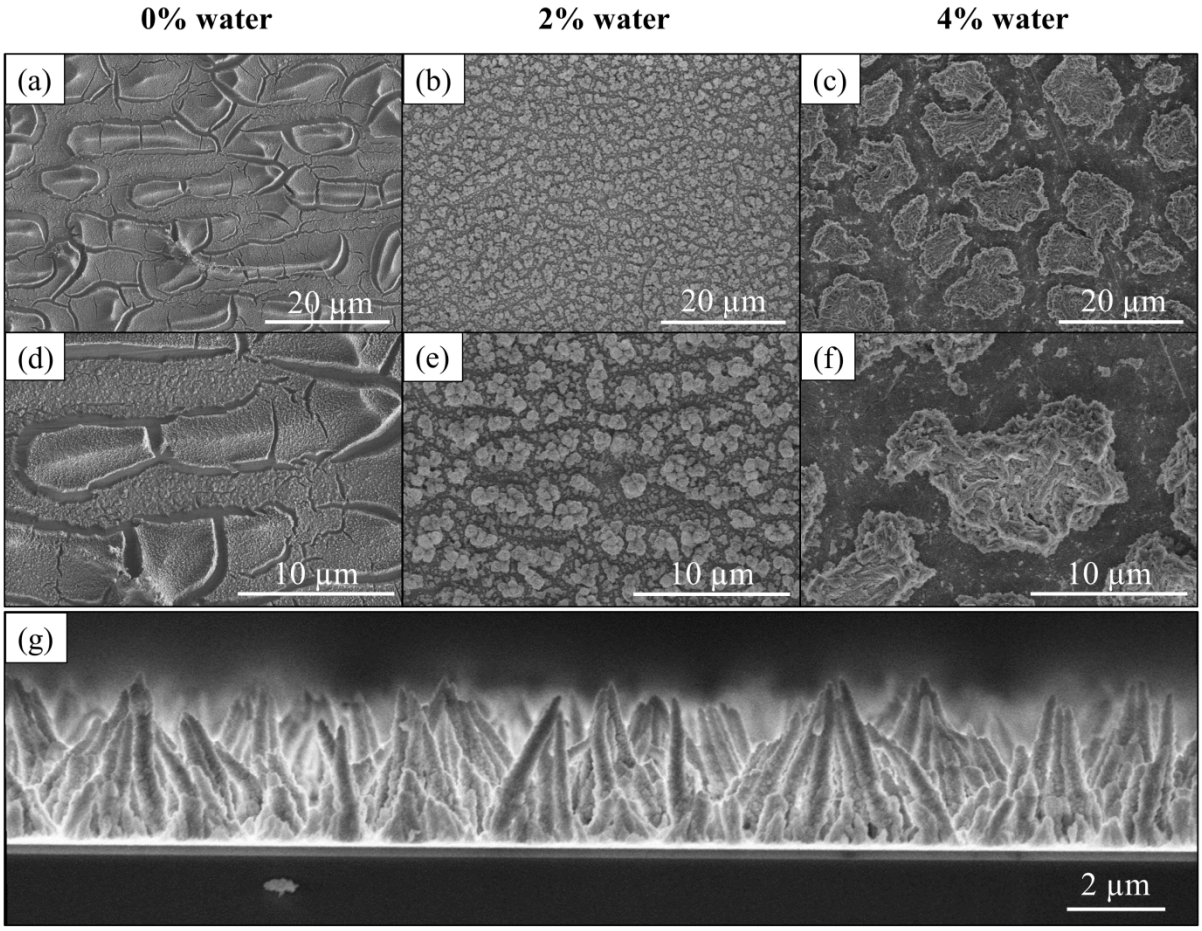

Figure 3-1. Top- view FE-SEM images of different deposit morphologies of α-phase $Ni(OH)_2$ electrodeposits obtained by varying added water content in the deposition solution **(a, d)** 0% added water; **(b, e)** 2% added water; **(c, f)** 4% added water. Figures (a, b, c) and (d, e, f) are obtained at lower and higher magnifications respectively**. (g)** Cross-sectional image of $Ni(OH)_2$ nanodendrite forests obtained when electrolyte contains 2% added water.

bubble-templated growth of the dendritic structures. The references henceforth to 0%, 2%, and 4% water indicate the amount of extraneous water content being introduced to the ethanol-isopropanol electrolyte solution.

The FESEM images in **Figure 3-1** show that the quantity of water in the electrolyte seems to have a direct and significant effect on the morphology of the deposit. For the 0% water deposit, when the electrolyte lacks any extraneous water (besides the nominal amount incorporated via absorption of ambient humidity and the water of crystallization from the dissolved metal salt), a highly cracked, yet somewhat porous thick film of $Ni(OH)_2$ is obtained (Figure 3-1a, d). The porosity (Figure S3-1a) is likely a result of extremely small hydrogen bubbles evolved during deposition. When 2% water is added to the electrolyte, however, a clear emergence of isolated structures can be observed (Figure 3-1b, 1e). The cross-sectional image (Figure 3-1g, Figure S3-1b) further establishes the vertical orientation and unprecedented nanodendritic structure of the deposited material. The nanodendrites show similar structural characteristics to some copper electrodeposits influenced by bubble related microstreaming effects.[43-44] Increasing the electrolyte water content further, to 4%, results in completely different overall deposit morphology Figure 3-1c, f. The structures now formed appear to be made up of islands of densely packed intertwined nanodendrites (Figure S3-1c). We attribute these structural differences to the increased rate of electrolysis of the additional water content added to the electrolyte solution.

We propose that the growth mechanism here is hydrogen bubble-templated[40, 42] and directly influenced by the rate and amount of electrolysis of the water contained in the electrolyte. A schematic of the growth mechanism is presented in **Figure 3-2**. Concomitant with the application of the electric field, several phenomena occur in rapid succession. The instantaneous electrolysis of the incorporated water generates hydrogen bubbles that result in the blockage of several sites[40, 42, 45] on the substrate. Additionally, the consumption of protons to produce hydrogen bubbles causes relatively alkaline conditions[46-47] localized at the electrode-electrolyte interface

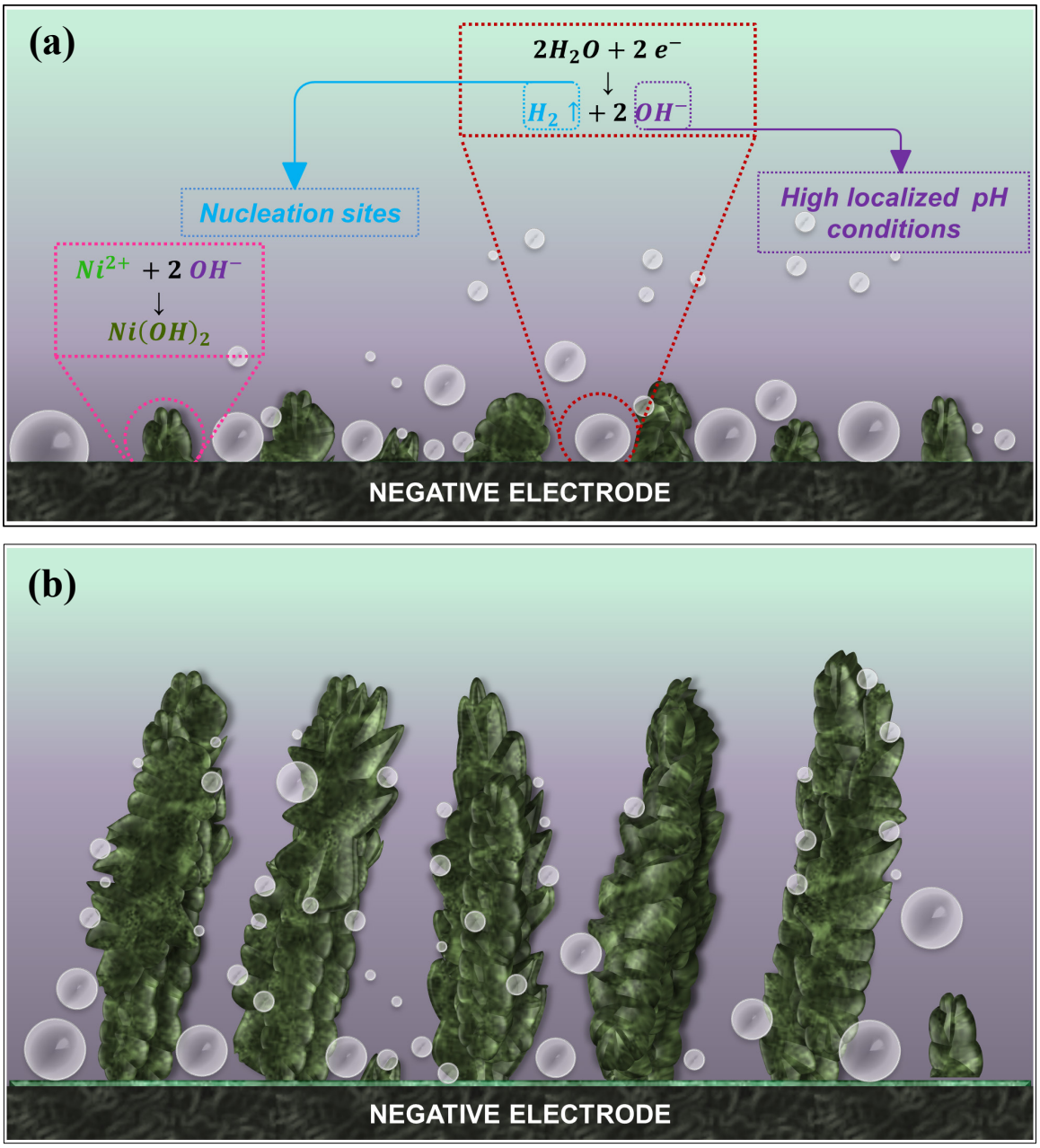

Figure 3-2. Schematic representation of the proposed growth mechanism of the vertically aligned 3-D nanodendrite forests (a) initial stages (b) later stages of deposition.

due to the relatively high concentration of OH^- ions therein. Thus, the metal ions in the electrolyte diffusing towards the electrode surface are forced to selectively nucleate in a high pH

environment in the form of their corresponding metal hydroxides [$M^{2+}+OH^- \rightarrow M(OH)_2\downarrow$][46] in the regions lacking bubble coverage, leading to dendritic branching. The nucleation of miniscule hydrogen bubbles would continue to occur on the surface of these isolated metal hydroxide structures limiting further growth to only those regions on the deposits that are exposed. As the deposition proceeds, it would occur preferentially in regions of field concentration, i.e. the tips of the nucleated regions. If the rate of electrolysis is slow enough to not disrupt the diffusion-limited deposition conditions existing at the electrode surface, the growth of the structures should result in being relatively vertically oriented, directed towards the electric field[38] aided by the electrolyte microstreams induced by bubble collapse.[47] This preferential electric field-directed growth caused by the dynamic hydrogen bubble templating leads to dendritic growth not seen previously in the electrodeposition of metal hydroxides.

During the deposition process from the electrolyte containing 2% water, the hydrogen evolution was not clearly seen, with the bubbles being presumably too small to be visible to the naked eye. The rate of electrolysis in this case, also perhaps limited by diffusion would lead to the relatively slow nucleation and coalescence of hydrogen bubbles. For the 4% water sample, however, several extremely small bubbles could clearly be seen leaving the cathode surface during the deposition process. This increased rate of electrolysis leads to a rapid release of bubbles during the deposition causing a vigorous stirring effect at the electrode/electrolyte interface leading to a great increase of mass transport of metal ions to the electrode.[42, 44, 47] The effect of this is evidenced by the loss of vertical orientation in the 4% water sample as opposed to the sample prepared with 2% water content. Under given deposition conditions, 2% water concentration, appears to facilitate optimal rate of electrolysis as well as deposition that can engender dendritic growth of vertically oriented $Ni(OH)_2$ nanodendrite forests. **Figure 3-3**a

shows a HRTEM image of a $Ni(OH)_2$ nanodendrite. The diffused rings seen in the selected-area electron diffraction pattern (Figure 3-3a inset) as well as a magnified HRTEM image (Figure S3-2) clearly illustrate its amorphous nature. The disorder arising from incorporated water and

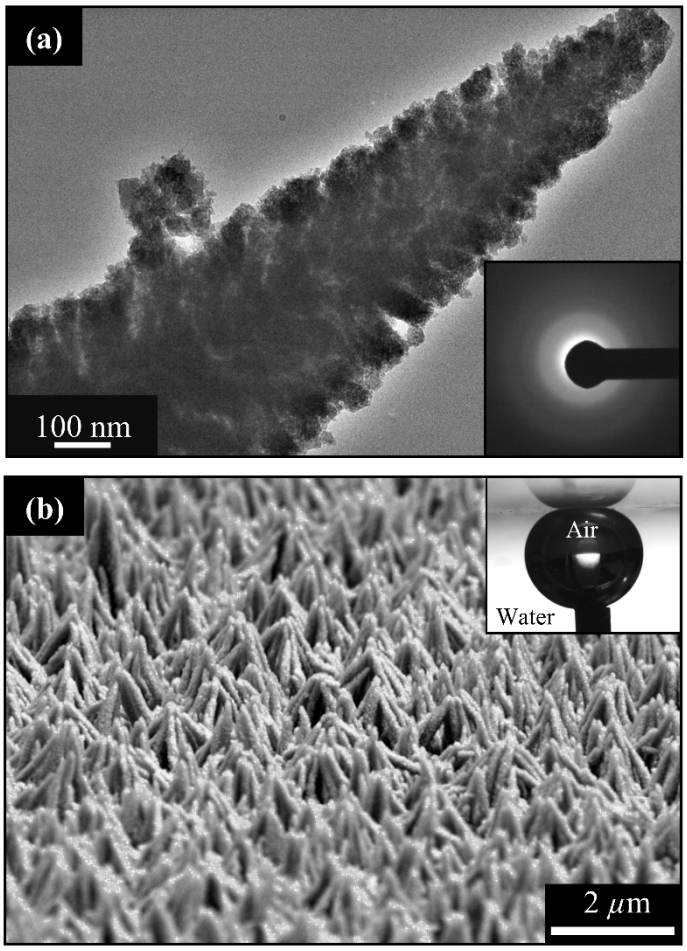

Figure 3-3. (a) HRTEM image of a $Ni(OH)_2$ nanodendrite. Inset shows the selected-area diffraction patterns indicating the amorphous nature of the structure; **(b)** Tilted cross-sectional view of electrodeposited hierarchical 3-D $Ni(OH)_2$ nanodendrite forests. Inset shows near spherical air bubble making contact with the deposited surface under water due to ultralow bubble adhesion.

chloride anions within the $Ni(OH)_2$ structure probably hinders the origin of long-range crystalline order,[48] thus leading to the formation of amorphous α-$Ni(OH)_2$. As a result of the unique nanostructure in combination with the microscale roughness seen in Figure 3-3a, the $Ni(OH)_2$ deposits are superhydrophilic in air and superaerophobic underwater. The inset of Figure 3-3b shows a near spherical air bubble in contact with an immersed nanodendritic forest surface, on account of these extreme wetting properties.

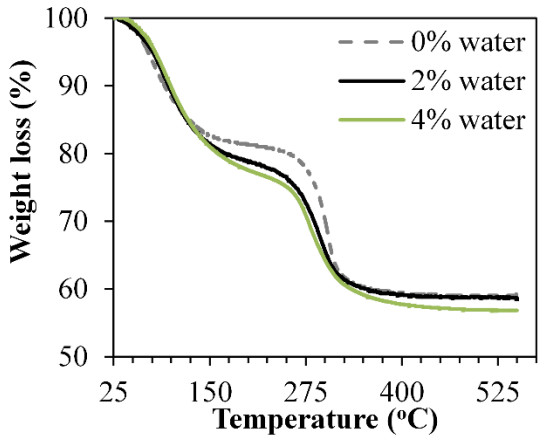

Figure 3-4. Thermogravimetric analysis (TGA) curves of the three $Ni(OH)_2$ deposits showing two distinct weight loss steps typical of α-$Ni(OH)_2$.

The preparation method has been known to significantly influence catalytic activity of materials.[6, 49] This could be on account of the variations in morphology or subtle differences in obtained material composition under different deposition conditions. We used thermogravimetric analysis (TGA) to further study the influence of the electrolyte water content on the composition of the deposited $Ni(OH)_2$. The TGA curves (**Figure 3-4)** show that all the deposits exhibit similar thermal decomposition profiles with two distinct weight loss steps typical of α-$Ni(OH)_2$.[50] The FTIR spectra of all three deposits (Figure S3-3) show features between 650-675

cm^{-1} corresponding to α-$Ni(OH)_2$ along with a broad O-H feature around 3380, seen only in the α-phase $Ni(OH)_2$ and not β-$Ni(OH)_2$.[48, 50-51] The first weight loss step occurring at the lower temperature range stems primarily from the removal of physisorbed water as well as intercalated water molecules within the hydrated $Ni(OH)_2$ crystal structure.[51] It is these water molecules that distort the well-ordered layered structure characteristic of the more common β-$Ni(OH)_2$ to give rise to the more electrochemically active α-$Ni(OH)_2$ polymorph with lower crystallinity.[51] Comparing the weight loss of the three deposits within this temperature range, it is evident that the amount of intercalated water molecules in the hydrated $Ni(OH)_2$ structure is directly related to the amount of water content initially present in the bath. Water content is present in the deposition bath from the water of crystallization of the dissolved $NiCl_2$ salt even when extraneous water is not specifically introduced to the electrolyte This leads to formation of hydrated $Ni(OH)_2$ in all three cases, even when extraneous water is not specifically introduced into the bath. Compared to the 19.6% weight loss in the non-dendritic α-$Ni(OH)_2$ produced when 0% water was added to the bath, the 2% and 4% water samples lose ~4% and 5% more water respectively at a nominal temperature of 250 °C. These differences in weight loss are likely on account of differences in adsorbed water. Beyond this temperature, the second and final weight loss step occurs representing the decomposition of $Ni(OH)_2$ to NiO and loss of any anions.[51] As demonstrated by the TGA curves, these metal hydroxide structures can be easily converted to their corresponding oxides by simple annealing process in air.

The electrochemical characterization of $Ni(OH)_2$ deposited on stainless steel (SS304) from electrolytes containing 0.1 mg ml^{-1} dissolved $NiCl_2.6H_2O$ and three different amounts of added water: 0, 2 and 4%, are shown in **Figure 3-5**. The initial electrochemical behavior after ten stabilizing cycles at 5 mV s^{-1} is shown in Figure 3-5a. All three deposits show the characteristic

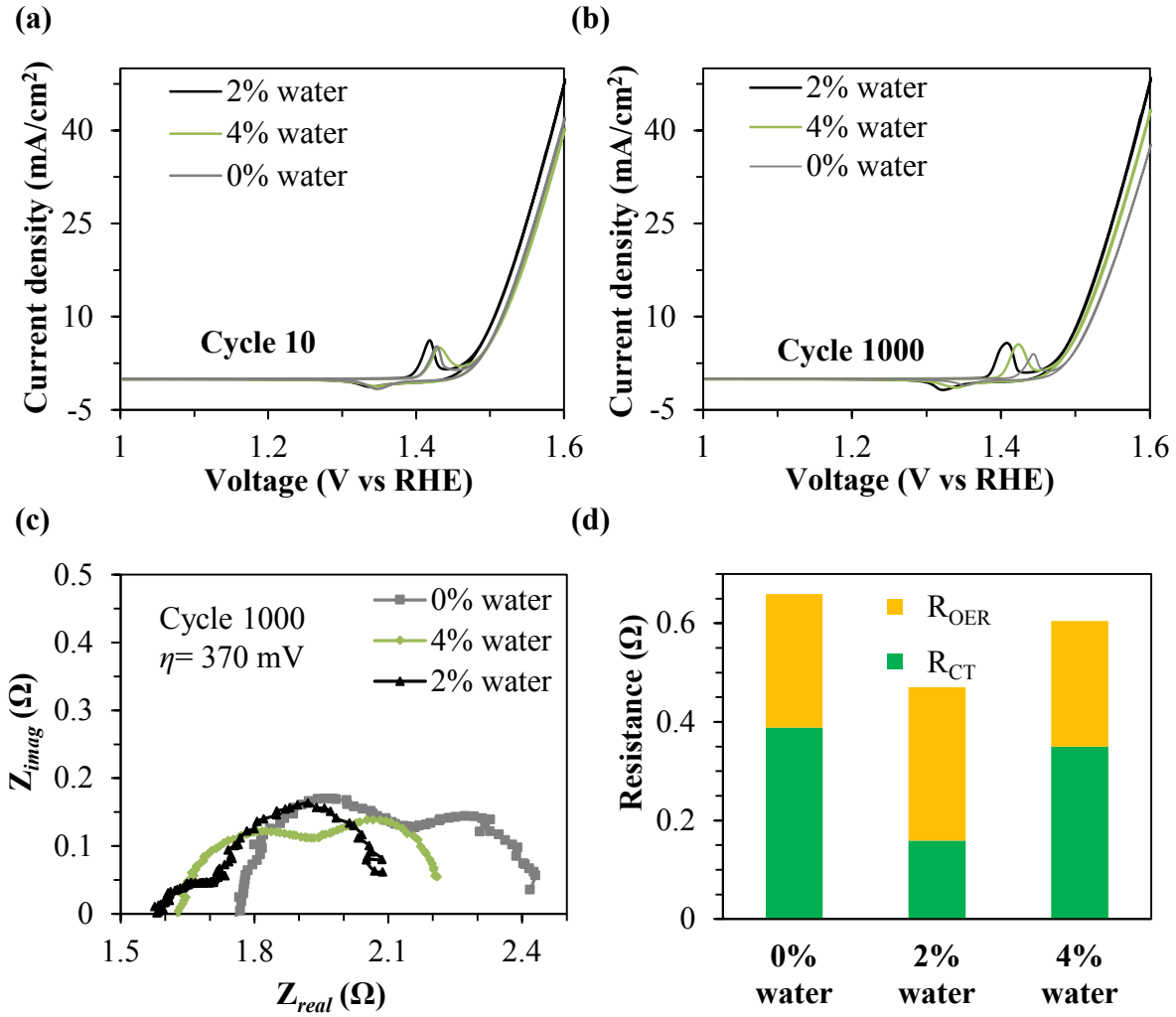

Figure 3-5. Comparison of cyclic voltammograms of three different α-Ni(OH)$_2$ deposits prepared from electrolytes containing 0, 2 and 4% added water: (a) after 10 stabilizing cycles; (b) after 1000 cycles of accelerated stability testing in 1 M KOH at 5 mV s^{-1}; (c) Electrochemical impedance spectroscopy (EIS) data represented as Nyquist plots for the three α-Ni(OH)$_2$ deposits recorded potentiostatically at η = 370 mV after 1000 accelerated stability test cycles; (d) Comparison of total Faradaic resistance values the three α-Ni(OH)$_2$ deposits after 1000 cycles.

anodic peak corresponding to the oxidation of Ni^{2+} to Ni^{3+} signifying the conversion from $Ni(OH)_2$ to NiOOH followed by a steep increase in the current density owing to the onset of the OER process. Initially, the 0% and 4% water deposit show similar electrochemical activity, consistent with the comparatively low exposed surface area of the compact cracked deposits as opposed to the well-distributed vertically aligned nanodendritic 2% water sample. Yet, both these deposits show a low overpotential value (η_{10mA}) of 285 mV to achieve a current density of 10 $mA.cm^{-2}$, the preferred Figure 3-of merit.[7] This suggests that the deposited amorphous metal hydroxide deposited on steel possesses inherently high activity which is underutilized due to the deposit morphology. The 2% water deposit exhibits an even lower η_{10mA} of 273 mV after 10 cycles with a 15% higher current density at an overpotential of 370 mV (η_{370mV}) as compared to the two other deposits. The superiority of this deposit is more apparent from the CV recorded after 1000 cycles of accelerated stability testing (Figure 3-5b). The vertically aligned nanodendritic deposit continues to outperform the 4% and 0% water deposits with excellent durability after accelerated cycling with no apparent loss in activity. These differences in performance are also clearly reflected in the Nyquist curves (Figure 3-5c) obtained potentiostatically at η_{370mV} after 1000 cycles. Figure S3-4 shows the equivalent circuit used to analyze the electrochemical impedance spectroscopy (EIS) data and obtain values by fitting the EIS curves seen in Figure 3-5c.

The equivalent circuit is made up of three resistances: solution resistance (R_S), charge transfer resistance (R_{CT}) and oxygen evolution resistance (R_{OER}) coupled with two constant phase elements (CPE) related to double layer capacitance (CPE_{DL}) and oxygen evolution (CPE_{OER}).[52] The Nyquist curves of all the three $Ni(OH)_2$ deposits, under applied potential in the OER range, typically tend to show two depressed semicircles. The first semicircle in the high frequency

region is representative of the overall charge transfer resistance (R_{CT}) of the electrode.[53] Generally speaking, the second semicircle in the low frequency region is indicative of the resistance to the oxygen evolution reaction (R_{OER}) in terms of ease of formation of reaction intermediates.[52-53] The diameter of this semicircle is overpotential dependent, being inversely proportional to the potential at which the curves are recorded, implying faster reaction kinetics. Figure 3-5d compares the total faradaic resistance[53] (R_{CT} + R_{OER}) of each deposit. At $\eta_{370mV,}$ owing to its excellent charge transfer and lower overall Faradaic resistance, the 2% water deposit is able to sustain a higher current density than the two other deposits.

We attribute this to the well distributed dendritic structures that are in intimate contact with the substrate, allowing for efficient ion diffusion, catalyst access and material utilization. The R_{CT} values of 0 and 4% water deposits are higher given the rather condensed nature of those deposits that hamper charge transfer. A comparison of the total faradaic resistances of the deposits after 10 and 1000 cycles (Figure S3-5) shows that 2% and 4% water samples show a slight decrease in overall resistance. Such improvement in performance of $Ni(OH)_2$ materials during cycling or aging in KOH is generally observed and typically attributed to incidental Fe incorporation[54] from the electrolyte into the $Ni(OH)_2$ matrix. The more pronounced loss in activity of the 0% water deposit upon cycling is reflected in the 15% increase in its total faradaic resistance. This deterioration is probably induced by the instability arising from the composition and morphology of the deposit. The low and stable faradaic resistance values of the 2% water sample establishes clearly that the overall structure and composition of the deposit is critical to long term durability and activity of the deposits. Particularly, the well-spaced and aligned 3-D nanodendritic amorphous $Ni(OH)_2$ structures clearly appear to be the ideal morphology to maximize available catalytic sites and achieve durability.

The comparison of the electrochemical behavior of the α-$Ni(OH)_2$ produced from deposition baths with different water content allows us to study the implications of their unique morphology on their catalytic performance. Specifically, the 0 and 2% water deposits allow for comparison between the cracked thick films obtained in the absence of added water to the vertically aligned, highly accessible dendritic structures obtained by 2% water addition. The morphological differences between 2% and 4% water samples allow for comparison between well distributed and oriented structures to the randomly oriented tightly packed dendritic structures both of which contain a high amount of intercalated water within the $Ni(OH)_2$ structure. From the cyclic voltammograms at different scan rates between 5-100 mV s^{-1} for the three deposits, as shown in Figure S3-6, the anodic redox peak current densities (i_p) of the $Ni(OH)_2$ to NiOOH conversion of each of the deposits was plotted against the square root of the scan rates ($\sqrt{\nu}$). The currents

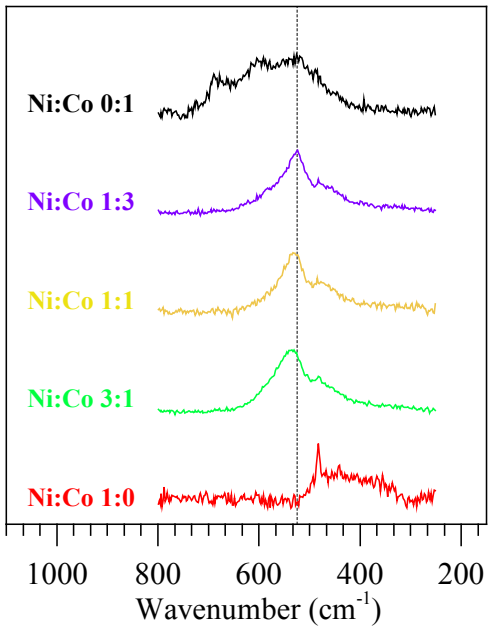

Figure 3-6. Raman spectra of amorphous α-phase Ni-Co hydroxides obtained at various Ni:Co ratios in deposition solutions.

increase linearly with the square root of scan rate, indicating that the electrode reactions are diffusion-controlled.[55] Among the three deposits, the plot of i_p vs $\sqrt{\nu}$ for the 2% water sample shows the highest slope, illustrating the rapid diffusion and charge transfer facilitated by the superior electrochemical accessibility and intimate contact of the individual vertically aligned nanodendrites with the substrate as compared to the other two electrodeposited morphological structures.

As mentioned previously, addition of elements such as cobalt has been known enhance electrochemical performance of nickel hydroxide due to synergistic interactions.[11, 13] The synergy between nickel and cobalt in these materials often results in improved durability especially under prolonged cycling.[13] This enhancement in electrochemical performance of nickel hydroxide with the addition of cobalt has been previously exploited for supercapacitors,[13] and catalysis.[16] Similarly, we expected significant improvement in performance in deposits containing both nickel and cobalt. Various α-phase nickel-cobalt hydroxide nanodendrite deposits were prepared from deposition solutions containing different ratios of Ni^{2+} and Co^{2+} ions. The Raman spectra of dendritic structures prepared with varying Ni:Co ratios are presented in **Figure 3-6**. The Ni:Co 0:1 shows several broad vibrational bands at wavenumbers of approximately 460, 485, 519, 590 and 690 cm^{-1} corresponding to amorphous $Co(OH)_2$.[33] The Raman spectrum of the Ni:Co 1:0 sample shows a broad band centered around 385 cm^{-1} and the band at ~455 cm^{-1} typically attributed to α-$Ni(OH)_2$.[48] The peak around 483 cm^{-1} is a feature of highly disordered $Ni(OH)_2$.[56] The three samples containing both nickel and cobalt have two broad vibrational bands at approximately 460 and 535 cm^{-1}.[57] The latter peak shows a redshift with increasing cobalt content within the structure. The XRD patterns of all the deposits (Figure S3-7) show broad, low intensity peaks owing to their lack of crystalline order.

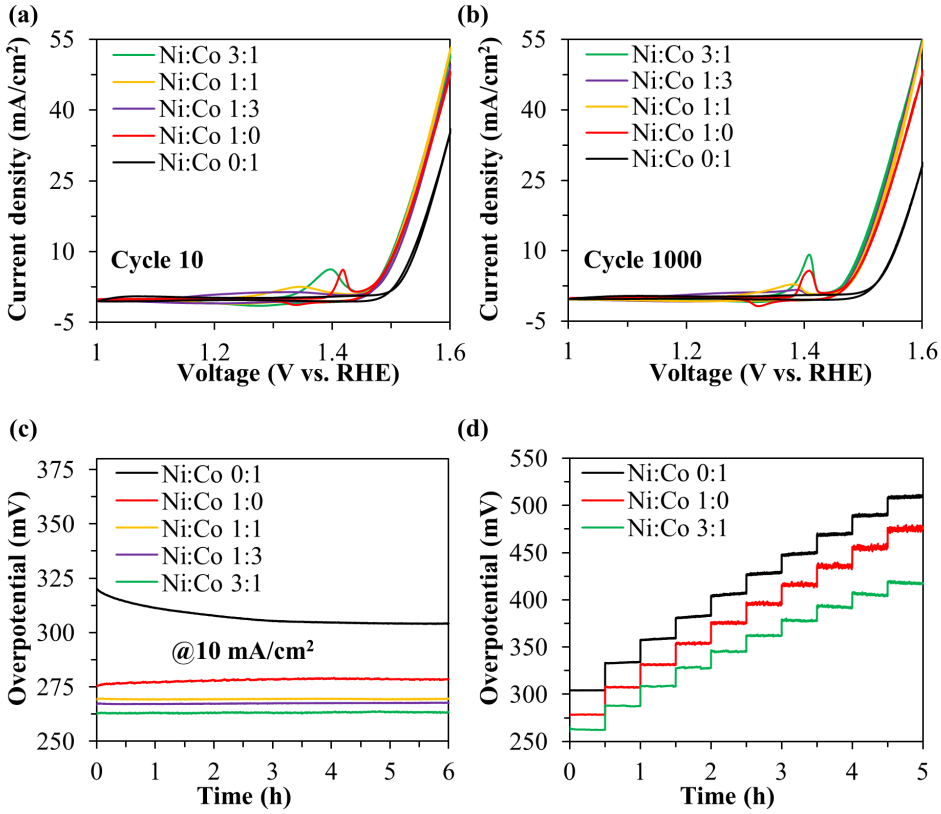

Figure 3-7. (a) Comparison of **c**yclic voltammograms of nanodendrite (1 min) deposits with varying Ni:Co ratios after 10 stabilizing cycles and **(b)** after 1000 cycles of accelerated stability testing. All CV curves were recorded at 5 mV s^{-1}. **(c)** Chronopotentiometry curves for various Ni:Co deposits recorded at j=10 mA cm^{-2} showcase their excellent stability. **(d)** Chronopotentiometry curves of Ni:Co 3:1 compared to $Ni(OH)_2$ and $Co(OH)_2$ deposits recorded at current densities ranging from 10 - 100 mA cm^{-2}. Current density values were stepped up by 10 mA cm^{-2} every 0.5 h.

FTIR spectra (Figure S3-8) show that all mixed nickel-cobalt hydroxide deposits are also similarly α-phase with characteristic broad O–H stretching peak around 3380 cm^{-1} and show various Ni and Co related features at lower wavenumbers below 1000 cm^{-1}.[33, 48] Elemental

mapping of the various dendrites (Figure S3-9) carried out via energy-dispersive X-ray spectroscopy show the ~~varying~~ different nickel and cobalt content within their structures. It can be noted that the deposit morphology remains unaffected even when the deposition is carried out in the presence of Co^{2+} ions. The nickel and cobalt content within the mixed metal hydroxide deposits was determined using inductively coupled plasma atomic emission spectroscopy (ICP-AES). The Ni/Co atomic ratios for the Ni:Co 3:1, 1:1 and 1:3 deposits were estimated to be approximately 3.62:1 , 0.95:1, and 1:3.98 respectively. Figure S3-10 a, b shows magnified views of the CVs, clearly illustrating different redox peak shapes and positions as nickel and cobalt content changes within the deposit. This is further confirmation that different mixed nickel-cobalt hydroxides with distinct electrochemical behaviors are formed by merely varying the ion composition in the deposition bath. Overall, addition of cobalt shifted the $Ni(OH)_2$ redox peak cathodically. The pure $Co(OH)_2$ after 10 cycles shows the highest η_{10mA} of 305 mV, among the tested samples. It is worth noting, however, this is among the lowest η_{10mA} values reported for $Co(OH)_2$.[58] All the other samples tested here show initial η_{10mA} of ~275 mV after the first 10 cycles between 1-1.6 V vs RHE. With prolonged accelerated cycling at 100 mV s^{-1}, the deposits containing both cobalt and nickel show some performance enhancement with slight reduction in η_{10mA} and a ~15% increase in current density obtained at $\eta_{370\text{mV}}$ after 1000 cycles as seen in **Figure 3-7a, 7b**. This illustrates that the incorporation of cobalt ions to the deposition solution can produce α-phase nickel-cobalt hydroxide nanodendritic structures with significantly higher OER performance. This may be a result of the typically higher conductivity or higher degree of oxidation of $Ni(OH)_2$ upon addition of cobalt to the structure.[59]

While the performance of the $Co(OH)_2$ sample appears to have deteriorated in the CV curve in Figure 3-7b, chronopotentiometry carried out at 10 mA cm^{-2} after the 1000 cycles of

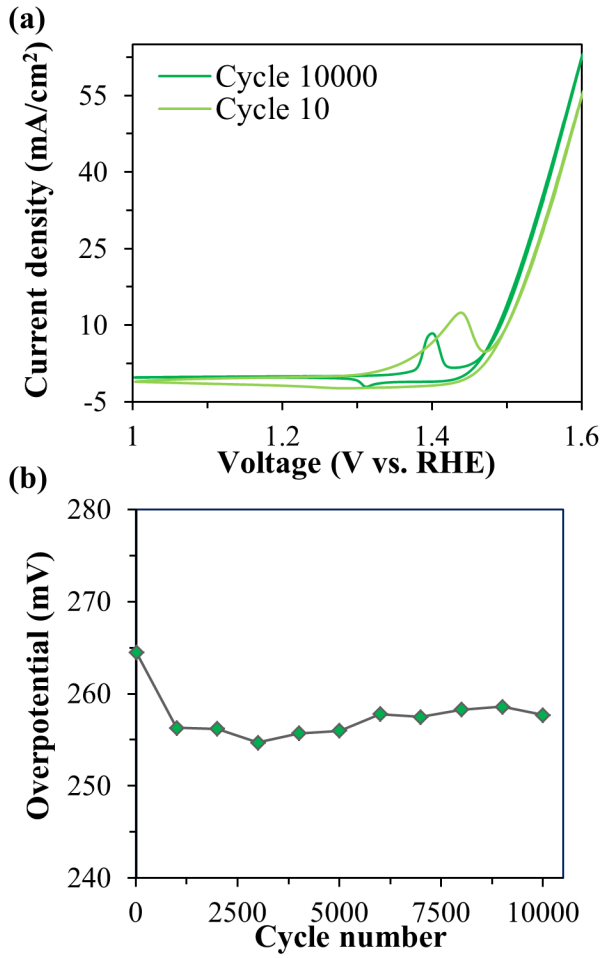

Figure 3-8. (a) Cyclic voltammograms of Ni:Co 3:1 (3 min) deposits before (Cycle 10) and after (Cycle 10,000) cycles of accelerated stability testing. CV curves were recorded at 5 mV s^{-1}; **(b)** OER overpotential values at j = 10 mA cm^{-2} of Ni:Co 3:1 (3 min) deposit versus accelerated stability test cycle number. The overpotential averages merely ~257 mV over 10,000 cycles.

accelerated stability testing shows that the $Co(OH)_2$ sample returns to the η_{10mA} values exhibited before the harsh cycling process (Figure 3-7c). The apparent loss of performance seen in the CV after 1000 cycles may be a function of phase change caused by overcharging during the accelerated stability testing between 1.3-1.8 V vs RHE. All the other compositions show similar

high activity and stable behavior over the 6 hour tests with the Ni:Co 3:1 deposit showing the lowest η_{10mA} of ~262 mV. After 1000 accelerated stability test cycles and 6 hours of chronopotentiometry at j = 10 mA cm^{-2} the same samples were immediately subjected to stepped chronopotentiometry from 10 to 100 mA cm^{-2} over a 5 h period. Current densities were stepped up by 10 mA cm^{-2} increments every 30 minutes. Ni:Co 3:1 outperforms plain $Ni(OH)_2$ and $Co(OH)_2$ with η_{10mA} of 262 mV *versus* 278 and 304 mV for the pure samples respectively. This difference in performance is further amplified at higher current densities with η_{100mA} value of 417 mV versus 475 and 508 mV respectively (Figure 3-7d). Figure S3-10 c,d show the Tafel slopes of Ni:Co 3:1, 1:0 and 0:1 samples after 10 and 1000 cycles respectively. All deposits show low Tafel slopes of between 25-30 mV/dec indicating excellent OER catalysis. Visually, upon cycling, all the deposits (initially light colored) become a black color. FTIR spectra of the Ni:Co 3:1 sample as prepared and after 1000 cycles is shown in Figure S3-11. The α–phase nickel-cobalt hydroxide deposit appears to have converted to a γ-NiOOH phase upon the prolonged testing, providing further insight into the excellent stability of the deposits.[9]

The deleterious effects of binders and carbonaceous additives on OER catalyst performance, especially with higher catalyst loadings, have been previously well documented.[2, 18] The loss in performance despite higher catalyst loading has also been attributed to increased bubble related impedance and ohmic losses therein. Due to their direct growth on to the steel substrate, each nanodendrite in the deposit is intimately attached to the conductive electrode minimizing ohmic losses. This, along with the lack of binder, conductive carbon additives, and easy electrolyte access along with their superaerophobic nature, allow us to deposit a larger amount of material with improved performance. We tested the Ni:Co 3:1 sample deposited for 3 min, with an aim to increase catalyst loading, given its exemplary performance among all the samples deposited for 1

min. We subjected the deposit to 10,000 accelerated stability test cycles. **Figure 3-8**a shows the comparison of the CVs obtained after 10 and 10,000 accelerated cycles. Despite the prolonged and harsh testing conditions, the deposit showed consistently low overpotentials of ~255 mV (Figure 3-8b) at j = 10 mA cm^{-2} and achieved higher current densities (~15% @ $\eta_{370\ mV}$) in the OER region compared to the 1 min deposit. Table S1 compares the performance of our nanodendritic deposits with a few other recently reported alkaline OER catalysts.

Rapid strides have been made recently in terms of fundamental understanding the catalysis of the OER process especially with regard to first row transition metal based materials. Enhanced catalyst performance arising from synergistic interactions between some nanomaterials leading to catalytic activity exceeding that shown by the individual components of the composites[60-62] has been observed and exploited. Several examples exist in literature of such unique systems like Co_3O_4/graphene,[63] Ni/NiO/CNT,[62] MnO_x on various noble metal nanoparticles[61] etc. The interface between the two materials has been found to be important. In case of the noble metal support materials, their electronegativity serving to stabilize a higher valance state of the catalytic material and also the interfacial sites have been demonstrated to be critical to this phenomenon of synergistic enhancement.[61, 64]

Another phenomenon that has been studied is the enhanced performance due to substrate-catalyst interactions. This has been seen more explicitly in case of MnO_x,[60-61] CoO_x,[65] NiO[64] deposits on Au substrates. Beyond a certain monolayer thickness, the effects were seen to diminish. The interaction between deposits and substrates in the case of non-noble materials has been relatively less studied. There have been observations of particular deposits performing significantly better on specific substrates as well.[66-68] McCrory *et al.* noticed a significant

difference in reported overpotential of electrodeposited $NiCeO_x$ on nickel versus that on glassy carbon electrodes.[5] More recently, Ni deposits on steel showed significantly enhanced OER performance as compared to similar deposits on other substrate materials.[36] As mentioned previously, the significant improvement of $Ni(OH)_2$ and $Co(OH)_2$ electrodeposits over prolonged voltage cycling or merely aging in electrolyte has been attributed to the incorporation of iron impurities present in the supporting KOH electrolyte.[54] The OER enhancement results from the effect of the Fe^{3+} present in the NiOOH structure.[69] This is in line with the highest performing transition-metal catalysts typically being combinations of nickel and iron.[54, 68] The enhanced activity in our deposits, however, is apparent right from the first voltammetry cycle specifically after deposition on steel substrate immediately after being introduced into the 1 M KOH electrolyte. This is not seen when deposited on other substrates such as nickel, graphite, and copper. Thus, the enhancement effect due to of Fe incorporation[54] from the electrolyte within the $Ni(OH)_2$ structure during cycling is less likely to be the primary cause.

To avoid the effect of potential incorporation of Fe impurities within the deposits via cycling or aging in the KOH electrolyte, Figure S3-12 shows the first CV curve of pure $Ni(OH)_2$, $Co(OH)_2$, and Ni:Co 3:1 samples on several different substrates. It is readily apparent that using a steel substrate has a dramatic impact on the OER catalytic activity on all the deposits. This may indicate that the Ni/Fe or Co/Fe interactions at the deposit/steel interface may be synergistically amplifying the catalytic activity of the nickel, cobalt hydroxide deposits. There have been a few instances of reports of excellent OER catalytic activity of materials deposited on steel.[36, 70] For further confirmation of the contribution of the deposit-substrate interface on the high activity, $Ni(OH)_2$ nanodendrite samples on stainless steel and nickel foil were sonicated in KOH for an hour, in order to remove the nanodendrite deposits, after an initial CV scan (Figure S3-13 a, b

respectively) was recorded. In both cases, samples showed an inordinate decrease in oxygen evolution overpotential as compared to the bare substrate despite removal of the dendritic superstructures from the surface. This is likely due to a synergistic interaction between the Fe content on the steel surface and the electrodeposited metal hydroxide material. However, it is possible that the interactions are far more complex given the composition of stainless steel surface and worthy of detailed analysis in the future. Ultimately, such robust hierarchical nanostructures on synergistic 3-D substrates so as to maximize interfacial area along with their low bubble adhesion would be outstanding and durable OER catalysts.

3.4 Conclusion

In summation, electrodeposition of novel hierarchically structured α-phase nickel-cobalt hydroxides from a primarily alcohol-based solution has been made possible by introducing a small amount of water to the deposition bath. The high localized pH at the deposition electrode/electrolyte interface induced by the limited water electrolysis along with the rapid hydrogen bubble templated growth in a diffusion-controlled deposition regime, leads to the growth of dense 3-D nanodendrite forests of amorphous α-phase nickel-cobalt hydroxides. An optimal amount of water (~2% v/v) in the deposition solution was found to facilitate the deposition conditions required for the growth of vertically aligned nanodendrite structures. The resulting superaerophobic α-phase nickel-cobalt hydroxide deposits especially when deposited on a stainless steel electrode substrate, showed enhanced performance as an oxygen evolution reaction catalyst providing current densities of 10 mA cm^{-2} at overpotentials as low as 255 mV durably over 10,000 accelerated stability test cycles. These results demonstrate the importance of direct growth of hierarchical catalyst structures devoid of any polymeric binders onto synergistic

substrates in order to maximize electrochemical performance for practical OER catalysis applications.

3.5 Methods and Materials

Electrodeposition

A mixture of ethanol-isopropanol (1:1) was used in all cases as the base electrolyte with additional DI water (0, 2, or 4 %) and dissolved metal salt (0.1 mg ml^{-1}) being added for modification. The metal salts, $NiCl_2.6H_2O$ and $CoCl_2.6H_2O$ were obtained from Sigma-Aldrich (St. Louis, MO, USA). The electrolyte was sonicated for 5 minutes in an ultrasonic bath before deposition. All deposits were prepared by electrodeposition in a two electrode system. Typically, 1 cm^2 area of the electrodes were exposed to each other separated by a distance of 0.7 cm in 20 ml of electrolyte. Stainless steel 304 foil and nickel for electrodes were obtained from McMaster-Carr (Elmhurst, IL, USA). The electrodes were typically subjected to degreasing in acetone and isopropanol, followed by thorough washing in deionized (DI) water. Prior to deposition, the foil was additionally dipped in 1 M HCl and rinsed with DI water to remove some surface oxides. A graphite foil (CeraMaterials, New York, USA) electrode was used as the counter electrode in all cases to avoid contamination of the electrolyte resulting from counter electrode etching. 200 V were applied to the electrodes using a Matsusada Precision high-voltage power source (Model EJ-2R100) typically for 60 seconds unless stated otherwise.

Material Characterization

Field emission scanning electron microscope (FESEM) images and elemental maps of the deposits were obtained using a Hitachi S-4800 FESEM at accelerating voltages of 5 and 20 kV respectively. High-resolution transmission electron microscope (HRTEM) images and selected

area electron diffraction patterns were obtained in a Hitachi H-9500 electron microscope operated at 300 kV.

A Thermo Nicolet 6700 FTIR Spectrometer was used to record FTIR spectra (4 cm^{-1} resolution; 256 scans). Thermogravimetric analysis (TGA) was carried with a TGA-51 (Shimadzu Scientific Instruments) at a rate of $10^{o}C\ min^{-1}$ in air from room temperature up to 550°C. A Shimadzu ICPE-9800 Atomic Emission Spectrophotometer was used to measure Ni:Co ratio within the deposits.

Raman spectra were collected using a Thermo Scientific™ DXR™ Raman imaging microscope utilizing a 532 nm laser excitation source operating at 0.5 mW to avoid sample heating effects.–Spectra were averaged from 5 scans collected for 35 s each. X-ray diffraction (XRD) data was collected using a Bruker D-8 Advance diffractometer (40 kV; 40 mA) utilizing Cu Kα radiation with a step size of 0.04^{o} at a rate of 1.8 s per step. A zero-background Si holder (MTI Corporation, Richmond, CA, USA) with a central cavity of 10 mm diameter and 0.2 mm depth was utilized for XRD and Raman in order to maximize signal and avoid substrate interference.

Electrochemical testing

All tests were carried out in 1 M KOH (pH 13.6). Potassium hydroxide was obtained from Sigma-Aldrich (St. Louis, MO, USA). All potentials were recorded against Ag/AgCl reference electrode. Recorded potentials were converted to the reversible hydrogen electrode (RHE) scale according to the equation (1):

$$E_{RHE} = E_{Ag/AgCl} + 0.059*pH + E^{o}_{Ag/AgCl} \quad (1)$$

Where $E_{Ag/AgCl}$ is the measured potential and $E^{o}_{Ag/AgCl}$ is the standard electrode potential (0.20 V) of the Ag/AgCl electrode filled with 4 M KCl solution.

All electrochemical testing was performed using a Gamry Reference 3000 potentiostat (Gamry Instruments, Warminster, PA, USA) and a standard glass three-electrode test cell with graphite rod as counter electrode. An Ag/AgCl reference electrode (Pine Research Instrumentation, Durham, NC, USA) with a ceramic frit was used as reference electrode in all tests. Overpotential (η) values mentioned, refer to the difference between the applied voltage value and 1.23 V. For brevity, overpotential value to achieve a current density of 10 mA.cm^{-2} is referred to as $\eta_{10mA.}$ Similarly, η_{370mV} is used to refer to an applied overpotential of 370 mV.

Cyclic voltammograms (CV) shown comparing OER activity were obtained between 0-0.6 V vs Ag/AgCl electrode i.e. ~ 1 - 1.6 V vs RHE. All CV data was *i*R corrected automatically by the instrument using the current interrupt method. Typically, 10 CV cycles were carried out to ensure stable redox behavior of the deposits. Anodic peak current was plotted against square root of scan rate from data obtained from CVs carried out at 5, 10, 20, 50, 75, and 100 mV s^{-1}.

Typically, after initial cycling to ensure stability, samples were subjected to accelerated stability testing by cycling between a voltage window between 1.3–1.8 V vs RHE at a relatively fast scan rate of 100 mV s^{-1} for 1000 cycles. CVs were recorded between 1-1.6 V vs RHE at 5 mV.s^{-1} before and after accelerated cycling for comparison. After 1000 cycles, samples were further subjected to chronopotentiometry at current density of 10 mA cm^{-2}. Finally, the samples

were subjected to chronopotentiometry from 10-100 mA cm^{-2} in 10 mA cm^{-2} increments every 30 min.

In the case of the prolonged accelerated stability testing of the Ni:Co 3:1 (3 min deposit for higher mass loading), the sample was subjected to 10,000 cycles of testing using the same accelerated testing protocol previously mentioned. Chronopotentiometry was carried out for 15 min at current density of 10 mA cm^{-2} after every 1000 cycles to determine change in overpotential over extended cycle life. Electrochemical impedance spectroscopy of samples was carried out potentiostatically at 0.6 V vs Ag/AgCl between 100000-1 Hz with an AC perturbation of 10 mV. The EIS data was fit using EChem Analyst™ (Gamry Instruments, Warminster, PA, USA).

3.6 Acknowledgements

The authors acknowledge the guidance of Late Dr. Dennis Desheng Meng during the initial stages of this work. The authors also acknowledge the financial support from the National Science Foundation (NSF Awards 1439494 and 1444473). We sincerely thank Dr. Hyejin Moon for her help reviewing the draft of this manuscript. The authors would like to thank Dr. Matthew Loocke for his assistance with running the ICP analysis.

3.7 References

1. Zeng, K.; Zhang, D. Recent Progress in Alkaline Water Electrolysis for Hydrogen Production and Applications. *Prog. Energy Combust. Sci.* **2010,** *36*, 307-326.

2. Wang, H.; Lee, H. W.; Deng, Y.; Lu, Z.; Hsu, P. C.; Liu, Y.; Lin, D.; Cui, Y. Bifunctional Non-Noble Metal Oxide Nanoparticle Electrocatalysts through Lithium-Induced Conversion for Overall Water Splitting. *Nat. Commun.* **2015,** *6*, 7261.

3. Wang, M.; Wang, Z.; Gong, X.; Guo, Z. The Intensification Technologies to Water Electrolysis for Hydrogen Production – a Review. *Renew. Sust. Energ. Rev.* **2014,** *29*, 573-588.

4. Luo, J.; Im, J. H.; Mayer, M. T.; Schreier, M.; Nazeeruddin, M. K.; Park, N. G.; Tilley, S. D.; Fan, H. J.; Gratzel, M. Water Photolysis at 12.3% Efficiency Via Perovskite Photovoltaics and Earth-Abundant Catalysts. *Science* **2014,** *345*, 1593-1596.

5. McCrory, C. C.; Jung, S.; Peters, J. C.; Jaramillo, T. F. Benchmarking Heterogeneous Electrocatalysts for the Oxygen Evolution Reaction. *J. Am. Chem. Soc.* **2013,** *135*, 16977-16987.

6. Minguzzi, A.; Fan, F.-R. F.; Vertova, A.; Rondinini, S.; Bard, A. J. Dynamic Potential–pH Diagrams Application to Electrocatalysts for Water Oxidation. *Chem. Sci.* **2012,** *3*, 217-229.

7. Gorlin, Y.; Jaramillo, T. F. A Bifunctional Nonprecious Metal Catalyst for Oxygen Reduction and Water Oxidation. *J. Am. Chem. Soc.* **2010,** *132*, 13612-13614.

8. Lee, Y.; Suntivich, J.; May, K. J.; Perry, E. E.; Shao-Horn, Y. Synthesis and Activities of Rutile IrO_2 and RuO_2 Nanoparticles for Oxygen Evolution in Acid and Alkaline Solutions. *J. Phys. Chem. Lett.* **2012,** *3*, 399-404.

9. Gao, M.; Sheng, W.; Zhuang, Z.; Fang, Q.; Gu, S.; Jiang, J.; Yan, Y. Efficient Water Oxidation Using Nanostructured α-Nickel-Hydroxide as an Electrocatalyst. *J. Am. Chem. Soc.* **2014,** *136*, 7077-7084.

10. Li, Y.; Hasin, P.; Wu, Y. $Ni_xCo_{3-x}O_4$ Nanowire Arrays for Electrocatalytic Oxygen Evolution. *Adv. Mater.* **2010,** *22*, 1926-1929.

11. Balram, A.; Jiang, J. C.; Hernández Fernández, M.; Meng, D. D. S. Nickel-Cobalt Double Hydroxide Decorated Carbon Nanotubes Via Aqueous Electrophoretic Deposition Towards Catalytic Glucose Detection. *Key Eng. Mater.* **2015,** *654*, 70-75.

12. Li, H. B.; Yu, M. H.; Wang, F. X.; Liu, P.; Liang, Y.; Xiao, J.; Wang, C. X.; Tong, Y. X.; Yang, G. W. Amorphous Nickel Hydroxide Nanospheres with Ultrahigh Capacitance and Energy Density as Electrochemical Pseudocapacitor Materials. *Nat. Commun.* **2013,** *4*, 1894.

13. Chen, H.; Jiang, J.; Zhang, L.; Zhao, Y.; Guo, D.; Ruan, Y.; Xia, D. One-Pot Fabrication of Layered *α*-Phase Nickel-Cobalt Hydroxides as Advanced Electrode Materials for Pseudocapacitors. *ChemPlusChem* **2015,** *80*, 181-187.

14. Li, H.; Gao, Y.; Wang, C.; Yang, G. A Simple Electrochemical Route to Access Amorphous Mixed-Metal Hydroxides for Supercapacitor Electrode Materials. *Adv. Energy Mater.* **2015,** *5*, 1401767.

15. Dong, L.; Chu, Y.; Sun, W. Controllable Synthesis of Nickel Hydroxide and Porous Nickel Oxide Nanostructures with Different Morphologies. *Chemistry* **2008,** *14*, 5064-72.

16. Nai, J.; Yin, H.; You, T.; Zheng, L.; Zhang, J.; Wang, P.; Jin, Z.; Tian, Y.; Liu, J.; Tang, Z.; Guo, L. Efficient Electrocatalytic Water Oxidation by Using Amorphous Ni-Co Double Hydroxides Nanocages. *Adv. Energy Mater.* **2015,** *5*, 1401880.

17. Jeevanandam, P.; Koltypin, Y.; Gedanken, A. Synthesis of Nanosized α-Nickel Hydroxide by a Sonochemical Method. *Nano Lett.* **2001,** *1*, 263-266.

18. Lu, X.; Zhao, C. Electrodeposition of Hierarchically Structured Three-Dimensional Nickel-Iron Electrodes for Efficient Oxygen Evolution at High Current Densities. *Nat. Commun.* **2015,** *6*, 6616.

19. Matsushima, H.; Nishida, T.; Konishi, Y.; Fukunaka, Y.; Ito, Y.; Kuribayashi, K. Water Electrolysis under Microgravity. *Electrochim. Acta* **2003,** *48*, 4119-4125.

20. Zeradjanin, A. R.; Topalov, A. A.; Van Overmeere, Q.; Cherevko, S.; Chen, X.; Ventosa, E.; Schuhmann, W.; Mayrhofer, K. J. J. Rational Design of the Electrode Morphology for Oxygen Evolution – Enhancing the Performance for Catalytic Water Oxidation. *RSC Adv.* **2014,** *4*, 9579-9587.

21. Matsushima, H.; Fukunaka, Y.; Kuribayashi, K. Water Electrolysis under Microgravity. *Electrochim. Acta* **2006,** *51*, 4190-4198.

22. Lu, Z.; Zhu, W.; Yu, X.; Zhang, H.; Li, Y.; Sun, X.; Wang, X.; Wang, H.; Wang, J.; Luo, J.; Lei, X.; Jiang, L. Ultrahigh Hydrogen Evolution Performance of under-Water "Superaerophobic" MoS_2 Nanostructured Electrodes. *Adv. Mater.* **2014,** *26*, 2683-2687.

23. Li, Y.; Zhang, H.; Xu, T.; Lu, Z.; Wu, X.; Wan, P.; Sun, X.; Jiang, L. Under-Water Superaerophobic Pine-Shaped Pt Nanoarray Electrode for Ultrahigh-Performance Hydrogen Evolution. *Adv. Funct. Mater.* **2015,** *25*, 1737-1744.

24. Lu, Z.; Li, Y.; Lei, X.; Liu, J.; Sun, X. Nanoarray Based “Superaerophobic” Surfaces for Gas Evolution Reaction Electrodes. *Mater. Horiz.* **2015,** *2*, 294-298.

25. Zhang, P.; Wang, S.; Wang, S.; Jiang, L. Superwetting Surfaces under Different Media: Effects of Surface Topography on Wettability. *Small* **2015,** *11*, 1939-1946.

26. Salvatore, D. A.; Dettelbach, K. E.; Hudkins, J. R.; Berlinguette, C. P. Near-Infrared-Driven Decomposition of Metal Precursors Yields Amorphous Electrocatalytic Films. *Sci. Adv.* **2015,** *1*, e1400215.

27. Gao, Y.; Li, H.; Yang, G. Amorphous Nickel Hydroxide Nanosheets with Ultrahigh Activity and Super-Long-Term Cycle Stability as Advanced Water Oxidation Catalysts. *Cryst. Growth Des.* **2015,** *15*, 4475-4483.

28. Gao, Y. Q.; Liu, X. Y.; Yang, G. W. Amorphous Mixed-Metal Hydroxide Nanostructures for Advanced Water Oxidation Catalysts. *Nanoscale* **2016,** *8*, 5015-5023.

29. Indra, A.; Menezes, P. W.; Sahraie, N. R.; Bergmann, A.; Das, C.; Tallarida, M.; Schmeisser, D.; Strasser, P.; Driess, M. Unification of Catalytic Water Oxidation and Oxygen

Reduction Reactions: Amorphous Beat Crystalline Cobalt Iron Oxides. *J. Am. Chem. Soc.* **2014,** *136*, 17530-17536.

30. Koza, J. A.; He, Z.; Miller, A. S.; Switzer, J. A. Electrodeposition of Crystalline Co_3O_4—a Catalyst for the Oxygen Evolution Reaction. *Chem. Mater.* **2012,** *24*, 3567-3573.

31. Kuai, L.; Geng, J.; Chen, C.; Kan, E.; Liu, Y.; Wang, Q.; Geng, B. A Reliable Aerosol-Spray-Assisted Approach to Produce and Optimize Amorphous Metal Oxide Catalysts for Electrochemical Water Splitting. *Angew. Chem. Int. Ed.* **2014,** *53*, 7547-7551.

32. Kast, M. G.; Cochran, E. A.; Enman, L. J.; Mitchson, G.; Ditto, J.; Siefe, C.; Plassmeyer, P. N.; Greenaway, A. L.; Johnson, D. C.; Page, C. J.; Boettcher, S. W. Amorphous Mixed-Metal Oxide Thin Films from Aqueous Solution Precursors with near-Atomic Smoothness. *J. Am. Chem. Soc.* **2016,** *138*, 16800-16808.

33. Li, H. B.; Yu, M. H.; Lu, X. H.; Liu, P.; Liang, Y.; Xiao, J.; Tong, Y. X.; Yang, G. W. Amorphous Cobalt Hydroxide with Superior Pseudocapacitive Performance. *ACS Appl. Mater. Interfaces* **2014,** *6*, 745-749.

34. Binninger, T.; Mohamed, R.; Waltar, K.; Fabbri, E.; Levecque, P.; Kotz, R.; Schmidt, T. J. Thermodynamic Explanation of the Universal Correlation between Oxygen Evolution Activity and Corrosion of Oxide Catalysts. *Sci. Rep.* **2015,** *5*, 12167.

35. Burke, M. S.; Enman, L. J.; Batchellor, A. S.; Zou, S.; Boettcher, S. W. Oxygen Evolution Reaction Electrocatalysis on Transition Metal Oxides and (Oxy)Hydroxides: Activity Trends and Design Principles. *Chem. Mater.* **2015,** *27*, 7549-7558.

36. Hoang, T. T. H.; Gewirth, A. A. High Activity Oxygen Evolution Reaction Catalysts from Additive-Controlled Electrodeposited Ni and NiFe Films. *ACS Catal.* **2016,** *6*, 1159-1164.

37. Jung, H.; Lee, S. H.; Yang, J.; Cho, M.; Lee, Y. $Ni(OH)_2$@Cu Dendrite Structure for Highly Sensitive Glucose Determination. *RSC Adv.* **2014,** *4*, 47714-47720.

38. Fleury, V. Branched Fractal Patterns in Non-Equilibrium Electrochemical Deposition from Oscillatory Nucleation and Growth. *Nature* **1997,** *390*, 145-148.

39. Choi, K. S. Shape Control of Inorganic Materials Via Electrodeposition. *Dalton Trans.* **2008,** 5432-5438.

40. Yang, M. Fern-Shaped Bismuth Dendrites Electrodeposited at Hydrogen Evolution Potentials. *J. Mater. Chem.* **2011,** *21*, 3119-3124.

41. Trigueros, P. P.; Claret, J.; Mas, F.; Sagués, F. Pattern Morphologies in Zinc Electrodeposition. *J. Electroanal. Chem. Interfac.* **1991,** *312*, 219-235.

42. Plowman, B. J.; Jones, L. A.; Bhargava, S. K. Building with Bubbles: The Formation of High Surface Area Honeycomb-Like Films Via Hydrogen Bubble Templated Electrodeposition. *Chem. Commun.* **2015,** *51*, 4331-4346.

43. Offin, D. G.; Birkin, P. R.; Leighton, T. G. Electrodeposition of Copper in the Presence of an Acoustically Excited Gas Bubble. *Electrochem. Commun.* **2007,** *9*, 1062-1068.

44. Nikolic, N. D.; Pavlovic, L. J.; Pavlovic, M. G.; Popov, K. I. Morphologies of Electrochemically Formed Copper Powder Particles and Their Dependence on the Quantity of Evolved Hydrogen. *Powder Technol.* **2008,** *185*, 195-201.

45. Nikolić, N. D.; Pavlović, L. J.; Pavlović, M. G.; Popov, K. I. Formation of Dish-Like Holes and a Channel Structure in Electrodeposition of Copper under Hydrogen Co-Deposition. *Electrochim. Acta* **2007,** *52*, 8096-8104.

46. Therese, G. H. A.; Kamath, P. V. Electrochemical Synthesis of Metal Oxides and Hydroxides. *Chem. Mater.* **2000,** *12*, 1195-1204.

47. Santato, C.; López, C. M.; Choi, K.-S. Synthesis and Characterization of Polycrystalline Sn and SnO_2 Films with Wire Morphologies. *Electrochem. Commun.* **2007,** *9*, 1519-1524.

48. Hall, D. S.; Lockwood, D. J.; Poirier, S.; Bock, C.; MacDougall, B. R. Raman and Infrared Spectroscopy of α and β Phases of Thin Nickel Hydroxide Films Electrochemically Formed on Nickel. *J. Phys. Chem. A* **2012,** *116*, 6771-6784.

49. Galán-Mascarós, J. R. Water Oxidation at Electrodes Modified with Earth-Abundant Transition-Metal Catalysts. *ChemElectroChem* **2015,** *2*, 37-50.

50. Aghazadeh, M.; Ghaemi, M.; Sabour, B.; Dalvand, S. Electrochemical Preparation of α-$Ni(OH)_2$ Ultrafine Nanoparticles for High-Performance Supercapacitors. *J. Solid State Electrochem.* **2014,** *18*, 1569-1584.

51. Hall, D. S.; Lockwood, D. J.; Bock, C.; MacDougall, B. R. Nickel Hydroxides and Related Materials: A Review of Their Structures, Synthesis and Properties. *Proc. R. Soc. A* **2015,** *471*, 20140792.

52. Lyons, M. E. G.; Brandon, M. P. The Significance of Electrochemical Impedance Spectra Recorded During Active Oxygen Evolution for Oxide Covered Ni, Co and Fe Electrodes in Alkaline Solution. *J. Electroanal. Chem.* **2009,** *631*, 62-70.

53. Doyle, R. L.; Lyons, M. E. An Electrochemical Impedance Study of the Oxygen Evolution Reaction at Hydrous Iron Oxide in Base. *Phys. Chem. Chem. Phys.* **2013,** *15*, 5224-5237.

54. Klaus, S.; Cai, Y.; Louie, M. W.; Trotochaud, L.; Bell, A. T. Effects of Fe Electrolyte Impurities on $Ni(OH)_2$/NiOOH Structure and Oxygen Evolution Activity. *J. Phys. Chem. C* **2015,** *119*, 7243-7254.

55. Wu, Z.; Huang, X. L.; Wang, Z. L.; Xu, J. J.; Wang, H. G.; Zhang, X. B. Electrostatic Induced Stretch Growth of Homogeneous β-$Ni(OH)_2$ on Graphene with Enhanced High-Rate Cycling for Supercapacitors. *Sci. Rep.* **2014,** *4*, 3669.

56. Deabate, S.; Fourgeot, F.; Henn, F. X-Ray Diffraction and Micro-Raman Spectroscopy Analysis of New Nickel Hydroxide Obtained by Electrodialysis. *J. Power Sources* **2000,** *87*, 125-136.

57. Vidotti, M.; Salvador, R. P.; Ponzio, E. A.; Cordoba de Torresi, S. I. Mixed Ni/Co Hydroxide Nanoparticles Synthesized by Sonochemical Method. *J. Nanosci. Nanotechnol.* **2007,** *7*, 3221-3226.

58. Jin, H.; Mao, S.; Zhan, G.; Xu, F.; Bao, X.; Wang, Y. Fe Incorporated α-$Co(OH)_2$ Nanosheets with Remarkably Improved Activity Towards the Oxygen Evolution Reaction. *J. Mater. Chem. A* **2017,** *5*, 1078-1084.

59. Cressent, A.; Pralong, V.; Audemer, A.; Leriche, J.-B.; Delahaye-Vidal, A.; Tarascon, J.-M. Electrochemical Performance Comparison between β-Type Mixed Nickel Cobalt Hydroxides Prepared by Various Synthesis Routes. *Solid State Sci.* **2001,** *3*, 65-80.

60. Gorlin, Y.; Chung, C. J.; Benck, J. D.; Nordlund, D.; Seitz, L.; Weng, T. C.; Sokaras, D.; Clemens, B. M.; Jaramillo, T. F. Understanding Interactions between Manganese Oxide and Gold That Lead to Enhanced Activity for Electrocatalytic Water Oxidation. *J. Am. Chem. Soc.* **2014,** *136*, 4920-4926.

61. Seitz, L. C.; Hersbach, T. J.; Nordlund, D.; Jaramillo, T. F. Enhancement Effect of Noble Metals on Manganese Oxide for the Oxygen Evolution Reaction. *J. Phys. Chem. Lett.* **2015,** *6*, 4178-4183.

62. Gong, M.; Zhou, W.; Tsai, M. C.; Zhou, J.; Guan, M.; Lin, M. C.; Zhang, B.; Hu, Y.; Wang, D. Y.; Yang, J.; Pennycook, S. J.; Hwang, B. J.; Dai, H. Nanoscale Nickel Oxide/Nickel Heterostructures for Active Hydrogen Evolution Electrocatalysis. *Nat. Commun.* **2014,** *5*, 4695.

63. Liang, Y.; Li, Y.; Wang, H.; Zhou, J.; Wang, J.; Regier, T.; Dai, H. Co_3O_4 Nanocrystals on Graphene as a Synergistic Catalyst for Oxygen Reduction Reaction. *Nat. Mater.* **2011,** *10*, 780-786.

64. Yeo, B. S.; Bell, A. T. In Situ Raman Study of Nickel Oxide and Gold-Supported Nickel Oxide Catalysts for the Electrochemical Evolution of Oxygen. *J. Phys. Chem. C* **2012,** *116*, 8394-8400.

65. Yeo, B. S.; Bell, A. T. Enhanced Activity of Gold-Supported Cobalt Oxide for the Electrochemical Evolution of Oxygen. *J. Am. Chem. Soc.* **2011,** *133*, 5587-5593.

66. Swesi, A. T.; Masud, J.; Nath, M. Nickel Selenide as a High-Efficiency Catalyst for Oxygen Evolution Reaction. *Energy Environ. Sci.* **2016,** *9*, 1771-1782.

67. Iwakura, C.; Honji, A.; Tamura, H. The Anodic Evolution of Oxygen on Co_3O_4 Film Electrodes in Alkaline Solutions. *Electrochim. Acta* **1981,** *26*, 1319-1326.

68. Dionigi, F.; Strasser, P. NiFe-Based (Oxy)Hydroxide Catalysts for Oxygen Evolution Reaction in Non-Acidic Electrolytes. *Adv. Energy Mater.* **2016,** 1600621.

69. Friebel, D.; Louie, M. W.; Bajdich, M.; Sanwald, K. E.; Cai, Y.; Wise, A. M.; Cheng, M. J.; Sokaras, D.; Weng, T. C.; Alonso-Mori, R.; Davis, R. C.; Bargar, J. R.; Norskov, J. K.; Nilsson, A.; Bell, A. T. Identification of Highly Active Fe Sites in (Ni,Fe)OOH for Electrocatalytic Water Splitting. *J. Am. Chem. Soc.* **2015,** *137*, 1305-1313.

70. Chen, J. S.; Ren, J.; Shalom, M.; Fellinger, T.; Antonietti, M. Stainless Steel Mesh-Supported NiS Nanosheet Array as Highly Efficient Catalyst for Oxygen Evolution Reaction. *ACS Appl. Mater. Interfaces* **2016,** *8*, 5509-5516.

3.8 Supporting Information

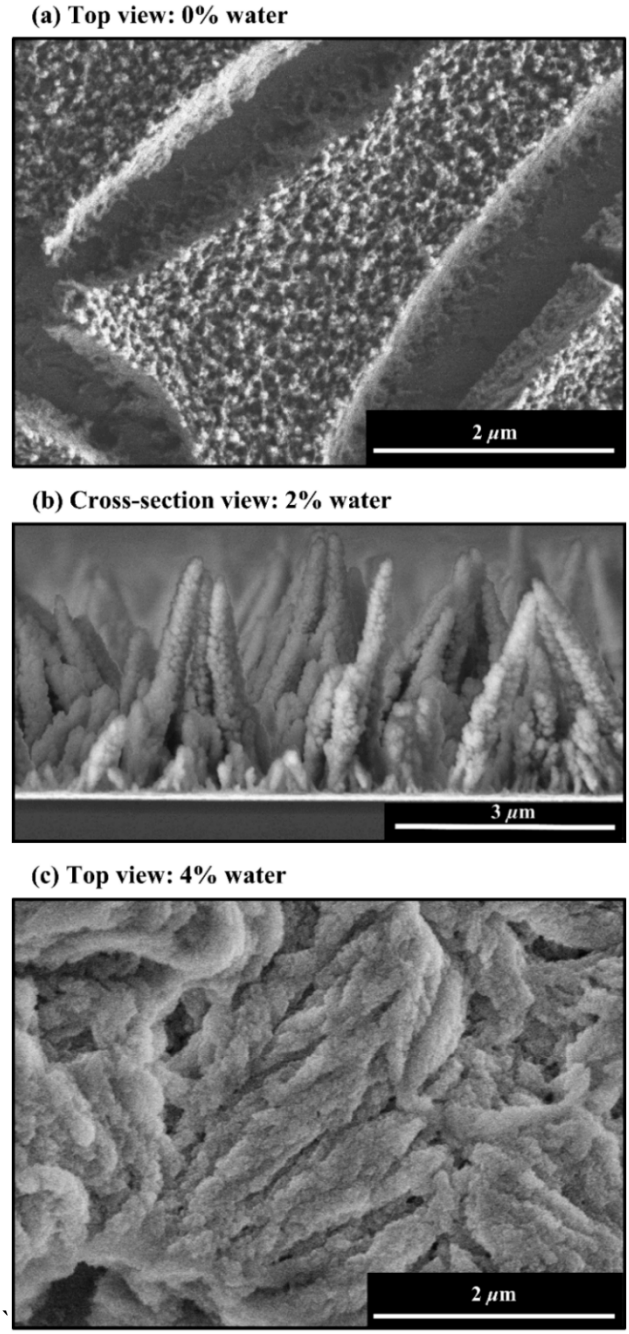

Figure S3-1. (a) Magnified top-view of 0% water sample showing a dense yet somewhat porous structure; **(b)** Magnified cross-sectional view of the nanodendrite forest produced with 2% added water; **(c)** Magnified top-view of 4% water sample showing a dense entangled nanodendritic structure.

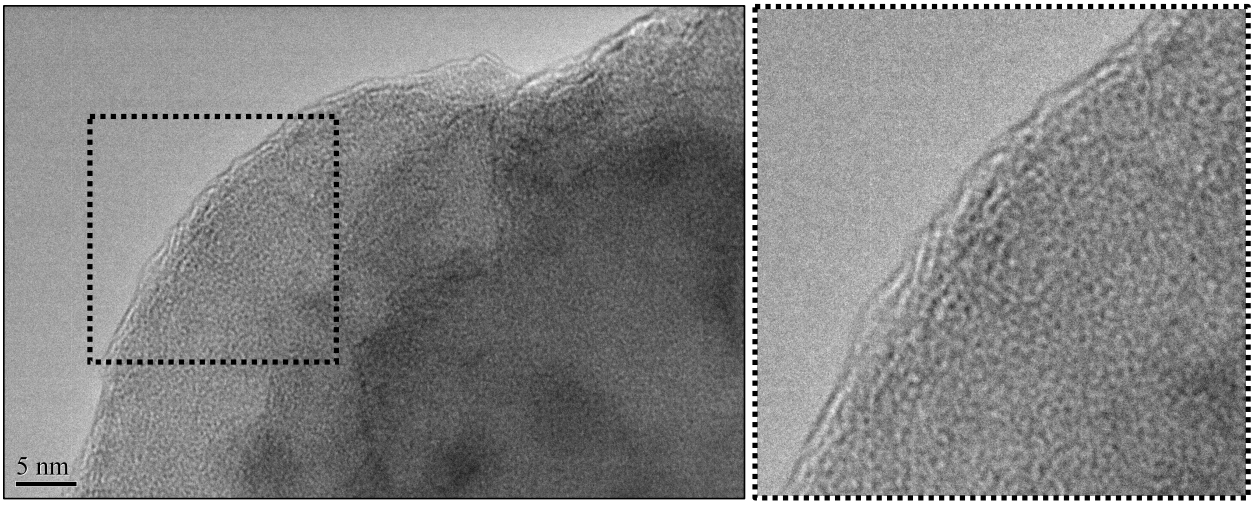

Figure S3-2. Magnified HRTEM image of amorphous $Ni(OH)_2$ nanodendrite.

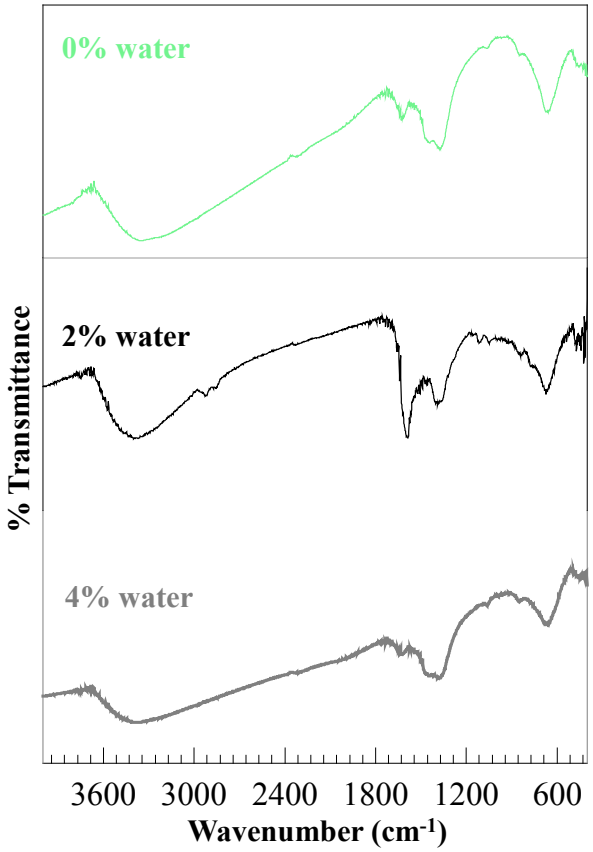

Figure S3-3. FTIR spectra of α-$Ni(OH)_2$ prepared with 0%, 2%, and 4% water added to the electrolyte. Peaks between 650-675 cm^{-1} correspond to α-$Ni(OH)_2$ lattice mode vibrations while broad feature around 3380 cm^{-1} and others between 1300-1700 cm^{-1} are a feature of various O-H related vibrations.[S1-2]

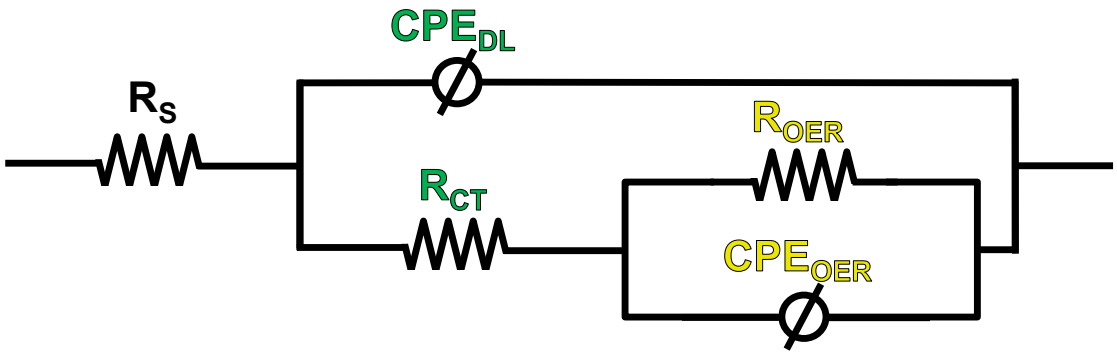

Figure S3-4. The equivalent circuit model used to fit the electrochemical impedance spectroscopy (EIS) data obtained for the OER catalysts at oxygen evolving overpotentials.

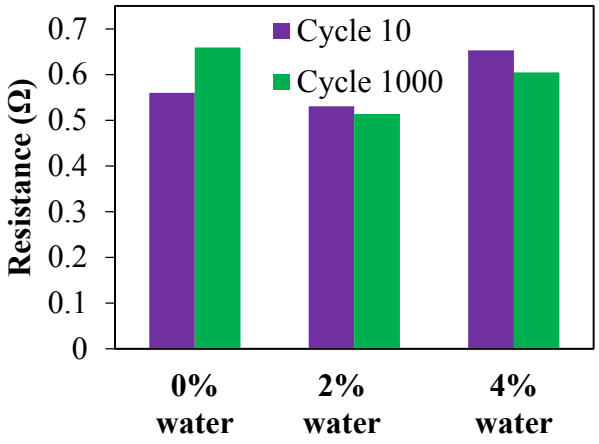

Figure S3-5. Comparison of the total Faradaic resistances ($R_{CT} + R_{OER}$) of deposits made with 0, 2 and 4% added water content in the deposition bath before and after accelerated stability testing. Values were obtained by fitting EIS data obtained potentiostatically at η=370 mV.

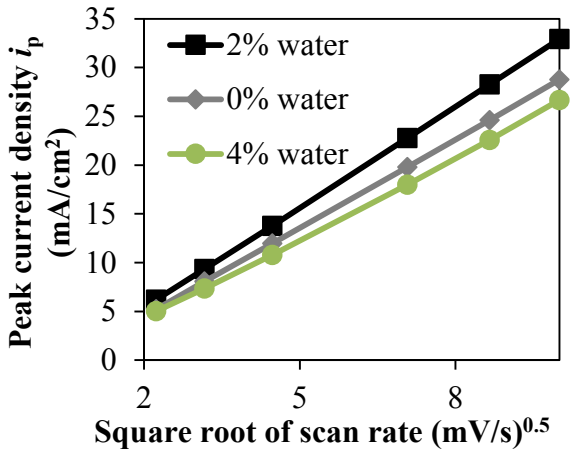

Figure S3-6. Plot of anodic peak current density (i_p) obtained during cyclic voltammetry versus square root of the scan rate. CVs were recorded at scan rates of 5, 10, 20, 50, 75, and 100 mV s^{-1}.

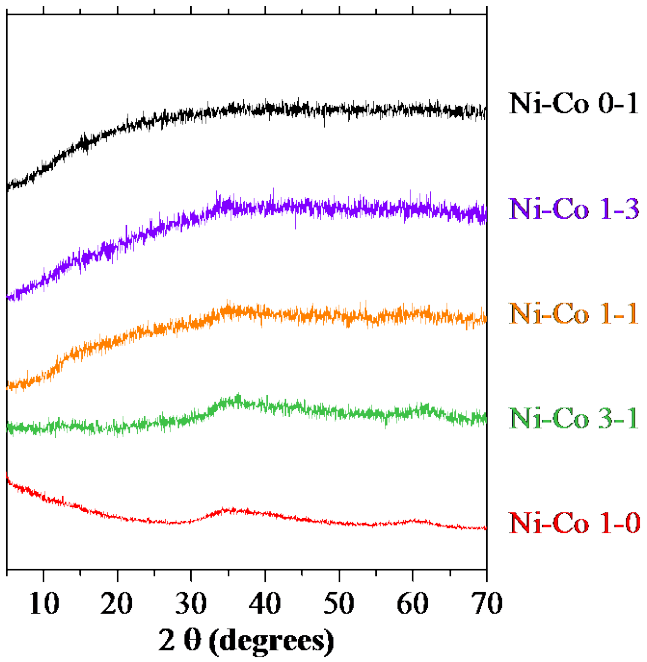

Figure S3-7. X-ray diffraction (XRD) patterns of the various amorphous Ni:Co hydroxide nanodendrite materials. All samples show broad and undefined peaks indicating the amorphous nature of deposited materials. A zero-background sample holder was used to avoid interference from the substrate.

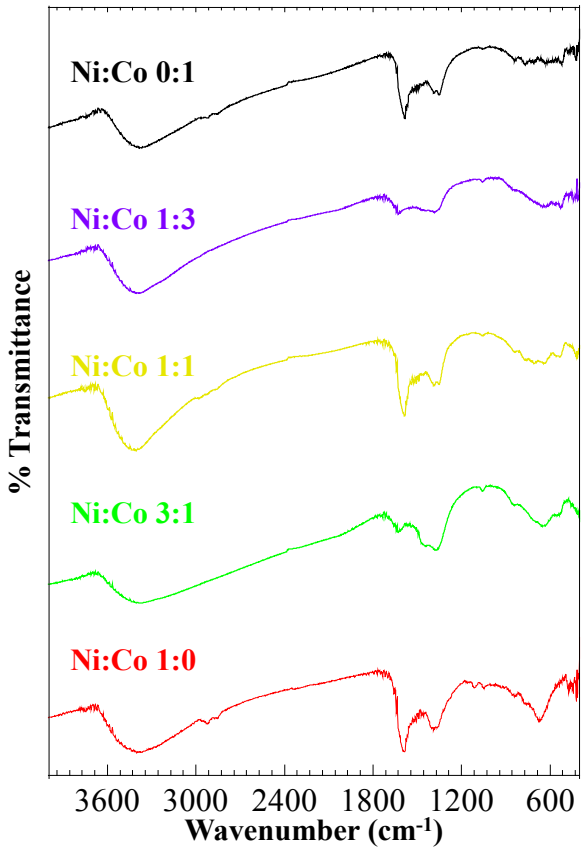

Figure S3-8. FTIR spectra of mixed α-phase mixed nickel cobalt hydroxides prepared with 2% water added to the electrolyte.

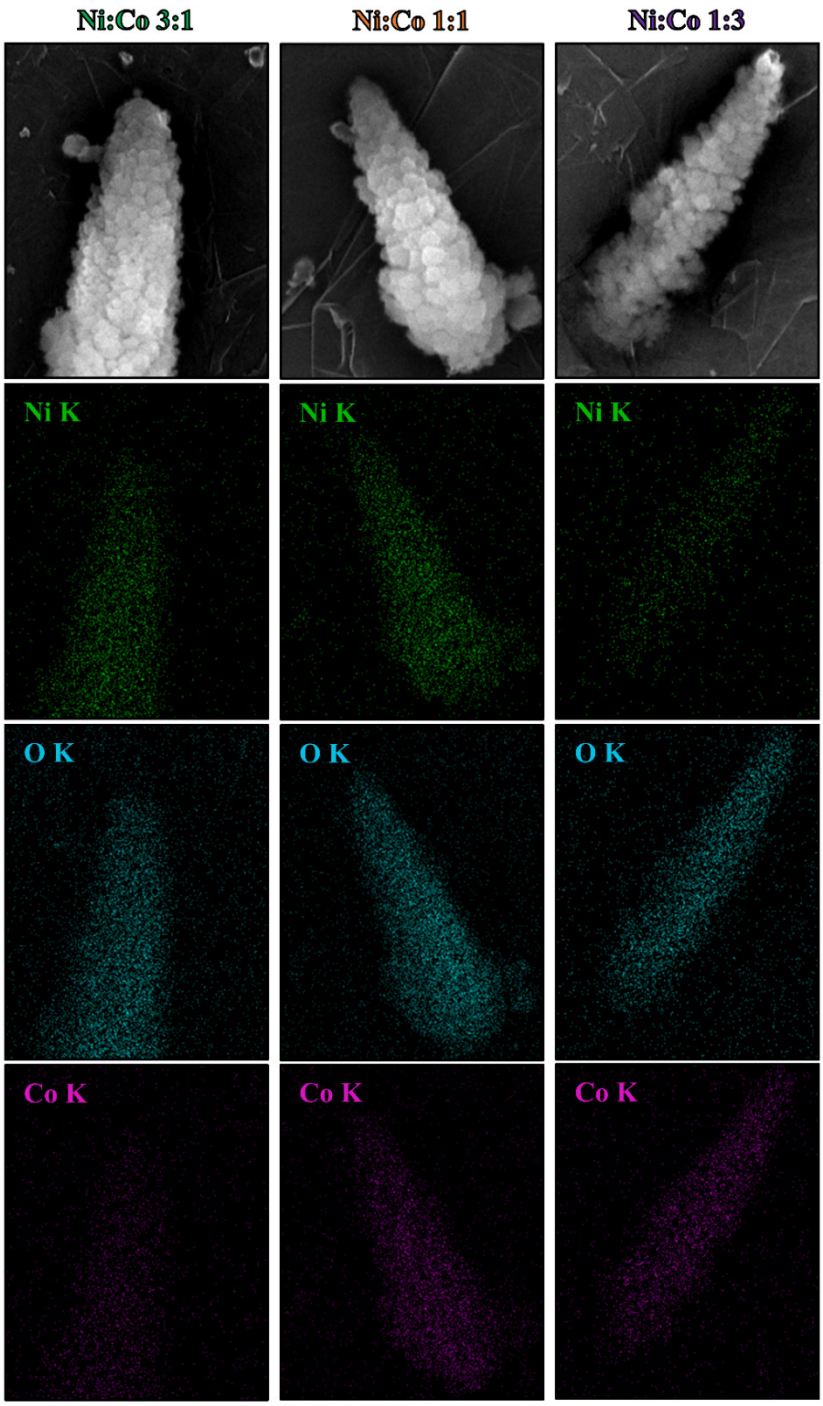

Figure S3-9. X-ray elemental maps of nickel-cobalt hydroxide nanodendrites prepared with Ni:Co salt concentrations of approximately 3:1, 1:1 and 1:3 in the deposition electrolyte solution. Based on the inductively coupled plasma emission spectroscopy (ICP) results, the Ni:Co atomic ratio within the nanodendrites was estimated to be approximately 3.62:1, 0.95:1, and 1:3.98 respectively.

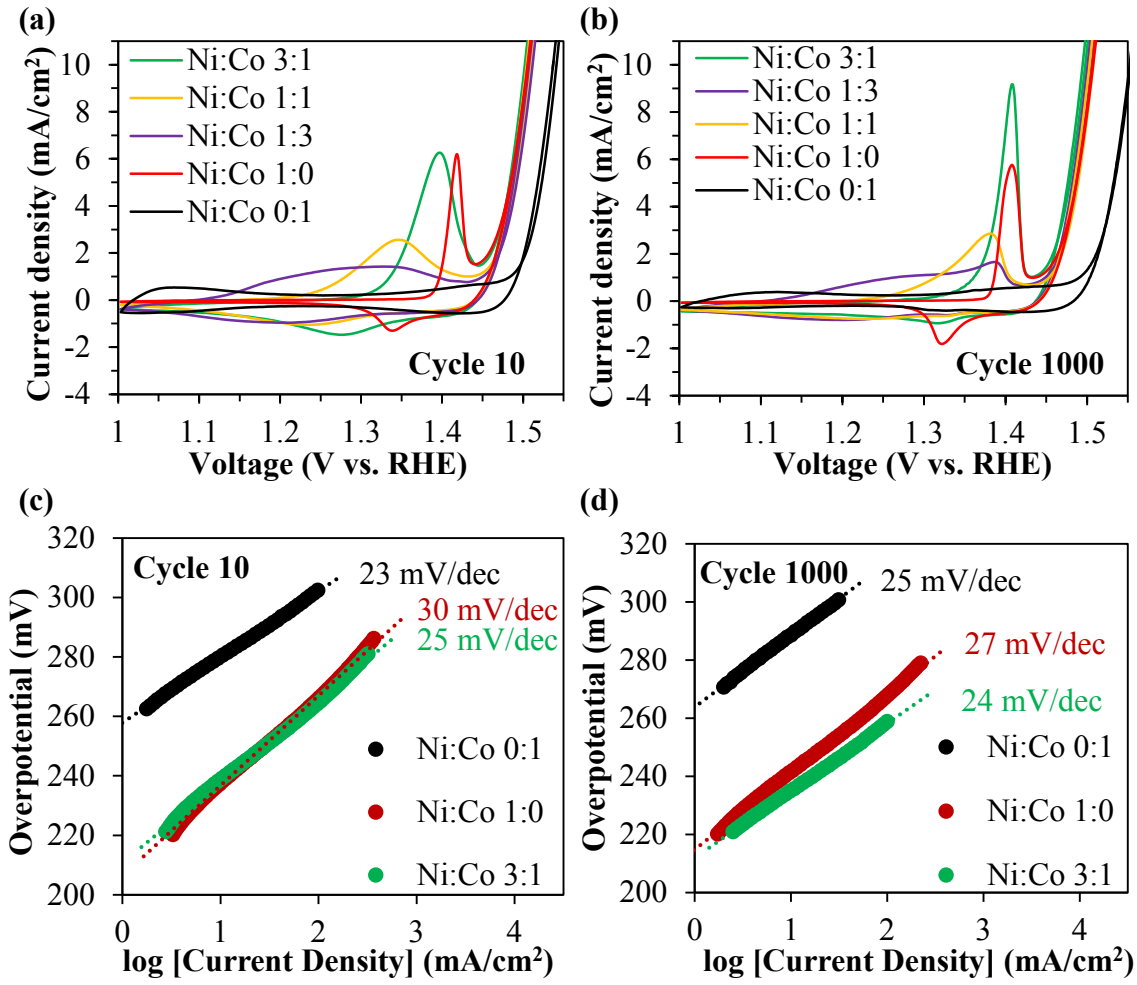

Figure S3-10. Magnified views of cyclic voltammograms of **(a)** cycle 10; **(b)** cycle 1000, seen in Figure 3-6 a, b of the main manuscript, clearly illustrating different redox peak positions for deposits obtained by varying the metal ion composition ratio in the deposition bath. The oxidation peak of the deposits shifts to more anodic potentials with increasing nickel content. Tafel slopes of Ni:Co 1:0, 3:1, 0:1 deposits **(c)** after 10 CV cycles; **(d)** after 1000 accelerated stability cycles.

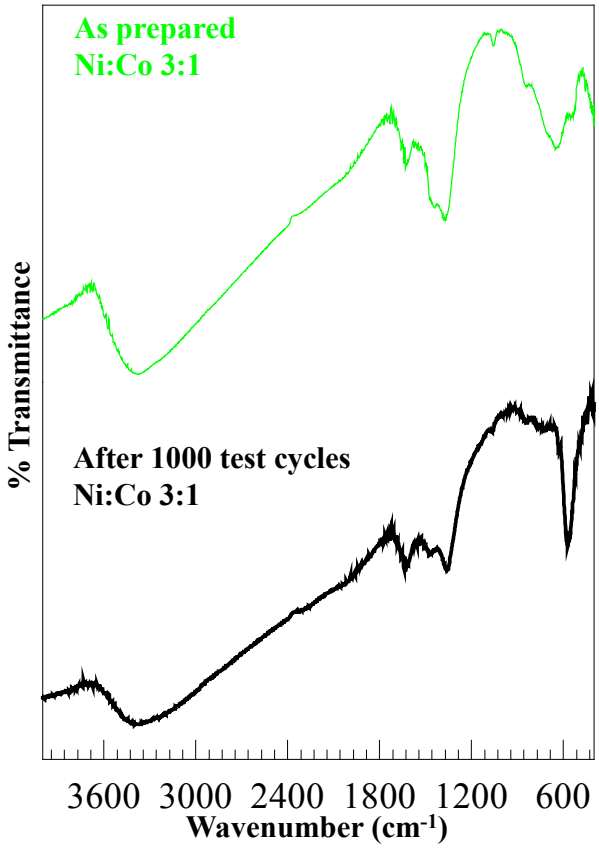

Figure S3-11. FTIR spectra of Ni:Co 3:1 deposit as prepared and after 1000 accelerated stability tests. The originally green colored α-phase Ni-Co hydroxide converts to a black colored γ-NiOOH phase after cycling, signified by the prominent peak of Ni^{3+}–O vibration seen at ~575 cm^{-1} after cycling.[S3]

Table S1. Comparison of OER overpotentials reported for other Ni/Co based catalysts

Material	Substrate	Electrolyte	η (mV) @ 10 mA.cm^{-2}	Reference
Amorphous α-phase Ni-Co hydroxide **Amorphous α-phase $Ni(OH)_2$** **Amorphous α-phase $Co(OH)_2$**	Stainless steel foil (planar)	1 M KOH	257 273 305	This work
$CoNi(OH)_x$ nanotubes	Cu foil (planar)	1 M KOH	280	S4
α -$Co_4Fe(OH)_x$	Glassy carbon (planar)	1 M KOH	295	S5
Amorphous $Co(OH)_2$	Au (planar)	1 M NaOH	360	S6
Amorphous $NiCo_{2.7}(OH)_x$ nanocages	Glassy carbon (planar)	1 M KOH	350	S7
Amorphous $Ni_{0.71}Fe_{0.29}(OH)_x$	Graphite (planar)	0.1 M KOH	296	S8
Amorphous $Ni(OH)_2$	Graphite (planar)	0.1 M KOH	344	S9
NiS nanosheets	Stainless steel mesh	0.1 M KOH	294	S10
NiCoP	Ni foam	1 M KOH	280	S11
α -$Ni(OH)_2$	Carbon paper	0.1 M KOH	331	S12
NiCo LDH	Carbon paper	1 M KOH	367	S13

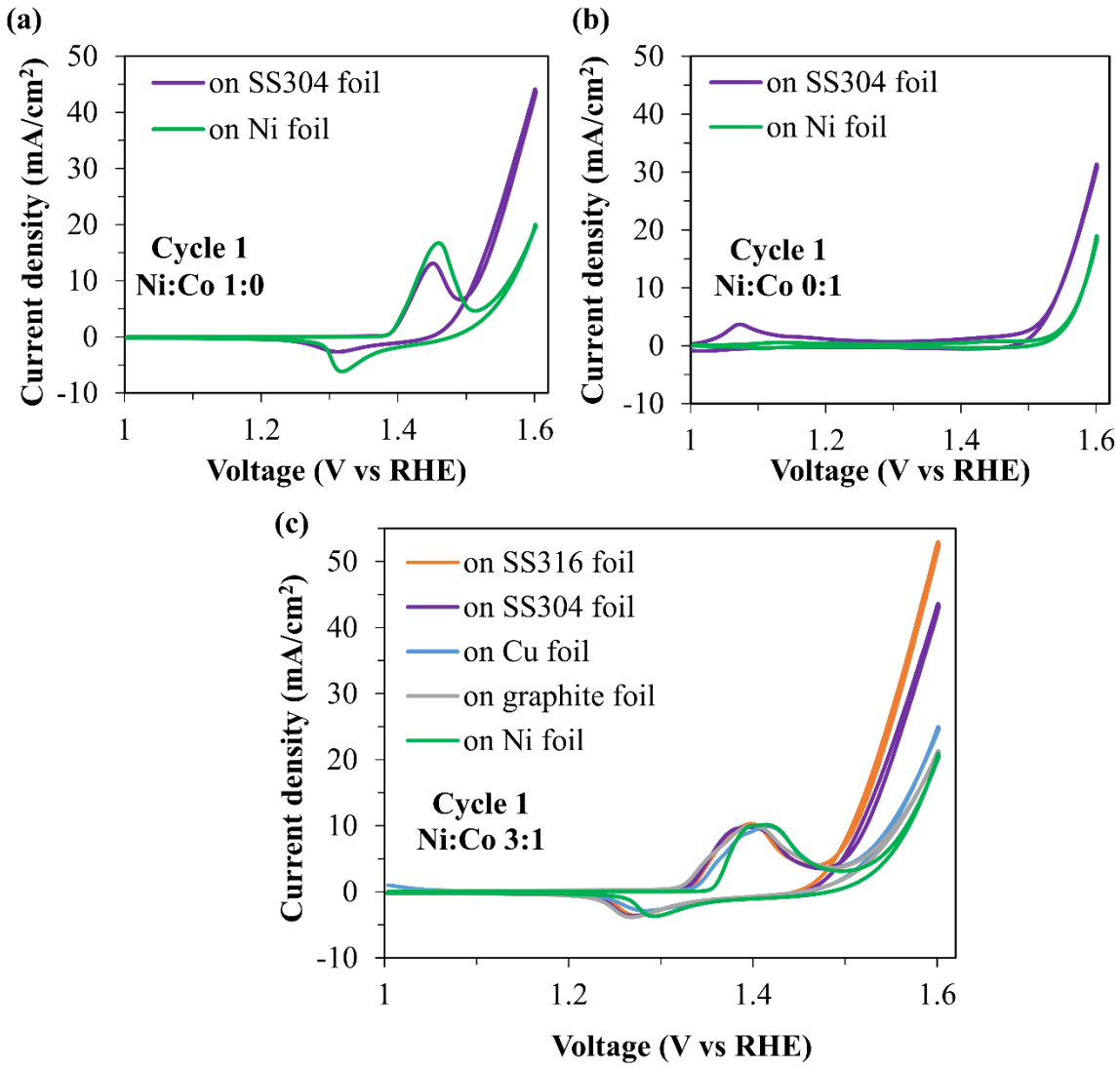

Figure S3-12. Cyclic voltammograms of **(a)** Ni:Co 1:0 ; **(b)** Ni:Co 0:1 ; **(c)** Ni:Co 3:1 nanodendritic deposits showing the synergistic enhancement of OER activity with stainless steel substrate as compared to nickel, copper and graphite foil substrates.

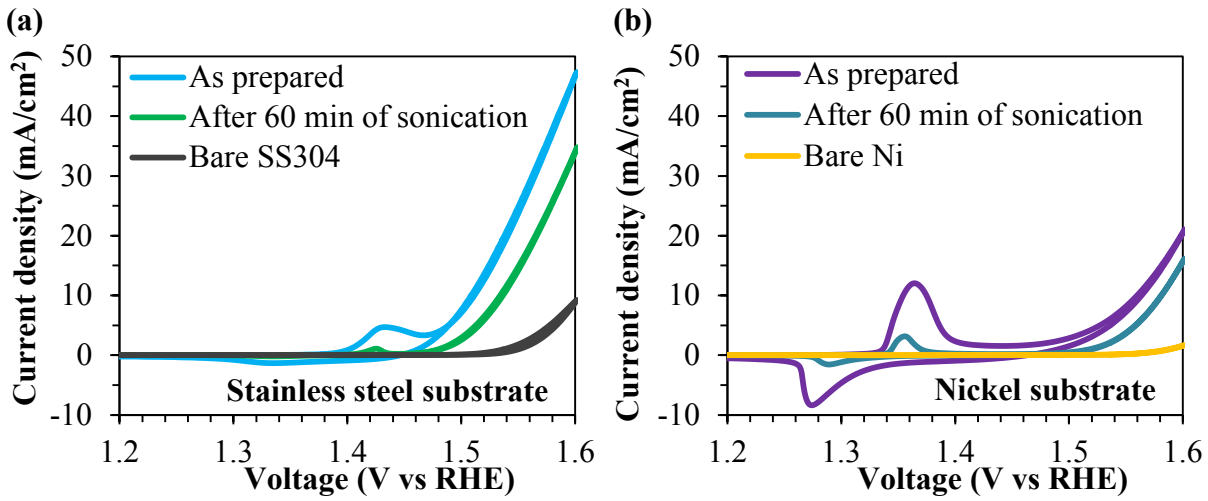

Figure S3-13. Cyclic voltammograms of Ni:Co 1:0, i.e. $Ni(OH)_2$ nanodendrite deposit on **(a)** stainless steel; **(b)** nickel substrates before and after being subjected to 1 hour of ultrasonication to remove the deposited nanodendrites.

3.9 Supporting Information References

S1. Hall, D. S.; Lockwood, D. J.; Poirier, S.; Bock, C.; MacDougall, B. R. Raman and Infrared Spectroscopy of α and β Phases of Thin Nickel Hydroxide Films Electrochemically Formed on Nickel. *J. Phys. Chem. A* **2012,** *116*, 6771-6784.

S2. Hall, D. S.; Lockwood, D. J.; Bock, C.; MacDougall, B. R. Nickel Hydroxides and Related Materials: A Review of Their Structures, Synthesis and Properties. *Proc. R. Soc. A* **2015,** *471*, 20140792.

S3. Fu, X.-Z.; Wang, X.; Xu, Q.-C.; Li, J.; Xu, J.-Q.; Lin, J.-D.; Liao, D.-W. Physical Characterization, Electrochemical Performance and Storage Stability of Spherical Al-Substituted γ-NiOOH. *Electrochim. Acta* **2007,** *52*, 2109-2115.

S4. Li, S.; Wang, Y.; Peng, S.; Zhang, L.; Al-Enizi, A. M.; Zhang, H.; Sun, X.; Zheng, G. Co-Ni-Based Nanotubes/Nanosheets as Efficient Water Splitting Electrocatalysts. *Adv. Energy Mater.* **2016,** *6*, 1501661.

S5. Jin, H.; Mao, S.; Zhan, G.; Xu, F.; Bao, X.; Wang, Y. Fe Incorporated α-$Co(OH)_2$ Nanosheets with Remarkably Improved Activity Towards the Oxygen Evolution Reaction. *J. Mater. Chem. A* **2017,** *5*, 1078-1084.

S6. Sayeed, M. A.; Herd, T.; O'Mullane, A. P. Direct Electrochemical Formation of Nanostructured Amorphous $Co(OH)_2$ on Gold Electrodes with Enhanced Activity for the Oxygen Evolution Reaction. *J. Mater. Chem. A* **2016,** *4*, 991-999.

S7. Nai, J.; Yin, H.; You, T.; Zheng, L.; Zhang, J.; Wang, P.; Jin, Z.; Tian, Y.; Liu, J.; Tang, Z.; Guo, L. Efficient Electrocatalytic Water Oxidation by Using Amorphous Ni-Co Double Hydroxides Nanocages. *Adv. Energy Mater.* **2015,** *5*, 1401880.

S8. Gao, Y. Q.; Liu, X. Y.; Yang, G. W. Amorphous Mixed-Metal Hydroxide Nanostructures for Advanced Water Oxidation Catalysts. *Nanoscale* **2016,** *8*, 5015-5023.

S9. Gao, Y.; Li, H.; Yang, G. Amorphous Nickel Hydroxide Nanosheets with Ultrahigh Activity and Super-Long-Term Cycle Stability as Advanced Water Oxidation Catalysts. *Cryst. Growth Des.* **2015,** *15*, 4475-4483.

S10. Chen, J. S.; Ren, J.; Shalom, M.; Fellinger, T.; Antonietti, M. Stainless Steel Mesh-Supported NiS Nanosheet Array as Highly Efficient Catalyst for Oxygen Evolution Reaction. *ACS Appl. Mater. Interfaces* **2016,** *8*, 5509-5516.

S11. Liang, H.; Gandi, A. N.; Anjum, D. H.; Wang, X.; Schwingenschlogl, U.; Alshareef, H. N. Plasma-Assisted Synthesis of NiCoP for Efficient Overall Water Splitting. *Nano Lett.* **2016,** *16*, 7718-7725.

S12. Gao, M.; Sheng, W.; Zhuang, Z.; Fang, Q.; Gu, S.; Jiang, J.; Yan, Y. Efficient Water Oxidation Using Nanostructured α-Nickel-Hydroxide as an Electrocatalyst. *J. Am. Chem. Soc.* **2014,** *136*, 7077-7084.

S13. Liang, H.; Meng, F.; Caban-Acevedo, M.; Li, L.; Forticaux, A.; Xiu, L.; Wang, Z.; Jin, S. Hydrothermal Continuous Flow Synthesis and Exfoliation of NiCo Layered Double Hydroxide Nanosheets for Enhanced Oxygen Evolution Catalysis. *Nano Lett.* **2015,** *15*, 1421-1427.

CHAPTER 4

IN SITU DECORATION OF STAINLESS STEEL NANOPARTICLES FOR SYNERGISTIC ENHANCEMENT OF α–$Ni(OH)_2$ OXYGEN EVOLUTION REACTION CATALYSIS

In Situ Decoration of Stainless Steel Nanoparticles for Synergistic Enhancement of α–$Ni(OH)_2$ *Oxygen Evolution Reaction Catalysis, Anirudh Balram, Hanfei Zhang, and Sunand Santhanagopalan, 2017*

A version of this manuscript was submitted to Materials Chemistry Frontiers (Royal Society of Chemistry) and was in peer review (as of 24th August 2017)

4.1 Abstract

Alkaline water-splitting is a promising clean technology for hydrogen production. However, reducing the oxygen evolution reaction (OER) overpotential is critical to overall process efficiency and economic feasibility. To this end, we demonstrate novel 3D hierarchical α-$Ni(OH)_2$ nanoparticle decorated stainless steel nanoparticles (SSNP) catalyst deposits on Ni foam substrates. SSNP deposition along with simultaneous in-situ $Ni(OH)_2$ decoration of the SSNP is facilitated via a facile single-step electrophoretic deposition (EPD) based co-deposition method. The enhanced OER catalytic activity of α-$Ni(OH)_2$ owing to the synergetic SSNP support could sustain current densities of 10 and 125 mA cm^{-2} at overpotentials of 220 and 250 mV respectively, in 1 M KOH. These robust deposits could survive accelerated cycling and prolonged oxygen generation at higher current densities despite the lack of any polymeric binders. In 10 M KOH, current density of 500 mA cm^{-2} could be maintained at an overpotential of 450 mV (*i*R-uncorrected).

4.2 Introduction

Water splitting is an extremely promising route to sustainable and clean hydrogen production.[1] The present challenge is to economically minimize the overpotentials required to facilitate the two electrode reactions: the hydrogen evolution reaction (HER) and the oxygen evolution reaction (OER). The overall system overpotential, however, is typically dominated by the OER side due to its comparatively sluggish kinetics.[2] Thus, reducing OER overpotentials is a crucial component in the economic viability of electrolytic water splitting.[3] From a practical viewpoint, the improved OER kinetics and the remarkable performance of non-precious catalysts in reducing OER potentials in alkaline media makes alkaline water splitting particularly attractive.[4] Nickel based catalysts such as $Ni(OH)_2$,[2] Ni_2P/NiO_x,[5] Ni-Co hydroxide,[6] especially Ni-Fe hydroxide[7] etc. in various nanostructured morphologies have been found to perform exceptionally well. More recently, the excellent catalytic activity observed in the cases of pure $Ni(OH)_2$,[8] NiO,[5] Ni,[9] $Co(OH)_2$ structures[10], has also been attributed primarily to the inadvertent Fe doping via contaminants present in the KOH electrolyte.[11] Catalytic activity has also been found to be significantly influenced by the deposit substrate and support materials.[9, 12-14] Generally, noble metal substrates and supports have been observed to greatly enhance catalytic activity of OER catalysts.[15-20] However, more interesting from a commercial perspective, have been reports of high activity of such Ni-based deposits on relatively inexpensive stainless steel (SS) substrates.[3, 9, 21]

Presumably, in these instances, the unintended doping of the deposit with trace iron via the substrate during the fabrication process,[9] greatly amplifies the OER activity of the catalyst. For scalability, consistent production of such high activity deposits as a serendipitous consequence of synergistic interactions naturally engendered during electrode fabrication is very appealing. For

example, co-deposition of desired Ni-Fe materials requires precise monitoring and control of the deposition conditions such as potential, pH, Ni and Fe ion concentrations within the electrodeposition bath etc. to correct for anomalous deposition rates of one species over another during deposition.[22-24] However, when the steel substrate itself acts as the dopant source by its mere presence, only the relatively facile deposition of $Ni(OH)_2$ needs to be controlled. In our work, we observed a similar enhancement in $Ni(OH)_2$ catalyst performance for OER when deposited on SS substrates. We hypothesized that utilizing steel nanoparticles (SSNP) as the $Ni(OH)_2$ catalyst support could provide greatly increased SS/$Ni(OH)_2$ interfacial area and improve performance due to nanostructuring effects.[25] Additionally, the stability of stainless steel in OER conditions makes an excellent choice for support material.[26]

Thus, to realize a truly hierarchical 3D structure with maximized SS/$Ni(OH)_2$ interface, we prepared a deposit comprised of $Ni(OH)_2$ nanoparticle decorated SS nanoparticles deposited on a 3D Ni foam substrate. With scalability in mind, the widespread use and relatively inexpensive nature of Ni foam would make it an obvious candidate for the substrate. We electrophoretically co-deposited SS nanoparticles (SSNP) while simultaneously decorating them with $Ni(OH)_2$ in-situ on the Ni foam in a single-step process requiring no pre or post-treatment. The decoration of individual nanoparticles along with the intimate contact between all the deposit components can facilitate excellent electrochemical performance. We expect the SSNP to behave as an conductive pathway from the $Ni(OH)_2$ to the Ni foam backbone helping improve charge transfer. Especially for higher current density applications, it is necessary to produce deposits with low internal resistance and the robustness to survive the rigors of violent gas evolution. EPD allows us to achieve these results while avoiding polymeric binder materials that typically hamper performance[27, 28] and can lead to increased internal resistances due to bubble coverage.[29] This

highly accessible 3D Ni foam structure coated with the unique binderless SS/$Ni(OH)_2$ nanocomposite rendered a highly active OER catalyst deposit.

4.3 Results and Discussion

First, to illustrate the effect of deposition substrate on electrochemical performance, particularly on the OER, we first deposited $Ni(OH)_2$ on planar nickel and stainless steel foil. For consistency, both substrates were cleaned for 10 minutes in 6 M HCl prior to deposition. The $Ni(OH)_2$ was then deposited via electrodeposition potentiostatically at 200 V for 2 min from a 1:1 solution of ethanol and isopropanol with 0.2 mg ml^{-1} of dissolved $NiCl_2.6H_2O$. High localized pH at the electrode-electrolyte interface[30] during deposition causes Ni^{2+} to deposit in the form of nickel

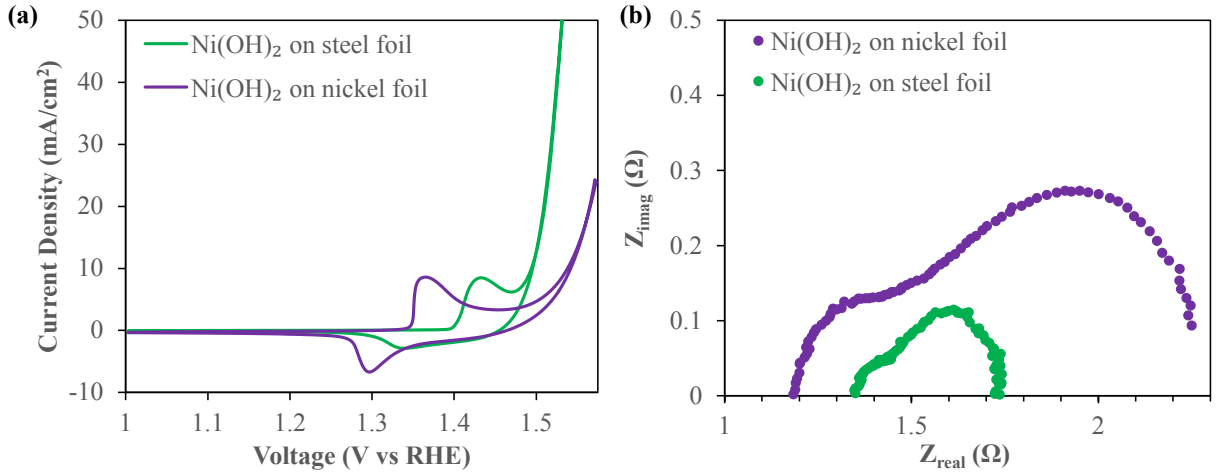

Figure 4-1. Comparison of OER performance of $Ni(OH)_2$ deposits on planar Ni foil and SS foil substrates: (a) Cyclic voltammetry (CV) curves recorded at 5 mV s^{-1}; (b) Nyquist curves of the deposits recorded at an oxygen evolving overpotential of 370 mV.

hydroxide. Thermogravimetric analysis (TGA) of the deposit (Figure S4-1) confirms the characteristic two step weight loss associated with α-$Ni(OH)_2$,[31] the hydrated phase of $Ni(OH)_2$ containing water molecules intercalated within the $Ni(OH)_2$ crystal. **Figure 4-1**a shows the *i*R-

corrected cyclic voltammograms (CV) of these α-$Ni(OH)_2$ deposits made on stainless steel (SS) and nickel foil substrates under similar deposition conditions. These CV curves were recorded at 5 mV s^{-1} in oxygen purged 1 M KOH. Both the $Ni(OH)_2$ deposits shows anodic peaks signifying a conversion to NiOOH. However, there is a clear anodic shift of the redox peaks of the $Ni(OH)_2$ on the SS substrate. The anodic peak and cathodic peaks of $Ni(OH)_2$ deposited on SS shift anodically by ~70 and 45 mV respectively. This anodic shift of the redox peaks of suggests Fe-doping of the $Ni(OH)_2$ crystal[8, 32, 33] which is known to play a critical role in OER overpotential reduction. It is readily apparent that the deposit on SS foil shows a greatly enhanced OER performance as witnessed by the steep increase in current density around 1.45 V vs RHE, associated with oxygen gas evolution, after the oxidation of $Ni(OH)_2$. At the Figure 4-of merit typically considered for OER applications i.e. the overpotential required to evolve oxygen at a current density of 10 mA cm^{-2}, the SS requires merely 275 mV, over 50 mV lesser than the $Ni(OH)_2$ deposit prepared on the nickel substrate.

Electrochemical impedance spectra (EIS) obtained at an oxygen evolving overpotential of 370 mV (Figure 4-1b) clearly show the lower Faradaic resistances[34] associated with the deposits on SS as opposed to nickel. The smaller size of the first semicircle is an indicator of easier charge transfer between the deposit and substrate. The smaller diameter of the second semicircle[35] signifies improved OER kinetics related to easier formation of intermediates,[34] critical to efficient OER catalysis. Clearly, the deposit on SS has a significantly lower overall faradaic resistance and greatly superior OER kinetics enabling excellent OER catalysis. The electrochemical behavior seen in Figure 4-1 clearly suggests that $Ni(OH)_2$ deposits on SS are clearly superior OER catalysts than similar deposits on Ni. We attribute it to the well-studied

interaction of Fe and $Ni(OH)_2$ leading to excellent OER catalysis.[8, 11] As mentioned previously, while typically Fe incorporation induced OER catalysis performance enhancement of $Ni(OH)_2$

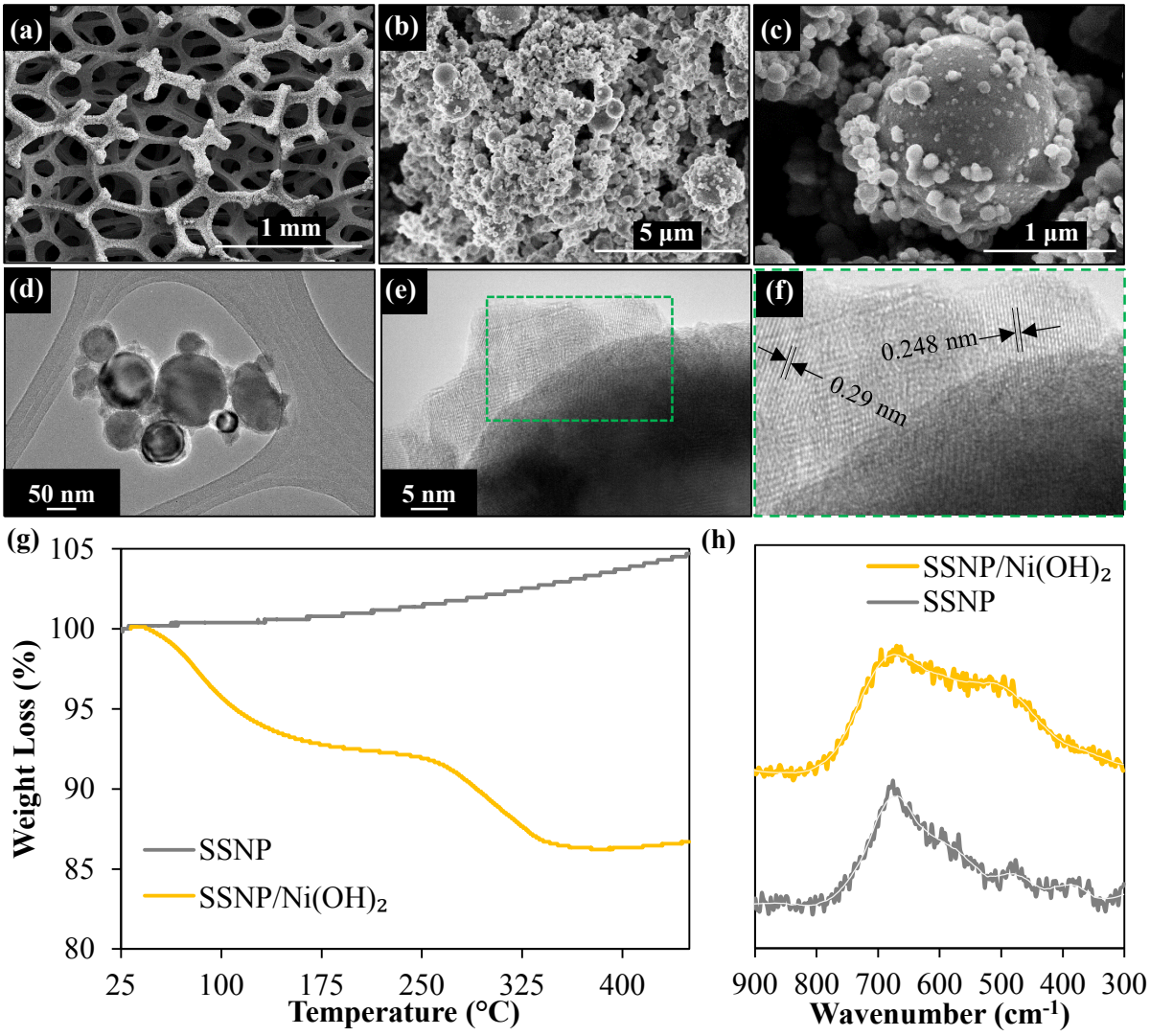

Figure 4-2. (a,b,c) Scanning electron microscope images of hybrid SSNP/$Ni(OH)_2$ deposits on Ni foam substrate; **(d,e,f)** HRTEM images of co-deposited SSNP/$Ni(OH)_2$ nanocomposite; **(g)** Thermogravimetric analysis (TGA) curves comparing thermal behavior of as-purchased SSNP to the nanocomposite SSNP/Ni(OH)2 deposit; **(h)** Raman spectra of SSNP and SSNP/$Ni(OH)_2$ recorded using 532 nm laser source (3 mW laser power).

occurs due to incidental iron incorporation from within the alkaline electrolyte used in electrolysis, use of steel substrate during our electrodeposition allows for immediate exploitation of this synergy. To maximally harness this activity enhancement observed while utilizing a planar steel and significantly lower the overpotential further, it is imperative to somehow increase the interfacial surface area between the deposit and substrate. An approach that allows for nanostructuring while enabling thicker deposits and higher loading without compromising on performance would be highly beneficial. An EPD based co-deposition strategy would greatly simplify the controls required during deposition as compared to traditional Ni/Fe electrodeposition systems.

EPD allows for facile voltage induced deposition of a wide range of nanoparticles when optimally suspended within a suitable dispersion medium.[36] Additionally, EPD was selected as the method to deposit the hybrid SS/$Ni(OH)_2$ given its ability to produce high performance and robust deposits that can withstand the demands of electrochemical applications.[37, 38] A particular advantage of using electrophoresis based co-deposition, as we do here, is that it facilitates deposition of SSNP onto the Ni foam electrode while simultaneously decorating those deposited SSNP with $Ni(OH)_2$ in-situ during a single-step deposition process. Briefly, 0.25 mg ml^{-1} SS nanoparticles (SSNP) were suspended in an ethanol-isopropanol (1:1) solution containing 0.2 mg ml^{-1} nickel chloride. A schematic of the deposition working mechanism is provided in Figure S4-2. Upon application of an electric field, the SSNP charged positively on account of adsorbed Ni^{2+} ions, migrate towards and deposit upon the negatively polarized Ni foam electrode. Upon contact with the Ni foam electrode, given the high localized pH at the electrode-electrolyte interface, the Ni^{2+} get deposited in the form of $Ni(OH)_2$ nanoparticles on the SSNP surface, following a mechanism similar to the case with the planar substrate previously discussed.

The electron micrographs (**Figure 4-2)** of the resultant SSNP/$Ni(OH)_2$ deposit on Ni foam substrate show the dense deposit on SSNP on the Ni foam decorated by smaller $Ni(OH)_2$ nanoparticles. Figure 4-2 d, e show high-resolution transmission electron microscope (HRTEM) images indicate some nanoparticle decoration on the surface of SSNP. The X-ray diffraction (XRD) data obtained (Figure S4-3) show no obvious $Ni(OH)_2$ peaks with only sharp well defined SS related peaks visible. This may be attributable to the generally disordered and small particle size of the $Ni(OH)_2$ on the SSNP. However, Figure 4-2f shows lattice spacing of 0.29 and 0.248 nm attributable to α-$Ni(OH)_2$.[39, 40] Further confirmation of formation of a SSNP/$Ni(OH)_2$ hybrid was attained via TGA as seen in the curves in Figure 4-2g obtained under air flow at a ramp rate of 10 $^oC\ min^{-1}$. As-purchased SSNP show only a gradual increase in weight as the temperature increases due to the oxidation of the SS surface. The SSNP/$Ni(OH)_2$ hybrid on the other hand show three distinct features, the two weight loss steps as seen previously in Figure 4-1, associated with $Ni(OH)_2$ and an additional feature of weight increase after the complete conversion to NiO that is attributable to the previously observed oxidation of the exposed SSNP surfaces. The Raman spectra of as-purchased SSNP and the hybrid deposit are shown in Figure 4-2h. Due to the low Raman scattering intensities obtained from $Ni(OH)_2$, no clear signal of $Ni(OH)_2$ could be obtained at lower powers of the 532 nm laser source. Higher Raman intensities could be obtained at slightly higher laser powers (≥ 3 mW), however laser induced heating appears to convert the hydroxide into the corresponding oxide,[41] NiO showing a broad feature around 508 cm^{-1}.[42] Both bare SSNP and SSNP/$Ni(OH)_2$ deposits show a similar feature around 690 cm^{-1} attributable to $FeCr_2O_4$ spinel phase in the SS.[43] The material characterization data in Figure 4-2 supports the formation of a SSNP/$Ni(OH)_2$ hybrid during the electrophoretic co-deposition process.

All the OER performance characterization was performed in O_2 purged 1M KOH. **Figure 4-3** shows the SSNP/$Ni(OH)_2$ comprehensively outperform two control samples -electrophoretically

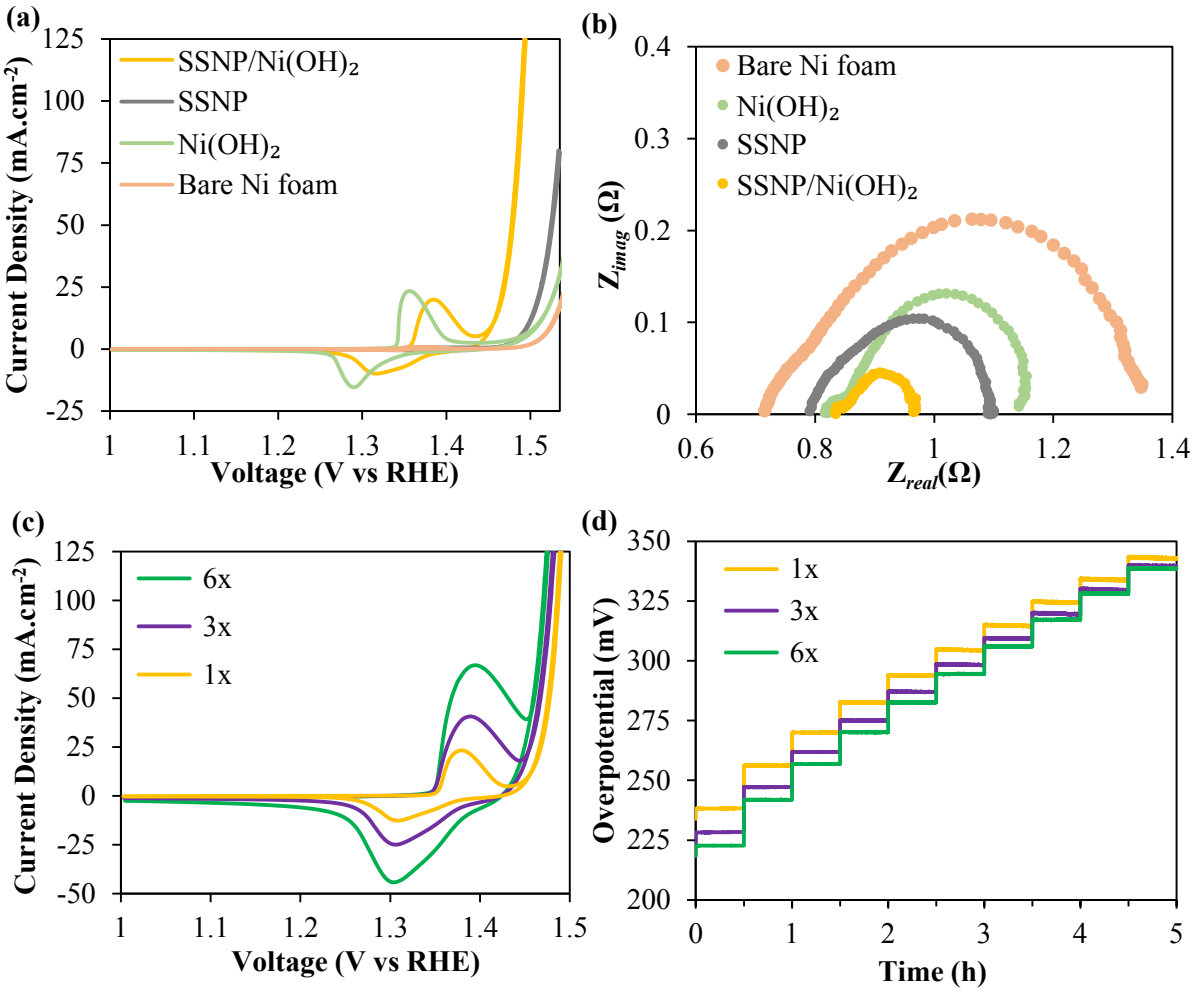

Figure 4-3. Comparison of OER performance of electrophoretically co-deposited SSNP/$Ni(OH)_2$ nanocomposite, electrophoretically deposited SSNP, electrodeposited $Ni(OH)_2$ and bare Ni foam control sample in 1 M KOH: **(a)** Cyclic voltammetry (CV) curves recorded at 2 mV s^{-1}; **(b)** Nyquist curves recorded at 1.6 V vs RHE; Comparison of various SSNP/$Ni(OH)_2$ deposits **(c)** CV curves recorded at 2 mV s^{-1}. EPD was performed either 1, 3, or 6 times consecutively, corresponding to designations of 1x, 3x and 6x respectively. **(d)** Chronopotentiograms (iR-uncorrected) recorded at 10 to 100 mA cm^{-2} in 10 mA cm^{-2} increments every 30 min.

deposited bare SSNP as well as electrodeposited bare $Ni(OH)_2$- deposited under similar conditions at 200 V for 2 min. The hybrid deposit requires an ultralow overpotential of ~255 mV required for a current density of 10 mA cm^{-2}. The overpotential required by the hybrid at all higher current densities is significantly lower than the individual SSNP and $Ni(OH)_2$ deposits. In part, the nanostructuring of the $Ni(OH)_2$ surface would increase electrochemically active area. Yet again, the $Ni(OH)_2$ redox peaks in the hybrid SSNP/$Ni(OH)_2$ deposit show an anodic shift seen previously suggesting some Fe infiltration within the $Ni(OH)_2$. This indicates the significant influence of the intimate interface formed between the SSNP/$Ni(OH)_2$ during deposition on the greatly enhanced OER catalysis properties of the deposit. The EIS data acquired at an oxygen evolving overpotential of 370 mV, seen in Fig 3b, corroborates the trends seen in the cyclic voltammograms. The composite deposit shows the lowest total Faradaic resistances than both the exclusively SSNP and $Ni(OH)_2$ deposits leading to excellent OER performance characteristics. The inordinate reduction in resistance to OER as represented by the greatly diminished second semicircle is indicative of the synergy of the SSNP and $Ni(OH)_2$ within the hybrid deposit to facilitate facile oxygen evolution.

To further lower OER overpotentials, thicker deposits were produced by performing multiple depositions of SSNP/$Ni(OH)_2$ on Ni foam substrate using the same deposition parameters (200 V; 2min) and fresh deposition dispersion was used after every deposition step. The deposits were designated 1x, 3x and 6x, corresponding to a single, three and six consecutive deposits i.e. 2, 6 and 12 total minutes of deposition respectively. Figure 4-3c shows the CV of the 1x, 3x and 6x deposits. The overpotential to achieve 10 mA cm^{-2} decreases by ~35 mV to merely 220 mV for the 6x sample. Since typically hydrophobic binders are avoided in these EPD produced deposits, improved performance is witnessed even at higher overall mass loadings. Generally the binders

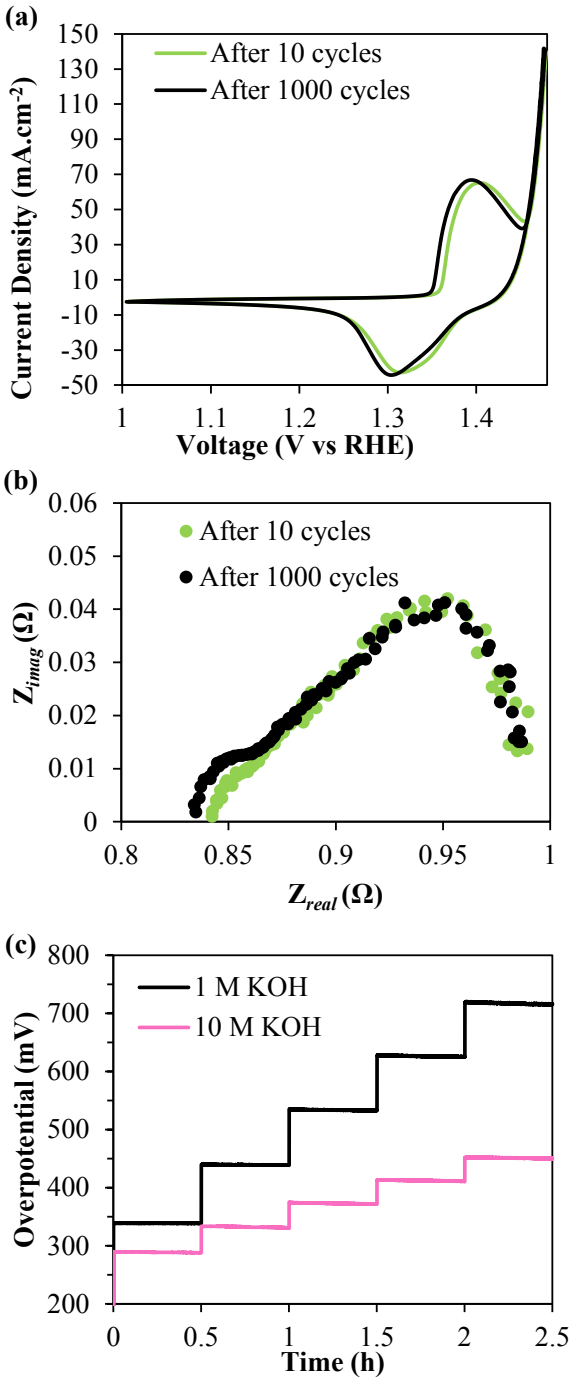

Figure 4-4. (a) Comparison of CV of SSNP/$Ni(OH)_2$ recorded at 2 mV s^{-1} and **(b)** Nyquist curves recorded at 1.6 V vs RHE nanocomposite recorded before and after 1000 cycles of accelerated stability testing in 1 M KOH; **(c)** Chronopotentiograms (iR-uncorrected) recorded at 100 to 500 mA cm^{-2} in 100 mA cm^{-2} increments every 30 min in 1 M and 10 M KOH.

and carbonaceous support can cause severe drops in performance due to increased bubble trapping, especially at higher loadings.[29] The chronopotentiograms for the three samples performed in 10 mA cm^{-2} increments from 10 to 100 mA cm^{-2} every 30 min are shown in Figure 4-3d. Similar to the trends in the CV curves, the thicker deposits outperform the 1x deposit and significantly lower the onset potential of OER. At higher current densities there appears to be a slightly lower disparity in performance between the lower and higher loading samples, likely owing to mass transport limitations.[3] Most significantly, the samples prove to be robust, able to survive the conditions of vigorous bubble generation without damage as seen from the stability,

Prior to recording the chronopotentiograms seen in Figure 4-3d, the deposits were also subjected to accelerated stability testing protocol by cycling 1000 times between a voltage window of 1.3-1.8 V vs RHE at 100 mV s^{-1}. **Figure 4-4**a shows *i*R-corrected CV curves of the 6x deposit. It is observable that there is no loss in performance even after being subjected to the harsh testing protocol. The EIS curves recorded at 370 mV similarly show near identical curves before and after accelerated cycling confirming the durability of the deposits. The same deposit was then tested for higher current density applications in 10 M KOH. Figure 4-4c compares the *i*R-uncorrected chronopotentiograms recorded in 1 M and 10 M KOH solutions. The current densities were stepped up from 100 to 500 mA cm^{-2} in 100 mA increments. It is evident that performance is significantly improved in the more concentrated KOH electrolyte. In 10 M KOH, the deposit only requires only (*i*R uncompensated) 290 mV @ 100 mA cm^{-2} and 450 mV @ 500 mA cm^{-2}. Most significantly, Even at these high current densities, the SSNP/$Ni(OH)_2$ deposit proves to be highly durable with no apparent increase in overpotential over time.

4.4 Conclusions

In conclusion, by electrophoretically co-depositing $Ni(OH)_2$ nanoparticle decorated SS nanoparticles onto a 3D Ni foam substrate, we were able to maximize the synergistic interactions between the two components in the deposit. The performance of the composite deposit far exceeds the individual components, likely owing to some Fe doping of the $Ni(OH)_2$ in the deposit induced during the deposition process itself. The engineered 3D nanostructuring of the SS/$Ni(OH)_2$ interface (i.e. $Ni(OH)_2$ nanoparticle decoration of the nanoscale SS particles) onto the 3D Ni foam support allows for greater exposed catalyst surface. These robust deposits produced by EPD are able to sustain high current electrolysis despite the lack of typically used binder materials. This allows the entire deposit to be available for the catalytic action with improved wettability and catalyst accessibility. In typically studied 1 M KOH, merely 220 mV and 250 mV are required to sustain 10 and 125 mA cm^{-2} respectively. This allows for overpotentials as low as 450 mV (*i*R uncorrected) to generate 500 mA cm^{-2} in 10 M KOH.

4.5 Materials and Methods

Nanomaterial Deposition: Electrodeposition of $Ni(OH)_2$ was performed from an ethanol/isopropanol (1:1) electrolyte containing 0.2 mg ml^{-1} dissolved $NiCl_2.6H_2O$ (Sigma-Aldrich, St. Louis, MO, USA). Deposition was carried out under applied potential of 200 V using a high voltage power source (Matsusada Precison, Model EJ-2R100) for 2 min each on stainless steel and nickel foil substrates (McMaster-Carr, Elmhurst, IL, USA). 20 ml of dispersion was used in each deposition with 1 cm^{-2} exposed area on the substrate. Substrates were cleaned in 6 M HCl for 10 minutes, rinsed thoroughly in deionized water and dried prior to deposition.

Electrophoretic deposition (EPD) was performed using the same ethanol:isopropanol solution as the dispersion medium. Ni foam substrates (MTI Corporation, Richmond, CA, USA) were also cleaned using a similar protocol as the planar substrates. Stainless steel 316L nanopowder (40 - 100 nm) was purchased from US Research Nanomaterials, Inc., Houston, TX, USA. SS nanoparticles (SSNP) were dispersed in the dispersion medium using an ultrasonic probe sonicator for 5 minutes. The Ni foam substrate (1 cm^2 projected area) was suspended in between the two graphite foil counter electrodes, spaced 1.5 cm from each other in a beaker containing 20 ml of dispersion. EPD was then performed by applying 200 V for two minutes. Pure $Ni(OH)_2$ was deposited as described before. Pure SSNP deposition was performed using a dispersion containing only 0.25 mg ml^{-1} suspended SSNP with no additional surfactants added to the dispersion. The SSNP/$Ni(OH)_2$ nanocomposite was deposited from a dispersion containing 0.25 mg ml^{-1} suspended SSNP and 0.2 mg ml^{-1} of dissolved $NiCl_2.6H_2O$. Typically, SSNP were dispersed first for 10 minutes, after which appropriate amount of $NiCl_2$ dissolved in ethanol was introduced into the dispersion and further sonicated for 10 minutes. For multiple depositions, after every 2 min deposition, fresh 20 ml of dispersion was used and deposition process repeated. The deposit was not allowed to dry in between steps.

Material Characterization: Hitachi S-4800 field emission scanning electron microscope was used to obtain secondary electron images of the nanocomposite deposits on Ni foam. Hitachi H-9500 HRTEM operated at 300 KeV was used to record transmission electron images of the SSNP/$Ni(OH)_2$ deposits. Deposits were removed from foam substrate via sonication in isopropanol and then drop cast on to TEM grid for imaging.

Thermogravimetric analysis (TGA) curves were recorded using a TGA-51 (Shimazu Scientific Instruments). Samples were heated in air flow (10 ml min^{-1}) at a ramp rate of 10 $^oC.min^{-1}$. Raman

spectra were recorded using a Thermo Scientific™ DXR™ Raman imaging microscope. A 532 nm laser excitation source operated at 3 mW power was used to record the spectra (average of 5 exposures; 45 s each). XRD was performed using Bruker D-8 Advance diffractometer (40 kV, 40mA; Cu Kα radiation). A zero-background Si holder (MTI Corporation, Richmond, CA, USA) was used to avoid substrate interference.

Electrochemical testing: All electrochemical characterization was performed using a basic three-electrode setup (graphite rod counter electrode; Ag/AgCl (4 M KCl) reference electrode) and a Gamry Reference 3000 potentiostat (Gamry Instruments, Warminster, PA, USA). The 1 M KOH electrolyte (pH 13.6) was first saturated with oxygen by bubbling oxygen gas for 20 minutes. Voltages versus RHE are reported as follows: $E_{RHE}(V) = E_{vs\ Ag/AgCl} + 0.20 + (0.059*pH)$.

95% *i*R correction was applied manually to all cyclic voltammograms based on the uncompensated solution resistance measured prior to testing. Electrochemical impedance spectra (EIS) data was recorded from 10^5-0.1 Hz under an AC perturbation of 10 mV at an applied voltage of ~1.6 V vs RHE. All deposits on Ni foam were stabilized by cycling 10 times at scan rate of 5 mV s^{-1} in 1 M KOH. Scan rates used (5 mV s^{-1} or 2 mV s^{-1}) are specified appropriately within the manuscript. For the accelerated stability test, the deposit was cycled 1000 times between 1.3-1.8 V *vs* RHE electrode at 100 mV.s^{-1}.

Chronopotentiograms were recorded with applied current densities of 10-100 mA cm^{-2} incremented by 10 mA.cm^{-2} every half hour. For higher current density testing (both in 1 M and 10 M KOH), current was stepped from 100-500 mA cm^{-2} in 100 mA cm^{-2} increments every 30 min. No *i*R correction was performed on any chronopotentiometry curves.

4.6 Acknowledgements

The authors acknowledge the financial support of the National Science Foundation (NSF Award 1444473). The authors sincerely thank Dr. Hyejin Moon for reviewing a draft of this work.

4.7 References

1. M. Wang, Z. Wang, X. Gong and Z. Guo, *Renew. Sust. Energ. Rev.*, 2014, **29**, 573-588.

2. M. Gao, W. Sheng, Z. Zhuang, Q. Fang, S. Gu, J. Jiang and Y. Yan, *J. Am. Chem. Soc.*, 2014, **136**, 7077-7084.

3. F. J. Pérez-Alonso, C. Adán, S. Rojas, M. A. Peña and J. L. G. Fierro, *Int. J. Hydrogen Energy*, 2014, **39**, 5204-5212.

4. Y. Yan, B. Y. Xia, B. Zhao and X. Wang, *J. Mater. Chem. A*, 2016, **4**, 17587-17603.

5. L.-A. Stern, L. Feng, F. Song and X. Hu, *Energy Environ. Sci.*, 2015, **8**, 2347-2351.

6. J. Nai, H. Yin, T. You, L. Zheng, J. Zhang, P. Wang, Z. Jin, Y. Tian, J. Liu, Z. Tang and L. Guo, *Adv. Energy Mater.*, 2015, **5**, 1401880.

7. J. Luo, J. H. Im, M. T. Mayer, M. Schreier, M. K. Nazeeruddin, N. G. Park, S. D. Tilley, H. J. Fan and M. Gratzel, *Science*, 2014, **345**, 1593-1596.

8. L. Trotochaud, S. L. Young, J. K. Ranney and S. W. Boettcher, *J. Am. Chem. Soc.*, 2014, **136**, 6744-6753.

9. T. T. H. Hoang and A. A. Gewirth, *ACS Catal.*, 2016, **6**, 1159-1164.

10. M. S. Burke, M. G. Kast, L. Trotochaud, A. M. Smith and S. W. Boettcher, *J. Am. Chem. Soc.*, 2015, **137**, 3638-3648.

11. S. Klaus, Y. Cai, M. W. Louie, L. Trotochaud and A. T. Bell, *J. Phys. Chem. C*, 2015, **119**, 7243-7254.

12. A. T. Swesi, J. Masud and M. Nath, *Energy Environ. Sci.*, 2016.

13. F. Dionigi and P. Strasser, *Adv. Energy Mater.*, 2016, **6**, 1600621.

14. I. Najdovski, P. R. Selvakannan and A. P. O'Mullane, *ChemElectroChem*, 2015, **2**, 106-111.

15. Y. Gorlin, C. J. Chung, J. D. Benck, D. Nordlund, L. Seitz, T. C. Weng, D. Sokaras, B. M. Clemens and T. F. Jaramillo, *J. Am. Chem. Soc.*, 2014, **136**, 4920-4926.

16. L. C. Seitz, T. J. Hersbach, D. Nordlund and T. F. Jaramillo, *J. Phys. Chem. Lett.*, 2015, **6**, 4178-4183.

17. B. S. Yeo and A. T. Bell, *J. Phys. Chem. C*, 2012, **116**, 8394-8400.

18. M. A. Sayeed, T. Herd and A. P. O'Mullane, *J. Mater. Chem. A*, 2016, **4**, 991-999.

19. B. S. Yeo and A. T. Bell, *J. Am. Chem. Soc.*, 2011, **133**, 5587-5593.

20. Y. Zhou and H. C. Zeng, *J. Phys. Chem. C*, 2016, **120**, 29348-29357.

21. N. Naseri, A. Esfandiar, M. Qorbani and A. Z. Moshfegh, *ACS Sustain. Chem. Eng.*, 2016, **4**, 3151-3159.

22. D. Gangasingh and J. B. Talbot, *J. Electrochem. Soc.*, 1991, **138**, 3605-3611.

23. P. Tsay and C.-C. Hu, *J. Electrochem. Soc.*, 2002, **149**, C492.

24. K. H. Kim, J. Y. Zheng, W. Shin and Y. S. Kang, *RSC Adv.*, 2012, **2**, 4759.

25. F. M. Sapountzi, J. M. Gracia, C. J. Weststrate, H. O. A. Fredriksson and J. W. Niemantsverdriet, *Prog. Energy Combust. Sci.*, 2017, **58**, 1-35.

26. F. Moureaux, P. Stevens, G. Toussaint and M. Chatenet, *J. Power Sources*, 2013, **229**, 123-132.

27. J. Ji, L. L. Zhang, H. Ji, Y. Li, X. Zhao, X. Bai, X. Fan, F. Zhang and R. S. Ruoff, *ACS Nano*, 2013, **7**, 6237-6243.

28. X. Lu and C. Zhao, *Nat. Commun.*, 2015, **6**, 6616.

29. H. Wang, H. W. Lee, Y. Deng, Z. Lu, P. C. Hsu, Y. Liu, D. Lin and Y. Cui, *Nat. Commun.*, 2015, **6**, 7261.

30. M. Mishra, Y. Sakka, T. Uchikoshi and L. Besra, *J. Ceram. Soc. Jpn.*, 2013, **121**, 348-354.

31. M. Aghazadeh, M. Ghaemi, B. Sabour and S. Dalvand, *J. Solid State Electrochem.*, 2014, **18**, 1569-1584.

32. D. A. Corrigan, *J. Electrochem. Soc.*, 1987, **134**, 377.

33. M. W. Louie and A. T. Bell, *J. Am. Chem. Soc.*, 2013, **135**, 12329-12337.

34. R. L. Doyle and M. E. Lyons, *Phys. Chem. Chem. Phys.*, 2013, **15**, 5224-5237.

35. Z. Zheng, W. Geng, Y. Wang, Y. Huang and T. Qi, *Int. J. Hydrogen Energy*, 2017, **42**, 119-124.

36. A. R. Boccaccini, S. Keim, R. Ma, Y. Li and I. Zhitomirsky, *J R Soc Interface*, 2010, **7 Suppl 5**, S581-613.

37. S. Santhanagopalan, A. Balram and D. D. Meng, *ACS Nano*, 2013, **7**, 2114-2125.

38. D. H. Ha, M. A. Islam and R. D. Robinson, *Nano Lett.*, 2012, **12**, 5122-5130.

39. C. Wang, R. B. Moghaddam, M. J. Brett and S. H. Bergens, *ACS Sustain. Chem. Eng.*, 2017, **5**, 1106-1112.

40. D. Su, M. Ford and G. Wang, *Sci. Rep.*, 2012, **2**, 924.

41. J. M. Gonçalves, R. R. Guimarães, C. V. Nunes, A. Duarte, B. B. N. S. Brandão, H. E. Toma and K. Araki, *RSC Adv.*, 2016, **6**, 102504-102512.

42. M. Marciuš, M. Ristić, M. Ivanda and S. Musić, *J. Alloys Compd.*, 2012, **541**, 238-243.

43. T. L. S. L. Wijesinghe and D. J. Blackwood, *Appl. Surf. Sci.*, 2006, **253**, 1006-1009.

4.8 Supporting Information

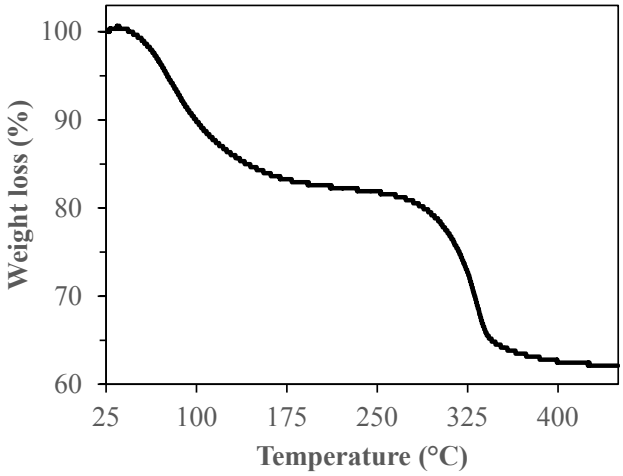

Figure S4-5. Representative TGA curve of electrodeposited α-$Ni(OH)_2$

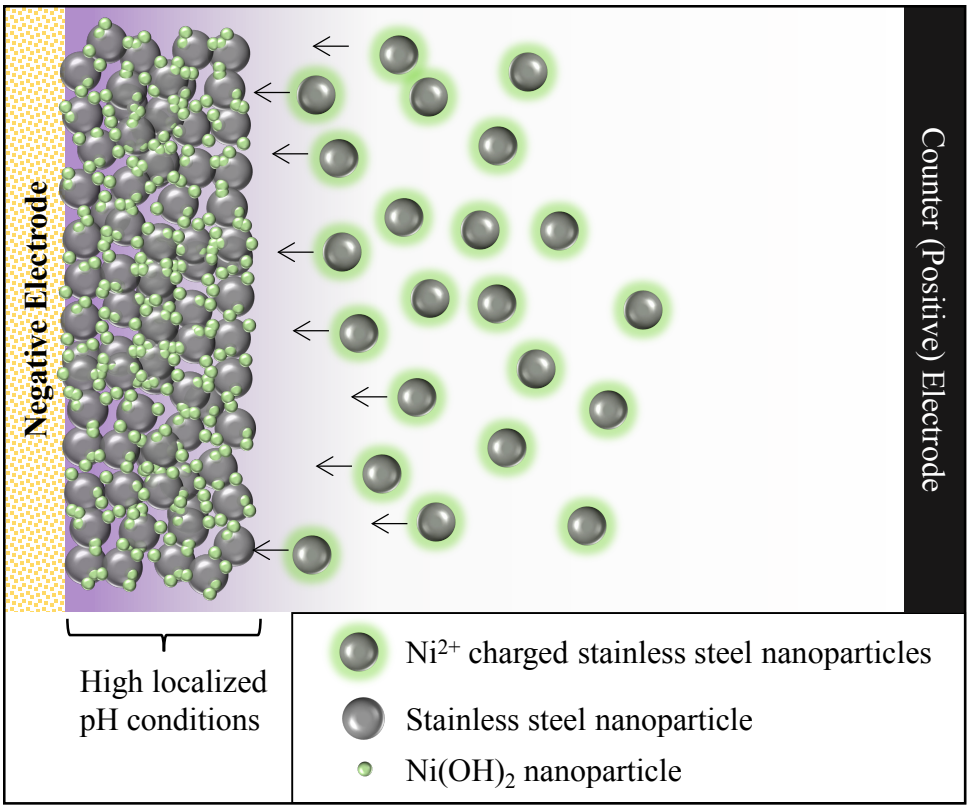

Figure S4-2. Schematic sketch of electrophoretic co-deposition of $Ni(OH)_2$ nanoparticle decorated stainless steel nanoparticles.

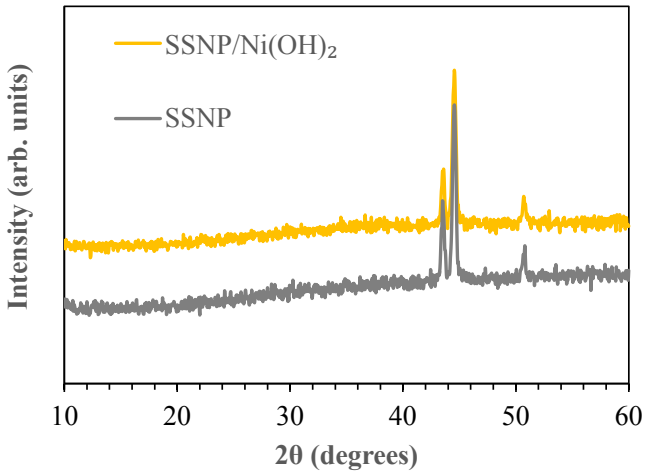

Figure S4-3. Representative X-ray diffraction (XRD) data of as-purchased stainless steel nanoparticles (SSNP) and electrophoretically deposited SSNP/$Ni(OH)_2$ nanocomposite. No α-$Ni(OH)_2$ peaks are apparent owing to disordered structure or small particle size.

CHAPTER 5

ADAPTABLE ELECTROPHORETIC DEPOSITS OF AMORPHOUS METAL HYDROXIDE DECORATED CARBON NANOTUBES FOR OVERALL WATER SPLITTING

5.1 Abstract

A catalyst that could optimally catalyze both, the oxygen evolution reaction (OER) as well as the hydrogen evolution reaction (HER) to split water at low overall overpotentials would be highly beneficial to the widespread applicability of electrolytic water-splitting. However, performance compromises on one or both sides of the reaction are typically encountered when using a single bifunctional water-splitting catalyst material. To overcome this issue, we propose electrophoretic deposition (EPD) as an effective technique to produce CNT-metal hydroxide based deposits that serve as an adaptable platform in order optimize both sides of the water splitting reaction in alkaline water electrolysis. Synergistic substrate/deposit interactions were exploited by electrophoretically depositing binder-free amorphous $Ni(OH)_2$, $Co(OH)_2$, and mixed Ni-Co hydroxide nanoparticle decorated carbon nanotubes (CNT) deposits directly onto inexpensive metal mesh substrates. As prepared, the CNT-metal hydroxide deposits on stainless steel mesh could generate oxygen at overpotentials as low as 245 mV @ 10 $mA.cm^{-2}$. The metal hydroxide present in the deposits allowed for subsequent modification to optimize the HER performance. To minimize the HER overpotentials, the same deposits were further decorated with platinum nanoparticles via a simple galvanic replacement process. The resultant novel hybrid nickel-cobalt metal hydroxide/platinum decorated CNTs could generate 10 $mA.cm^{-2}$ of hydrogen at ~50 mV. The optimized OER/HER combination could split water at the specified current density at ~1.55 V stably for a period of 24 hours. This work provides basis for the use of EPD to produce conductive, binderless, and high activity deposits amenable to subsequent application specific modification.

5.2 Introduction

Alkaline water-splitting via renewable sources could be a viable sustainable solution for emission-free hydrogen production.[1, 2] Cost-effective catalyst electrodes that maximize system efficiency by lowering operating overpotentials for the hydrogen evolution reaction (HER) and oxygen evolution reaction (OER) are key to widespread implementation.[3] Ideally, a truly bifunctional OER/HER catalyst that can catalyze both, HER as well as OER at modest overpotentials would be highly beneficial to the cost effectiveness of electrolytic hydrogen production by reducing overall electrode manufacturing costs and reducing system complexity.[4, 5] Various transition-metal selenides,[6] phosphides,[7-9] sulfides,[10] nitrides[11] etc. have emerged as popular materials for this application. In practice, however, there tends to be a compromise in performance on one or both sides of the water-splitting reaction when using a single catalyst material to facilitate water-splitting.[2] For instance, a material such as NiFe layered double hydroxide shows extremely low OER overpotentials but as an HER catalyst, it required 210 mV to produce 10 $mA.cm^{-2}$, ~100 mV higher than the benchmark platinum catalyst.[5] Therefore, another and perhaps more effective approach might be utilizing a material that has been optimized for OER (or HER) and a modification thereof which can ensure optimal catalytic performance for the reaction on the other side as well. Metal hydroxides ($M(OH)_2$) such as nickel hydroxide, cobalt hydroxides and especially bimetallic nickel-cobalt hydroxides are excellent candidates to enable such a strategy. Despite their excellent performance catalyzing alkaline OER, these hydroxides by themselves tend to be mediocre HER catalysts.[5] This limits their direct use as bifunctional HER/OER catalysts. Nevertheless, these metal hydroxides could serve as precursors that can be subsequently transformed or adapted using some kind of post-synthesis procedure into a more active phase for HER catalysis. For instance, nickel and cobalt hydroxides

have previously served as precursors for subsequent conversion into metal/metal oxide hybrids,[12, 13] chalcogenides,[14] phosphides,[15] nitrides[16] etc. using thermal, vapor phase or electrochemical treatments geared towards more efficient HER catalysis.

Thus, if a highly active metal hydroxide based deposit fine-tuned towards efficient OER catalysis could first be produced, with some post deposition treatment, a similarly high performance HER catalyst could also be obtained. Extracting maximum catalytic performance requires simultaneously harnessing several factors that individually contribute to improved electrochemical performance. Decoration of active nanomaterials on graphitic materials such as carbon nanotubes (CNTs) and graphene has been known to improve their electrocatalytic performance due to hierarchical nanostructuring, improved conductivity and synergistic interactions between the nanoparticles and the carbon based nanomaterials.[2, 17-20] Another factor that influences performance is crystallinity. More recently, amorphous phases have been found to outperform crystalline counterparts.[21-23] Non-participating electrode binder materials used during electrode assembly that tend to increase impedances and decrease surface wettability tend to significantly hinder performance.[4, 24] Additionally, the loss of intimate substrate/deposit contact due to the presence of binder in the assembled electrode may also significantly hamper synergistic enhancement effects.[25, 26] However, preparing such hydrophilic, robust yet binderless deposits of amorphous metal hydroxide decorated CNTs intimately attached to the substrate using traditional material and electrode fabrication techniques is quite challenging.

Electrophoretic deposition (EPD)[27, 28] has been shown previously to be a versatile deposition method that can maximize electrochemical performance from carbonaceous nanomaterial deposits by eliminating polymeric binder, facilitating in-situ active nanoparticle decoration,[27] offering control over orientation[27, 28] etc. Avoiding binders is especially prudent as they could be

incompatible with the post-treatment procedures, generally high temperature treatments in special atmospheres,[12, 29] used to transform the metal hydroxides to other phases. EPD has been previously shown to produce $Ni(OH)_2$ decorated CNT and graphene deposits with excellent electrochemical performance for applications such as supercapacitors and glucose detection.[30-32] Therefore, we first adopted a facile, versatile and scalable single-step electrophoretic deposition (EPD) process that could rapidly produce robust amorphous nickel, cobalt and nickel-cobalt hydroxide decorated CNTs deposits on synergetic metal mesh electrodes without need for any extraneous binders.

Our deposition process involving simultaneous metal hydroxide nanoparticle decoration and deposition of CNTs may be viewed as a combination of EPD and electrodeposition. As prepared, their binder-free, hydrophilic nature as well as low Faradaic resistances due to intimate contact with the stainless steel substrate, ensures extremely high electrochemical activity toward OER in alkaline medium. In order to optimize the HER catalysis and illustrate the adaptability of our deposits, we performed a simple galvanic replacement procedure wherein the $M(OH)_2$ decorated CNT coated mesh were further decorated with platinum nanoparticles. Using a process like galvanic replacement to produce such catalysts is very appealing due to the low energy expenditure involved. Previously, Pt nanoparticle decorated $Ni(OH)_2$ nanoflakes have been shown to greatly reduce HER overpotentials in alkaline medium.[33] This metal hydroxide/Pt combination provides optimal conditions for water dissociation, adsorption of intermediates and eventual recombination to form H_2, overcoming the deficiencies of either material when used individually for alkaline HER.[33, 34] To the best of our knowledge, there have been no such prior studies of hybrid carbon nanotube deposits decorated with both platinum and Ni/Co hydroxides

or even carbon-free $Co(OH)_2$/Pt or mixed Ni-Co hydroxide/Pt deposits for HER. All three resulting hybrid deposits in this work show high HER catalytic activity.

These Pt enhanced CNT/$M(OH)_2$ deposits could have a wide range of electrochemical applicability beyond the HER studied here. As-prepared, the CNT/$M(OH)_2$ deposits would easily lend themselves to these various downstream processes for subsequent conversion into more active noble metal-free compositions, if required. The best OER performance was obtained when using stainless steel mesh as a substrate while nickel derived the best HER performance. Among our deposits, CNTs decorated with a mixed nickel-cobalt hydroxides were determined to be the best candidate to employ to achieve optimal OER and subsequent hybridization for HER. Ultimately, the best OER/HER catalyst combination was able to durably split water at 10 $mA.cm^{-2}$ at as low as 1.55 V.

5.3 Results and Discussion

Electrophoretic deposition or EPD,[35-38] is a versatile technique known for its ability to deposit virtually any suspended nanomaterial given the right combination of surface charge and deposition voltage. The deposition process hinges on first producing a dispersion of a sufficiently charged nanomaterial in a liquid medium, followed by the electric field induced deposition on an electrode (substrate) with the opposite charge. The charge on a nanomaterial may stem from native surface charges or foreign ionic species introduced into the medium. Ideally, the co-deposited charging agent should enhance the performance of a deposit and at the very least not hinder the intended application. In the case of CNTs, the presence of weak negative charges on their surface from dissociated functional groups (introduced during preliminary acid treatment/purification), allows for facile adsorption of positively charged metal ions, when available in the medium. Upon exposure to an electric field, they tend to migrate to and

flocculate on the negatively charged electrode, as previously described. A schematic sketch of the deposition mechanism is shown in Figure S5-1.When the deposition conditions induce high localized pH at the electrode/electrolyte interface,[39] the metal ions in the electrolyte tend to take the form of corresponding hydroxides on the CNT surface upon deposition.[31, 40] Unlike typical electrodeposition, however, the concentration of metal ions in the deposition bath is extremely limited, leading to nanoparticle decoration on the CNT surface rather than embedding the CNTs in a metal hydroxide matrix. Briefly, the electrophoretic deposition process was carried out as follows. A metal mesh working electrode (1 cm^2 projected area) was typically sandwiched between two similarly sized graphite counter electrodes 14 mm apart. This electrode assembly was then immersed in a CNT-metal salt dispersion and a voltage of 200 V was applied for 3 minutes.

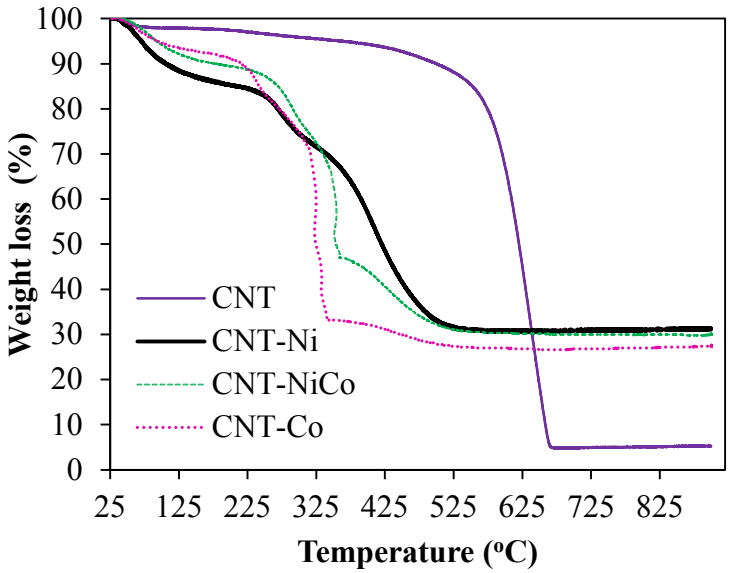

Figure 5-1. Representative thermogravimetric analysis (TGA) curves of plain CNT and the three hybrid metal hydroxide decorated CNT deposits: CNT-Ni, CNT-NiCo, and CNT-Co.

We have previously reported metal hydroxide decorated CNT deposits prepared by depositing CNTs with metal ions via EPD in a purely aqueous medium.[31] While those deposits performed well under the relatively benign test conditions of non-enzymatic glucose sensing, their adhesion was found lacking when utilized in highly challenging environments encountered in gas evolving reactions such as water-splitting. The deposits would rapidly peel off the substrate when subjected to even relatively mild bubble generation. The interfacial conditions during the deposition process at the substrate/deposit interface, owing to significant electrolysis in a purely aqueous deposition medium may have played a significant role in compromising the deposit adhesion. We found that this problem could be alleviated by replacing the exclusively water based deposition medium to an alcohol based one. We found that metal hydroxide decorated CNTs, when deposited from an ethanol-isopropanol solution containing nickel and/or cobalt ions, were robust enough to survive the harsh conditions of oxygen and hydrogen generation. The small amount of water content inherent in the deposition bath via water of hydration associated with the dissolved metal salts allows for localized deposition conditions forcing metal hydroxide deposition on the CNT surface. At the same time, the significantly lower availability of water ensures that the electrolysis during deposition is limited enough to not violate the structural integrity of the deposit as in the case of a purely aqueous medium.

For the sake of brevity, the CNT-$M(OH)_2$ deposits containing nickel hydroxide, cobalt hydroxide and nickel-cobalt hydroxide will be referred to as CNT-Ni, CNT-Co and CNT-NiCo respectively henceforth. Thermogravimetric analysis (TGA) was first used to confirm the deposition of metal hydroxides on the CNT surface. As expected, the TGA curves (**Figure 5-1**) provide a clear indication that the co-deposited nanoparticles on the CNT are α-phase of the corresponding metal hydroxides. The removal of large amount of intercalated water within the hydrated $Ni(OH)_2$

crystal structure at temperatures lower than 200 ^{o}C is characteristic of the α-M(OH)$_2$ phase.[41] The TGA curves of all the deposits show multiple weight loss steps corresponding the loss of adsorbed and intercalated water, dehydration of the hydroxides to oxides, and the eventual decomposition of CNTs. The derivative thermogravimetric analysis (DTG) curves are presented in Figure S5-2. The pure refluxed CNTs as prepared completely decompose by ~625 ^{o}C. However, the nanoparticles on the decorated CNTs, promote their decomposition at lower temperatures[42] with all three deposits reaching a stable final weight by ~525 ^{o}C. CNT-Ni contained the largest amount of intercalated water at ~15% with Co(OH)$_2$ containing 10%. At 900 ^{o}C, approximately 25% weight in the form of metal oxides remain in the samples after the removal of the CNTs.

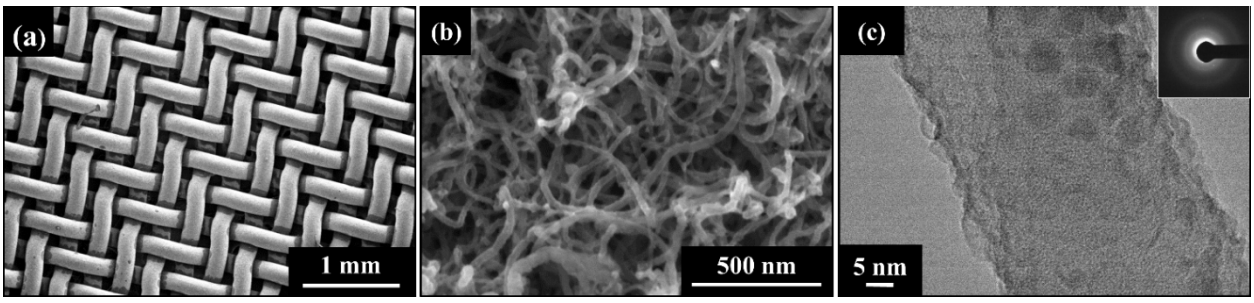

Figure 5-2. (a, b) FE-SEM images of stainless steel 80 x 80 mesh coated electrophoretically with Ni(OH)$_2$ nanoparticle decorated carbon nanotube (CNT) **(c)** HR-TEM image of Ni(OH)$_2$ nanoparticle decorated CNT, (designated CNT-Ni); **(inset)** electron diffraction pattern.

Given the similar deposition mechanism for all the samples, CNT-Ni deposits were chosen to be representative samples for imaging. **Figure 5-2** a, b show secondary electron micrographs of representative Ni(OH)$_2$ decorated CNT deposits on 80 x 80 SS mesh at low and high

magnifications respectively. The deposited nanoparticles are not readily apparent on the CNT surface from the FE-SEM images. The HRTEM image, along with the diffused rings seen in the electron diffraction pattern (inset) confirms the presence of deposited amorphous nanoparticles (generally <5 nm) on the CNT. Although the two weight loss steps seen in the TGA results confirm that the deposited nanoparticles are the hydrated α– polymorph of the $Ni(OH)_2$, when observed in the HRTEM, under electron irradiation, the nanoparticles tended to dehydrate

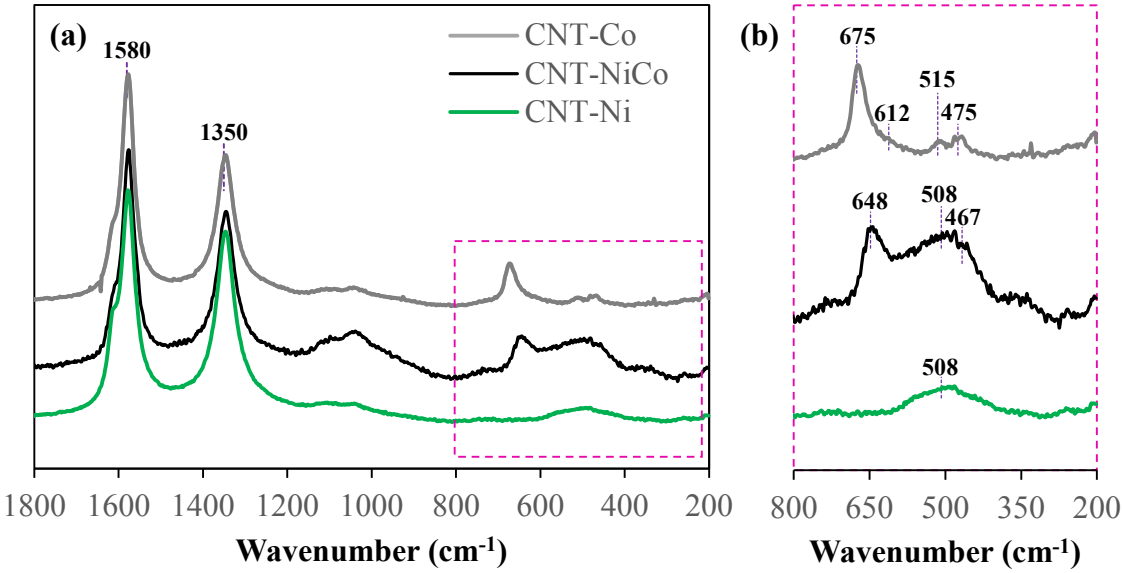

Figure 5-3. (a) Representative Raman spectra of the hybrid metal hydroxide decorated CNT deposits obtained at 10 mW; **(b)** Magnified view of the low wavenumber region. The metal hydroxides experience laser heating induced phase transformation into their corresponding oxides as shown.

and rapidly transform into NiO with lattice spacing of 0.21 nm (Figure S5-3). This phase transformation of α-$Ni(OH)_2$ under electron beam irradiation has been previously documented by others.[43, 44]

The Raman spectra of the as-deposited CNT-$M(OH)_2$ samples did not show any distinct peaks of the metal hydroxide materials at lower laser powers (< 2 mW). This is likely a consequence of the absorption from CNTs as well as low Raman scattering of the metal hydroxides. As laser power was increased, however, localized heating induced a phase transformation[45] of the metal hydroxides into their corresponding oxides that were easier to detect. Figure S5-4-6 show the influence of laser power on the Raman spectra acquired from the deposits. **Figure 5-3** shows the Raman spectra of the deposits acquired using a 532 nm laser at a power setting of 10 mW. All the deposits showed peaks at ~1580 and ~1345 cm^{-1} typical of multi-walled CNTs.[46] A broad feature at round 508 cm^{-1} corresponding to nickel oxide,[47] three bands at 467, 508, and 651 cm^{-1} corresponding to $NiCo_2O_4$[48] and 192, 475, 515, 612, and 681 cm^{-1} are seen in the case of Co_3O_4[49] respectively upon laser induced phase transformation.

For further confirmation of metal hydroxide deposition, deposits devoid of CNTs were prepared by depositing from electrolyte containing only 0.2 mg. ml^{-1} metal salts, similar to the electrolyte used during CNT-$M(OH)_2$ co-deposition. The Raman spectra of the pure metal hydroxide deposits are shown in Figure S5-7. Spectra for cobalt hydroxide and nickel-cobalt hydroxide were obtained at 2 mW, while nickel hydroxide was collected at 10 mW laser power to improve quality of the Raman signal. Higher Raman intensities could be obtained due to the lack of absorption from the CNTs. These deposited materials were more resistant to phase transformation under laser irradiation as compared to the smaller nanoparticles decorating the CNTs. Those deposits were produced using the exact sample deposition conditions but without CNTs in the deposition solution. The peak at ~465 cm^{-1} is assigned to $Ni(OH)_2$ while the feature at ~481 cm^{-1} is attributed to $Ni(OH)_2$ with high degree of disorder.[50] The bands at ~465 and ~528 cm^{-1} are assigned to mixed nickel-cobalt hydroxides[51] where the band of 528 cm^{-1} tends to reflect

the degree of disorder within the $Ni(OH)_2$ structure owing to the presence of the cobalt ions. Bands at 463, 480, 521 and 580 cm^{-1} confirm $Co(OH)_2$.[52]

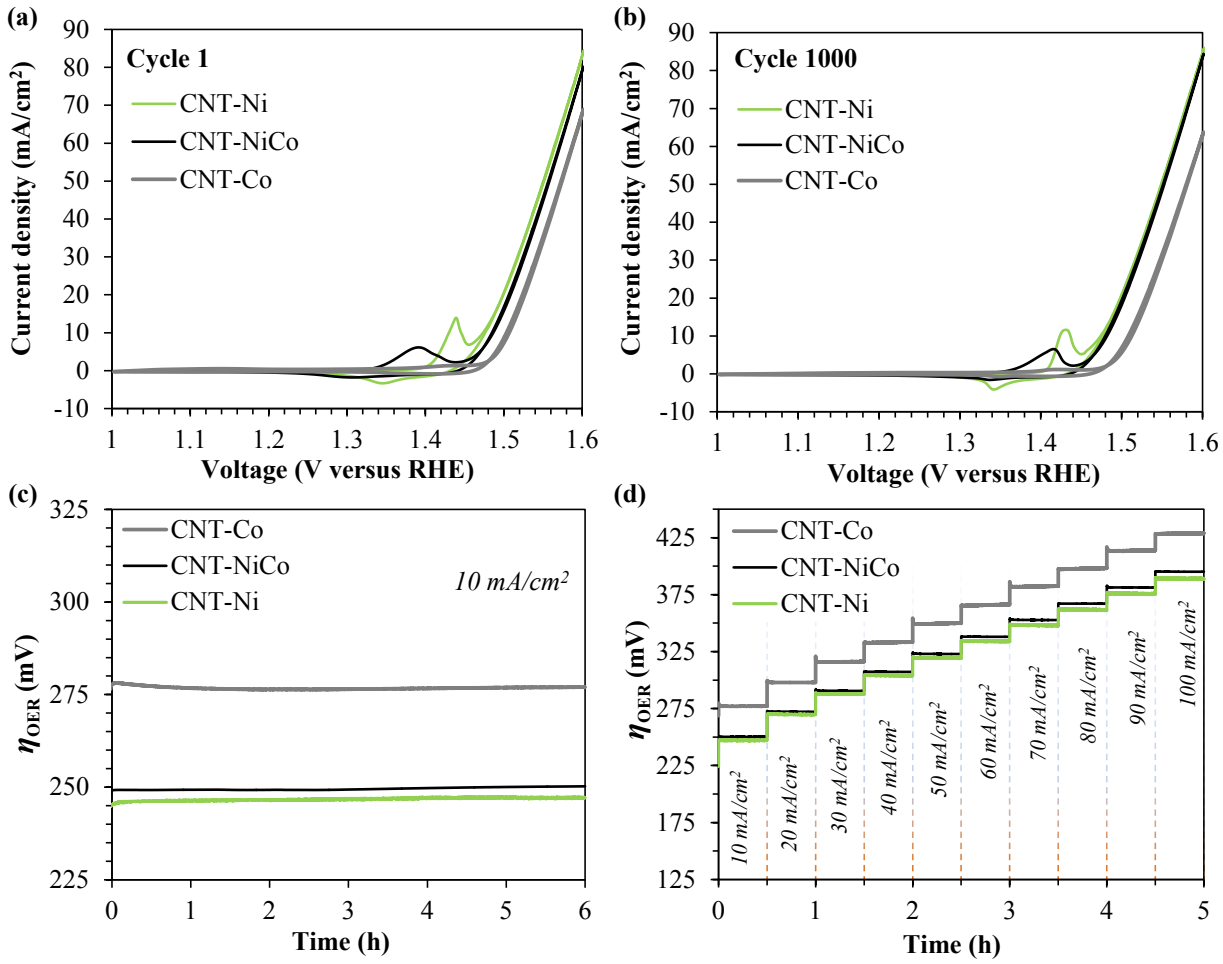

Figure 5-4. Cyclic voltammograms of CNT-Ni, CNT-NiCo, and CNT-Co deposits (a) before and (b) after 1000 cycles of accelerated stability testing protocol. All CV curves were recorded in 1 M KOH at 2 mV s^{-1}. (c) Chrononopotentiometry curves recorded after the accelerated stability testing for 6 h at 10 mA. cm^{-2} indicate excellent durability of the OER catalysts. (d) Chronopotentiograms of the CNT-$M(OH)_2$ deposits obtained at various current densities. Current densities were incremented in steps of 10 mA. cm^{-2} every 30 minutes.

The three variants: CNT-Ni, CNT-NiCo and CNT-Co deposits on stainless steel mesh were tested to determine electrochemical OER performance and durability. Stainless steel mesh was chosen as the substrate for OER due to the significantly lower overpotentials and higher current densities obtained with the steel as opposed to nickel substrate, as seen in Figure S5-8. We hypothesize that a small amount of Fe from the substrate dopes the metal hydroxide during the deposition process, leading to this higher activity.[26] The anodic shift of the oxidation peak seen in the deposit on SS as opposed to that on nickel substrate, seems to indicate some addition of Fe to the deposit.[53] This is consistent with previous reports of Fe incorporation in $Ni(OH)_2$ and $Co(OH)_2$ leading to improved OER performance.[53, 54] The deposits were first stabilized by electrochemical cycling 10 times at 5 mV. s^{-1} between 1 - 1.6V vs RHE. Subsequently, the deposits were subjected to an accelerated testing protocol which involved rapid cycling (100 mV. s^{-1}) between 1.3 – 1.8 V versus RHE for a 1000 cycles. **Figure 5-4**a and b show the cyclic voltammograms recorded at 2 mV.s^{-1} obtained initially and after 1000 cycles respectively. The differing redox peak positions of the three samples confirms the formation of three different metal hydroxides on the CNTs during the electrophoretic deposition process with the sample containing pure $Ni(OH)_2$ showing the most anodic redox peak position representing the conversion to the corresponding oxyhydroxide. In terms of OER overpotential, the CNT-Ni and CNT-NiCo show the best performance indicated by the low overpotentials of ~245 mV at nominal current density of 10 mA.cm^{-2}, the Figure 5-of merit typically considered.[55] This high level of performance remains unaffected even after the accelerated stability testing indicating high durability of the catalyst deposits. The CNT-Co sample shows comparatively lower performance with $\eta_{10\ mA}$ of ~275 mV and ~25% lower current density at an overpotential of 370 mV at the end of a 1000 cycles. However, the overpotential is still one of the lowest obtained for

pure $Co(OH)_2$ based OER catalyst in alkaline medium. The durability and performance of the same catalyst deposits under steady state operation at 10 $mA.cm^{-2}$ was tested immediately after the accelerated potential cycling tests. Figure 5-4c shows the chronopotentiograms obtained at η_{10mA}. The durability of the deposits is further evidenced by the negligible change in overpotential over 6 hours of operation. The deposits were further subjected to stepped current increased from 10-100 $mA.cm^{-2}$ in increments of 10 $mA.cm^{-2}$ every 30 min. The potentials recorded at every current density for each sample appear to be consistent with previously obtained cyclic voltammetry data and show no significant degradation in performance over the entire electrochemical testing process. The low overpotentials of all the deposits and their durability are a testament to the excellent synergy between the CNTs and the decorating amorphous metal hydroxide nanoparticles and the robustness of the deposits.

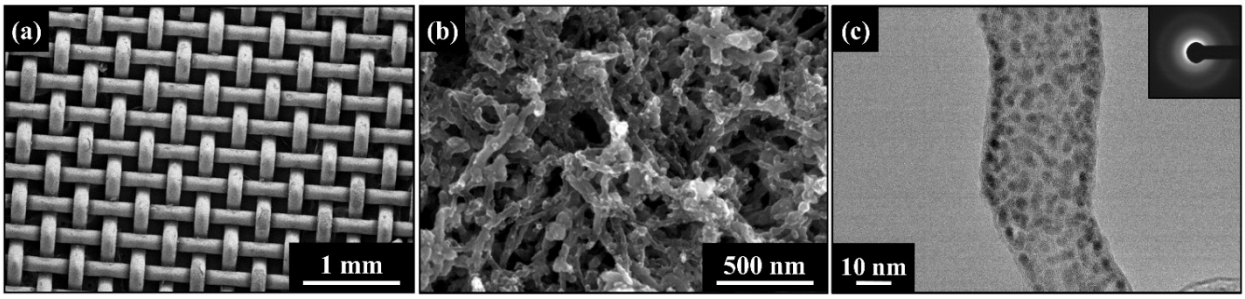

Figure 5-5. (a, b) FE-SEM images of 80 x 80 mesh copper wire cloth coated with a hybrid deposit of CNT decorated with $Ni(OH)_2$/Pt nanoparticles (CNT-Ni/Pt); (c) HR-TEM image of CNT-Ni/Pt; (inset) diffused rings in the electron diffraction pattern shows the amorphous nature of the nanoparticles.

In order to test the HER catalysis ability of the deposits, chronopotentiograms were recorded at 10 $mA.cm^{-2}$ while generating hydrogen gas (Figure S5-9). As prepared, on SS mesh, the HER overpotential is almost -400 mV. The HER overpotential further deteriorated when deposited on

copper mesh. There was a significant reduction in HER overpotential, however, when nickel plated copper mesh was utilized as the substrate. When deposited on nickel, the CNT-Ni deposits exhibited an overpotential of ~300 mV, making it the most suitable substrate for all subsequent HER tests. As mentioned previously, by themselves, $Ni(OH)_2$ and $Co(OH)_2$ are known to not be especially good HER catalysts. Providing Pt metal sites near the metal hydroxide is known to eliminate the bottleneck in intermediates on $M(OH)_2$ recombining to form molecular H_2.[33, 34] Hence, in order to optimize the HER side performance so as to make overall water-splitting viable, we adopted a simple galvanic replacement method. Galvanic replacement typically is self-sustained and does not require additional energy input. It allows for preparation of unique material combinations with intimate interfacial contact, critical especially in catalytic applications.[56] Galvanic replacement,[57] in and of itself, is extremely facile and versatile. It involves immersion of the target material or deposit in a solution of ions, typically, although not limited to noble metal ions such as Pt, Au, Ru etc. The difference in electrode potentials of the target as opposed to the free ions, provides the necessary impetus for the spontaneous deposition of the noble metals on to the target. Previously, galvanic replacement has been used to spontaneously decorate CNTs with noble metal nanoparticles,[58] prepare metal/metal oxide hybrid structures,[59] prepare core-shell structures,[57] etc. In the case of our deposits, the galvanic replacement could occur at the expense of the substrate, oxidation of the metal hydroxide nanoparticles or surface functional groups on the CNTs. The exact mechanism at work in our deposits is worth further study. After soaking overnight in platinum chloride solution, the samples were allowed to dry for an hour at 100 ^{o}C in a heated oven. Nickel plated (25 mA.cm^{-2} projected area; 60s) copper mesh 80 x 80 was used for all HER tests unless specified otherwise.

Secondary electron micrographs of CNT/Ni-Pt deposits on nickel plated copper mesh (80 x 80) are shown in **Figure 5-5** a,b. The nanoparticles are more apparent on the surface of the CNT as opposed to the as-prepared only metal hydroxide decorated CNT electrophoretic deposits. The HRTEM images (Figure 5-5c) clearly show the nanoparticle decoration on the CNT. Similar to the CNT/Ni samples seen previously, the electron diffraction pattern shows diffused rings suggesting amorphous deposits. The presence of Pt nanoparticles is confirmed by the lattice fringes (Figure S5-10) corresponding to crystalline Pt and NiO that can clearly be seen. Similar to the $M(OH)_2$ nanoparticles, the crystalline phases for Pt and NiO seem to appear under electron beam irradiation. This transformation under the beam of amorphous Pt has also been recently reported.[60] Representative TGA curves for CNT-Ni/Pt, CNT-NiCo/Pt, and CNT-Co/Pt are shown in **Figure 5-6**a. All three curves show the two initial weight loss steps stemming from dehydration from the hydrated metal hydroxide to corresponding metal oxide similar to those seen in the case of the original deposits devoid of platinum. This further indicates that the deposits contain both Pt nanoparticles as well as hydrated metal hydroxide after the galvanic replacement process.

Two significant differences were noted in the TGA curves of the hybrids when compared to the originally prepared pure CNT-$M(OH)_2$ deposits. Firstly, the onset of CNT decomposition is delayed significantly with the addition of Pt to the hybrid as illustrated by the DTG curves in Figure S5-11 a, b, and c. Secondly, the initial water weight loss is lower than the as-prepared CNT/$M(OH)_2$ deposits seen previously in Figure 5-1. This appears to primarily result from the drying process (100 ^{o}C for an hour) after the immersion in platinum ion solution. This is corroborated by the TGA curves in Figure S5-12. CNT-Ni control samples were immersed in pure DI water for a similar duration as the CNT-Ni/Pt deposits and dried either at room

temperature or at 100 °C. At a nominal temperature of 225 °C, the sample dried at elevated temperature loses 8.6 % weight in the form of intercalated and adsorbed water as opposed to 14.6 % lost by the sample dried at room temperature. The weight loss experienced by the latter sample is similar to that of the as-prepared CNT-Ni. The delay in onset of CNT decomposition also appears to be on account of the Pt in the hybrid, not the drying process. Further evidence of the formation of a CNT/$M(OH)_2$/Pt hybrid was obtained from the Raman spectra of the three deposits .The Raman spectra seen in Figure 5-6b further confirm the presence of the corresponding metal oxides[61-64] in the deposits as seen in the original CNT-$M(OH)_2$ samples due to laser heating.

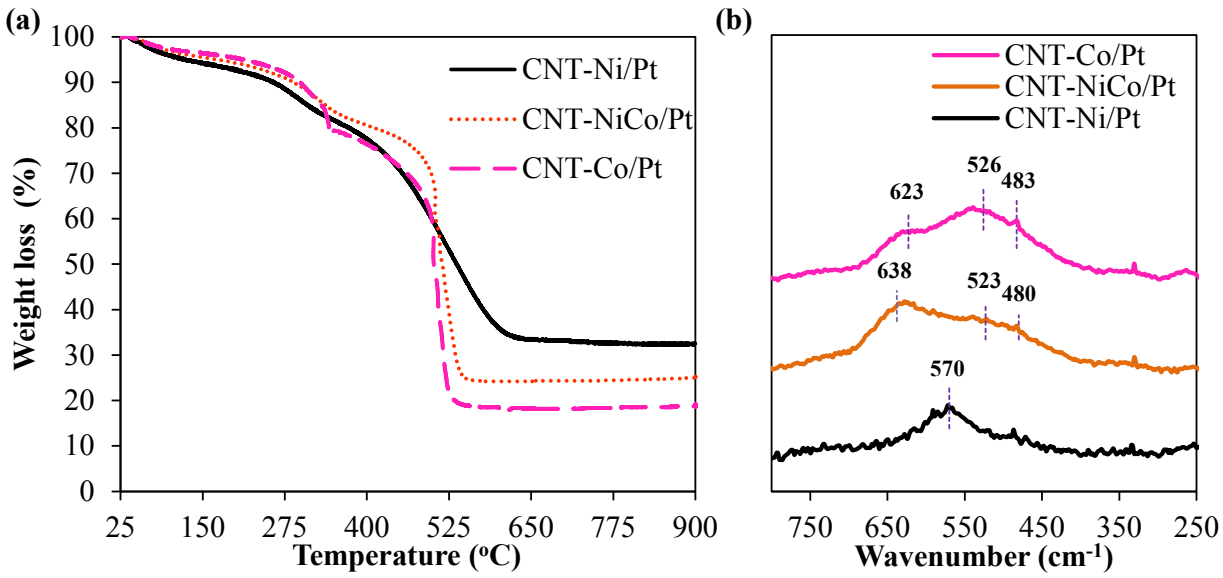

Figure 5-6. (a) Representative TGA curves of the hybrid CNT-Ni/Pt, CNT-NiCo/Pt and CNT-Co/Pt deposits; (b) Raman spectra of CNT-Ni/Pt, CNT-NiCo/Pt and CNT-Co/Pt deposits after galvanic replacement procedure.

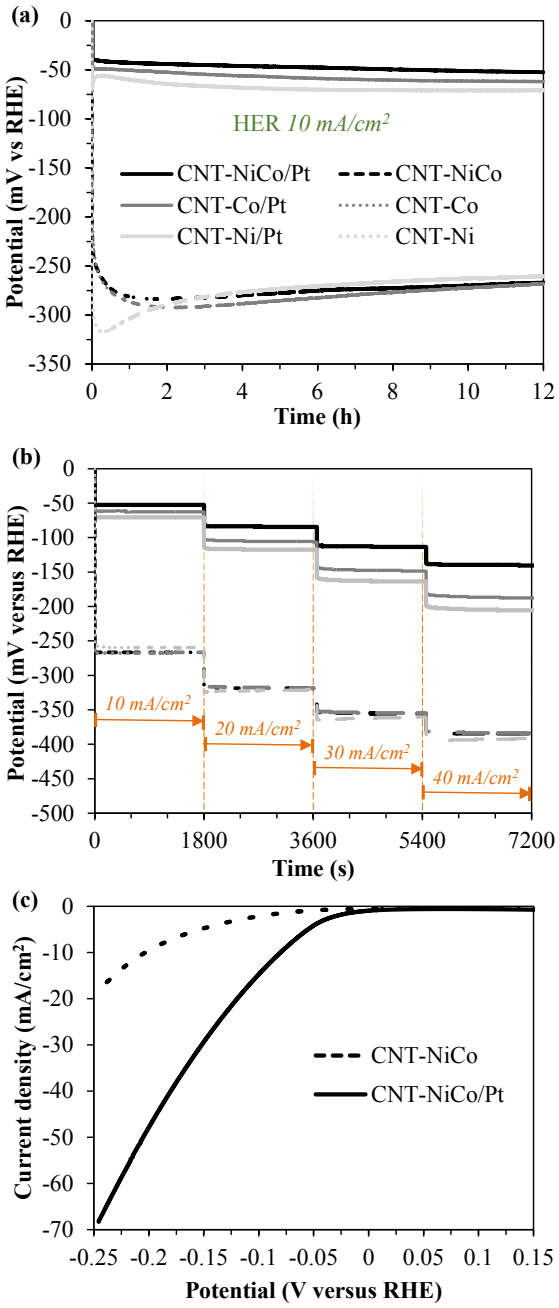

Figure 5-7. Electrochemical characterization of alkaline HER performance of the various as-deposited and post-galvanic replacement samples: (a) Chronopotentiograms acquired at 10 $mA.cm^{-2}$; (b) Chronopotentiometry curves obtained in 10 $mA.cm^{-2}$ increments every 0.5 h; (c) LSV curves comparing HER performance of CNT-Ni/Pt to CNT-Ni at 2 $mV.s^{-1}$.

In terms of HER performance (**Figure 5-7**), at 10 $mA.cm^{-2}$ all three as-prepared deposits lacking platinum showed similar behavior with overpotentials of ~260 mV recorded after 12 hours at constant current density. In comparison, samples containing platinum showed exemplary behavior with an approximately 200 mV reduction in overpotential to generate hydrogen at the same current density. Among the three hybrids produced, CNT-NiCo/Pt clearly outperformed the samples containing only $Ni(OH)_2$ and $Co(OH)_2$ in combination with platinum. CNT-NiCo/Pt only required an average overpotential 50 mV at 10 $mA.cm^{-2}$ as opposed to the 60 mV and 70 mV required by the CNT-Co/Pt and CNT-Ni/Pt deposits respectively over 12 h of testing. The difference between the three variants was more apparent in subsequent testing where the current density was incremented by 10 $mA.cm^{-2}$ up to 40 $mA.cm^{-2}$ every 30 min. The overall superior catalytic ability of the CNT-NiCo/Pt deposit is evident from Figure 5-7b as it outperforms the other two deposits by approximately 50 mV at current density of 40 $mA.cm^{-2}$. The deposits devoid of platinum, however, show no real disparity in terms of performance even at the higher current densities. This indicates the favorable kinetics in the presence of the unique combination of the nickel-cobalt hydroxide along with platinum which amplifies the catalytic performance as opposed to the platinum loaded deposits of CNTs decorated with either pure $Ni(OH)_2$ or $Co(OH)_2$. The LSV curve performed at 2 $mV.s^{-1}$ shown in Figure 5-7c also illustrates the superiority of the CNT-NiCo/Pt sample over CNT-NiCo as prepared over the entire swept voltage range. At -250 mV vs RHE, the platinum loaded sample was able to sustain 70 $mA.cm^{-2}$ as opposed to the 20 $mA.cm^{-2}$ managed by its platinum-free counterpart.

Given the excellent performance of the CNT-NiCo (on SS mesh substrate) on the OER side and CNT-NiCo/Pt (on nickel plated mesh substrate) towards HER, the combination was utilized to

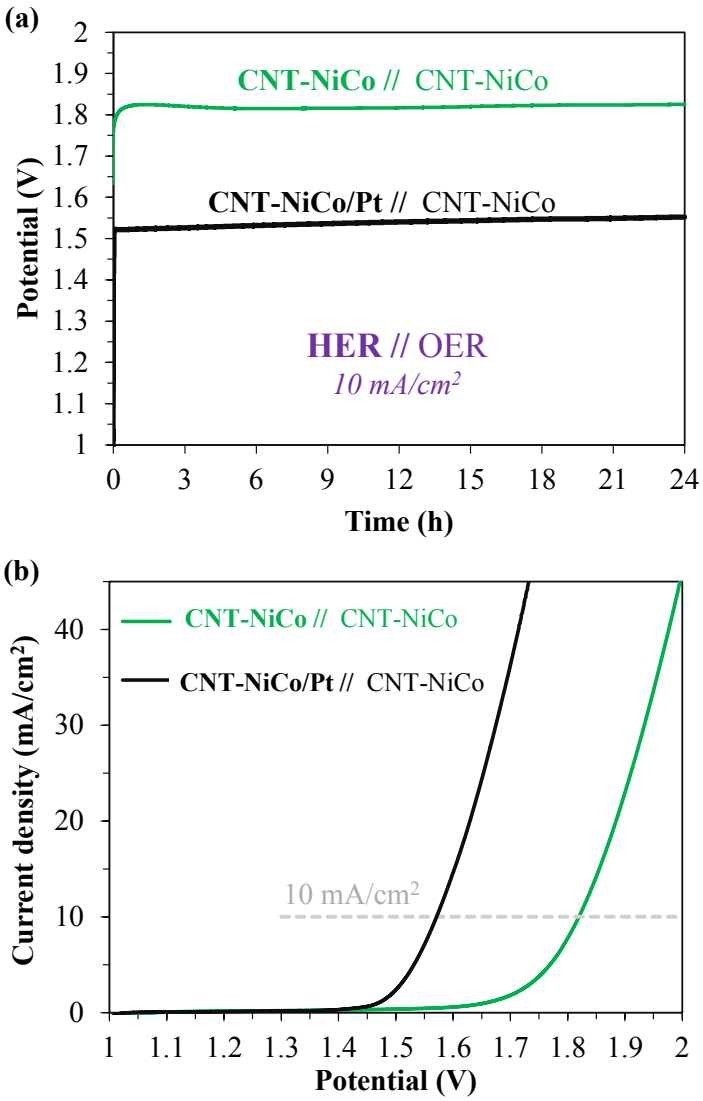

Figure 5-8. Overall water-splitting curves obtained using combinations of the hybrid deposits for OER and HER catalysis. CNT-NiCo is used as OER catalyst in both combinations (Bold font is used here to indicate HER side catalyst; regular font indicates OER side catalyst) : (a) Chronopotentiometry curves recorded for 24 hours at 10 $mA.cm^{-2}$. CNT-NiCo/Pt // CNT-NiCo combination splits water at ~1.55 V at the given current density; (b) LSV curves recorded at a scan rate of 1 $mV.s^{-1}$.

facilitate overall water splitting in a two-electrode configuration in 1 M KOH (13.6 pH). The chronopotentiometry curves obtained at 10 $mA.cm^{-2}$ for 24 h are presented in **Figure 5-8**a. The CNT-NiCo/Pt:CNT-NiCo combination is able to split water at an average of ~1.55 V over a period of 24 hours. The combined overpotential of this hybrid electrode system is ~280 mV lower than the 1.82 V required to achieve the same current density using a combination of platinum-free CNT-NiCo on SS and Ni plated mesh to catalyze OER and HER, respectively. The

LSV of the two electrode combinations shows the platinum-free system was consistently outperformed by ~250 mV at all current densities owing to the superior HER catalysis ability of the hybrid CNT-NiCo/Pt deposit. These metal hydroxides can be converted easily to corresponding oxides when heated in air. Fine tuning the $Pt/Ni(OH)_2$ or Pt/NiO interface on the CNT surface could further enhance the HER performance. It is worth noting that we utilized the noble metal here as a demonstration of the how our deposits lend themselves to further modification. The deposited metal hydroxide in these deposits could serve as precursors to other noble metal-free active forms as reported elsewhere in published literature[9, 12, 29, 65, 66] which eliminate need for noble metals completely. Using 3D stainless steel or nickel foams for OER and HER respectively instead of mesh could further boost the obtained current densities at given overpotentials.

5.4 Conclusions

By careful selection of deposition medium and substrate, we were able to produce highly electrocatalytically active, robust and durable hydrophilic metal hydroxide decorate CNT deposits. These binder-less deposits when coupled with a synergistic stainless steel mesh substrate could generate oxygen at 10 $mA.cm^{-2}$ at overpotentials as low as 245 $mA.cm^{-2}$. To

overcome the modest HER performance of the as-prepared deposits, the deposits were further subjected to a room temperature galvanic replacement method to additionally decorate them with platinum nanoparticles. These CNT/mixed metal hydroxide/Pt hybrids deposits on a nickel-plated copper mesh could produce hydrogen at 10 $mA.cm^{-2}$ at as low as ~50 mV. Our results indicate further reduction of the overpotential could be achieved with substrate optimization. The combination of the as-produced and modified electrodes can durably catalyze overall water splitting at merely 1.55 V. These highly conductive electrophoretically deposited metal hydroxide deposits could serve as efficient precursors to other application specific post-synthesis modifications.

5.5 Materials and Methods

Deposition: Multi-walled CNT (10-20 nm diameter; 5-15 μm length) were purchased from Nanostructured and Amorphous Materials Inc., Houston, TX, USA. Prior to deposition, the CNTs were acid treated using a 3:1 mixture of H_2SO_4:HNO_3 at 90 ^oC for 90 min. Typically, 60 ml of total acid was used per gram of CNT. After acid refluxing, CNTs were vacuum filtered through glass microfiber filter (Sterlitech Corporation, Kent, WA, USA) down to neutral pH with deionized (DI) water. The final product was dispersed in a small amount of water and allowed to dry at 90 ^oC overnight. Typically the process yield was around 45-50%.

For electrophoretic deposition, an ethanol:isopropanol (1:1) mixture was used as the suspension medium for the refluxed CNTs. 0.1 $mg.ml^{-1}$ CNTs were dispersed for 5 minutes using an ultrasonic probe sonicator. Then, $NiCl_2.6H_2O$ or $CoCl_2.6H_2O$ (Sigma-Aldrich, St. Louis, MO, USA) was added to the suspension and further sonicated for 10 minutes. In all cases, total salt content in the dispersion was maintained at 0.2 $mg.ml^{-1}$. For the CNT-NiCo samples, 0.1 $mg.ml^{-1}$

of the two metal salts were added to the suspension within 5 minutes of each other, with the nickel salt being introduced first.

Electrophoretic deposition was carried out on 1 cm^2 exposed projected area of 80 x 80 metal mesh immersed in 20 ml of dispersion by applying a voltage of 200 V using a high-voltage power source, high-voltage power source (Matsusada Precison, Model EJ-2R100). Stainless steel (SS) 304 and copper mesh were purchased from McMaster-Carr (Elmhurst, IL, USA). Meshes were typically cleaned sequentially in ethanol, isopropanol and water prior to use. Typically, the mesh was sandwiched between two parallel graphite foil (CeraMaterials, New York, USA) counter electrodes, separated by 7 mm on either side.

For nickel plating of the copper mesh, a nickel chloride plating bath containing 300 $g.L^{-1}$ $NiCl_2.6H_2O$ and 40 $g.L^{-1}$ boric acid was used. Nickel foil counter electrodes were used and 25 $mA.cm^{-2}$ of projected area was applied of 60s. After deposition, the mesh was thoroughly rinsed in DI water prior to further use.

Platinum decoration was done by simply immersing 1 cm^2 (projected area) of the metal mesh after CNT/$M(OH)_2$ deposition in 5 ml of $PtCl_4$ solution (0.2 mg/ml) for ~18 hours. The mesh was then gently rinsed and dried for an hour at 100 ^oC.

Material Characterization

Secondary electron images of the deposits were obtained using a Hitachi S-4800 field emission scanning electron microscope (FESEM). Transmission electron images and diffraction patterns were obtained in a Hitachi H-9500 high-resolution transmission electron microscope operated at 300 kV. Deposits were removed from the mesh by sonicating in isopropanol and drop cast on to a carbon supported copper grid for imaging.

Raman spectroscopy: A Thermo Scientific™ DXR™ Raman imaging microscope was used with a 532 nm laser excitation source. Spectra were collected at various laser power settings between 1-10 mW as mentioned in the manuscript. Spectra were averaged from 5 scans collected for 60 s each.

Thermogravimetric analysis (TGA): A TGA-51 (Shimazu Scientific Instruments) was used for thermogravimetric analysis at a rate of 10 $^{o}C.min^{-1}$ in air flow of 10 $ml.min^{-1}$ from room temperature up to 900 °C. Multiple deposits on planar substrates were manually scraped off to produce adequate quantities of sample for TGA and XRD analysis. A Bruker D-8 Advance diffractometer operating at 40 kV (Cu Kα radiation) was used to obtain X-ray diffraction data. Substrate interference was avoided by using a zero-background Si holder (MTI Corporation, Richmond, CA, USA) to avoid interference . Scans were obtained with a step size of 0.04 ^{o} at a rate of 1.8 s per step.

Electrochemical testing

For all three-electrode tests, a graphite rod was used as the counter electrode along with an Ag/AgCl reference electrode (4 M KCl). iR correction was applied automatically by the potentiostat using the current interrupt method. OER test samples were subjected to the following test protocol similar to a previous publication. Briefly, samples were first stabilized with 10 cycles between 0-0.6 V vs Ag/AgCl at 5 $mV.s^{-1}$ in oxygen purged 1 M KOH (pH 13.6). After repeatable cycles were obtained, samples were accelerated stability tested by cycling between 0.3 - 0.8 V vs Ag/AgCl electrode at 100 $mV.s^{-1}$. Cyclic voltammograms were recorded periodically at 2 $mV.s^{-1}$. After 1000 accelerated cycles, 6 h of chronopotentiometry at 10 $mA.cm^{-2}$ was performed to evaluate steady state durability. Finally, stepped chronopotentiograms were

recorded with applied current densities of 10-100 $mA.cm^{-2}$ incremented by 10 $mA.cm^{-2}$ every half hour.

HER performance of samples was evaluated using the following test protocol: All tests were performed in 1 M KOH purged with nitrogen for 20 min. The as-prepared deposits were subjected to 12 h chronopotentiometry at 10 $mA.cm^{-2}$. Thereafter, chronopotentiometry was performed at 10, 20, 30 and 40 $mA.cm^{-2}$ in 30 min increments. Finally, linear sweep voltammetry (LSV) curves were obtained at 2 $mV.\ s^{-1}$.

Two electrode overall water-splitting tests were performed using CNT-M(OH)2 deposits on steel mesh for OER side and CNT-$M(OH)_2$/Pt nickel plated copper mesh for HER side. Chronopotentiometry was performed 24 hours at 10 $mA.cm^{-2}$. LSV was then obtained at a sweep rate of 1 $mV.s^{-1}$ from 1 - 1.85 V.

For all three-electrode tests, a graphite rod was used as the counter electrode along with an Ag/AgCl reference electrode (4 M KCl). iR correction was applied automatically by the potentiostat using the current interrupt method. OER test samples were subjected to the following test protocol similar to a previous publication. Briefly, samples were first stabilized with 10 cycles between 0-0.6 V vs Ag/AgCl at 5 $mV.s^{-1}$ in oxygen purged 1 M KOH (pH 13.6). After repeatable cycles were obtained, samples were accelerated stability tested by cycling between 0.3 - 0.8 V vs Ag/AgCl electrode at 100 $mV.s^{-1}$. Cyclic voltammograms were recorded periodically at 2 $mV.s^{-1}$. After 1000 accelerated cycles, 6 h of chronopotentiometry at 10 $mA.cm^{-2}$ was performed to evaluate steady state durability. Finally, stepped chronopotentiograms were recorded with applied current densities of 10-100 $mA.cm^{-2}$ incremented by 10 $mA.cm^{-2}$ every half hour.

HER performance of samples was evaluated using the following test protocol: All tests were performed in 1 M KOH purged with nitrogen for 20 min. The as-prepared deposits were subjected to 12 h chronopotentiometry at 10 $mA.cm^{-2}$. Thereafter, chronopotentiometry was performed at 10, 20, 30 and 40 $mA.cm^{-2}$ in 30 min increments. Finally, linear sweep voltammetry (LSV) curves were obtained at 2 $mV.\ s^{-1}$.

Two electrode overall water-splitting tests were performed using CNT-$M(OH)_2$ deposits on steel mesh for OER side and CNT-$M(OH)_2$/Pt nickel plated copper mesh for HER side. Chronopotentiometry was performed 24 hours at 10 $mA.cm^{-2}$. LSV was then obtained at a sweep rate of 1 $mV.s^{-1}$ from 1 - 1.85 V.

5.6 Acknowledgments

The authors acknowledge the financial support from the National Science Foundation (NSF Awards 1439494 and 1444473). The authors also sincerely thank Dr. Hyejin Moon for her help reviewing a draft of this manuscript.

5.7 References

1. M. Wang, Z. Wang, X. Gong and Z. Guo, *Renew. Sust. Energ. Rev.*, 2014, **29**, 573-588.
2. Y. Yan, B. Y. Xia, B. Zhao and X. Wang, *J. Mater. Chem. A*, 2016, **4**, 17587-17603.
3. K. Zeng and D. Zhang, *Progr. Energy Combust. Sci.*, 2010, **36**, 307-326.
4. H. Wang, H. W. Lee, Y. Deng, Z. Lu, P. C. Hsu, Y. Liu, D. Lin and Y. Cui, *Nat. Commun.*, 2015, **6**, 7261.
5. J. Luo, J. H. Im, M. T. Mayer, M. Schreier, M. K. Nazeeruddin, N. G. Park, S. D. Tilley, H. J. Fan and M. Gratzel, *Science*, 2014, **345**, 1593-1596.
6. J. Masud, A. T. Swesi, W. P. Liyanage and M. Nath, *ACS Appl. Mater. Interfaces*, 2016, **8**, 17292-17302.
7. L. Jiao, Y.-X. Zhou and H.-L. Jiang, *Chem. Sci.*, 2016, **7**, 1690-1695.
8. N. Jiang, B. You, M. Sheng and Y. Sun, *Angew. Chem. Int. Ed.*, 2015, **54**, 6251-6254.
9. H. Jin, J. Wang, D. Su, Z. Wei, Z. Pang and Y. Wang, *J. Am. Chem. Soc.*, 2015, **137**, 2688-2694.
10. W. Zhu, X. Yue, W. Zhang, S. Yu, Y. Zhang, J. Wang and J. Wang, *Chem. Commun.*, 2016, **52**, 1486-1489.
11. Q. Zhang, Y. Wang, Y. Wang, A. M. Al-Enizi, A. A. Elzatahry and G. Zheng, *J. Mater. Chem. A*, 2016, **4**, 5713-5718.
12. M. Gong, W. Zhou, M. C. Tsai, J. Zhou, M. Guan, M. C. Lin, B. Zhang, Y. Hu, D. Y. Wang, J. Yang, S. J. Pennycook, B. J. Hwang and H. Dai, *Nat. Commun.*, 2014, **5**, 4695.
13. Y. Kuang, G. Feng, P. Li, Y. Bi, Y. Li and X. Sun, *Angew. Chem. Int. Ed.*, 2016, **55**, 693-697.
14. X. Wu, B. Yang, Z. Li, L. Lei and X. Zhang, *RSC Adv.*, 2015, **5**, 32976-32982.
15. H. Liang, A. N. Gandi, D. H. Anjum, X. Wang, U. Schwingenschlogl and H. N. Alshareef, *Nano Lett.*, 2016, **16**, 7718-7725.

16. S. Li, Y. Wang, S. Peng, L. Zhang, A. M. Al-Enizi, H. Zhang, X. Sun and G. Zheng, *Adv. Energy Mater.*, 2016, **6**, 1501661.

17. M. Gong, Y. Li, H. Wang, Y. Liang, J. Z. Wu, J. Zhou, J. Wang, T. Regier, F. Wei and H. Dai, *J. Am. Chem. Soc.*, 2013, **135**, 8452-8455.

18. X. Zhang, H. M. Xu, X. X. Li, Y. Y. Li, T. B. Yang and Y. Y. Liang, *ACS Catal.*, 2016, **6**, 580-588.

19. Y. Liang, Y. Li, H. Wang, J. Zhou, J. Wang, T. Regier and H. Dai, *Nat. Mater.*, 2011, **10**, 780-786.

20. Y. Liang, Y. Li, H. Wang and H. Dai, *J. Am. Chem. Soc.*, 2013, **135**, 2013-2036.

21. A. Indra, P. W. Menezes, N. R. Sahraie, A. Bergmann, C. Das, M. Tallarida, D. Schmeisser, P. Strasser and M. Driess, *J. Am. Chem. Soc.*, 2014, **136**, 17530-17536.

22. K. J. May, C. E. Carlton, K. A. Stoerzinger, M. Risch, J. Suntivich, Y.-L. Lee, A. Grimaud and Y. Shao-Horn, *J. Phys. Chem. Lett.*, 2012, **3**, 3264-3270.

23. D. A. Salvatore, K. E. Dettelbach, J. R. Hudkins and C. P. Berlinguette, *Sci. Adv.*, 2015, **1**, e1400215.

24. X. Lu and C. Zhao, *Nat. Commun.*, 2015, **6**, 6616.

25. A. T. Swesi, J. Masud and M. Nath, *Energy Environ. Sci.*, 2016.

26. T. T. H. Hoang and A. A. Gewirth, *ACS Catal.*, 2016, **6**, 1159-1164.

27. A. Balram, S. Santhanagopalan, B. Y. Hao, Y. K. Yap and D. D. Meng, *Adv. Funct. Mater.*, 2016, **26**, 2571-2579.

28. S. Santhanagopalan, A. Balram and D. D. Meng, *ACS Nano*, 2013, **7**, 2114-2125.

29. X. G. Liu, X. Wang, X. T. Yuan, W. J. Dong and F. Q. Huang, *J. Mater. Chem. A*, 2016, **4**, 167-172.

30. P. Subramanian, J. Niedziolka-Jonsson, A. Lesniewski, Q. Wang, M. Li, R. Boukherroub and S. Szunerits, *J. Mater. Chem. A*, 2014, **2**, 5525.

31. A. Balram, J. Jiang, M. H. Fernández and D. D. Meng, *Key Eng. Mater.*, 2015, **654**.

32. H. Zhang, X. Zhang, D. Zhang, X. Sun, H. Lin, C. Wang and Y. Ma, *J. Phys. Chem. B*, 2013, **117**, 1616-1627.

33. H. Yin, S. Zhao, K. Zhao, A. Muqsit, H. Tang, L. Chang, H. Zhao, Y. Gao and Z. Tang, *Nat. Commun.*, 2015, **6**, 6430.

34. R. Subbaraman, D. Tripkovic, D. Strmcnik, K. C. Chang, M. Uchimura, A. P. Paulikas, V. Stamenkovic and N. M. Markovic, *Science*, 2011, **334**, 1256-1260.

35. A. R. Boccaccini, S. Keim, R. Ma, Y. Li and I. Zhitomirsky, *J. R. Soc. Interface*, 2010, **7 Suppl 5**, S581-613.

36. O. O. Van der Biest and L. J. Vandeperre, *Annu. Rev. Mater. Sci.*, 1999, **29**, 327-352.

37. L. Besra and M. Liu, *Prog. Mater. Sci.*, 2007, **52**, 1-61.

38. P. Sarkar and P. S. Nicholson, *J. Am. Ceram. Soc.*, 1996, **79**, 1987-2002.

39. M. Mishra, S. Bhattacharjee, L. Besra, H. S. Sharma, T. Uchikoshi and Y. Sakka, *J. Eur. Ceram. Soc.*, 2010, **30**, 2467-2473.

40. M. A. Sayeed, T. Herd and A. P. O'Mullane, *J. Mater. Chem. A*, 2016, **4**, 991-999.

41. P. Jeevanandam, Y. Koltypin and A. Gedanken, *Nano Lett.*, 2001, **1**, 263-266.

42. L. Zhang, Q. Ding, Y. Huang, H. Gu, Y. E. Miao and T. Liu, *ACS Appl. Mater. Interfaces*, 2015, **7**, 22669-22677.

43. T. Gao and B. P. Jelle, *J. Phys. Chem. C*, 2013, **117**, 17294-17302.

44. K. Zhang, J. Wang, X. Lu, L. Li, Y. Tang and Z. Jia, *J. Phys. Chem. C*, 2009, **113**, 142-147.

45. T. Pauporté, L. Mendoza, M. Cassir, M. C. Bernard and J. Chivot, *J. Electrochem. Soc.*, 2005, **152**, C49.

46. C. Singh, S. Srivastava, M. A. Ali, T. K. Gupta, G. Sumana, A. Srivastava, R. B. Mathur and B. D. Malhotra, *Sensors and Actuators B: Chemical*, 2013, **185**, 258-264.

47. M. Marciuš, M. Ristić, M. Ivanda and S. Musić, *J. Alloys Compd.*, 2012, **541**, 238-243.

48. W. Li, L. Xin, X. Xu, Q. Liu, M. Zhang, S. Ding, M. Zhao and X. Lou, *Sci. Rep.*, 2015, **5**, 9277.

49. J. Yang, H. W. Liu, W. N. Martens and R. L. Frost, *J. Phys. Chem. C*, 2010, **114**, 111-119.

50. S. Deabate, F. Fourgeot and F. Henn, *J. Power Sources*, 2000, **87**, 125-136.

51. M. Vidotti, R. P. Salvador, E. A. Ponzio and S. I. Cordoba de Torresi, *J. Nanosci. Nanotechnol.*, 2007, **7**, 3221-3226.

52. H. B. Li, M. H. Yu, X. H. Lu, P. Liu, Y. Liang, J. Xiao, Y. X. Tong and G. W. Yang, *ACS Appl. Mater. Interfaces*, 2014, **6**, 745-749.

53. S. Klaus, Y. Cai, M. W. Louie, L. Trotochaud and A. T. Bell, *J. Phys. Chem. C*, 2015, **119**, 7243-7254.

54. H. Jin, S. Mao, G. Zhan, F. Xu, X. Bao and Y. Wang, *J. Mater. Chem. A*, 2017, **5**, 1078-1084.

55. Y. Gorlin and T. F. Jaramillo, *J. Am. Chem. Soc.*, 2010, **132**, 13612-13614.

56. Y. Tian, B. Chang, Z. Yang, B. Zhou, F. Xi and X. Dong, *RSC Adv.*, 2014, **4**, 4187-4193.

57. X. Xia, Y. Wang, A. Ruditskiy and Y. Xia, *Adv. Mater.*, 2013, **25**, 6313-6333.

58. S.-L. Yang, C.-Y. Cao, F.-F. Wei, P.-P. Huang, Y.-B. Sun and W.-G. Song, *ChemCatChem*, 2014, **6**, 1868-1872.

59. K. W. Kim, S. M. Kim, S. Choi, J. Kim and I. S. Lee, *ACS Nano*, 2012, **6**, 5122-5129.

60. A. Balouch, A. Ali Umar, E. R. Mawarnis, S. K. Md Saad, M. Mat Salleh, M. Y. Abd Rahman, I. V. Kityk and M. Oyama, *ACS Appl. Mater. Interfaces*, 2015, **7**, 7776-7785.

61. N. Mironova-Ulmane, A. Kuzmin, I. Steins, J. Grabis, I. Sildos and M. Pärs, *Journal of Physics: Conference Series*, 2007, **93**, 012039.

62. C. F. Windisch, G. J. Exarhos, K. F. Ferris, M. H. Engelhard and D. C. Stewart, *Thin Solid Films*, 2001, **398-399**, 45-52.

63. L. An, L. Huang, P. Zhou, J. Yin, H. Liu and P. Xi, *Adv. Funct. Mater.*, 2015, **25**, 6814-6822.

64. H. Xia, Y. Wan, W. Assenmacher, W. Mader, G. Yuan and L. Lu, *NPG Asia Mater.*, 2014, **6**, e126.

65. M. Ledendecker, S. Krick Calderon, C. Papp, H. P. Steinruck, M. Antonietti and M. Shalom, *Angew. Chem. Int. Ed.*, 2015, **54**, 12361-12365.

66. J. Yu, G. Cheng and W. Luo, *J. Mater. Chem. A*, 2017.

5.8 Supporting Information

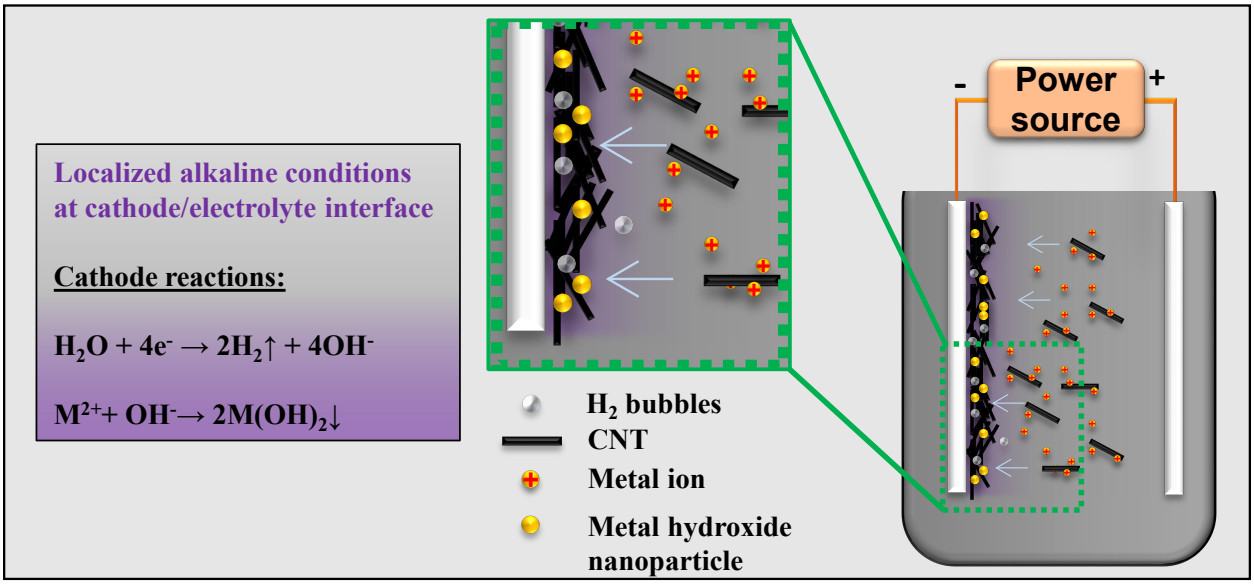

Figure S5-1. Schematic sketch of the CNT-$M(OH)_2$ nanocomposite deposition process.

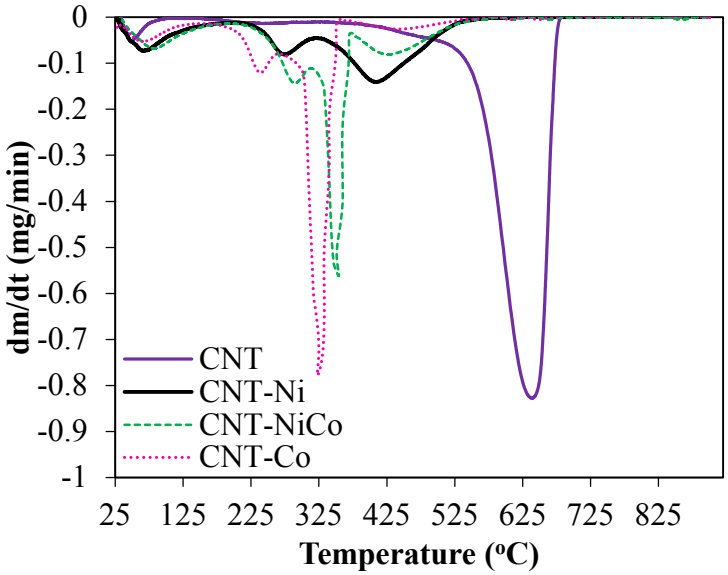

Figure S5-2. Representative differential thermogravimetry (DTG) curves of plain CNT and the three hybrid metal hydroxide decorated CNT deposits: CNT-Ni, CNT-NiCo, and CNT-Co.

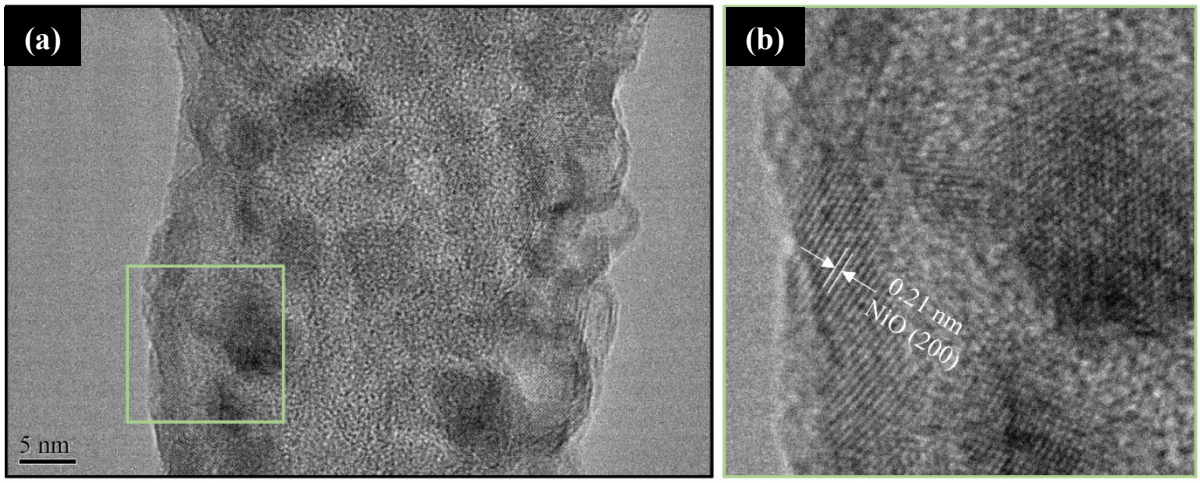

Figure S5-3. (a) HR-TEM image of $Ni(OH)_2$ nanoparticle decorated CNT after being exposed to the electron beam for a few minutes. Electron beam irradiation induced dehydration of $Ni(OH)_2$ leads to conversion to NiO. **(b)** Magnified view of selected region show lattice fringes 0.21 nm apart corresponding to (200) of NiO.

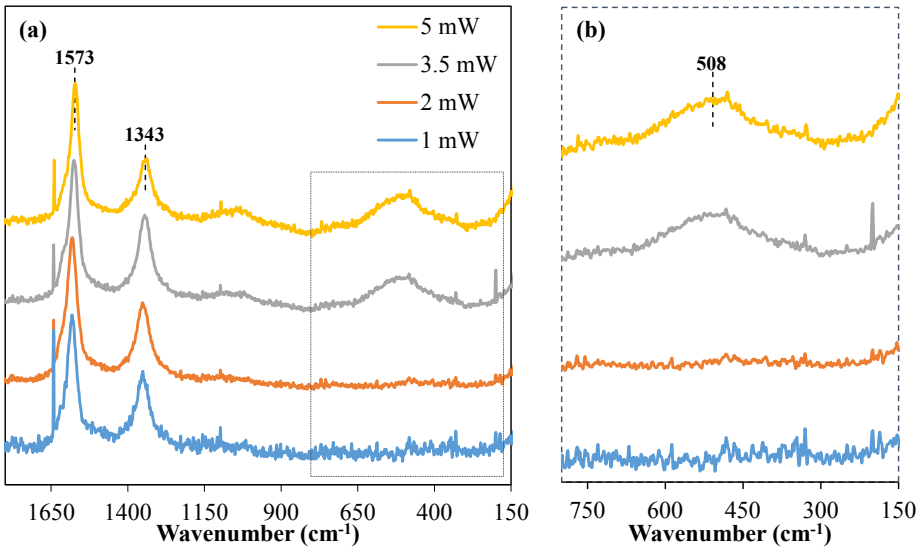

Figure S5-4. (a) Representative Raman spectra of the amorphous nickel hydroxide decorated CNT deposits obtained at laser powers of 1, 2, 3.5, and 5 mW. Increasing laser power eventually leads to heating induced conversion to of the $Ni(OH)_2$ to NiO (b) Magnified view of the low wavenumber region shows NiO band around 508 cm^{-1}.

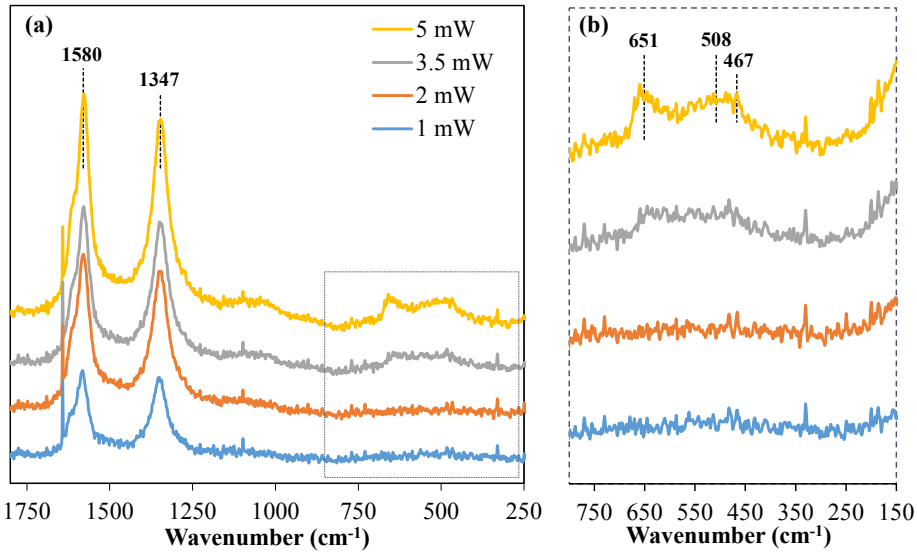

Figure S5-5. (a) Representative Raman spectra of the amorphous nickel-cobalt hydroxide decorated CNT deposits obtained at laser powers of 1, 2, 3.5, and 5 mW. Increasing laser power eventually leads to heating induced conversion to from the metal hydroxide to the corresponding oxide phase; **(b)** Magnified view of the low wavenumber region shows nickel-cobalt oxide related bands around 467, 508, and 651 cm^{-1}.

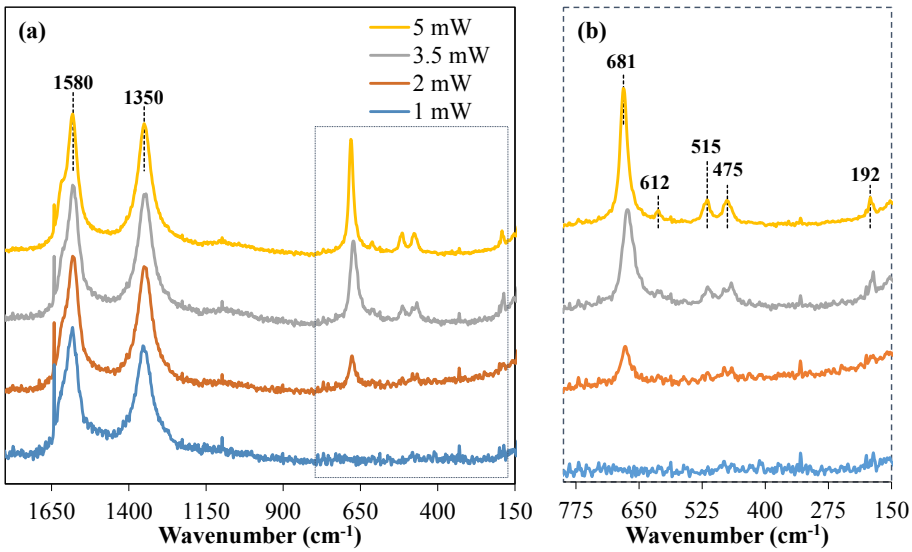

Figure S5-6. (a) Representative Raman spectra of the amorphous cobalt hydroxide decorated CNT deposits obtained at laser powers of 1, 2, 3.5, and 5 mW. Increasing laser power eventually leads to heating induced conversion to from the metal hydroxide to the corresponding oxide phase; **(b)** Magnified view of the low wavenumber region shows Co_3O_4 related bands around 192, 475,515, 612, and 681 cm^{-1}.

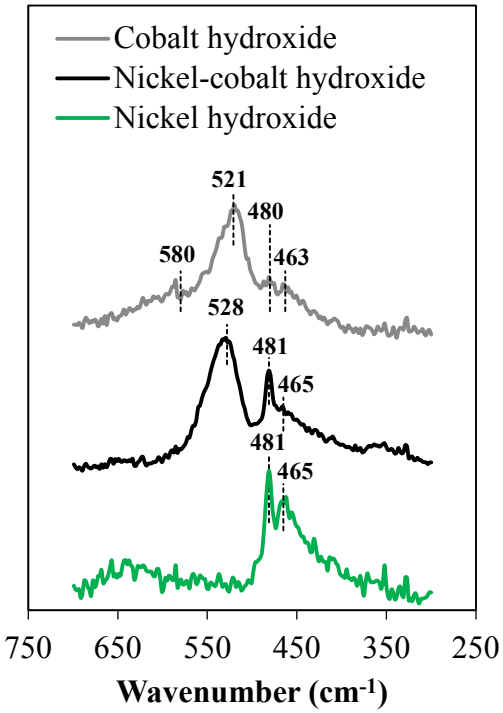

Figure S5-7. Representative Raman spectra of the pure metal hydroxide deposits obtained via deposition from deposition electrolyte containing only dissolved metal salts (No CNT present). Pure nickel hydroxide shows peak at 465 cm^{-1} and 481 cm^{-1}. $Co(OH)_2$ shows features at 463, 480, 521, and 580 cm^{-1}. The mixed metal hydroxide shows distinct peaks at 465, 481 and 528 cm^{-1}.

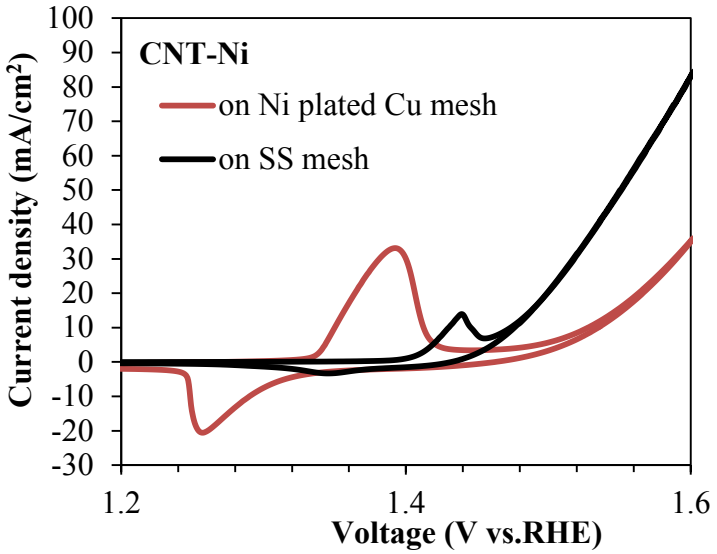

Figure S5-8. Cyclic voltammograms showing OER performance of CNT-Ni deposits on stainless steel and Ni substrates. Electrolyte:1 M KOH; Scan rate 2 $mV.s^{-1}$.

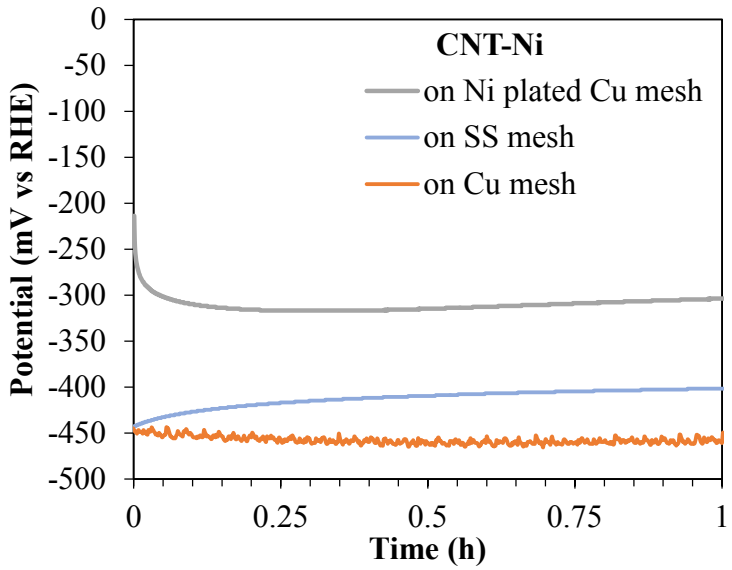

Figure S5-9. Effect of substrate on HER performance of the deposits on stainless steel (SS) mesh, copper mesh and nickel plated copper mesh substrates: Chronopotentiometry curves recorded at 10 mA.cm^{-2} in 1M KOH.

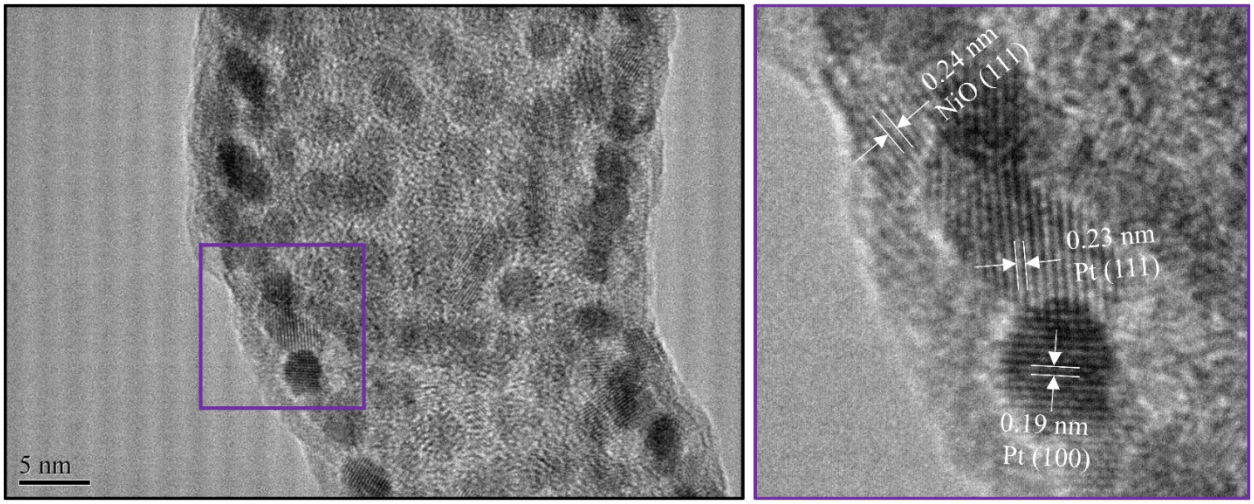

Figure S5-10. (a) HR-TEM image of CNT-Ni/Pt after a few minutes of electron beam exposure. Electron beam irradiation induces conversion of $Ni(OH)_2$ to NiO and amorphous Pt nanoparticles to crystalline. **(b)** Magnified view of selected region show lattice finges spaced at 0.24, 0.23, and 0.19 nm corresponding to NiO (111), Pt(111) and Pt (100) respectively.

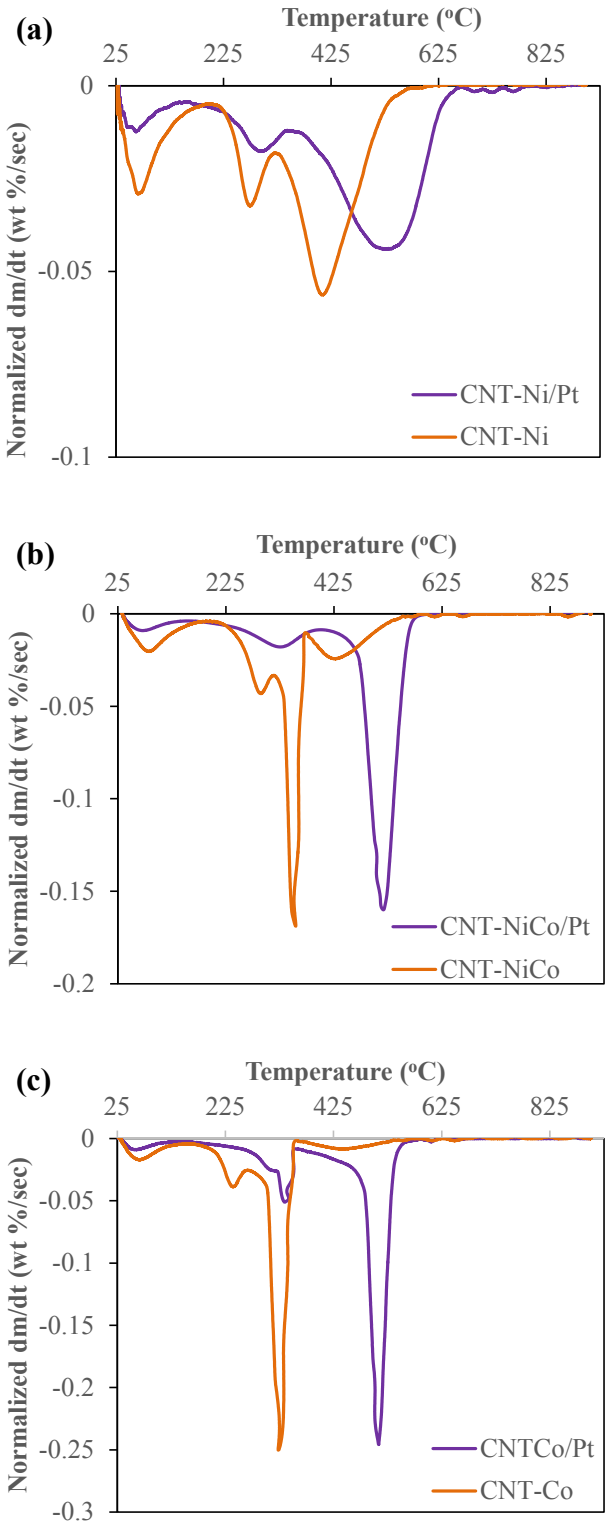

Figure S5-11. DTG curves of (a) CNT-Ni and CNT-Ni/Pt; (b) CNT-NiCo and CNT-NiCo/Pt; (c) CNT-Co and CNT-Co/Pt.

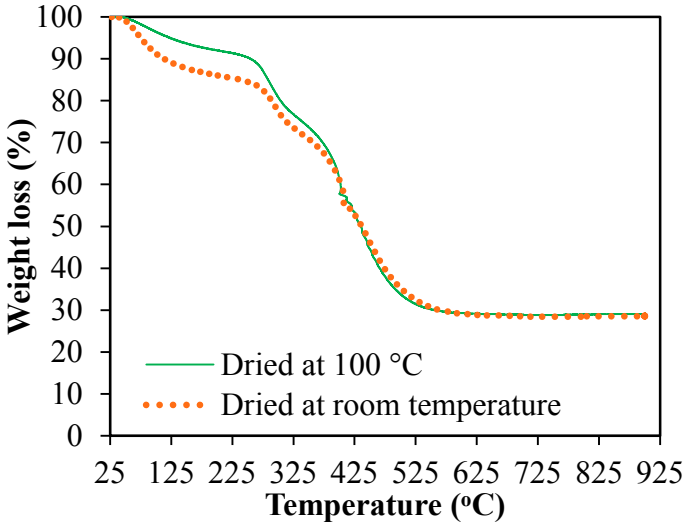

Figure S5-12. TGA curves of CNT-Ni control samples dried at room temperature and 100 ^{o}C after overnight immersion in DI water. The curves indicate the difference in intercalated water content is a function of the drying temperature. The drying process does not appear to have any effect on the delay in onset of CNT decomposition.

CHAPTER 6

SCALABLE FABRICATION OF VERTICALLY ALIGNED NANOMATERIAL COATED HIERARCHICAL STRUCTURES VIA SELF-WOUND NICKEL NANOMEMBRANES

6.1 Introduction

Self-wound nanomembranes based on rolled-up nanotechnology[1] with multilayer, ultrathin materials have been reported as a promising approach in several applications such as supercapacitor,[2] lithium ion batteries,[1] sensors[3] etc. In electrochemical applications where significant volumetric changes can occur during phase transformation, the released energy due to rolling usually lends more stability to the structure.[4] Importantly, it allows for decreasing footprint area as compared to a planar situation.[4-5] Typically, demonstrations of such self-wound membranes have relied on microfabrication processes such as evaporation and sputtering have to deposit ultrathin films onto a sacrificial material. Significant internal stresses arise within the thin films due to factors such as lattice mismatch between substrate and deposited film.[5-6] Upon etching of the underlying sacrificial layer, in a bid to minimize the intrinsic stress, the released nano-membranes spontaneously roll up forming compact structures. A simple, scalable inexpensive method to produce such rolled nanomembranes would be especially beneficial for several electrochemical applications. It is proposed that electrodeposition could be effectively employed in order to produce self-wound metal rolls by controlling the stresses in the deposited metal thin films.

Electrodeposition, as mentioned previously, offers great versatility in terms of the kinds of materials (metals, metal hydroxides, metal phosphides etc.) that can be deposited in a relatively rapid and facile manner. Further, electrodeposition allows for morphological control of deposited materials.[7-10] Electroplating, specifically, has now been a well understood and popular industrial scale fabrication process to deposit pure metal coatings for several decades.[11] Given our motivation towards high surface area hierarchical structures geared toward electrochemical applications, electroplating a conductive layer to form the backbone of our desired rolled-up structure is the

most viable scalable technique. One of the challenges lies in the fact that typically electroplaters have strived to obtain deposits with minimal stress to maximize deposit life and performance.[12] Hence, typically a heavy emphasis has generally been laid on stress mitigating strategies via bath composition and plating conditions optimization. Our unique situation dictates that we maximize the amount of stress achieved within the electroplated film to enable stress-induced spontaneous rolling with minimum possible diameter, upon release. Electroplating offers a variety of control parameters such as pH, temperature of the plating bath, impurities, current density, bath composition etc. that can influence the properties such as intrinsic stress of a deposit.[11] Thus, it can be safely assumed that manipulation of these factors could yield sufficient stress gradients within the deposits to facilitate spontaneous rolling upon release from the substrate. In addition, when ultrathin films are deposited on dissimilar substrates, the lattice mismatch in the case of epitaxial films, different thermal expansion coefficients between the deposit and the underlying substrate, dislocations, voids and other factors can contribute significantly film stress.[6, 13]

While micro/nanoscale hierarchical nanostructures are excellent in terms of providing increased surface area, broadly speaking, the overall active area available for electrochemical applications still remains limited when grown or deposited on 2D planar substrates. To be able to further exploit the properties of hierarchical nanomaterial deposits, introducing another level of hierarchy is critical to maximize the areal electrochemical performance. This has motivated several researchers to utilized high surface area metal foams, most popularly made of nickel, as the substrate for nanomaterial deposition. Another strategy was attempted here to convert originally 2D planar substrates to 3D surfaces amenable to subsequent nanomaterial deposition. As conceived, the idea was to first deposit the desired hierarchical nanostructures on planar substrate coated with a

metallic thin film. Thereafter, the thin films could be released from the substrate along with the attached nanomaterials and assembled in some sort of 3D configuration.

If these films could be rolled up into a more compact form and then assembled vertically aligned, the nanomaterial loading per footprint area could be greatly increased. Several challenges exist with regard to this approach. However, if fully realized, such an approach could greatly improve utilization. While the metal film and nanomaterial deposition in and of themselves are not challenging, the subsequent release, roll up, and assembly require effort. It is critical for the nanomaterial to not affect the roll up characteristics of the underlying metal film. The nanomaterial must be compatible with the etchant utilized to release the underlying metal film. If a mask needs to be used to protect the nanomaterial coating, it too needs to survive the etching, the assembly process, be easily removable in a manner compatible with the deposited nanomaterial coating while not having a negative effect on the metal film rolling process.

6.2 Results and Discussion

The scalability of every stage of the fabrication was the driving motivation behind the design of this process. First, eliminating the need for the use of a mask (generally lithographically defined) to obtain films of appropriate dimensions would greatly minimizes processing time and effort.

Nickel and copper plating are extremely well understood and widely utilized industrial scale processes and are extremely amenable to scalable fabrication.[11] Interestingly, the spontaneous rolling up of nickel electrodeposits was reported even as early as 1909 by Stoney.[14] As mentioned earlier, to truly maximize the increase of areal density with the self-would rolls, it is critical to align them vertically on a substrate. Besides the ubiquity of nickel electroplating and scalability, the rationale for selection of nickel as the conductive self-wound backbone of the structure was

driven by the aim to eventually assemble the nanomaterial coated roll in a vertically aligned configuration in the final electrode structure. Magnetophoretic assembly[15-16] offers a facile technique to collect self-would rolls to the deposition electrode. Alignment of nickel nanowires by magnetic field has been reported recently.[16] When exposed to the magnetic field produced by a strong neodymium magnet, it was found that the self-wound Ni rolls aligned themselves along their length in direction of the field. The magnetic field would further serves to align the rolls parallel to the magnetic field i.e. vertically aligned on the deposition electrode.

Now, based on the selection of nickel, the sacrificial layer would have to be one that could be selectively etched while nickel would remain unaffected in the etching solution. Copper plating[11] is relatively simple and several possible formulations of liquid etchants with selectivity of copper over nickel already exist. The nickel nanomembranes can be easily released by wet chemical etching of the underlying copper sacrificial layer. Methods like supercritical drying and further handling for electrode assembly would add unnecessary complexity to the process. In order to avoid stiction[17] induced collapse of the released structures, all processing needed to occur in liquid. In order to etch the sacrificial layer, a selective etchant (acetic acid : hydrogen peroxide : water :: 1:1:18) was selected.[18] Unlike ammoniacal copper etchants, this etchant does not saturate rapidly and allows for highly controlled and reproducible etching. The etching process takes around 10-15 minutes to completely release the rolls. Upon release the rolls must be carefully collected and rinsed several times in water until neutral pH is reached. Again, it is critical to make sure the rolls always remain in liquid so as to avoid collapse of the rolls due to surface tension effects. Figure 1 b, c, d show images of various stages of the etch/release process.

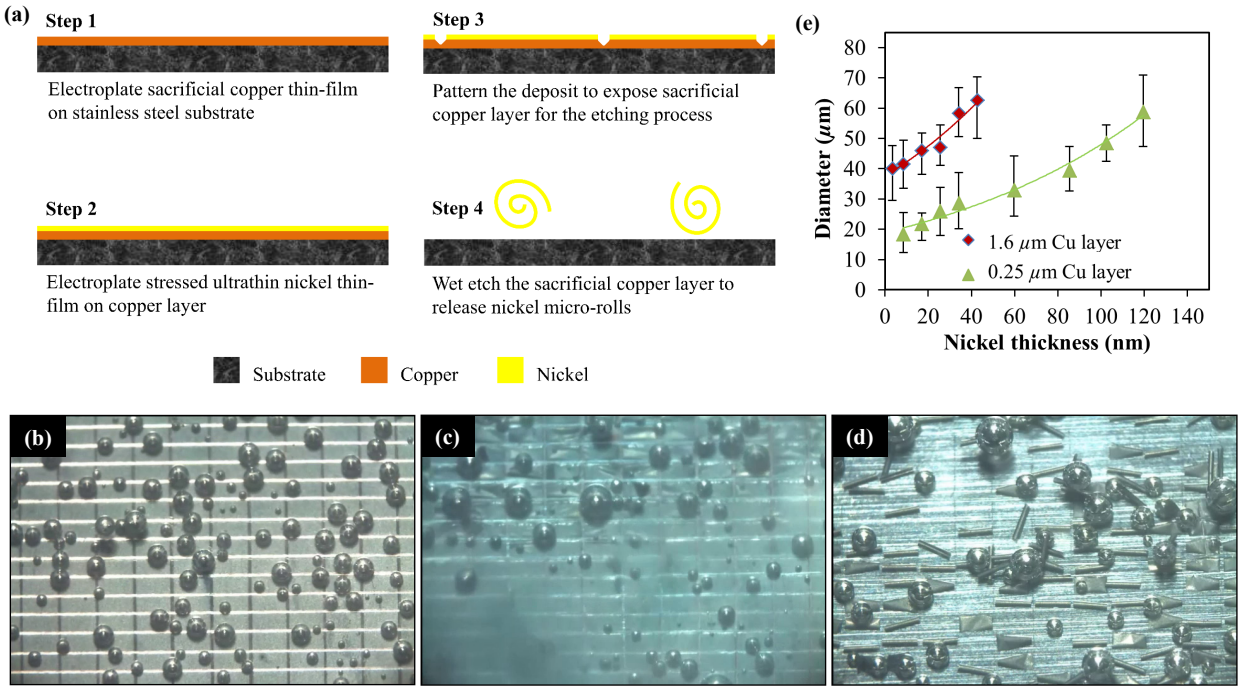

Figure 1. (a) Process flow diagram for self-wound nickel micro-roll fabrication utilizing scalable techniques; Representative optical microscope images of various stages of the etch/release process; (b) Influence of sacrificial Cu layer thickness on self-wound nickel roll diameter; (c) Optical micrographs of patterned substrate introduced into etchant, (the bubbles are a result of the etching process), (d) Intermediate stage of etch/release process: ripples can be seen to appear in the nickel thin films as etching proceeds. The blue hue of the image is a result of the increased concentration of dissolved copper ions (e) Completely released self-wound nickel rolls can be seen as copper layer is completely etched. Rolls seen here are ~500 μm long

.

The influence of the electroplating parameters to optimize the current density and the film thickness to minimize rolling diameter of the nickel rolls were first established. Considering roll diameter to be an indicator of residual stress, it was determined that current densities of above 100

mA cm^{-2} did not yield significant roll diameter reduction (Figure S6-1). Crucially, other than the bath composition, plating current density, and nickel layer thickness the critical factor for roll diameter reduction was determined to be the sacrificial layer thickness (**Figure 1e**). A potentiostat was utilized to apply precise and accurately timed and current densities during electroplating. One of the most salient features of the developed processes is the rapid processing times involved in

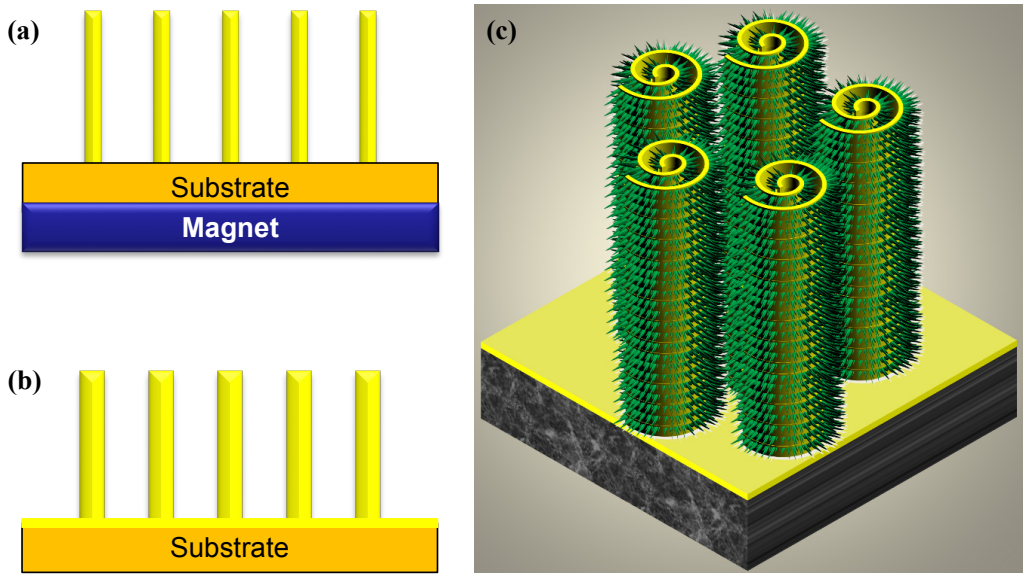

Figure 2 Schematic representation of self-wound nickel micro-roll assembly: (a) Nickel micro-rolls will be magnetophoretically assembled onto copper substrate. Rolls spontaneously align vertically to the substrate in response to the magnetic field; (b) A nickel holding layer is then electroplated over the nickel rolls to permanently fix them in vertical orientation even after removal of magnetic field. Additionally, the holding layer thickens the walls of the rolls, reinforcing them against stiction when dried (c) Schematic of intended final hierarchical structure consisting of vertically aligned nickel micro-rolls coated with hierarchical nanomaterial. Hierarchical nanomaterials can be grown on the nickel backbone using scalable electric field-directed deposition processes such as electrophoretic deposition and electrodeposition.

the deposition stages. Based on the studies performed, the copper plating step (@33 mA cm^{-2}) lasting typically between 10-30 sec and nickel plating duration (@ 100 mA cm^{-2}) determined to be 250 ms was determined to be optimal. At 10s or lower copper deposition time, film release was very difficult, if not impossible without significant damage to their structure. To summarize, with the use of chloride bath and post deposition xurography based patterning, we were able to consistently obtain high aspect ratio self-wound nickel nanomembranes in ambient conditions with relatively inexpensive equipment and no requirement of a clean room environment or microfabrication techniques. This is a significant advantage making it viable for high throughput processing.

The influence of the nickel chloride content in the plating bath on the process was also briefly studied. It is known that the chloride concentration in plating baths significantly affects deposit stress.[19] Typical chloride baths operate with nickel chloride content within the range of 225-300 g L^{-1}.[11, 19] This is primarily to minimize the high stresses induced by the presence of chloride, the effects of which are catastrophic in typical plating applications. To maximize the residual stresses, the use of higher nickel chloride contents well beyond the standard operating range was explored. Specifically, the behavior of the deposits with baths containing 300, 450 and 600 g L^{-1} nickel chloride were studied. Firstly, the 600 g L^{-1} $NiCl_2$ plating bath was highly viscous and corrosive. Further, the deposits were too highly stressed to adhere to the substrate upon deposition. The deposits were seen to peel in several locations even before being removed from the plating bath (Figure S6-2). Further deposition of nanomaterials was unviable on such deposits given the spontaneous damage due to peeling during and after the plating. This was however a positive indication of stress levels being increased when chloride content increased. When using a 450 g L^{-1} $NiCl_2$ bath, rolling was reliably achieved upon release with no spontaneous rolling/peeling as in

the case of 600 g L^{-1} baths. However, since no major reduction in roll diameter was observed when using 450 g L^{-1} bath, the 300 g L^{-1} $NiCl_2$ bath was chosen for subsequent use to minimize waste and avoid other potential issues when using solutions with high chloride concentrations.

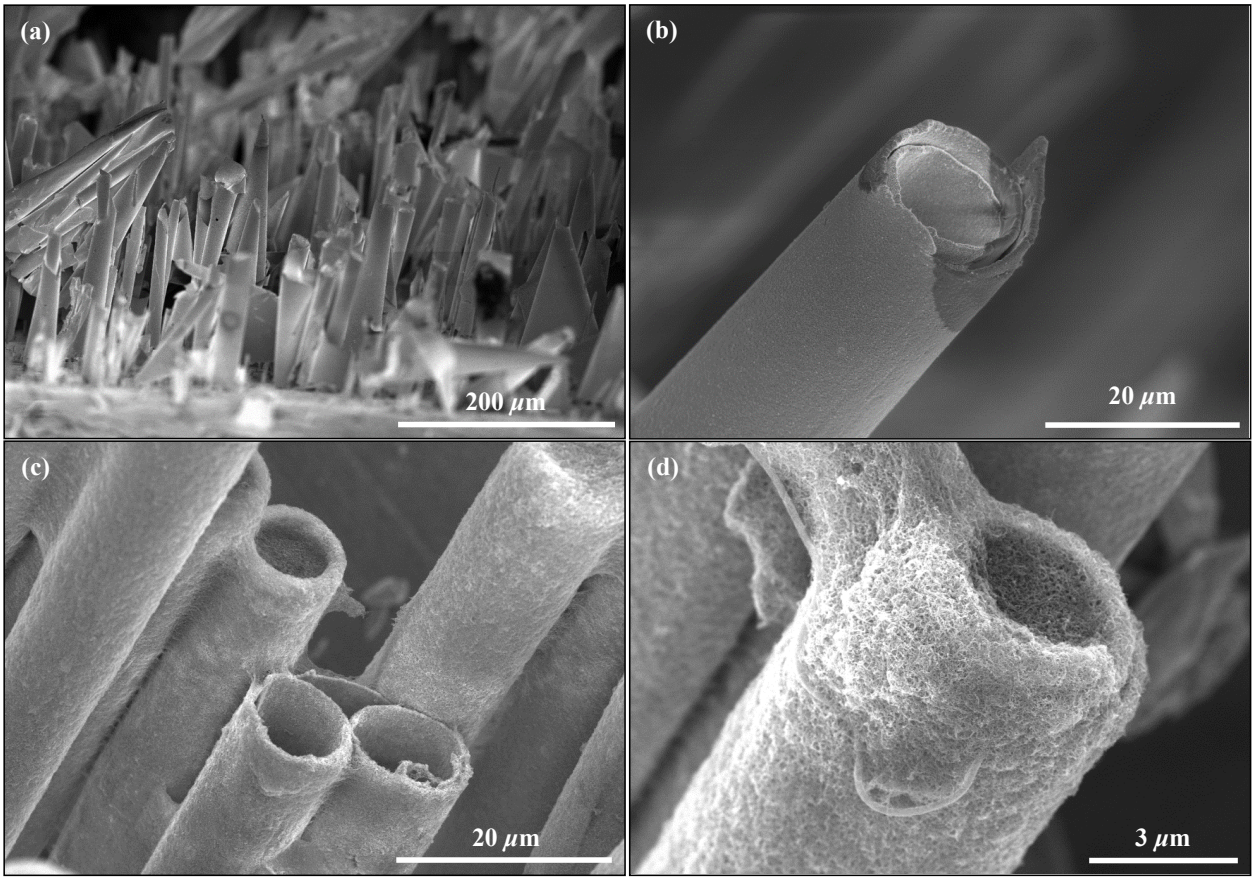

Figure 3. (a) Micrograph of a self-wound nickel micro-roll after magnet induced vertical alignment and nickel holding layer deposition; (b) Magnified view of an individual nickel micro-roll after nickel holding layer deposition. The holding layer deposition process reinforces the walls of the roll, preventing stiction related collapsing when dried; (c) Nickel micro-roll coated with electrophoretically deposited CNT; (d) Magnified view of CNT coated nickel micro-roll.

For the final stage of the process, although it was initially intended to deposit nanomaterial onto the nickel film prior to release and rolling, significant hurdles were faced on account of incompatibility between nanomaterial and etchant. Additionally, it was impossible to avoid the

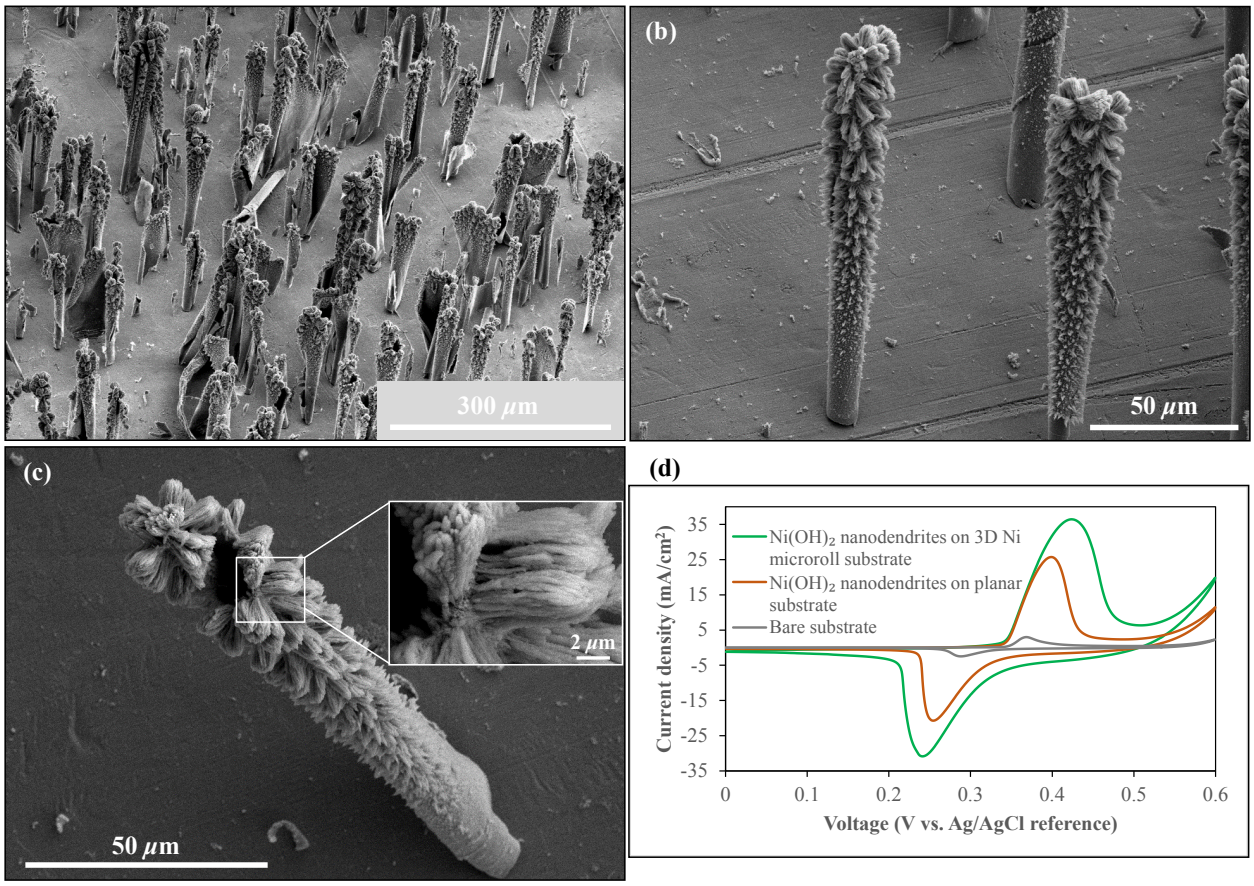

Figure 4 (a, b) Micrograph of a 3D, vertically aligned nickel micro-roll substrates after growth of $Ni(OH)_2$ nanodendrite forests on the roll surface. Nanodendrites were grown using the electrodeposition method developed during this project; (c) Magnified view of an individual nickel micro-roll deposited with $Ni(OH)_2$ nanodendrite; (inset) the hierarchical dendritic structure of the deposits; (d) Comparison of cyclic voltammograms of $Ni(OH)_2$ nanodendrite decorated 3D nickel micro-roll substrate and planar substrate. The 3D $Ni(OH)_2$ shows superior performance due to the larger available surface area.

over deposition of nanomaterial layer by the holding layer during final assembly of the electrode. Attempts to mask the nanomaterial with a non-conductive polystyrene layer for protection during etchant exposure and final electroplating step were largely unsuccessful. Coatings sufficiently thick to achieve both tasks were generally too thick to allow for any rolling of the nickel. Briefly, upon etching, the released self-wound nickel micro-rolls were magnetophoretically assembled and aligned vertically to a copper substrate using a neodymium magnet. The decision was made to first assemble electrodes with vertically aligned uncoated nickel rolls with subsequent coating of hierarchical nanomaterials being applied by the field-directed nanomaterial assembly techniques developed thus far (Figure 2). These rolls were then fixed in place by an electroplated layer of nickel. The wall thickness of nickel rolls typically increased from ~20 nm to 1 μm making them strong enough to overcome stiction effects upon drying (Figure 3 a, b).

The 3D vertically aligned nickel micro-roll based substrate could then be subjected to electrodeposition or EPD for nanomaterial deposition. This type of unique 3D hierarchical structure should be able to offer high surface area electrode structures for several electrochemical applications with excellent electrolyte penetration within the structure, intimate contact between nanomaterial and substrate and consequently minimized path lengths for ion diffusion and electron transport. Figure 3c, 3d show images of the final hierarchical structures produced after electrophoretic deposition of a layer of CNT/$Ni(OH)_2$. Figure 4 shows FESEM images and electrochemical characterization of a hierarchical nickel micro-roll based substrate with the previously demonstrated electrodeposited H_2 bubble templated $Ni(OH)_2$ nanodendrites grown on them using electrodeposition. As expected, the 3D substrate developed outperforms deposits on a planar substrate owing to the salient features of the structure. Further improvements to performance can be achieved by strategies such as increasing the packing density of the rolls on

the substrate, increasing the length of the rolls, increasing the nanomaterial loading. This work seeks to be a foundation for further refining and optimization of the overall fabrication process to prepare such electrode structures.

Finally, in order to further illustrate the versatility of all the processes explored in this work, CNT/$Ni(OH)_2$ as well as MnO_2 nanorods were also deposited on the aligned nickel structures using EPD. The unique structure of the substrate should allow for increased nanomaterial loading without as much of the typical increase in internal resistance accompanying thicker deposits on

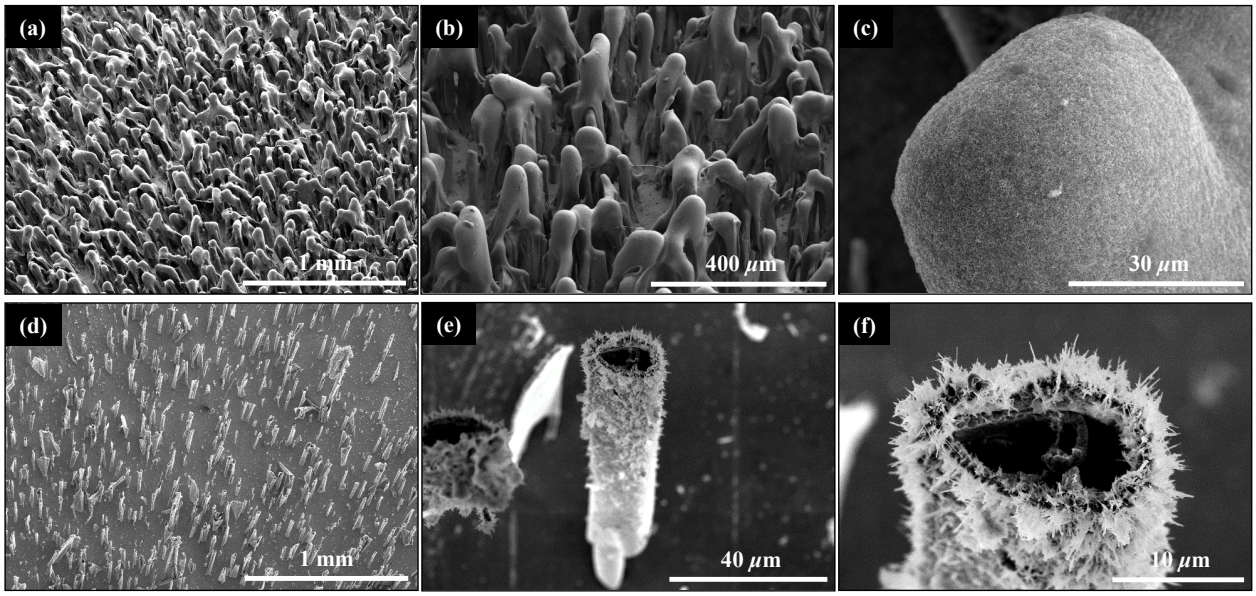

Figure 5. (a, b, c) 3D nickel micro-roll substrate with a very thick coating of electrophoretically deposited CNT. The CNTs are further decorated by $Ni(OH)_2$ nanoparticles as seen in Figure 8c; (d, e, f) 3D nickel micro-roll substrate coated with vertically aligned α-MnO_2 nanorods deposited via HVEPD at various magnifications .

planar substrates because of the presence of the nickel backbone. Figure 5 a-c shows one such scenario with a nickel micro-roll based substrate heavily overcoated with a thick CNT/$Ni(OH)_2$

electrophoretic deposit. Figure 5d-e show α-MnO_2 nanorods[20] vertically aligned to the nickel micro-roll surface. This alignment is relatively simple given the manner in which the field lines distribute around the rolled structures during the HVEPD process. This demonstrates the versatility of the field based deposition processes, developed during this project, allowing for orientation control of a wide variety of nanomaterials during assembly/deposition. Most importantly, every aspect of the process developed here should lend itself to scalable and rapid fabrication with no need for complex instrumentation or any cumbersome microfabrication techniques.

6.3 Conclusions

A highly facile and scalable fabrication process to produce genuinely 3D hierarchical electrodes for electrochemical applications has been developed. The influence of the deposition parameters such as bath composition, plating current density, sacrificial layer thickness, nickel layer thickness etc. on the final roll diameter of the nickel micro-rolls was studied. The thickness of the sacrificial Cu layer on the stainless steel substrate was critical to minimizing roll diameter. The process is rapid with the deposition time of the nickel nanomembranes lasting merely 250 ms. Furthermore, we have completely eliminated to need for the use of a mask to obtain patterned films. Significantly, micro-rolls as small as 10-20 μm diameter, 250+ μm long were consistently obtained within a few minutes upon selective etch/release in a simple acetic acid/hydrogen peroxide based etchant. Since the entire process occurs in ambient conditions, this is a major advantage over the traditionally used microfabrication techniques making high throughput processing feasible. Thus, by combining the various scalable processes such as electroplating with HVEPD and electrodeposition to fabricate electrodes with unique 3D architecture across several length scales as originally envisioned.

6.4 Methods and Materials

Electrodeposition: All chemicals were purchased from Sigma-Aldrich. To ensure adhesion of the copper to the stainless steel, it was first pretreated with a nickel Wood's strike at 100 mA cm^{-2} for 2 min.[11] The bath composition was as follows: $NiCl_2.6H_2O$-240 g L^{-1}, HCl-125 ml L^{-1}. The copper plating solution was formulated as follows: $CuSO_4$- 200 g L^{-1}, H_2SO_4 5 g L^{-1}, Rochelle's salt 0.5 g L^{-1}. The all-chloride nickel plating bath contained- $NiCl_2.6H_2O$ 300-600 g L^{-1} and boric acid- 38 g L^{-1}. All plating was carried out at room temperature with no external agitation in a plastic container with electrodes spaced at ~7 cm. Nanomaterial coating with CNT and $Ni(OH)_2$ was carried out as described in previous chapters and α-MnO_2 was prepared and deposited as described by Santhanagopalan et. al.[20]

A potentiostat (Gamry Reference 3000) was used to accurately apply 250 ms pulse (@100 mA cm^{-2}) for the deposition step critical to obtain the strained ultrathin nickel layer. Other plating requiring less precision was carried out using a Techtronix PWS2721 power source. The Ni deposits were patterned using a commercial craft cutter (Silhouette Cameo) by replacing the traditional cutter blade with a commercially available engraving tip. Etching was performed in a 1:1:18 solution of H_2O_2: acetic acid: water. A diamond scribe coupled with the craft cutter could also be used to pattern the nickel deposit into appropriately sized sections before introducing into the etchant. Stainless steel 304 substrates, copper foil and nickel sheets, neodymium magnets were all purchased from McMaster-Carr, IL.

Electrode assembly: First, a magnet was used first to agglomerate the released nanomembranes within the etching solution. Then, the rolls were moved to a water bath from the etchant using a micropipette. The 'washed' rolls were transferred to a nickel plating bath, a 2.5 cm x 2.5 cm plastic container (Ted Pella). A copper substrate was placed at the bottom of the container for deposition

of the rolls. A neodymium magnet was placed below the deposition substrate to facilitate aggregation of the vertically aligned rolls on it. A nickel layer, a few microns thick, was then deposited at 25 mA cm^{-2} for a minute in order to hold the rolls in place and also reinforce the structures to prevent surface tension induced collapse upon removal from the plating bath and subsequent drying. The choice of using nickel as the holding layer was made keeping in mind the electrochemical applications where nickel is typically used. Electrochemical testing (cyclic voltammetry) was performed using a Gamry Reference 3000 potentiostat using a three electrode configuration electrochemical test setup. 1 M KOH was used as the electrolyte and an Ag/AgCl reference electrode was used. A graphite rod was counter electrode in all three cases.

6.5 Acknowledgements

I gratefully acknowledge Dr. Dennis Meng's guidance through a large portion of the conception of this work. Funding from NSF award 1439494 is also acknowledged.

6.6 References

1. Deng, J.; Yan, C.; Yang, L.; Baunack, S.; Oswald, S.; Wendrock, H.; Mei, Y.; Schmidt, O. G. Sandwich-Stacked SnO_2/Cu Hybrid Nanosheets as Multichannel Anodes for Lithium Ion Batteries. *ACS Nano* **2013,** *7*, 6948-54.
2. Ji, H.; Mei, Y.; Schmidt, O. G. Swiss Roll Nanomembranes with Controlled Proton Diffusion as Redox Micro-Supercapacitors. *Chemical Communications* **2010,** *46*, 3881-3.
3. Zhang, J.; Zhong, J.; Fang, Y. F.; Wang, J.; Huang, G. S.; Cui, X. G.; Mei, Y. F. Roll up Polymer/Oxide/Polymer Nanomembranes as a Hybrid Optical Microcavity for Humidity Sensing. *Nanoscale* **2014,** *6*, 13646-50.
4. Deng, J.; Lu, X.; Liu, L.; Zhang, L.; Schmidt, O. G. Introducing Rolled-up Nanotechnology for Advanced Energy Storage Devices. *Advanced Energy Materials* **2016,** *6*, 1600797.
5. Wang, X.; Chen, Y.; Schmidt, O. G.; Yan, C. Engineered Nanomembranes for Smart Energy Storage Devices. *Chem Soc Rev* **2016,** *45*, 1308-30.
6. Kim, S.-H.; Woo, Y.; Boyd, J. G. The Effect of Electrodeposition Process Parameters on Residual Stress-Induced Self-Assembly under External Load. *Journal of Micromechanics and Microengineering* **2014,** *24*, 115014.
7. Lu, X.; Zhao, C. Electrodeposition of Hierarchically Structured Three-Dimensional Nickel-Iron Electrodes for Efficient Oxygen Evolution at High Current Densities. *Nature Communications* **2015,** *6*, 6616.
8. Li, Y.; Zhang, H.; Xu, T.; Lu, Z.; Wu, X.; Wan, P.; Sun, X.; Jiang, L. Under-Water Superaerophobic Pine-Shaped Pt Nanoarray Electrode for Ultrahigh-Performance Hydrogen Evolution. *Advanced Functional Materials* **2015,** *25*, 1737-1744.
9. Hoang, T. T. H.; Gewirth, A. A. High Activity Oxygen Evolution Reaction Catalysts from Additive-Controlled Electrodeposited Ni and NiFe Films. *Acs Catal* **2016,** *6*, 1159-1164.
10. Masud, J.; Swesi, A. T.; Liyanage, W. P.; Nath, M. Cobalt Selenide Nanostructures: An Efficient Bifunctional Catalyst with High Current Density at Low Coverage. *ACS Applied Materials & Interfaces* **2016,** *8*, 17292-302.
11. Electrochemical, S. *Modern Electroplating / Edited by Frederick A. Lowenheim*. Wiley: New York [N.Y.], **1974**.
12. Dini, J. The Materials Science of Coatings and Substrates. *Metal Finishing* **1998,** *50*, 47.

13. Murray, C. E.; Ryan, E. T.; Besser, P. R.; Witt, C.; Jordan-Sweet, J. L.; Toney, M. F. Evolution of Stress Gradients in Cu Films and Features Induced by Capping Layers. *Microelectronic Engineering* **2012,** *92*, 95-100.

14. Stoney, G. G. The Tension of Metallic Films Deposited by Electrolysis. *Proceedings of the Royal Society of London. Series A, Containing Papers of a Mathematical and Physical Character* **1909,** *82*, 172-175.

15. Lim, J.; Yeap, S. P.; Leow, C. H.; Toh, P. Y.; Low, S. C. Magnetophoresis of Iron Oxide Nanoparticles at Low Field Gradient: The Role of Shape Anisotropy. *J Colloid Interface Sci* **2014,** *421*, 170-7.

16. Wright, A. C.; Faulkner, M. Magnetophoretic Assembly and Printing of Nanowires. *Journal of Vacuum Science & Technology B, Nanotechnology and Microelectronics: Materials, Processing, Measurement, and Phenomena* **2012,** *30*, 021603.

17. Witvrouw, A.; Tilmans, H. A. C.; De Wolf, I. Materials Issues in the Processing, the Operation and the Reliability of MEMS. *Microelectronic Engineering* **2004,** *76*, 245-257.

18. Arya, R.; Rashid, M. M.; Howard, D.; Collins, S. D.; Smith, R. L. Thermally Actuated, Bistable, Oxide/Silicon/Metal Membranes. *Journal of Micromechanics and Microengineering* **2006,** *16*, 40-47.

19. Rose, I.; Whittington, C. Nickel Plating Handbook. **2014**.

20. Santhanagopalan, S.; Balram, A.; Meng, D. D. Scalable High-Power Redox Capacitors with Aligned Nanoforests of Crystalline MnO_2 Nanorods by High Voltage Electrophoretic Deposition. *ACS Nano* **2013,** *7*, 2114-25.

6.7 Supporting Information

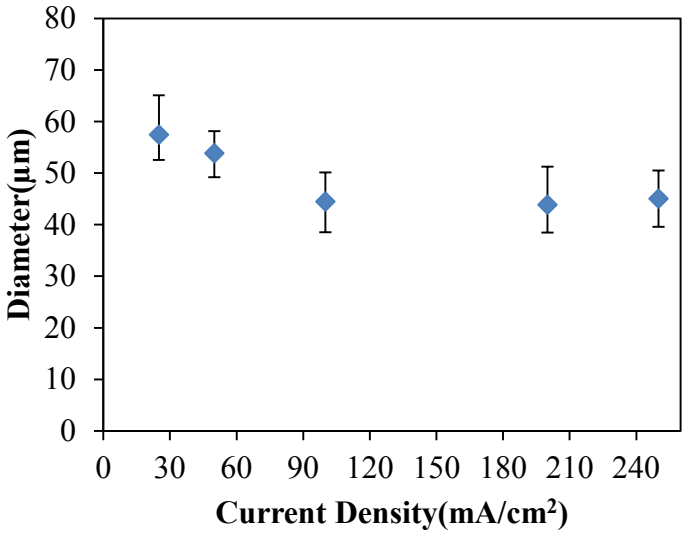

Figure S6-1 Influence of nickel plating current density on nickel roll diameter. All deposits performed on ~1.6 μm thick copper sacrificial layer.

Figure S6-2 Spontaneous peeling and failure of nickel deposited from high chloride (600 g L^{-1}) plating bath.

CHAPTER 7

CONCLUSIONS

In summation, several studies employing field-directed assembly/deposition techniques were developed and demonstrated. Material and electrode performance was extensively characterized. The following list briefly summarizes the several conclusions from the previous chapters:

1) By utilizing low nanomaterial and metal salt concentrations in a purely isopropanol-based deposition solution, the wettability of CNT deposits could be controlled by the deposition voltages being utilized. Metal decorated CNT deposits with wettability ranging from hydrophilic all the way up to superhydrophobic could be prepared by manipulating amount of material being deposited and the micro/nanostructure of the overall deposit. Owing to adsorbed hydrophobic groups and the induced hierarchical deposit structure, wettability could be controlled without further need for any hydrophobic polymer additives. By using a combination of xurography-based patterning in conjunction with either isopropanol or water based EPD of CNTs, surfaces with patterned extreme wettability could be prepared in a facile two-step process.
2) For better electrochemical performance in gas evolving reactions, in this case oxygen evolution during water-splitting, novel 3D hierarchical vertically aligned mixed metal hydroxide nanodendrite forests were prepared. By avoiding the typically used aqueous electrolyte, this unprecedented unique morphology could be engendered by a H_2 bubble templated method in an alcohol-based deposition medium with limited water content and field-directed diffusion limited growth mechanism. Owing to the hierarchical micro/nanostructure, the superhydrophilic deposits exhibited superaerophobicity when under water. The bubble repellence, amorphous crystal structure of the individual nanodendrites, synergistic steel substrate/deposit interactions, intimate binder-free and individual contact of the nanodendrites with the substrate produced highly active OER

catalyst deposits with overpotentials (@ 10 mA cm^{-2}) as low as 255 mV on planar substrates.

3) Having observed the positive influence of the stainless steel on the OER catalytic activity of the $Ni(OH)_2$ deposits, an EPD based single-step co-deposition method was used to deposit SS nanoparticles onto 3D nickel foam substrates, while simultaneously decorating the SSNP in situ with $Ni(OH)_2$ nanoparticles. Owing to Fe doping of the $Ni(OH)_2$ either during deposition or during actual electrode operation in electrolysis, ultralow overpotentials were required to generate oxygen in 1 and 10 M KOH from the robust binder-free deposits. Merely 220 and 250 mV were required to sustain 10 and 125 mA cm^{-2} respectively. A higher current density of 500 mA cm^{-2} could also be robustly maintained at only 450 mV (*i*R- uncorrected) overpotential in 10 M KOH.
4) By combining insights of synergistic substrate and/or support interactions with the active material, adaptable CNT/metal hydroxide deposits were produced for overall water splitting. Nickel-cobalt hydroxide decorated CNTs when deposited on SS mesh could produce 10 mA cm^{-2} of oxygen at an overpotential of 245 mV. The key feature of these deposits was their adaptability. By depositing the same material on nickel mesh and subjecting them to a galvanic replacement process in platinum chloride solution, hybrid CNT/nickel-cobalt hydroxide/Pt deposits requiring only 50 mV overpotential to generate hydrogen @ 10 mA cm^{-2} could be produced. These electrodes could split water at that current density with an applied potential of 1.55 V. These adaptable CNT/$M(OH)_2$ deposits could potentially be used for similar post-deposition modification processes to convert them into HER active forms devoid of any noble metal, making them even more commercially viable for wide-spread use.

5) By using magnetophoretic assembly of self-wound strain engineered nickel nanomembranes along with various other scalable field directed assembly techniques, truly 3D hierarchical structures could be produced containing components ranging from 100s of microns to a few nanometers in dimension. The study demonstrates the versatility of field-directed methods in terms of building functional hierarchical structures by growing micro/nanostructures in-situ or assembling nanomaterials produced via more convenient ex-situ means or a combination of both.

Various materials such as CNTs, stainless steel nanoparticles, MnO_2 nanorods, metals, mixed metal hydroxides etc. were deposited successfully. The unique hierarchical structures produced had extreme wetting properties in some cases. The hierarchical structuring also led to excellent electrochemical performance of the deposits owing to the large surface area characterized by the short diffusion length for reactive species as well as rapid charge transport due to intimate electrode/deposit contact. Several areas of interest worthy of further exploration have emerged in the course of this work.

Most notably, the interaction between the steel substrate and our metal hydroxide deposits. Although the idea of Fe doping during deposition or operation seems viable, more insight into the actual process, actual active phases during OER, incorporated iron content etc. would help elucidate the enhanced performance and help produce more active catalysts making water-splitting more viable commercially on a large scale. Finally, the 3D hierarchical structures nanomaterial coated self-wound nickel roll deposits produced showed a scalable fabrication technique of production and assembly. However, due to incompatibility between etchant and deposited metal oxide/hydroxide active material deposits, the nanomaterial deposition was limited to post-magnetophoretic assembly of the bare rolls. Due to the field-directed nature of the subsequent

nanomaterial deposition and mass transport limitations, there tends to be an underutilization of Ni roll area. Ideally, future work would be able to produce masks that can resist the etchant, thus protecting the nanomaterials. The mask would need to be thin enough so as to cover the nanomaterial, protect it from the etchant itself as well as the rigors of the etching process, and subsequent assembly. Just as important is that the mask has minimal effect on the self-winding characteristics of the rolls. Finally, the masking material should be able to be removed post-assembly via a simple technique that is compatible with the active nanomaterial deposit beneath.

The work in this dissertation aimed to present a case for use of field-directed techniques as a viable means to produce functional deposits for next generation electrochemical devices.

APPENDIX A

NICKEL-COBALT DOUBLE HYDROXIDE DECORATED CARBON NANOTUBES VIA AQUEOUS ELECTROPHORETIC DEPOSITION TOWARDS CATALYTIC GLUCOSE DETECTION

Balram, A.; Jiang, J. C.; Hernández Fernández, M.; Meng, D. D. Nickel-Cobalt Double Hydroxide Decorated Carbon Nanotubes Via Aqueous Electrophoretic Deposition Towards Catalytic Glucose Detection. *Key Engineering Materials* 2015, 654, 70-75

A.1 Abstract

In this work, we present a facile technique based on electrophoretic deposition (EPD) to produce transition metal hydroxide decorated carbon nanotubes (CNT) for electrochemical applications. We specifically explore the performance of nickel-cobalt hydroxides given their high activity, conductivity and stability as compared to the individual hydroxides. We exploit the high local pH at the negative electrodes during water-based EPD to form nanoparticles of nickel-cobalt hydroxides in situ on the CNT surface. We focus our work here on obtaining functional and conductive deposits on CNTs. The hydrophilic binderless deposits of Ni-Co double hydroxide decorated CNTs obtained here are used for non-enzymatic glucose detection. XPS data and electrochemical testing reveal difference in the deposited double hydroxide based on chronology of charging salt addition even at the same ratio. When cobalt and nickel salts are sequentially added at a ratio of 1:1, the deposited double hydroxides show excellent glucose sensitivity of ~3300μA/mM.cm^2 at applied potential of 0.55V vs. Ag/AgCl reference electrode.

A.2 Introduction

Reliable and sensitive glucose sensing is of great value in health and industrial applications. While the traditional glucose oxidase based enzymatic sensors are widely used, their instability and interfering species have led to the interest in non-enzymatic sensors that show greater stability and sensitivity. Transition metal based hydroxides and oxides have been primarily studied on account of their low cost, high stability and good electrochemical activity for catalytic oxidation of glucose[2-4]. For example, both $Ni(OH)_2$ and $Co(OH)_2$ have received a lot of attention for various electrochemical applications ranging from batteries, supercapacitors, to sensors. However, sensors based on transition metal oxides and hydroxides are typically limited by their poor conductivity which undermines their electrochemical performance. Additionally, the use of binders such as Nafion during the pasting or drop-casting methods could further block electrochemically active sites, hampering the performance further. The poor conductivity of oxides and hydroxides can usually be alleviated by either growing them electrochemically or hydrothermally on the surface of conductive materials. It has also been established that both the conductivity and electrochemical activity can be improved by employing double hydroxides or oxides [5]. However, there have not been many reports on a suitable fabrication approach to combine the two efforts for synergistic effects.

Electrophoretic deposition (EPD)[6] has been used recently by a few groups to produce high performance nano carbon-$Ni(OH)_2$ electrodes[7, 8], which demonstrated the superiority of EPD over some alternative electrode preparation techniques. These well-adhered deposits can be produced in a single-step process under mild conditions, completely eliminating the need for non-contributing binders. In this work, we employ EPD to form CNT deposits decorated by nickel-cobalt hydroxides as highly sensitive electrodes for non-enzymatic glucose detection. Both

nickel and cobalt are earth-abundant and low-cost transition metals. We utilize ions of nickel and cobalt to charge carbon nanotubes so that they can be stabilized in the dispersion and deposited by an applied electric field. The precipitation of adsorbed metal ions on the CNT surface under conditions of high local pH at the cathode surface leads to metal hydroxide decorated CNT deposits [9]. Such an approach is proposed to co-deposit double hydroxide of nickel and cobalt in a highly conductive CNT network to take advantage of their synergistic effects for high-performance electrochemical sensors. At the same time, a key of the study is on process control, such as tuning of the double hydroxide composition/property and obtaining desirable wettability.

A.3 Results and Discussion

In this work, we attempt to move beyond the use of metal salts as mere charging agents during EPD and attempt to use their products after EPD as the active material towards glucose detection. As outlined in other sections, acid-refluxed CNTs were dispersed in water before addition of nickel and/or cobalt charging salts to the solution. The deprotonation of the functional groups on the treated CNT surface in aqueous media has been known to render a net negative charge to CNTs in aqueous dispersion. Metal ions introduced to this solution are thus adsorbed onto the CNTs, rendering them net positive charges. Under the influence of the applied voltage, the positively charged CNTs move towards and eventually get deposited onto the negatively charged electrode. Given the voltages applied, the hydrogen evolution at the negative electrode gives rise to a highly alkaline condition at the electrode interface. This leads to the conversion of the charging metal ions to their corresponding hydroxides. The deposited hydroxide as produced tends to show poor crystallinity.

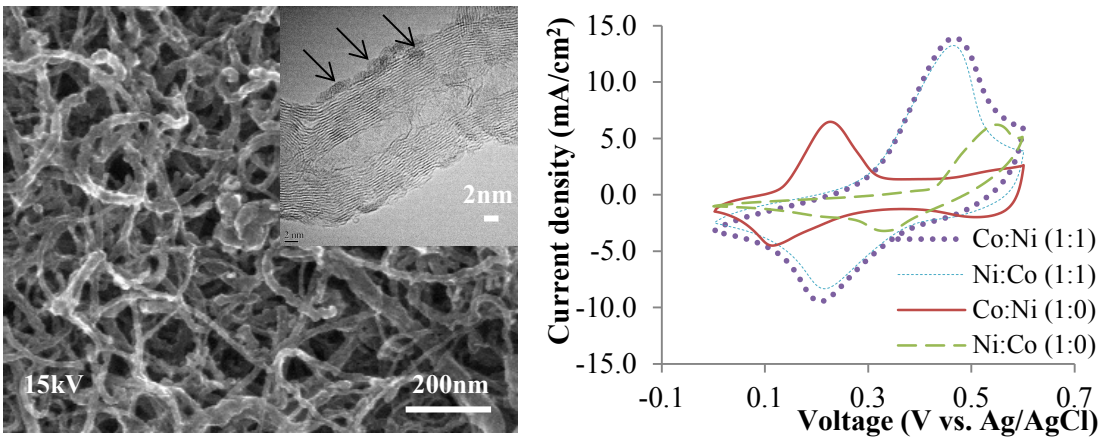

Fig. 1 (a)Representative FE-SEM image of CNT-metal hydroxide deposit; (inset) HR-TEM image of Co:Ni(1:1) sample showing nanoparticle decoration of CNT ; (b)Cyclic voltammograms of the various deposits in 0.1M NaOH at a scan rate of 50mV/s.

Fig. 1a shows a FE-SEM image and HRTEM image (inset) of a sample produced with cobalt salt added first and then nickel salt (at a ratio of 1:1) represented as Co:Ni (1:1). It must be noted that all deposits showed similar porous nature and the nanoparticles or precipitates were successfully attached to the CNT. The CNT-$Co(OH)_2$ samples, however, tended to show precipitates in the form of thin sheets within the CNT matrix that could be studied further. The high surface energy of the hydroxide and acid treated CNTs in combination with its porosity makes these deposits especially hydrophilic. This is critical for adequate utilization of available active material as compared to the use of binders which tend to not only physically block active sites, but also reduce electrolyte penetration due to their hydrophobic nature, in most cases.

The redox behavior of the samples is often a good indicator of performance. Basic comparisons of the electrochemical activity, therefore, were made using cyclic voltammetry between the voltage window of 0-0.6V against a Ag/AgCl counter electrode. Fig. 1b shows the comparison between the

various samples that were tested for their electrochemical behavior in 0.1M NaOH solution after 50 cycles at 50mV/s. All samples show well defined and distinct redox peaks indicating the electrochemical activity of the co-deposited hydroxides. The deposits produced with the combination of the nickel and cobalt salts show a single pair of peaks indicating the formation of a single mixed nickel-cobalt hydroxide. They show far superior electrochemical activity as opposed to the pure CNT-nickel (or cobalt) hydroxide samples. The better performance of the Co:Ni sample can be attributed to the differences in composition as shown by the XPS results in Fig.2.

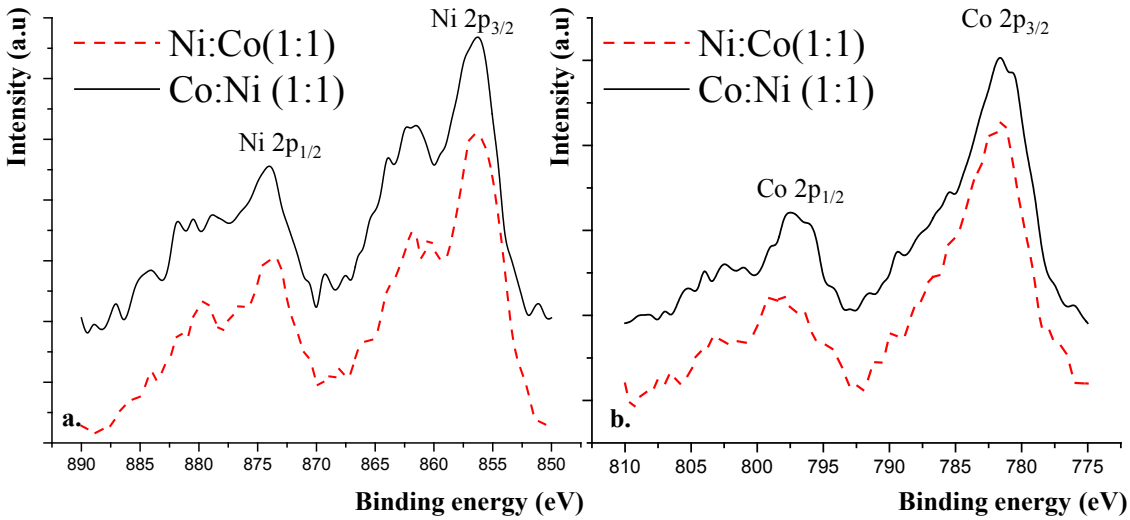

Fig. 2 XPS of (a) Ni 2p (b) Co 2p of Co:Ni (1:1) and Ni:Co(1:1) samples.

XPS analysis of the Co:Ni(1:1) and Ni:Co(1:1) samples show a clear difference in composition of the hydroxides depending on the chronology of the charging salt addition. The data was calibrated to the common low energy C peak at 285eV. Fig.2a shows the two Ni 2p peaks [7] separated by 17.7eV corresponding to nickel in $Ni(OH)_2$ centered around 856 for Ni $2p_{3/2}$ and 874eV for Ni $2p_{1/2}$ for the Co:Ni(1:1) sample. Binding energy values are observed of around 856 and 873.5eV in the case of Ni:Co(1:1). Correspondingly, in the case of XPS peak Co2p [10, 11] of

Ni:Co(1:1) shows Co $2p_{3/2}$ and Co $2p_{1/2}$ peaks shift from around 781.5eV and 798eV to 781eV and 797eV respectively in the Co:Ni(1:1) sample implying a decrease in the Co^{3+}/Co^{2+} ratio when the cobalt salt is added first[12]. The peak separation decreases from 16.5 to 16eV as seen in Fig. 2b in the Ni:Co(1:1) and Co:Ni(1:1) cases respectively. Based on the XPS data, the chronology of charging salt addition into the solution is believed to influence the valence of nickel and cobalt ions in the corresponding hydroxides. Several factors may influence this such as the time of contact between specific ions and CNTs, electrostatic interactions between oxygen containing functional groups, the availability of functional groups for adsorption. The mechanism involved in this phenomenon requires further exploration.

Fig.3a shows the cyclic voltammograms of the Co:Ni (1:1) deposit over the first 50 cycles. The redox potentials can be seen to move to less positive values over the first few cycles and eventually stabilize whereas the peak current shows slight increase with every scan. This shows the enhancement of activity with electrochemical cycling indicating the excellent stability and activity of the deposit. This enhancement of activity was shown by all our samples. Although additional cycling could potentially further improve the performance, all the glucose detection tests are performed right after 50 cycles as the standard stabilization procedure. Fig.3b shows the influence of scan rate on the peak current and redox potential. The inset of Fig.3b shows the linear trend of peak current i_p versus the square root of the scan rate establishing that the reaction is diffusion controlled.

Glucose detection tests were run by using chronoamperometry to study the influence of the current upon addition of various concentrations of glucose periodically. Fig.4a shows

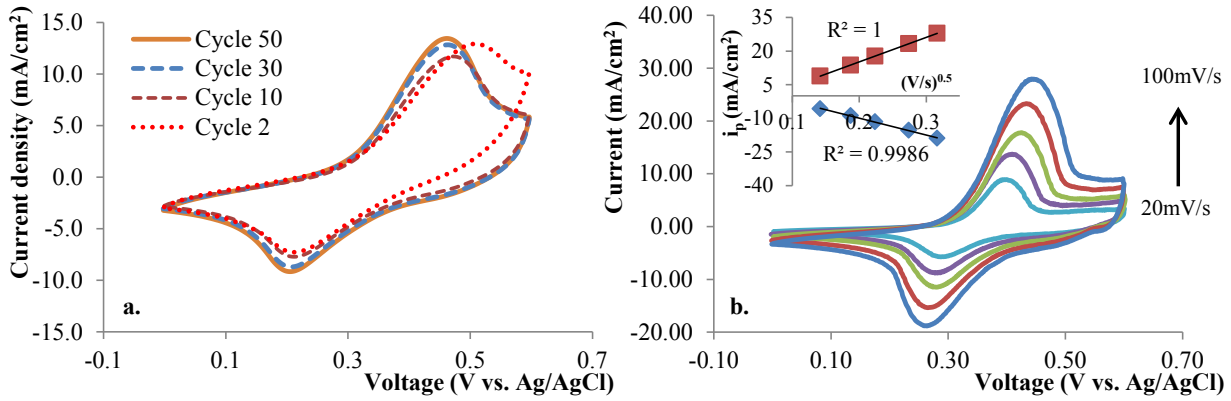

Fig. 3 (a) Selected cyclic voltammograms from the first 50 cycles of Co:Ni (1:1) sample in NaOH showing the enhancement of current with cycling; (b) Cyclic voltammograms of the sample obtained at various scan rates, inset shows linear behavior of i_p vs. Square root of scan rate indicating diffusion controlled process.

chronoamperometric curves of various samples obtained at an applied potential of 0.55V. All samples show the characteristic stepwise increase of current. Glucose sensor measurements were typically begun after allowing about 150s for the sensor to achieve a stable background current. The sensitivity of the CNT-$Co(OH)_2$ is the lowest among the samples being compared while the Co:Ni (1:1) sample is consistently better than the Ni:Co (1:1) sample, showing the highest sensitivity.

Fig.4b shows the calibration curves obtained from chronoamperometric data of the Co:Ni (1:1) deposits under the applied voltages of 0.5 and 0.55V. While up to 1.5mM of glucose, there is a sensitivity difference of ~120μA/mM·cm^2 between the performance at 0.5V and 0.55V, it is clearly seen that higher sensitivity is obtained at 0.55V. Inset in Fig.4b shows the calibration curve in the linear range between 0.1-1.5mM at 0.5 and 0.55V. At 0.55V, the Co:Ni sample shows an excellent sensitivity of ~3300 μA/mM·cm^2 up to a concentration of 1.5mM. A relatively lower sensitivity of

~1900 μA/mM·cm^2 is obtained for a second linear range between 1.5mM and 5.5mM which is quite high compared to values seen in literature for typical $Ni(OH)_2$-based glucose sensors [2].

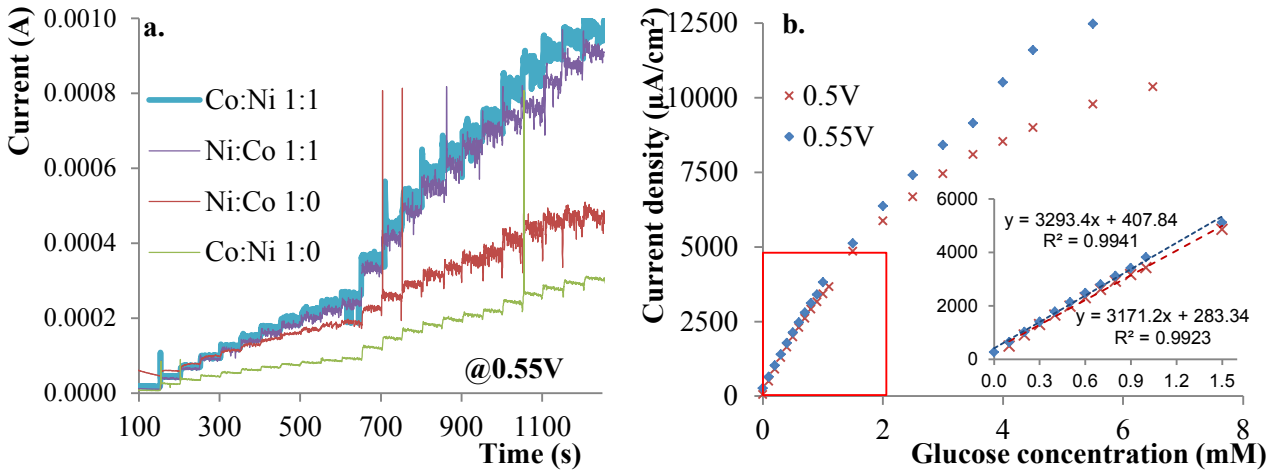

Fig. 4 (a) Comparative chronoamperometric curves of various samples, performed at an applied voltage of 0.55V vs. Ag/AgCl reference. Between 100-650s, 0.1mM was added every 50s , thereafter 0.5mM glucose was added at every step; (b) Calibration curves for Co:Ni (1:1) sample. Inset shows the boxed region showing linear between 0.1-1.5mM glucose concentration.

A.4 Conclusions

EPD was carried out in aqueous medium in order to produce nickel-cobalt double hydroxide decorated CNT deposits. The double hydroxides made with 1:1 ratio of cobalt and nickel charging salts show highest sensitivity for non-enzymatic glucose detection. The order of addition of charging salt to the dispersion has been seen to influence the properties of the deposits and their performance. The best performance was achieved by the sample in which cobalt salt was introduced first into the dispersion after which nickel salt was added at a 1:1 ratio. At 0.55V, the sensor showed an excellent sensitivity of ~3300 μA/mM·cm^2 in the linear glucose concentration range of 0.1-1.5mM. The proposed EPD-based deposition method is thus proved effective to

obtain nanostructured electrodes with high electrochemical activities under mild conditions, paving the way for its adoption in both sensing and other applications.

A.5 Methods and Materials

Preparation of deposits: Multiwalled CNTs (Nanoamor, Houston, TX,USA) were acid refluxed at 90^{o}C using 1:3 ratio of HNO_3 and H_2SO_4 for 90 minutes, vacuum filtered through glass fiber filters (Sterlitech, Kent, WA,USA) to a neutral pH and dried thereafter in an oven at 80^{o}C overnight. The refluxed CNTs (0.5mg/ml) were dispersed in deionized water using a probe sonicator along with various salt concentrations of $NiCl_2{\cdot}6H_20$ and $CoCl_2{\cdot}6H_20$. The total salt concentration was always maintained at 0.25mg/ml. Since the atomic mass of cobalt (58.93) and nickel (58.63) are very similar, the same total weight concentration of the salts can be taken as the same total molar concentration of them. The metal salt solutions were either added to the CNT dispersion 10 minutes apart from the addition of the other. The deposits were named based on the order in which the charging salts were introduced to the CNT dispersion with the numbers appearing after representing the ratio of the salts in the dispersion. For clarity, Ni:Co (1:1) represents a sample made with $NiCl_2$ solution(0.125mg/ml) added first to the CNT dispersion, 10 minutes after which $CoCl_2$ solution(0.125mg/ml) was added. Depositions were performed at 15V/cm for 30s on gold coated silicon wafer and stainless steel electrodes (for material characterization) or glassy carbon electrode (for electrochemical testing) and a stainless steel SS316 counter electrode. After deposition, the electrodes were transferred to a vacuum oven preheated at 90^{o}C and dried under house vacuum for 3hours. All chemicals used were acquired from Sigma-Aldrich (St.Louis, MO, USA).

Material Characterization: Material deposited on SS316 electrodes were used for Field emission scanning electron microscopy (FE-SEM) visualization. Secondary electron images of deposits were obtained using a Hitachi S-4800 FE-SEM at an accelerating voltage of 15kV. High-resolution transmission electron microscope (HRTEM) images were taken in a Hitachi H-9500 electron microscope (300 keV). X-ray photoelectron spectroscopy (XPS)data was obtained with a Perkin-Elmer ESCA/SAM Phi 560 system using an Al Kα excitation source with a step size of 0.5eV. Gold sputtered silicon substrates were used for the XPS samples.

Electrochemical testing: All electrochemical measurements were performed using a Gamry Reference 3000 (Gamry Instruments, Warminster, PA, USA) potentiostat. All electrochemical testing was done in fresh 0.1M NaOH using a standard three electrode configuration. Deposits were made directly onto the glassy carbon working electrode (3mm diameter) and dried as previously mentioned. The glassy carbon electrode was thoroughly polished with 0.5µm alumina slurry, washed with DI water and sonicated in DI water before every fresh deposit. An Ag/AgCl reference electrode (Pine Research Instrumentation, Durham, NC, USA) with 4M KCl was used along with a graphite counter electrode. Cyclic voltammetry (CV) was performed between 0-0.6V vs. Ag/AgCl reference electrode. All tests were carried out after cycling the deposits for 50 cycles. CV was carried out at different scan rates from 20,35,50, 75, and100mV/s. Chronoamperometric testing was done at applied voltages as specified, while glucose solution was introduced every 50s to the NaOH solution. The solution was continuously stirred during chronoamperometric measurements in order to rapidly homogenize the glucose concentration in the solution.

A.6 Acknowledgements

This material is based upon work supported by the National Science Foundation under Grant No. 1439494 and 1444473. Any opinions, findings, and conclusions or recommendations expressed in this material are those of the authors and do not necessarily reflect the views of the National Science Foundation.

A.7 References

1. Toghill, K.E. and R.G. Compton, *Electrochemical non-enzymatic glucose sensors: a perspective and an evaluation.* Int. J. Electrochem. Sci, 2010. **5**(9): p. 1246-1301.
2. Gao, Z.-D., et al., *One-Step to Prepare Self-Organized Nanoporous NiO/TiO_2 Layers and its Use in Non-Enzymatic Glucose Sensing.* Sci. Rep., 2013. **3**.
3. Lang, X.-Y., et al., *Nanoporous gold supported cobalt oxide microelectrodes as high-performance electrochemical biosensors.* Nat. Commun., 2013. **4**.
4. Wang, G., et al., *Free-standing nickel oxide nanoflake arrays: synthesis and application for highly sensitive non-enzymatic glucose sensors.* Nanoscale, 2012. **4**(10): p. 3123-3127.
5. Salunkhe, R.R., et al., *Aligned nickel-cobalt hydroxide nanorod arrays for electrochemical pseudocapacitor applications.* R. Soc. Chem. Adv., 2012. **2**(8): p. 3190-3193.
6. Mahajan, S.V., et al., *Carbon nanotube–nanocrystal heterostructures fabricated by electrophoretic deposition.* Nanotechnology, 2008. **19**(19): p. 195301.
7. Subramanian, P., et al., *Preparation of reduced graphene oxide–Ni $(OH)_2$ composites by electrophoretic deposition: application for non-enzymatic glucose sensing.* J. Mater. Chem. A, 2014. **2**(15): p. 5525-5533.
8. Wu, M.-S., et al., *Formation of nano-scaled crevices and spacers in NiO-attached graphene oxide nanosheets for supercapacitors.* J. Mater. Chem., 2012. **22**(6): p. 2442-2448.
9. Besra, L., et al., *Experimental verification of pH localization mechanism of particle consolidation at the electrode/solution interface and its application to pulsed DC electrophoretic deposition (EPD).* J. Eur. Ceram. Soc., 2010. **30**(5): p. 1187-1193.

10. Ma, R., et al., *Topochemical Synthesis of Co−Fe Layered Double Hydroxides at Varied Fe/Co Ratios: Unique Intercalation of Triiodide and Its Profound Effect.* J. Am. Chem. Soc., 2010. **133**(3): p. 613-620.

11. Roginskaya, Y.E., et al., *Characterization of Bulk and Surface Composition of $Co_xNi_{1-x}O_y$ Mixed Oxides for Electrocatalysis.* Langmuir, 1997. **13**(17): p. 4621-4627.

12. Li, J., et al., *The role of iron oxide in the highly effective Fe-modified Co_3O_4 catalyst for low-temperature CO oxidation.* R. Soc. Chem. Adv., 2013. **3**(30): p. 12409-12416.

APPENDIX B

COPYRIGHT PERMISSION FOR CHAPTER 2

TERMS AND CONDITIONS

This copyrighted material is owned by or exclusively licensed to John Wiley & Sons, Inc. or one of its group companies (each a"Wiley Company") or handled on behalf of a society with which a Wiley Company has exclusive publishing rights in relation to a particular work (collectively "WILEY"). By clicking "accept" in connection with completing this licensing transaction, you agree that the following terms and conditions apply to this transaction (along with the billing and payment terms and conditions established by the Copyright Clearance Center Inc., ("CCC's Billing and Payment terms and conditions"), at the time that you opened your RightsLink account (these are available at any time at http://myaccount.copyright.com).

Terms and Conditions

- The materials you have requested permission to reproduce or reuse (the "Wiley Materials") are protected by copyright.

- You are hereby granted a personal, non-exclusive, non-sub licensable (on a stand-alone basis), non-transferable, worldwide, limited license to reproduce the Wiley Materials for the purpose specified in the licensing process. This license, **and any CONTENT (PDF or image file) purchased as part of your order,** is for a one-time use only and limited to any maximum distribution number specified in the license. The first instance of republication or reuse granted by this license must be completed within two years of the date of the grant of this license (although copies prepared before the end date may be distributed thereafter). The Wiley Materials shall not be used in any other manner or for any other purpose, beyond what is granted in the license. Permission is granted subject to an appropriate acknowledgement given to the author, title of the material/book/journal and the publisher. You shall also duplicate the copyright notice that appears in the Wiley publication in your use of the Wiley Material. Permission is also granted on the understanding that nowhere in the text is a previously published source acknowledged for all or part of this Wiley Material. Any third party content is expressly excluded from this permission.

- With respect to the Wiley Materials, all rights are reserved. Except as expressly granted by the terms of the license, no part of the Wiley Materials may be copied, modified, adapted (except for minor reformatting required by the new Publication), translated, reproduced, transferred or distributed, in any form or by any means, and no derivative works may be made based on the Wiley Materials without the prior permission of the respective copyright owner.**For STM Signatory Publishers clearing permission under the terms of the STM Permissions Guidelines only, the terms of the license are extended to include subsequent editions and for editions in other languages, provided such editions are for the work as a whole in situ and does not involve the separate exploitation of the permitted figures or extracts,** You may not alter, remove or suppress in any manner any copyright, trademark or other notices displayed by the Wiley Materials. You may not license, rent, sell, loan, lease, pledge, offer as security, transfer or assign the Wiley Materials on a stand-alone basis, or any of the rights granted to you hereunder to any other person.

- The Wiley Materials and all of the intellectual property rights therein shall at all times remain the exclusive property of John Wiley & Sons Inc, the Wiley Companies, or their respective licensors, and your interest therein is only that of having possession of and the right to reproduce the Wiley Materials pursuant to Section 2 herein during the continuance of this Agreement. You agree that you own no right, title or interest in or to the Wiley Materials or any of the intellectual property rights therein. You shall have no rights hereunder other than the license as provided for above in Section 2. No right, license or interest to any trademark, trade name, service mark or other branding ("Marks") of WILEY or its licensors is granted hereunder, and you agree that you shall not assert any such right, license or interest with respect thereto

- NEITHER WILEY NOR ITS LICENSORS MAKES ANY WARRANTY OR REPRESENTATION OF ANY KIND TO YOU OR ANY THIRD PARTY, EXPRESS, IMPLIED OR STATUTORY, WITH RESPECT TO THE MATERIALS OR THE ACCURACY OF ANY INFORMATION CONTAINED IN THE MATERIALS, INCLUDING, WITHOUT LIMITATION, ANY IMPLIED WARRANTY OF MERCHANTABILITY, ACCURACY, SATISFACTORY QUALITY, FITNESS FOR A PARTICULAR

PURPOSE, USABILITY, INTEGRATION OR NON-INFRINGEMENT AND ALL SUCH WARRANTIES ARE HEREBY EXCLUDED BY WILEY AND ITS LICENSORS AND WAIVED BY YOU.

- WILEY shall have the right to terminate this Agreement immediately upon breach of this Agreement by you.

- You shall indemnify, defend and hold harmless WILEY, its Licensors and their respective directors, officers, agents and employees, from and against any actual or threatened claims, demands, causes of action or proceedings arising from any breach of this Agreement by you.

- IN NO EVENT SHALL WILEY OR ITS LICENSORS BE LIABLE TO YOU OR ANY OTHER PARTY OR ANY OTHER PERSON OR ENTITY FOR ANY SPECIAL, CONSEQUENTIAL, INCIDENTAL, INDIRECT, EXEMPLARY OR PUNITIVE DAMAGES, HOWEVER CAUSED, ARISING OUT OF OR IN CONNECTION WITH THE DOWNLOADING, PROVISIONING, VIEWING OR USE OF THE MATERIALS REGARDLESS OF THE FORM OF ACTION, WHETHER FOR BREACH OF CONTRACT, BREACH OF WARRANTY, TORT, NEGLIGENCE, INFRINGEMENT OR OTHERWISE (INCLUDING, WITHOUT LIMITATION, DAMAGES BASED ON LOSS OF PROFITS, DATA, FILES, USE, BUSINESS OPPORTUNITY OR CLAIMS OF THIRD PARTIES), AND WHETHER OR NOT THE PARTY HAS BEEN ADVISED OF THE POSSIBILITY OF SUCH DAMAGES. THIS LIMITATION SHALL APPLY NOTWITHSTANDING ANY FAILURE OF ESSENTIAL PURPOSE OF ANY LIMITED REMEDY PROVIDED HEREIN.

- Should any provision of this Agreement be held by a court of competent jurisdiction to be illegal, invalid, or unenforceable, that provision shall be deemed amended to achieve as nearly as possible the same economic effect as the original provision, and the legality, validity and enforceability of the remaining provisions of this Agreement shall not be affected or impaired thereby.

- The failure of either party to enforce any term or condition of this Agreement shall not constitute a waiver of either party's right to enforce each and every term and condition of this Agreement. No breach under this agreement shall be deemed waived or excused by either party unless such waiver or consent is in writing signed by the party granting such waiver or consent. The waiver by or consent of a party to a breach of any provision of this Agreement shall not operate or be construed as a waiver of or consent to any other or subsequent breach by such other party.

- This Agreement may not be assigned (including by operation of law or otherwise) by you without WILEY's prior written consent.

- Any fee required for this permission shall be non-refundable after thirty (30) days from receipt by the CCC.

- These terms and conditions together with CCC's Billing and Payment terms and conditions (which are incorporated herein) form the entire agreement between you and WILEY concerning this licensing transaction and (in the absence of fraud) supersedes all prior agreements and representations of the parties, oral or written. This Agreement may not be amended except in writing signed by both parties. This Agreement shall be binding upon and inure to the benefit of the parties' successors, legal representatives, and authorized assigns.

- In the event of any conflict between your obligations established by these terms and conditions and those established by CCC's Billing and Payment terms and conditions, these terms and conditions shall prevail.

- WILEY expressly reserves all rights not specifically granted in the combination of (i) the license details provided by you and accepted in the course of this licensing transaction, (ii) these terms and conditions and (iii) CCC's Billing and Payment terms and conditions.

- This Agreement will be void if the Type of Use, Format, Circulation, or Requestor Type was misrepresented during the licensing process.

- This Agreement shall be governed by and construed in accordance with the laws of the State of New York, USA, without regards to such state's conflict of law rules. Any legal action, suit or proceeding arising out of or relating to these Terms and Conditions or the breach thereof shall be instituted in a court of competent jurisdiction in New York County in the State of New York in the United States of America and each party hereby consents and submits to the personal jurisdiction of such court, waives any objection to venue in such court and consents to service of process by registered or certified mail, return receipt requested, at the last known address of such party.

WILEY OPEN ACCESS TERMS AND CONDITIONS

Wiley Publishes Open Access Articles in fully Open Access Journals and in Subscription journals offering Online Open. Although most of the fully Open Access journals publish open access articles under the terms of the Creative Commons Attribution (CC BY) License only, the subscription journals and a few of the Open Access Journals offer a choice of Creative Commons Licenses. The license type is clearly identified on the article.

The Creative Commons Attribution License

The Creative Commons Attribution License (CC-BY) allows users to copy, distribute and transmit an article, adapt the article and make commercial use of the article. The CC-BY license permits commercial and non-

Creative Commons Attribution Non-Commercial License

The Creative Commons Attribution Non-Commercial (CC-BY-NC)License permits use, distribution and reproduction in any medium, provided the original work is properly cited and is not used for commercial purposes. (see below)

Creative Commons Attribution-Non-Commercial-NoDerivs License

The Creative Commons Attribution Non-Commercial-NoDerivs License (CC-BY-NC-ND) permits use, distribution and reproduction in any medium, provided the original work is properly cited, is not used for commercial purposes and no modifications or adaptations are made. (see below)

Use by commercial "for-profit" organizations

Use of Wiley Open Access articles for commercial, promotional, or marketing purposes requires further explicit permission from Wiley and will be subject to a fee.

Further details can be found on Wiley Online Library http://olabout.wiley.com/WileyCDA/Section/id-410895.html

Other Terms and Conditions:

v1.10 Last updated September 2015

APPENDIX C

COPYRIGHT PERMISSION FOR CHAPTER 3

Title: Enhanced Oxygen Evolution Reaction Electrocatalysis via Electrodeposited Amorphous α-Phase Nickel-Cobalt Hydroxide Nanodendrite Forests

Author: Anirudh Balram, Hanfei Zhang, Sunand Santhanagopalan

Publication: Applied Materials

Publisher: American Chemical Society

Date: Aug 1, 2017

PERMISSION/LICENSE IS GRANTED FOR YOUR ORDER AT NO CHARGE

This type of permission/license, instead of the standard Terms & Conditions, is sent to you because no fee is being charged for your order. Please note the following:

- Permission is granted for your request in both print and electronic formats, and translations.
- If figures and/or tables were requested, they may be adapted or used in part.
- Please print this page for your records and send a copy of it to your publisher/graduate school.
- Appropriate credit for the requested material should be given as follows: "Reprinted (adapted) with permission from (COMPLETE REFERENCE CITATION). Copyright (YEAR) American Chemical Society." Insert appropriate information in place of the capitalized words.
- One-time permission is granted only for the use specified in your request. No additional uses are granted (such as derivative works or other editions). For any other uses, please submit a new request.

BACK | CLOSE WINDOW